UNIVERSITY OF CALIFORNIA, SAN DIEGO

Temporal Studies of Black Hole X-ray Transients During Outburst Decay

A dissertation submitted in partial satisfaction of the requirements for the degree Doctor of Philosophy in Physics

by

Emrah Kalemci

Committee in charge:

Laurence Peterson, Chair
Richard Rothschild, Co-Chair
Sadik Esener
George Fuller
Kim Griest
Barnaby Rickett

2002

The dissertation of Emrah Kalemci is approved, and it is acceptable in quality and form for publication on microfilm:

Co-Chair

Chair

University of California, San Diego

2002

To my wife Funda and my family...

TABLE OF CONTENTS

LIST OF FIGURES

LIST OF TABLES

ACKNOWLEDGMENTS

My wife always tells me that I am one lucky cat that always lands on four feet. I feel extremely lucky for spending my graduate career and finish my PhD at CASS. Continuous help of all the scientists at CASS has made this work possible. Rick Rothschild is one the coolest thesis advisors in the universe. His door has always been open to listen to my problems and answer my questions. I thank him very much for his guidance. I also feel very lucky to be able to work with John Tomsick. He was a recently graduated postdoc when we started to work together, and he had a genuine understanding of what I had been going through as a graduate student. We not only built a very strong collaboration, but also a strong friendship as well. Biff Heindl has always answered my questions patiently no matter how stupid they were and deserves a special thanks for his overall contribution to my scientific knowledge. I also would like to thank my faculty advisor Larry Peterson. During the time I was working on CdZnTe detectors I had a chance to work with Jim Matteson, who is like a huge library with endless knowledge on space instrumentation. I thank him for sharing his knowledge with me, although the library's hours of operation is so random and unexpected that it tests one's patience. Tom Skelton, Fred Duttweiler, George Huszar and Tom Gasaway at CASS and Kim Slavis from Univ. of Washington, St. Louis deserve my special thanks for their support for the CdZnTe research. A very very special thanks is for the computer support group at CASS. Absolutely everything I asked for in terms of computer support was done in a timely manner and best possible way, thanks to Pete James and Paul Yeatman. I believe only a few workplaces have a luxury of calling a computer person at 10 pm to restore a deleted directory in return for a cigar and some hanging out. I also thank the administrative assistants Cheryl Matson & Shirley Roy and the business office personnel, especially Susanna Pastell-Mendoza and Andi Stephans. Debra Bomar, the graduate secretary at the Physics Department, has been incredibly helpful and made everything as easy as possible for a new-coming student from Turkey. Also thanks to Doug Broadhurst at the International Center for his helps on the complicated INS paperwork.

"The monkeys" whom I shared office with, David Marsden and Wayne Coburn, and all graduate students, postdocs and friends I have worked and hung out with,

Joh3n (shut up!), Jeff, Nao, Neal, Dinesh, Lucas, Omar, Hugh Jorgan, Larry, Rune, Sean, Jason, Dawn, and others, thank you. Wayne deserves more than just mentioning his name, not only for sharing his expertise on RXTE data analysis with me while I was a freshman graduate student, but also for his helps on launching my postdoc position at SSL and being a buffer between me and my next boss, Steve Boggs. Steve, by the way, thanks a lot for offering me a very good position, and making my last days as a graduate student less stressful. I am looking forward to join Wayne and Steve at SSL, Berkeley.

I would like to thank my collaborators Katja Pottschmidt, Phil Kaaret, Stephane Corbel, Jon Miller, and Rudy Wijnands who contributed enormously to my research. Katja from AIT deserves special treatment in the acknowledgments, since without her IDL timing programs, this work would not be possible. During my collaboration with her, I had two visits to AIT, Tübingen. I want to thank Prof. Ruediger Staubert who not only made this visits possible, also provided me with recommendation letters during my job hunt. I also want to thank Jörn Wilms at AIT for his helps on Monte Carlo simulations of accretion disks and RXTE data analysis. I had really great time in Tübingen and looking forward to further collaborations. I had very nice and stimulating discussions with Dimitrios Psaltis, Ron Remillard, Mike Nowak, Craig Markwardt and Hank Spruit on my research, thank you also. I also would like to thank the crew of Cafe 976 at Pacific Beach where a considerable portion of this thesis was written.

I would like to thank to the people at High Energy Astrophysics Group at METU, Ali Alpar, Ümit Kızıloglu, Altan Baykal, Akif Esendemir and the graduate students which I had great time with, Ersin, Ünal, Çagdas (aslanım kaplanım), Aşkın, Atakan, Efe and Burçin. Prof. Alpar is one of the main reasons that I have chosen astrophysics as my specialty, and I really appreciate his continuous support throughout my career here. He has been an invaluable mentor, and I am looking forward to work with him in Turkey when I finish my career in the US. Bülent Akınoğlu and Bahtiyar Salamov also deserves my thanks since they introduced me to the wonders of research while I was still an undergrad. Thank you Oktel, Varol, Defne, Murat, Mohaç, Mithat, Ulaş and other friends whom I know from METU Physics, studying physics was more fun because of you. I thank Defne who also came to UCSD Physics and continued to be

one of my closest friends.

I would like to thank my Turkish buddies İsmet, Emel, Yavuz, Yeliz, Özgürs, Elif, Selim, and others during my stay in San Diego for their friendship. I cannot list everyone, the space is not enough. I want to thank all my friends whom I played basketball on Sundays, Süleyman, TI Barış, Emrah, team Costa Verde, Mehmet, and others. Special thanks to the members of the Turkish Student Association Executive Committee. Thank you Gökçe and Gala for your helps and hospitality during my first days in San Diego.

Special thanks go out to my friends, Arkadaş, Özge, Özlem, Kivanç, ÖC, Erkan, Hakan, Tümay, Bariş, Ahmet, Neslihan, Ezgi, Kerem from AFL. The days we spent together in the boarding school contributed my mental and intellectual development and resulted in very strong friendships that continue although we are scattered in different continents. Thank you my middle school buddies, Oğuzkan, Ege, Dinç, Ata, Taylan and Özgür for showing there is more to life than just classes.

I am sure I forgot many friends and scientist who contributed my development as a scientist and to this work, I apologize. Before stating my mandatory acknowledgments, I also want to thank my mom and dad who alway supported me regardless of what kind of stupidity that I had done. Mom, I wish you could see me graduated, huzur içinde uyu. Thank you my grandma Nezahat just for your unconditional caring for me, and all my other family members. Finally, I would like to thank my wife, Funda, who has sacrificed so much just to be with me and make my life infinitely better.

The text of section 4.1, in part, is reprint of the material as it has been recommended for publication to the Astrophysical Journal. The text of section 4.7, in part, is reprint of the material as it has been published in the Astrophysical Journal. I was the primary author in these works. I was partially supported at UCSD by NASA contract NAS5-30720, by the Scientific and Technical Research Council of Turkey (TÜBİTAK) through a NATO A1 scholarship, and also as CASS graduate researcher.

VITA

1974 May 28	Born, Denizli, Turkey
1996	B.S. with High Honors, Physics Middle East Technical University, Ankara, Turkey
1996-1997	Teaching Assistant, Department of Physics Middle East Technical University, Ankara, Turkey
1997	Teaching Assistant, Department of Physics University of California, San Diego
1998-2002	Graduate Student Researcher, University of California, San Diego
2000	M.S., Physics, University of California, San Diego
2002	Doctor of Philosophy University of California, San Diego

PUBLICATIONS

Kalemci, E., Tomsick, J. A., Rothschild, R. E., Pottschmidt, K., Corbel, S., Wijnands, R., Miller, J. M., Kaaret, P. 2002, "X-ray Temporal Properties of XTE J1650−500 During Outburst Decay", *ApJ*, in press

Kalemci, E., Tomsick, J. A., Rothschild, R. E., Pottschmidt, K., Kaaret, P. 2001, "X-ray observations of XTE J1550−564 During the Decay of the 2000 Outburst-II. Timing", *ApJ*, **563**, 239

Corbel, S., Kaaret, P., Jain, R. K., Bailyn, C. D., Fender, R. P., Tomsick, J. A., Kalemci, E., McIntyrem, V., Campbell-Wilson, D., Miller, J. M., McCollough, M. L. 2001, "X-ray States and Radio emission in the Black Hole Candidate XTE J1550−564", *ApJ*, **554**, 43

Kalemci, E., Tomsick, J. A., Rothschild, R. E., Pottschmidt, K., Corbel, S., Wijnands, R., Miller, J. M., Kaaret, P. 2002, "X-ray Temporal Properties of XTE J1650−500 During Outburst Decay", *Proceedings of the 4th Microquasar Workshop*

Kalemci E., Tomsick, J. A., Rothschild, R., Corbel, S., Kaaret, P., McClintock, J. 2002, "State Transition of the Black Hole Candidate 4U 1543−47" *ATEL*, **103**

Smith, D. M., Belloni, T., Heindl, W. A., Kalemci, E., Remillard, R., Nowak, M., Swank, J. H., Corbel, S. 2002, "GX 339-4", *I.A.U. Circular*, **7912**

Tomsick, J. A., Kalemci, E., Corbel, S., Kaaret, P. 2002, "XTE J1650−500", *I.A.U. Circular*, **7837**

Rodriguez, J. Corbel, S. Kalemci, E. and Tomsick, J. A. Tagger, M. 2002, "Timing analysis of XTE J1550−564 during the 2000 outburst revealing the nature of a low frequency QPO", *ApJ* submitted

Rodriguez, J. Corbel, S. Kalemci, E., Tomsick, J. A. Tagger, M. 2002, "Evolution of a low frequency QPO during the 2000 outburst of XTE J1550−564", *Proceedings of the 4th Microquasar Workshop*, **7649**

Kalemci, E., Matteson, J. L. 2002, "Charge Sharing among the electrodes of a CdZnTe Detector", *NIM-A*, **478/3**, 259

Kalemci, E., Matteson, J. L. 2000, "Charge Splitting Among the Electrodes of a CdZnTe Detector", *Proc. SPIE*, **4141**, 235

Kalemci, E., Matteson, J. L., Skelton, R. T., Hink, P. L., Slavis, K. R. 2000, "Modeling of CZT Strip Detectors", *Proceedings of the Fifth Compton Symposium*, 769

Kalemci, E., Matteson, J. L., Skelton, R. T., Hink, P. L., Slavis, K. R. 1999, "Model Calculations of the Response of CZT Strip Detectors", *Proc. SPIE*, **3768**, 360

Slavis, K. R., Dowkontt, P. F., Duttweiler, F., Epstein, J. W., Hink, P. L., Huszar, G. L., Kalemci, E., Leblanc, P. C., Matteson, J. L., Pelling, M. R., and Rothschild, R. E., Stephan, E. A., Tumer, T. O., Visser, G. J. 2000, "Performance of a prototype CdZnTe detector module for hard X-ray astrophysics", *Proc. SPIE*, **4140**, 249

Salamov, B. G., Kalemci, E., Bulur, E., Akinoglu, B. G. 1996, "A system to visualize the resistivity inhomogeneities in high-ohmic semiconductors", *Cryst. Res. Technol.*, **31**, 151

FIELDS OF STUDY

Major Field: Physics

Studies in Classical Mechanics
Professor Patrick Diamond

Studies in Statistical Mechanics
Professor Terrence Hwa

Studies in Mathematical Methods
Professor Anesh Manohar

Studies in Quantum Mechanics
Professor George Fuller

Studies in Electromagnetism
Professor Daniel Dubin

Studies in General Relativity and Cosmology
Professor George Fuller

Studies in Astrophysics
Professors George Fuller and Arthur Wolfe

Studies in Plasma Physics
Professor Vitali Shapiro

ABSTRACT OF THE DISSERTATION

Temporal Studies of Black Hole X-ray Transients
During Outburst Decay

by

Emrah Kalemci
Doctor of Philosophy in Physics
University of California, San Diego, 2002
Professor Laurence Peterson, Chair

Galactic black holes (GBH) are a class of astrophysical sources with X-ray emission that is powered by accretion from a companion star. An important goal of GBH research is to understand the accretion structure (i.e. relative orientation, temperature and density profiles of the accretion components) and the nature of the variability of these systems. The majority of GBHs are transient sources and are most often observed during outbursts. They sometimes show significant changes in the X-ray emission properties, and these changes are called state transitions. The transitions are believed to be caused by variation of the mass accretion rate and changes in accretion geometry. Thus, their study provides valuable information on the nature of the accretion structure.

In this thesis work, I present results from studying the spectral and temporal evolution of all GBH transients that have been observed with NASA's *Rossi X-ray Timing Explorer* during outburst decay. This study, which encompasses eleven sources and sixteen outbursts, is possible now because of recent observations with good coverage at the ends of outbursts. This is the first comprehensive and comparative study of GBHs during the transition to the low/hard state (LS), and in the LS with this many sources and outbursts. In this work, I explore the physical conditions before, during and after the state transition, characterize the quasi-periodic oscillations (QPO) and

continuum of power spectral density (PSD) in different energy bands, and study the correlations between spectral and temporal fit parameters. I also analyze the evolution of the frequency-dependent and frequency-averaged time lags and the coherence function during and after the transition.

I show that the appearance of the broad band variability is coincident with an increase of power-law flux, and the variability is only observed when the ratio of the power-law flux to the total flux in 3–25 keV band is greater than 0.45. The evolution of the characteristic frequencies and the spectral parameters after the transition are consistent with retreating of the inner accretion disk.

The energy dependent PSD analysis shows that the level of variability increases with energy when there is significant soft flux from the the optically thick accretion disk. This can be understood if the optically thick accretion disk provides mostly "Poissonic" emission, therefore increasing the DC level (and subsequently decreasing the rms amplitude) in lower energy bands. The variability level also increases with energy if the absorption column density to the source is high. This may be a result of small angle scatterings of lower energy X-ray photons with the ISM dust around these sources.

I find global correlations between the spectral index and three temporal fit parameters: the QPO frequency, the overall level of variability and the integrated time lag. The correlation with the QPO frequency has strong implications for the the low frequency QPO models. The relation between the spectral index and the time lags are interpreted within the context of the average number of Compton scatterings and the temperature of the scattering medium. Other correlations between the spectral and temporal parameters are also discussed.

During the transitions, the average lag is higher and average coherence is lower. Moreover, the PSD shape depends on energy. I discuss whether a hybrid accretion model, for which the hot electron corona is the base of an optically thin outflow or a jet, can explain the physical properties during the transition.

Chapter 1

Introduction

“Dünyanın en cesur insanları, hoşgeldiniz...”

- Cem Yılmaz

This dissertation is a study of the accretion structure and the physical environment in the vicinity of Galactic black hole binary systems. The analysis is concentrated on the temporal variability, thanks to the superior timing capability of NASA's *Rossi X-ray Timing Explorer* (*RXTE*) satellite. In particular, I used the modeling of the power spectral density of these systems, as well as other sophisticated timing related functions, such as the time lag and coherence, to understand the accretion structure and the nature of variability of these systems. I also used X-ray energy spectra to understand the physical environment of these systems better. I used eleven *RXTE* sources for this study. This is the first comprehensive, comparative study of the spectral and temporal parameters of these systems with this many sources with the same instrument.

The outline of the thesis is as follows: In the Introduction I summarize the spectral and temporal properties of black hole binary systems along with their basic physical interpretations. At the end of this chapter, I present the source and method selection criteria for this dissertation. In Instrumentation and Spectral Analysis I give information on the detectors of the *RXTE* satellite that I have used in this work. Data accumulation technique, methods of spectral analysis and the details of the spectral models are also given in this chapter. In Temporal Analysis the mathematical groundwork of the timing tools is covered. As in the spectral case, the details of data accumulation and the fit models are discussed at the end. The spectral and temporal analysis of all the individual sources are presented in Results. At the end of each source's section, I provide a summary which gives a quick overview of the interesting results from each source as well as its physical parameters such as the mass and the distance (if known). In Discussion, I mainly concentrate on the global properties of the black hole binary systems by combining individual results. At the end, I summarize my results in Conclusion and Outlook.

1.1 Black hole X-ray binaries

Black holes (BH) are very exotic and fascinating types of object in the universe. Intrinsically, they are simple objects in astronomy, however they have bizarre effects on nearby space and time, and provide a natural laboratory to test General Relativity theory. This work is mostly about the influence of the black holes on nearby matter and radiation. In this section, I will define BHs, and summarize their physical properties, and then discuss some of the physical processes that affect the X-ray spectral and temporal properties of these objects when they are in a binary system.

1.1.1 What is a black hole?

Before describing what a BH is, it is useful to give a very small introduction on "compact objects". Compact objects –white dwarfs, neutron stars (NS) and BHs result when most of their progenitor star's nuclear fuel has been consumed. Compact objects differ from normal stars in two fundamental ways. First, since there is no nuclear burning, they cannot support themselves against gravitational collapse by generating thermal pressure. Instead, white dwarfs are supported by degenerate electron pressure, and NSs are supported by degenerate neutron pressure. Black holes, on the other hand, are completely collapsed stars that could not find any means to hold back the gravitational pull, and therefore collapsed to singularities. Second, as the name implies, the compact objects are exceedingly small in size compared to their masses which results in very strong gravitational field at their surfaces (or close to their event horizons for BHs). Because of the very strong gravitational fields, the theory of General Relativity (GR) is often needed to be invoked to explain the physical environment of these objects.

The main physical parameter that determines the type of compact object formed is the mass of the progenitor star. White dwarfs are believed to originate from light stars ($M \leq 4\mathrm{M}_{\odot}$). Note that a white dwarf has a maximum mass of $\sim$1.4 $\mathrm{M}_{\odot}$ (Chandrasekhar mass). If this mass is exceed during the collapse of heavier stars, a supernova explosion occurs. The end product of this explosion is a NS or BH. However, the dividing line for the mass between the production of a BH or NS is uncertain due to the poor understanding of the final stages of the stellar evolution as well as the uncertainty in the maximum mass of a NS (Shapiro & Teukolsky 1983). A recent study by Fryer & Kalogera (2001) shows that if the main sequence mass of the progenitor is greater than 18 $\mathrm{M}_{\odot}$, it ends up as a BH. Note that BHs can also form if matter is accreted on a NS such that it exceeds its critical mass and cannot support itself against collapse.

As a summary, a BH is a type of compact object collapsed into a singularity after a supernova explosion. At this point, it is appropriate to make the distinction between stellar mass BHs and supermassive BHs. Up to now I have discussed the formation of stellar black holes, with masses on the order of 3 – 10 $\mathrm{M}_{\odot}$. Because of dynamical arguments, it is believed that most (if not all) galaxies contain a BH at its center with a mass of $10^6 - 10^9$ $\mathrm{M}_{\odot}$. These are called supermassive black holes. If a supermassive black hole is also active in X-rays, the host galaxy is designated as having an active galactic nuclei (AGN). Recently, claims of intermediate mass black holes at the center of globular clusters with a mass of $10^2 - 10^3$ $\mathrm{M}_{\odot}$ have been put forward (Miller & Hamilton 2002, and references therein). This thesis addresses only the stellar mass BHs, which are also called Galactic black holes (GBH). I will not discuss the formation mechanisms and physical details of the supermassive and intermediate mass black holes. From here on, BH, GBH, or black hole candidate (BHC) will refer to stellar mass black holes.

A BH, in essence, is the simplest of the compact objects. It is fully described by three parameters: mass, spin and charge, and charge is not relevant for accretion dynamics. The gravitational field around such a collapsed spherical object can be obtained by solving the Einstein's equations, which was successfully done by Schwarzschild (1916) for a neutral, non-rotating object and later generalized by Kerr (1963). That is why a non-rotating black hole is sometimes called a Schwarzschild hole and a rotating one is often called a Kerr hole.

One of the most important physical parameters of a BH is its Schwarzschild radius R_S (which determines the "event horizon") which is equal to:

$$R_S = \frac{2\,GM}{c^2} \sim 3\,\mathrm{km}\frac{M}{M_\odot} \tag{1.1}$$

for a non-rotating BH, where G is the gravitational constant, M is the mass of the BH and c is the speed of light. This is the radius inside of which no information could be sent out to infinity. Also, once matter passes this radius, it must eventually reach the singularity at the center. Another dynamically important parameter is the radius of the marginally stable orbit (or the innermost stable circular orbit, ISCO). Because of GR effects, matter orbiting around the black hole cannot sustain its circular Keplerian orbit for radii less than the ISCO and free falls into the BH. For a non-rotating BH, this radius is at $3R_S$. If the BH rotates, this radius decreases for matter in direct orbits (with a minimum of $R_S/2$), and increases for retrograde orbits (with a maximum of $4.5R_S$).

Finding black holes

It is very difficult to find isolated BHs in our Galaxy, because, by definition, they do not emit any photons[1]. However, nature has provided other means to find these objects. More than 50% of the stars in our Galaxy are in binary systems. As I will discuss in the next section, matter falling into the gravitational well of a compact object from the companion star in a binary system loses some of its potential energy in the form of radiation (mainly in X-rays). If the mass accretion rate is high enough, this radiation can be detected by the X-ray satellites orbiting the earth. These systems are called X-ray binaries (XRB). Therefore, the best places to look

1 Except Hawking radiation, which is impossible to detect from GBHs.

for BHs are in X-ray binary systems. However, an XRB indicates a compact object which is not necessarily a BH. In order to "prove" that the compact object is a BH, one has to show that the particular object is smaller than its event horizon. This is almost impossible to do with direct imaging, taking into account their small sizes and large distances. However, there are indirect methods to determine whether a compact object is a BH or not.

The best indirect method is to determine its mass. As discussed earlier, white dwarfs have a maximum mass. Likewise, NSs also have a maximum mass over which they are unstable to gravitational collapse. This mass has not been determined with good accuracy because of the uncertainty of the equation of state of NSs and other factors such as spin, however most theoreticians believe $3M_{\odot}$ is a safe upper limit for the mass of a NS, assuming no exotic particles preventing the collapse exist and general relativity is correct (Rhoades & Ruffini 1974). Therefore, if we measure the mass of the compact object, and determine that it is greater than 3 $M_{\odot}$, we claim that it is a BH.

Fortunately, being in a binary system helps not only in identifying compact objects but also in determining the masses. When the stellar companion in the binary system is bright, it is sometimes possible to identify absorption lines in the optical spectrum. These lines show a Doppler shift because of the motion around their companion, and the amplitude of this shift can be used in conjunction with the orbital period to obtain the mass function of a binary system as:

$$f(M_1, M_2, i) = \frac{(M_2 \sin i)^3}{(M_1 + M_2)^2} = \frac{P v_1^3}{2\pi G} \tag{1.2}$$

where v_1 is the radial velocity that is obtained from the amplitude of the Doppler shift, M_2 is the mass of the compact object, M_1 is the mass of the companion, P is the binary period and i is the inclination angle of the system with respect to the line of sight. Although the mass function does not provide the mass of the compact object directly, it provides a lower limit (by setting $M_1 = 0$ and $i = 90°$) , which is enough to claim a BH nature if $f \geq 3$. Moreover, better approximations for the mass of the companion through its spectral class and the inclination angle through eclipses (or lack of) can be made to improve the estimate of the compact object mass. The first dynamical measurement that led to the mass of the compact object in the BH

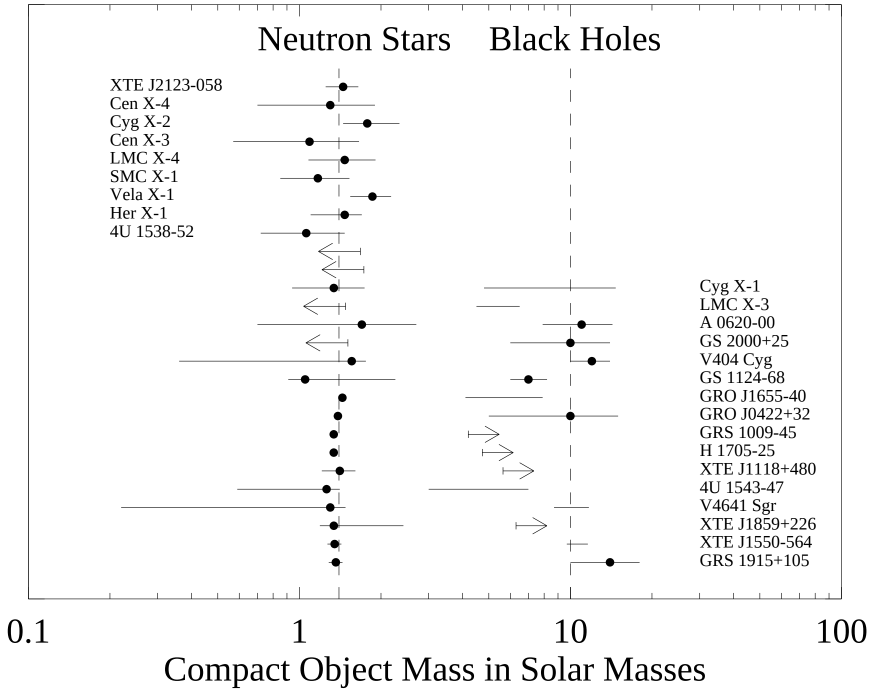

Figure 1.1: Masses of NSs and BHs. The NSs are clustered at around 1.4 $M_{\odot}$. The NSs without identifications are radio pulsars.

regime was for Cyg X-1 (Murdin & Webster 1971). In Fig. 1.1, I show the distinction between the NS and BH masses.

There are also some cases in which the compact object is believed to be a BH because its observational characteristics are very similar to that of the known GBHs. These observational properties are characteristic X-ray spectrum (hard power-law or cut-off power-law and sometimes a soft component modeled as blackbody emission from a range of temperatures), variability up to a few hundred Hz, quasi periodic oscillations (QPO) in 0.1–450 Hz range, and spectral state dependent variability. However, a neutron star's radius is only $\sim$3 times its Schwarzschild radius, hence the accretion onto a low magnetic field neutron star and black hole can be very similar, and most of these characteristic behaviors may also occur in neutron star binaries. Type I X-ray bursts and coherent pulsations can be used to identify the source as a NS because they require a surface. Recent results have presented more ways to distinguish NS and BH systems: e.g., it has been reported that the black hole binaries are generally under-luminous during quiescence as compared to neutron star binaries (possibly due to advection of energy into the black holes, see, Narayan, McClintock & Yi 1996) and that neutron star binaries show stronger aperiodic variability at very high frequencies, i.e., >100 Hz (possibly due to neutron star surface boundary layers, Sunyaev & Revnivtsev 2000).

Black hole systems in our Galaxy, and their classification

There are several ways to classify GBHs. The first one is to classify them according to their identification, i.e. mass function identified or observationally identified. Mass function identified ones either have $f \geq 3$ or their estimated masses are greater than $3M_{\odot}$. The sources without mass function measurement, but showing observationally similar characteristics to the known GBHs are called observationally identified. I show all known BH systems in two tables, the ones that are identified by mass function in Table 1.1 and the ones that are identified observationally in Table 1.2. GRO J0422+32 and 4U 1543−47 show a low mass function in Table 1.1, but they have low inclination, and their estimated masses are higher than $3M_{\odot}$. The second way is to classify them as persistent and transient sources (identified as “Per” and “Tr” respectively in Tables 1.1 and 1.2) since not all BH binaries are observable all the time. In fact, most of them are transients, and this work is based on the study of transient sources. The distinction between the persistent and the transient sources is believed to lie mainly in the nature of the companion star delivering the material: in case of an early type donor (O- or B-star) a strong stellar wind is usually continually present and the X-ray emission is comparatively steady resulting in persistent sources. These companions are high mass stars, which also identifies the third classification method based on the companion mass. High mass X-ray binaries (HMXB, denoted with “HM” in Tables 1.1 and 1.2) contain an early type companion whereas low mass X-ray binaries (LMXB, denoted with “LM” in Tables 1.1 and 1.2) contain a low mass, late type companion. Therefore the persistent GBHs are usually HMXBs. If the donor is a late type star, however, accretion proceeds via Roche lobe overflow. In this case, the accretion might follow cycles when the companion is over- and under-filling the Roche-lobe (see section 1.3), i.e, of enhanced mass transfer (leading to X-ray outbursts) and no mass transfer (leading to X-ray quiescence) to the compact object. I give a more

Table 1.1: Black holes identified with mass function or mass

Name[a]	Mass function ($M_\odot$)	Class[b]
GRO J0422+32	1.13 ± 0.09	LM, Tr
A 0620−00	2.91 ± 0.08	LM, Tr
GRS 1009−45	3.17 ± 0.12	LM, Tr
XTE J1118+480	6.00 ± 0.36	LM, Tr
GS 1124−68	3.01 ± 0.15	LM, Tr
4U 1543−47	0.22 ± 0.02	LM, Tr
XTE J1550−564	6.86 ± 0.71	LM, Tr, MQ
GRO J1655−40	2.73 ± 0.09	LM, Tr, MQ
H 1705−25	3.24 ± 0.09	LM, Tr
SAX J1819.3−2525	2.74 ± 0.12	HM, Tr
XTE J1859+226	7.4 ± 1.1	LM, Tr
GRS 1915+105	9.5 ± 3.0	LM, Tr, MQ
Cyg X-1	0.25 ± 0.01	HM, Per
GS 2000+25	5.01 ± 0.12	LM, Tr
GS 2023+338	6.07 ± 0.05	LM, Tr
Cyg X-3 (?)	2.3	HM, Per, MQ

a The sources used in this study are shown with boldface font.
b LM = low mass X-ray binary, Tr = transient, MQ = microquasar, Per = Persistent, HM = high mass X-ray binary

detailed discussion of transient mechanisms in section 1.2. The transients are usually LMXBs. Note that the companion star has not been identified for all known GBHs, especially for the transients, since the low luminosity companions can be difficult to detect. Also, the association of accretion mechanism with the nature of the companion star is not clear cut, there are Roche-lobe filling HM systems and transient systems that are HM.

Among the transient sources, there also exists a subclass called microquasars (denoted with "MQ" in Tables 1.1 and 1.2). These are sources that show discrete ejections of radio emitting blobs of material with apparent superluminal speeds [2]. Most GBHs show radio emission especially in certain states, and only the ones that show the superluminal material ejections are called microquasars in analogy with the extragalactic radio quasars.

2 The material is actually moving with a speed of several tenths of the speed of light.

Table 1.2: Observationally identified black holes

Name[a]	Mass function ($M_\odot$)	Class[b]
XTE J0421+560 (?)	-	HM,Tr
GS 1354−645	-	LM, Tr
A 1524−62	-	LM, Tr
4U 1630−47	-	LM, Tr
XTE J1650−500	0.64 ± 0.03	LM, Tr
GX 339−4	-	LM, Tr
GRS 1716−249	-	LM, Tr
KS 1730−312	-	LM, Tr
GRS J1737−31	-	LM, Tr
GRS 1739−278	-	LM, Tr
1E 1740.7−2942	-	LM, Per
H 1743−32	-	LM, Tr
SLX 1746−331	-	LM, Tr
XTE J1748−288	-	LM, Tr
XTE J1755−324	-	LM, Tr
4U 1755−338	-	LM, Tr
GRS 1758−258	-	LM, Per
SAX J1805.5−2031	-	LM, Tr
GS 1826−24	-	LM, Tr
EXO 1846−031	-	LM, Tr
XTE J1901+014	-	LM, Tr
XTE J1908+094	-	LM, Tr
4U 1957+11 (?)	-	LM, Per
XTE J2012+381	-	LM, Tr

a The sources used in this study are shown with boldface font.
b Same as Table 1.1

1.2 Outbursts and transient mechanisms

Outbursts and transient mechanisms are inherent to black holes in LMXBs. Because all LMXBs are variable, the distinction of transients from persistent sources undergoing a large intensity increase may be ambiguous. Tanaka & Shibazaki (1996) employed the following criteria to define an X-ray nova (i.e. an outburst):

- The X-ray flux increases by more than two orders of magnitude within several days,

- The flux declines on time scales of several tens of days to more than one hundred days, and it eventually returns to the pre-outburst level,
- In recurrent transients, the duration of an outburst is shorter than the quiescent period. The duty ratio over a long time span is less than unity,
- There is no fixed periodicity of recurrence.

An outburst is caused by a sudden dramatic increase of mass accretion onto the compact object. During an outburst, due to X-ray illumination, the disk also brightens in optical. Often radio outbursts are observed with the X-ray outbursts.

The X-ray light curve of the outburst differs from source to source (see Chapter 4 for several X-ray outburst light curves), however some of them show similarities. They start with a very fast rise, followed by a smooth exponential decay (Fast Rise, Exponential Decay, FRED).

The single most important parameter determining whether a source is a transient or persistent is the mass accretion rate. It is observed that the stable mass accretion onto the compact objects is not maintained below an accretion rate of $\sim 10^{16}\,\mathrm{g\,s^{-1}}$ (Tanaka & Shibazaki 1996). On the other hand, for some sources, optical emission during quiescence points to a disk origin indicating that the mass accretion into the disk from the companion star still continues. This means that a large fraction of the transferred matter remains in the disk during a quiescent interval. The potential energy of the accumulated matter can account for the total energy of the next outburst. Two competing models have been proposed to explain the outbursts. The first one is the disk instability models (Lin & Taam 1984; Cannizzo, Wheeler & Ghosh 1985; Mineshige & Wheeler 1989) and the second one is the mass transfer instability models (Osaki 1985; Hameury, King & Lasota 1990).

A thermal instability triggers the outburst in the disk instability models. An accretion disk is stable both in a cool, neutral state and in a hot, fully ionized state. During quiescence, the accretion disk is cool and neutral. As matter accumulates in the disk, both the surface density and the temperature increases. When the surface density reaches a critical point, a thermal instability sets in. This instability arises from a very steep temperature dependence of the opacity in a partially ionized accretion disk. The disk jumps to the hot state with much higher viscosity causing rapid infall of the matter onto the compact object creating an X-ray outburst. When the surface density falls below a lower critical value, the disk returns to the cool state (Tanaka & Shibazaki 1996). The advantage of this model is that it can explain the rise, decay and recurrence times of X-ray outbursts fairly well.

In the mass transfer instability models, the subphotospheric layers of a companion star are considered to be heated by relatively hard (>7 keV) X-rays from the compact object. These layers expand and bring the atmosphere into an unstable regime which leads to a sudden mass transfer. When the $L1$ region[3] is shielded by the accretion disk, the swelling of the companion star stops, ending the mass transfer. The outburst ends when all the mass in the accretion disk is transferred onto the compact object. Although this model can also explain the observed rise, decay and recurrence times, there is a severe problem. In order for this model to trigger an outburst, the hard X-ray flux at the $L1$ point must exceed the intrinsic stellar flux. However, the X-ray luminosity during quiescence is too low to induce this instability. Thus, this mechanism appears to be unlikely (Tanaka & Shibazaki 1996).

1.3 X-ray emission mechanisms of black hole binaries

In this section, I discuss the basic mechanisms for the mass transfer from the companion star to the BH. In addition, I summarize how this mass accretion turns into X-rays that we observe.

In order to understand the mass transfer in a binary system, the gravitational potential that characterizes such a system has to be taken into account. This potential has been derived for an idealized case by the French mathematician Edouard Roche in the 19th century. For two point masses M_1 and M_2 in circular Kepler orbits around their center of mass, it takes the following form, if calculated in coordinates co-rotating with the binary orbit and with their origin in the center of mass of the

3 The inner Lagrangian point through which mass transfer takes place, see section 1.3

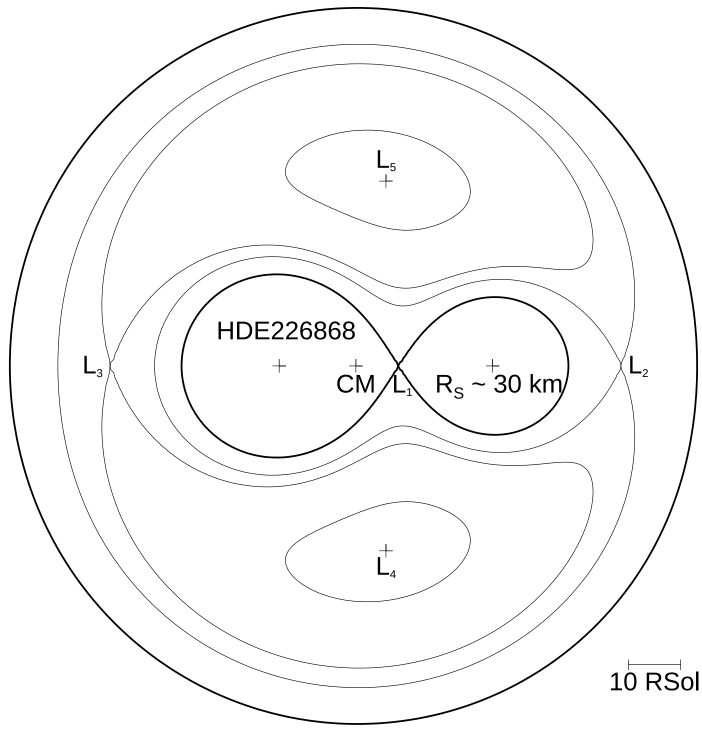

Figure 1.2: Equipotential lines of the Roche potential, Eq. (1.3), calculated for the system parameters of the HDE 226868/Cyg X-1 binary (as given by Herrero et al. 1995). Here the cross section of $\Phi(\mathbf{r})$ through the binary plane is shown.

system (Frank, King & Raine 1992, page 48):

$$\Phi(\mathbf{r}) = -\frac{GM_1}{|\mathbf{r} - \mathbf{r_1}|} - \frac{GM_2}{|\mathbf{r} - \mathbf{r_2}|} - \frac{(\boldsymbol{\omega} \times \mathbf{r})^2}{2} \tag{1.3}$$

where: $\mathbf{r}$: position, for which the potential is calculated,
ω: angular velocity in non-co-rotating coordinates,
$\mathbf{r_1}$, $\mathbf{r_2}$: position of the two binary components.

Fig. 1.2 shows the equipotential lines of the Roche potential (corresponding to equipotential surfaces in the three dimensional case), calculated for two point masses of $18\mathrm{M}_\odot$ and $10\mathrm{M}_\odot$ (Cyg X-1). In reality the two binary components are spatially extended, however the Roche approximation is adequate to illustrate the principal properties of the mass transfer in X-ray binaries. As can be seen from the figure, each component has its own potential well or "Roche Lobe" (innermost solid line). It defines a volume within which a mass element is bound to one of the two components. There are several equilibrium locations in the potential, where no force is acting on a point mass (Lagrange points L1–L5). The saddle point L1 between the two components is an important one. If material from the donor star reaches this point possessing momentum in the outward direction, it can enter the Roche lobe of the compact component. A similar case can be made for matter crossing L2 inwards. There are three mechanisms known by which such a mass transfer can proceed:

- Wind accretion: If the donor star is of an early type, it usually has a strong stellar wind that can send matter into the Roche lobe of the black hole. This may either happen directly, via L1, or the stellar wind may lose its kinetic energy and angular momentum in the neighborhood of L2. Typical mass loss rates via a stellar wind are in the range of $10^{-6} - 10^{-5}\,\mathrm{M}_\odot/\mathrm{yr}$, with an estimated $0.01 - 0.1\%$ of that being transferred to the black hole (Frank, King & Raine 1992).

- Roche lobe overflow accretion: If the companion star is a late type star, it may reach the advanced stage where the stellar radius increases. The star may fill its Roche lobe and mass transfer via L1 begins. Typical mass transfer rates are $10^{-11} - 10^{-8}\,\mathrm{M}_\odot/\mathrm{yr}$ (Frank, King & Raine 1992).

- Be-stars: These are binaries with a companion of Be type. These stars produce a strong equatorial outflow of material. If the compact object – a neutron star for all known Be X-ray binaries – passes through this disk on its usually eccentric orbit, mass is transferred.

For LMXBs (and therefore for all of our sources discussed in this work) the mass transfer is via Roche-lobe overflow. Because of the angular momentum of the accreting material as it leaves the companion star, it cannot fall directly onto the compact object, but must instead go into orbit around it, forming an *accretion disk*. Due to viscosity, the matter spirals into the BH after entering the disk. On its way down the potential well, the material loses its potential energy and angular momentum. A considerable fraction of that energy goes to heating the accretion disk, resulting in a disk luminosity that can be approximated by:

$$L_{\mathrm{acc}} = 2\eta \frac{GM\dot{M}}{R_{\mathrm{S}}} = \eta \dot{M} c^2 \tag{1.4}$$

(Shapiro & Teukolsky 1983, pages 394 and 439) where $\eta = 0.057 - 0.42$, depending on the angular momentum of the BH. Assuming realistic values for the mass transfer rate $\dot{M}$ and for η, a typical luminosity of $\sim 10^{37}$ erg/s can be obtained for the accretion onto a BH in a binary system. A maximum value exists for the X-ray flux produced by accretion. This limit is reached when the radiation pressure due to the X-ray luminosity equals the gravitational "pull" of the BH. An estimate for this limit is given by the "Eddington luminosity" which is derived under the assumption of spherical accretion. In this case the equilibrium of forces is given by:

$$\frac{GMm_{\mathrm{p}}}{r^2} = L_{\mathrm{Edd}} \frac{\sigma_{\mathrm{T}}}{4\pi c r^2} \tag{1.5}$$

where $m_{\mathrm{p}} = 1.67\,10^{-24}$ g is the proton mass and $\sigma_{\mathrm{T}} = 6.652\,10^{-25}\,\mathrm{cm}^2$ is the cross section for Thomson scattering. The Eddington luminosity for a black hole of mass $M/M_{\odot}$ is thus:

$$L_{\mathrm{Edd}} = \frac{4\pi c G M m_{\mathrm{p}}}{\sigma_{\mathrm{T}}} = 1.3\,10^{38} \left(\frac{M}{M_{\odot}}\right) \mathrm{erg/s} \tag{1.6}$$

with the related mass accretion rate

$$\dot{M}_{\mathrm{Edd}} = L_{\mathrm{Edd}}/c^2 = 1.7\,10^{17} (M/M_{\odot})\ \mathrm{g/s}. \tag{1.7}$$

In the following sections, I will summarize the historical accretion disk models and some of the current models and I will give more detailed information on the X-ray emission mechanisms of GBHs. To obtain more information about these models, see several overviews, by e.g. Poutanen (1998), Svensson (1998), Zdziarski (2000), Beloborodov (2000), Spruit (2001), and Done & Nayakshin (2001).

1.3.1 The standard α accretion disk

The standard α theory of disk accretion was first formulated by Shakura (1972) and Shakura & Sunyaev (1973). The model considers a geometrically thin gaseous disk that has Keplerian motion around the BH. Pressure, p, supports the disk against the vertical component of gravity. The viscous torques result in loss of angular momentum of the material which gradually spirals inward toward the BH. Shakura (1972) suggested that matter in the disk is turbulent and parameterized the turbulent viscous stress tensor by the disk pressure: $t_{r\phi} = \alpha p$, $\alpha < 1$. The α parameter

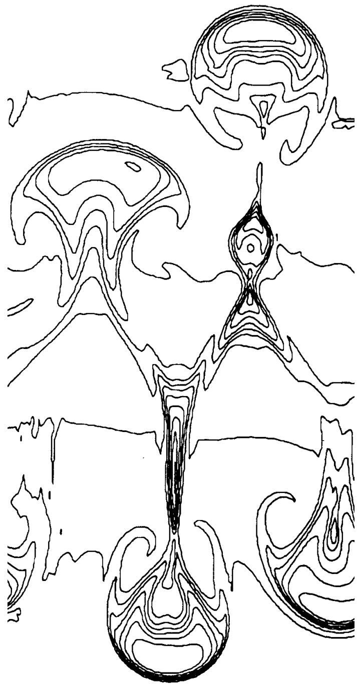

Figure 1.3: Angular momentum contour lines in a vertical cross section of the accretion disk that develop during a simulation of the magneto-rotational instability, demonstrating the angular momentum transfer out off the disk in bubbles due to this instability (Hawley & Balbus 1991, Fig. 5c).

has not been computed in detail and left as a free parameter for the standard model. Observations and modeling indicate that it has a value between 0.1 - 1 (Shapiro & Teukolsky 1983). Radiation from such a disk (optically thick, geometrically thin) is in the form of multi-color blackbody (MC, Mitsuda et al. 1984, see also Merloni, Fabian & Ross 2000). This spectrum is a sum of blackbodies with a radial temperature distribution of $T(r) \sim r^{-3/4}$.

Note that this theory has several limitations. In the vicinity of the BH, GR effects become important. Improved disk models taking into account these effects have been proposed and applied to explain the observed spectrum from several GBHs (Gierliński, Maciołek-Niedźwiecki & Ebisawa 2001). Another problem is that the standard model does not take into account the vertical structure of the disk, which has been shown to be important (Abramowicz, Björnsson & Igumenshchev 2000). Two or three dimensional description of the accretion process and the resultant radiation can only be done numerically, which several groups have performed and presented (Hawley, Balbus & Stone 2001; Agol et al. 2001; Caunt & Tagger 2001). These numerical methods concentrated on understanding the angular momentum transfer in the disk which is probably the result of turbulent viscosity. The most popular mechanism explaining

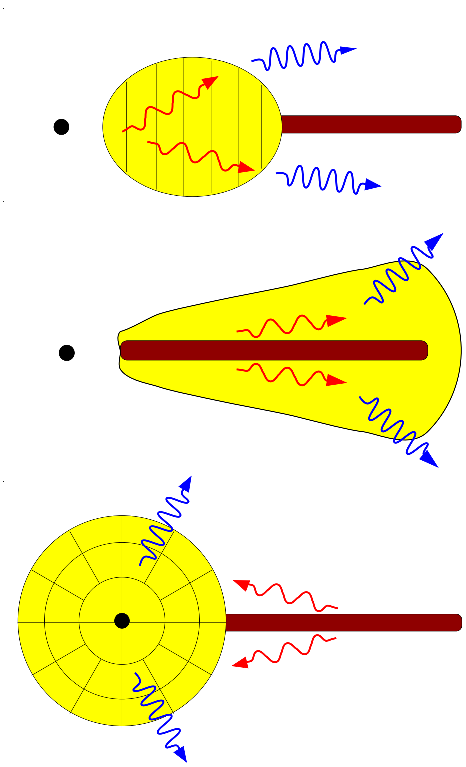

Figure 1.4: Different geometries that are discussed for the thin disk and hot plasma accretion components of GBHs and AGN. **Top:** "ADAF or SLE". **Center:** "Sandwich" or "slab". **Bottom:** "Sphere+disk"

the angular momentum transport is the Balbus-Hawley mechanism which is a result of magneto-rotational instability (Balbus & Hawley 1991; Hawley & Balbus 1991, and Fig. 1.3). This theory also gives a source for heating a hot coronal plasma above the accretion disk (see next section) and for introducing the short term variability of the hard X-ray emission via magnetic reconnection events. If no strong coupling between a magnetic field and the disk is present, a purely hydrodynamic means of angular momentum transport is required, such as the "Rossby wave instability" proposed by Li et al. (2001).

To explain the hard X-rays observed from GBHs, Shapiro, Lightman & Eardley (1976, SLE) proposed a two-temperature model of an accretion disk where the protons are much hotter than the electrons, $T_{\mathrm{p}} \gg T_{\mathrm{e}}$. The pressure of the protons keeps the disk geometrically thick and optically thin. While this description is in agreement with observed hard X-ray spectra of GBHs (see next section), it is shown to be thermally unstable against small perturbations of the proton temperature (Pringle 1976).

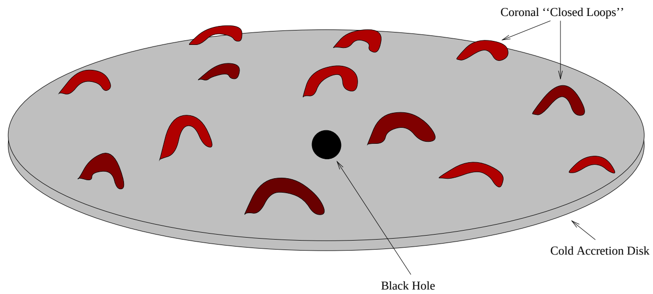

Figure 1.5: Illustration of magnetic loops above a thin accretion disk (Dove, Wilms & Begelman 1997).

1.3.2 The accretion disk coronae (ADC)

Although the standard model more or less explains the soft X-ray spectrum of most GBHs, these sources often also show a hard component in their spectra in the form of a power-law (see Fig. 2.12) which can extend up to MeV range. (This is the basis for developing the SLE model). This led several scientists to propose the existence of a hot, low density plasma (Compton-scattering corona) in addition to the accretion disk (Bisnovatyi-Kogan & Blinnikov 1977; Liang & Price 1977). The first models had an accretion geometry such that the accretion disk was covered by the corona on both sides (Fig. 1.4, center). However, it has been shown that this "sandwich" geometry poses great problems for GBHs (Dove et al. 1997).

There are two main classes of ADC models: in the first class the corona above the disk accretes rapidly (Janiuk, Czerny & Życki 2000), in the second and more widely used model, the corona is coupled to the disk by a magnetic field and accretes more slowly. In the latter type of models the corona is heated by magnetic loops emerging from the disk as first proposed by Galeev, Rosner & Vaiana (1979, and Fig. 1.5). The magneto-rotational instability (MRI) described by Balbus & Hawley (1991), can produce magnetic energy of the order of the total dissipated energy for these flares. The magnetic loops reach the corona via buoyant transport and the energy is released in magnetic reconnection events. Since the density of the disk has to be below a certain limit in order for the MRI to work (Balbus & Hawley 1991), there is a threshold $\dot{M}$ for generation of reconnecting magnetic loops above the disk.

It was quickly realized that the hard power-law component observed in Cyg X-1 could be explained by Compton upscattering of soft seed photons in a hot plasma

(Sunyaev & Trümper 1979). This idea quickly became the standard model to explain spectra of GBHs. In this model, the emission from the optically thick, geometrically thin accretion disk supplies the soft seed photons that subsequently Compton upscatter inside the ADC. Since ADC is optically thin, some disk photons pass through without any scatterings and hence both components are observed in the X-ray spectrum. Comptonization has been extensively worked on both analytically and numerically (e.g., by Sunyaev & Titarchuk 1980; Titarchuk 1994; Hua & Titarchuk 1995; Dove, Wilms & Begelman 1997; Zdziarski et al. 1998; Malzac, Beloborodov & Poutanen 2001; Psaltis 2001). The hard component of the spectrum, and therefore Comptonization, is very important for the studies of GBHs during outburst decays. Therefore, I will discuss the basic physical principles of this mechanism in the next section. For a thorough and much detailed analysis see Wilms (1998), and references therein.

Comptonization

In the classical case of Thomson scattering, incident photons are treated as continuous electromagnetic waves which then induce dipole radiation from an oscillating electron. The differential cross-section for unpolarized incident radiation scattering at angle θ is given by the classical Thomson formula:

$$\frac{d\sigma_{\mathrm{T}}}{d\Omega} = \frac{1}{2} r_0^2 (1 + \cos^2\theta) \tag{1.8}$$

where $r_0 = \frac{e^2}{m_e c^2} = 2.82 \times 10^{-13}\,\mathrm{cm}$ is the classical electron radius. Integrating equation 1.8 over all scattering angles yields the total Thomson cross-section:

$$\sigma_{\mathrm{T}} = \frac{8\pi}{3} r_0^2 = 6.652 \times 10^{-25}\,\mathrm{cm}^2 \tag{1.9}$$

In the classical case, the energy of the scattered photon is equal to that of the incident photon.

Compton scattering, in contrast, treats the photons as particles, and as they collide with electrons they exchange energy and momentum. In the basic Compton scattering process a photon of energy E collides with a stationary electron, transfers kinetic energy to the electron while reducing its own energy to E' (Fig. 1.6), which

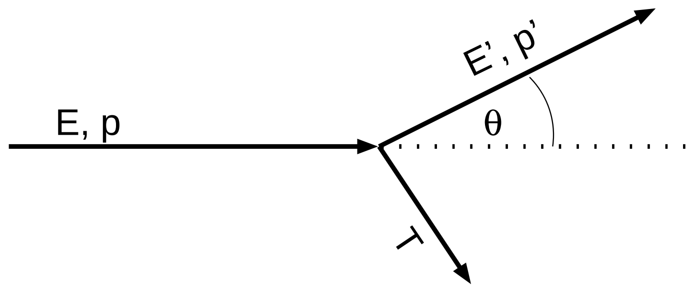

Figure 1.6: Illustration of Eq. (1.10) for Compton scattering of a photon from a stationary electron. T is the kinetic energy of the electron.

is given by:

$$E' = \frac{E}{1 + \frac{E}{m_e c^2}(1 - \cos\theta)} \tag{1.10}$$

The differential cross section of this process and the angular distribution of the electron after the collision is given by the Klein-Nishina formula which takes into account other quantum effects than just the kinematic ones (for full derivation, see, Heitler 1954):

$$\frac{d\sigma_{\rm es}}{d\Omega} = \frac{3}{16\pi}\sigma_{\rm T}\Big(\frac{E'}{E}^2\Big)\Big(\frac{E}{E'} + \frac{E'}{E} - \sin^2\theta\Big) \tag{1.11}$$

The total cross-section can be obtained by integrating the differential cross-section over all scattering angles (see for example, Rybicki & Lightman 1979). Note that for nearly coherent scattering ($E \approx E'$) equation 1.11 reduces to the classical expression given in 1.8.

For energies higher than 30 keV, quantum effects reduce the cross-section by more than 10% from the classical value. Another quantum effect is that, for higher E, Eq. (1.11) is highly dependent on θ: the scattering is concentrated in forward direction due to relativistic beaming. In a plasma, Compton scattering from protons is suppressed by a factor of $(m_{\rm e}/m_{\rm p})^2 \sim 10^{-7}$, as compared to Compton scattering from electrons.

So far our expressions assume that the electron is stationary and free. In astrophysical sources, the electrons are not stationary but have considerable thermal motion. Usually they are assumed to have a relativistic Maxwellian velocity distribution with a characteristic temperature, $T_{\rm e}$:

$$N(\gamma) \sim \gamma^2\beta\exp[-\gamma m_{\rm e}c^2/kT_{\rm e}] \tag{1.12}$$

where $\beta = v_{\rm e}/c$ is the electron velocity and $\gamma = (1-\beta^2)^{-1/2}$ is the associated Lorentz factor. In this case, if the incident photons have energies much lower than the electrons, on average they gain energy from the Compton collisions. Due to the Maxwellian electron distribution this process is called *thermal* Comptonization. In case of GBHs, ADC (with T_e ~100 keV, 10^9 K) is the hot electron plasma that Compton upscatters the soft photons from the accretion disk (with E ~100 eV, 10^6 K).

The equations given above for the stationary case have to be modified in order to take the electron energy into account: While in case of stationary electrons the average energy change of the scattered photons is given by:

$$\frac{\Delta E}{E} = -\frac{E}{m_{\rm e}c^2} \tag{1.13}$$

(obtained by averaging Eq. 1.10 over all Ω), electrons with $kT_{\rm e} < m_{\rm e}c^2$ cause an average photon energy change of (Rybicki & Lightman 1979):

$$\frac{\Delta E}{E} = \frac{4kT_{\rm e} - E}{m_{\rm e}c^2} \tag{1.14}$$

This expression establishes the conditions for the net energy transfer between the electron cloud and the photon field. The photons, on average, gain energy as long as $E < 4kT_{\rm e}$. Furthermore, the electron cloud will cool unless energy is deposited into the plasma by other processes.

We can determine the approximate total energy change for a photon which traverses a Comptonizing plasma of optical depth $\tau_{\rm c}$. Assuming soft seed photons have much smaller energy than the electron temperature, the average fractional energy change per scattering is $4kT_{\rm e}/m_{\rm e}c^2$ which we can multiply by the average number of scatterings to find the total energy change. The "random walk theory" dictates that the average number of scatterings is $\max(\tau_{\rm c}, \tau_{\rm c}^2)$. Hence, the total fractional energy change is given by:

$$y = \frac{4kT_{\rm e}}{m_{\rm e}c^2}\max(\tau_{\rm c}, \tau_{\rm c}^2) \tag{1.15}$$

which is also called the Compton "y-parameter".

The emerging spectrum of the Comptonized photons can be derived by describing the process as a diffusion problem. In the limit of large optical depths ($\tau_{\rm c} > 1$) and for $kT_{\rm e} \ll m_{\rm e}c^2$, this description is provided by the Kompaneets equation for the photon occupation number $n(E)$ (see Rybicki & Lightman (1979) for a through discussion). General solutions to the Kompaneets equation are analytically complex and typically must be calculated numerically (see, e.g. Sunyaev & Titarchuk (1980) for a study of the Kompaneets equation in several cloud geometries). Here, I will very briefly discuss two limiting cases of interest for astrophysical plasmas. For $y \ll 1$, only coherent scattering will be important, and the initial soft photon spectrum will not be modified. For $y \gg 1$, a "saturated" spectrum will be obtained, which is an equilibrium solution for the conserved photon number. It is represented by the familiar Wien law with a mean photon energy of $3kT_e$. In this case, the competition between Compton scattering of higher energy photons and inverse Compton scattering of lower energy photons "thermalizes" the spectrum to the cloud temperature T_e.

For $y \gtrsim 1$, the inverse Compton process does not saturate to the Wien spectrum for most photons. For input energy of very low energy photons, the Kompaneets equation reveals an "unsaturated" solution in which the spectrum evolves to the Wien shape only for high energies at which the soft input photons have been multiply scattered. For escaped photons of intermediate energies, a power-law solution describes the Comptonized spectrum:

$$I_\nu \propto E^{3+m}, \quad m = -\frac{3}{2} \pm \left(\frac{9}{4} + \frac{4}{y}\right)^{-1/2} \tag{1.16}$$

This unsaturated solution is the typical identification of the phenomenological power-law spectral fit component that has been commonly used in fitting GBH spectrum.

Fig. 1.7 gives an example for a photon spectrum emerging from a hot Comptonizing plasma and illustrates the special cases that I discussed. The decomposition of the total spectrum into spectra consisting of photons that underwent 1, 2, 3, 4, and 5 Compton collisions before leaving the plasma is also shown, illustrating how the observed power law spectrum is built up by several scattering orders. The optical depth is high, therefore the overall spectrum shows the Wien hump at ~600 keV. On the other hand, spectra for small scattering orders show the typical unsaturated energy spectrum, which has a power-law shape (for intermediate energies as the Kompaneets solution predicted) with a cut-off at higher energies.

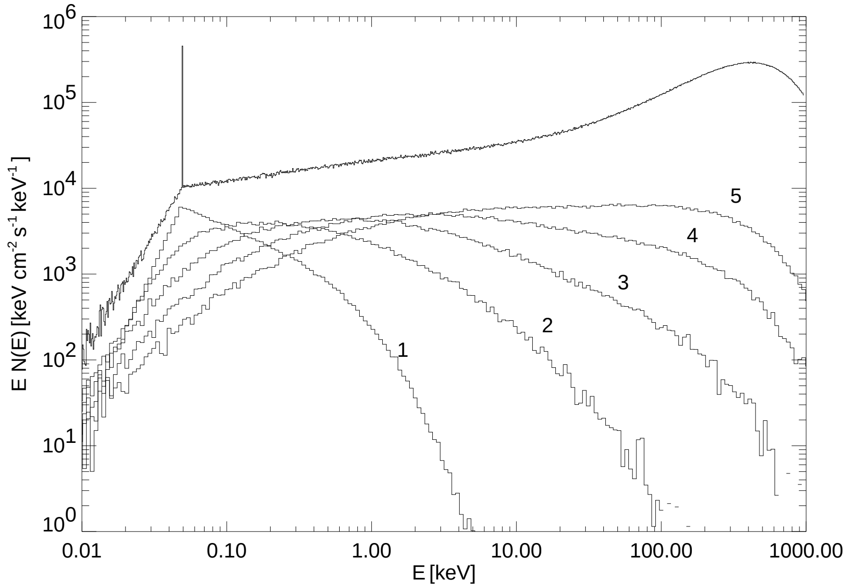

Figure 1.7: Monte Carlo simulation of spectra produced by thermal Comptonization of seed photons with an energy of $kT_{\rm seed} = 50\,{\rm eV}$ injected at the center of a spherical plasma with a temperature of $kT_{\rm e} \sim 200\,{\rm keV}$ and an optical depth of $\tau_{\rm c} = 5$. The total emerging spectrum (top) as well as the scattering orders 1–5 are shown (Wilms 1998, Fig. 2.4).

1.3.3 Advection dominated accretion flows (ADAF)

In the SLE model, only a fraction of the dissipated energy remains in the hot proton component, the bulk of the energy is passed on to the electrons and radiated. Ichimaru (1977) considered a disk of such low density that the protons – which are again assumed to be preferentially heated by the accretion process (see, e.g., Quataert 1998) – are unable to pass their energy to the electrons on the time scale of accretion. The protons advect the energy into the black hole or transport it outward in form of an outflow (Blandford & Begelman 1999). Recently, these models have been rediscovered (Narayan & Yi 1995) and have received much attention (for a review see Narayan, Mahadevan & Quataert 1998). Preferentially heating protons requires a very low density plasma and a low level of electron-proton collisions. Therefore, there is a maximum accretion rate for which the number of collisions are less than the ADAF can sustain, which is derived by Beloborodov (2000): $(\dot{M}/\dot{M}_{\rm Edd})_{\rm max} \sim 10\alpha^2$, where $\alpha < 0.1$. As in the SLE model, there is a radius $r_{\rm tr}$ where the standard cold accretion disk undergoes a transition to a hot two-temperature flow which emits hard X-rays by

Comptonizing soft radiation in the unsaturated regime. The source of seed photons in this case can be the outer accretion disk and/or synchrotron and bremsstrahlung radiation arising inside the ADAF.

The relation between the $\dot{M}$ and the $r_{\rm tr}$ led Esin, McClintock & Narayan (1997) to propose a relation between the different spectral states and ADAF for GBHs, illustrated in Fig. 1.14 and discussed in detail in section 1.4.5. Since the material is accreted into the hole before being able to radiate, the ADAFs are under-luminous, and applied mainly to low luminosity objects, such as Sgr A* (Narayan et al. 1998) or X-ray systems in quiescence (Menou et al. 1999). The hard state spectra of GBHs can also be modeled (Esin, McClintock & Narayan 1997; Esin et al. 2001). A drawback of these models is that they do not consider any timing properties. (The states of BH will be discussed in detail in section 1.4.)

There have been many additions to the original ADAF model and discussions about whether ADAFs can really exist in nature. It is out of scope of this work to discuss all of these models, for a recent review, see (Chakrabarti 2000).

1.3.4 Reflection

If simple continuum models (e.g. multi-color disk blackbody and power-law) are applied to the X-ray spectra[4] of GBHs, broad and shallow absorption features as well as iron emission line features may remain in the residuals. These features are a result of reprocessing of hard photons that are reflected back to the cold accretion disk. When X-rays are processed with optically thick matter, three observational features appear: A broad absorption feature in $\sim$7 – 20 keV, a reflection hump peaking at $\sim$30 keV, and an iron fluorescence line. The reflection hump is produced due to the reduction of the Klein-Nishina cross section at higher energies and Compton down-scatterings of high energy ($\gtrsim$30 keV) photons. The form of the reflection hump and the fluorescence lines for different ionization layers can be seen in Fig. 1.8. In GBHs, these features are often weak, possibly indicating small covering factor. On the other hand, the reflection signature from the disk can be masked by complex

4 Energy spectrum is the photon number measured per area-, time-, and energy-interval at a certain photon energy. See Fig. 1.10 for an example and section 2.2.2 for information on spectral fit models

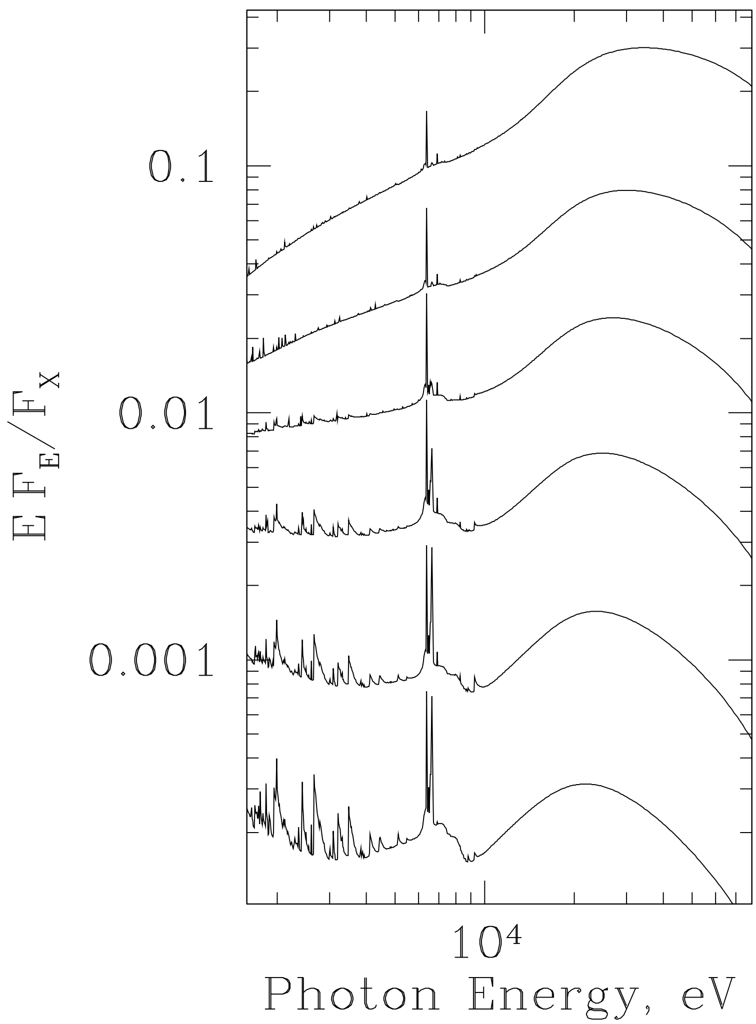

Figure 1.8: Spectra obtained from simulations of the reprocessing of an incident power-law continuum (not shown) as a function of the photon index ($\Gamma = 1.5, 1.7, \ldots, 2.5$). Depending on the hardness of the incident spectrum, ionization layers with different temperature distributions and optical depths develop. For softer power-laws stronger reflection signatures emerge (Done & Nayakshin 2001, Fig. 1, left panel). The spectra are normalized by dividing the reflected spectrum to the incident spectrum (F_X).

ionization effects (Ross, Fabian & Young 1999): For completely ionized gas, e.g., the reprocessed spectrum is only due to electron scattering and no characteristic iron feature is observed.

The numerical and analytical modeling of these reflection components led to the discovery of a very important correlation between the disk solid angle and the spectral index. This correlation is discussed in detail in section 1.6.3.

1.3.5 Jet dominated emission

Observations in the 1990s have shown that radio emission is an ubiquitous property of GBHs in their hard state (Fender 2001). For Cyg X-1 and GRS 1915+105, jets are resolved in radio. Whether the jet can be resolved or not, the observed radio

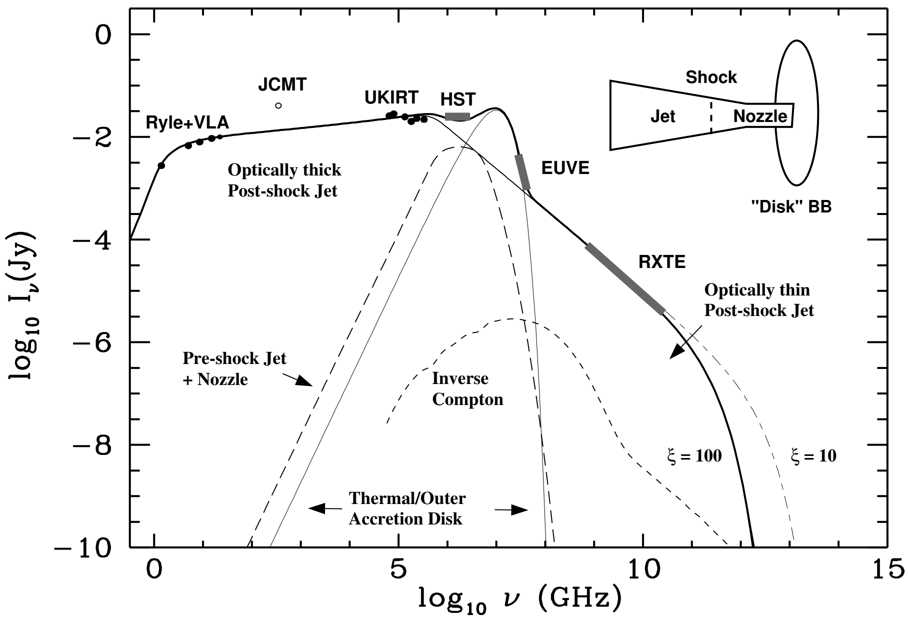

Figure 1.9: Broad band hard state spectrum of the GBH transient XTE J1118+480 from radio to X-ray energies. The overall shape can be well explained with synchrotron emission from different regions in a relativistic jet, a disk black body spectrum, and a comparatively small contribution due to inverse Compton scattering (Markoff, Falcke & Fender 2001, Fig. 1).

cores display a flat spectrum, i.e., the frequency-dependent energy flux density S_ν is approximately constant. The flat radio spectra can be explained with synchrotron emission of hot, relativistic electrons ($1 < \gamma < 10000$, power-law distribution) that are moving with relativistic bulk motion in the standard jet model, where the overall radio spectrum is built up from emission from different regions in a self-absorbed jet (Blandford & Konigl 1979; Falcke et al. 2001, and references therein). For GBHs synchrotron emission from the jet could thus contribute a considerable fraction of the observed X-ray emission (Falcke et al. 2001). It has been found that the broad band spectrum of the transient XTE J1118+480 in the hard state can indeed be described by a combination of a truncated disk, a small contribution from inverse Compton scattering, and a jet model contributing 90% of the observed power (Fig. 1.9 and Markoff, Falcke & Fender 2001). However, whether this model generally holds for other GBHs in the hard state and in the same detail as achieved by Comptonization models remains to be seen.

1.4 Spectral states

1.4.1 Phenomenology

X-ray observations of GBHs indicate that they are found in several distinct spectral states (Tanaka & Lewin 1995; van der Klis 1995). Although the initial distinction was made by comparing the X-ray (and sometimes gamma-ray) spectral information, after the launch of high time resolution instruments, it was observed that different spectral states also show very different characteristics in the short term variability properties. Recently, radio properties have also been included in defining these states.

In principle, the spectral states are determined by the relative strength of two different emission components that are discussed earlier: soft blackbody-like radiation from an optically thick, geometrically thin accretion disk and a harder component showing a power-law spectrum believed to originate by Compton upscattering of soft seed photons from the disk by a hot electron plasma. Often a relation between the X-ray luminosity of the source and spectral states also exists. When the soft component dominates the spectrum, the 2–10 keV luminosity is relatively high ($\gtrsim 10^{37}$ ergs/s), and therefore this state is called the "soft/high state" (HS). When the hard component dominates, then usually the 2–10 keV luminosity is low ($\lesssim 10^{37}$ ergs/s), and this state is called the "low/hard state" (LS). These two are the fundamental states and their difference in the X-ray spectrum can be seen in Fig. 1.10. As mentioned earlier, these states also differ in terms of their short-term timing properties. The HS is often characterized by lack of or a very low level of variability, whereas the LS shows very strong variability ($\sim$30% rms in 0.04–4 Hz). Fig. 1.11 shows this distinction in the power spectral densities (PSD[5]) for different states. Fig. 1.12 summarizes most of the important physical characteristics of GBHs during different states including radio emission properties and suggests a possible geometry.

Most of the GBHs also show transitions between these states. These transitions are very important phenomena that reveal information about the physical properties of these systems, especially the accretion geometry. The work presented in this thesis

5 The PSD is a Fourier frequency dependent quantity which gives the root mean square variability, rms, of the measured light curve at a given Fourier frequency normalized to the average observed count rate (= relative rms amplitude). It will be described in detail in Chapter 3.

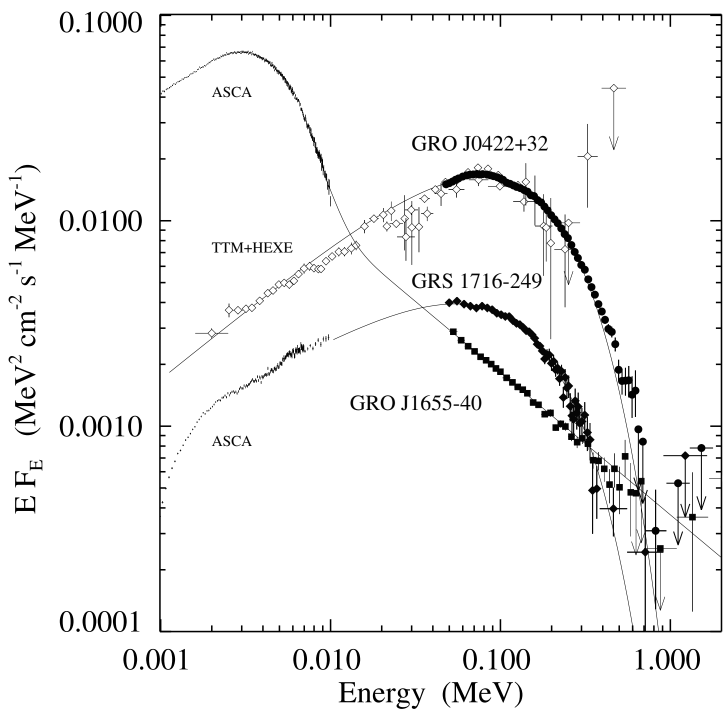

Figure 1.10: X- and gamma-ray spectra for those transient BHCs with best-quality broadband spectral data. Contemporaneous TTM, HEXE, ASCA, and OSSE data are shown. GRO J0422+32 and GRS 1716−249 are in the low state, and GRO J1655−40 is in the high state. From Grove et al. (1998).

is based on the analysis of state transitions to the LS at the end of outburst decays. In the following sections I will discuss the properties of these states and also the state transitions in more detail. For a more thorough overview and discussion of the states and transitions, see Tanaka & Lewin (1995), van der Klis (1995), Remillard (2000), Fender (2001), and Belloni (2001).

1.4.2 High-soft state

Optically thick accretion disk component

The soft component in the HS is considered emission from an optically thick accretion disk (see section 1.3.1). One of the simplest approximations of the optically thick accretion disk spectra is the multicolor disk blackbody model (MC, or diskbb, see section 2.2.2) worked out by Mitsuda et al. (1984) and Makishima et al. (1986),

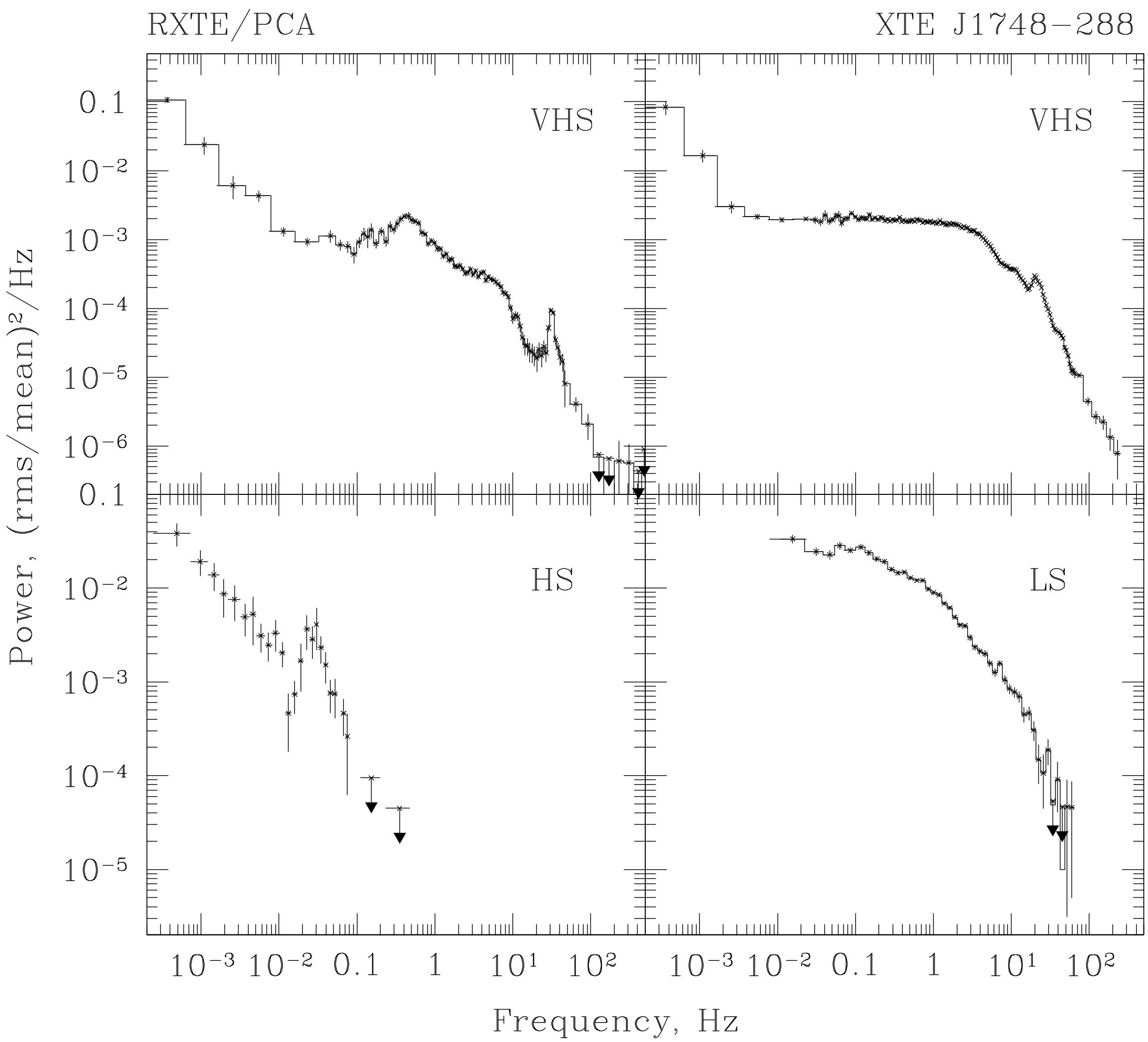

Figure 1.11: Typical examples of measured GBH power spectra as observed with the *RXTE* satellite during the 1998 outburst of the transient XTE J1748−288 (Revnivtsev, Trudolyubov & Borozdin 2000, Fig. 6). The source developed from the very high state (VHS) over the soft/high state (HS) to the hard/low state (LS).

in which the local emission is assumed to be blackbody with a radial temperature distribution of $r^{-3/4}$. This model has two free parameters, the normalization and the inner disk temperature T_{in}. The normalization is related to the inner radius of the accretion disk (Makishima et al. 1986). During the HS, it was observed that, although T_{in} varies with the disk luminosity, the normalization is virtually constant suggesting that the inner radius is not affected by the mass accretion rate (Ebisawa 2000, and references therein). When the inner disk radius is calculated from the normalization, it is found to be small, and often interpreted as the ISCO (see also Fig. 1.12). However,

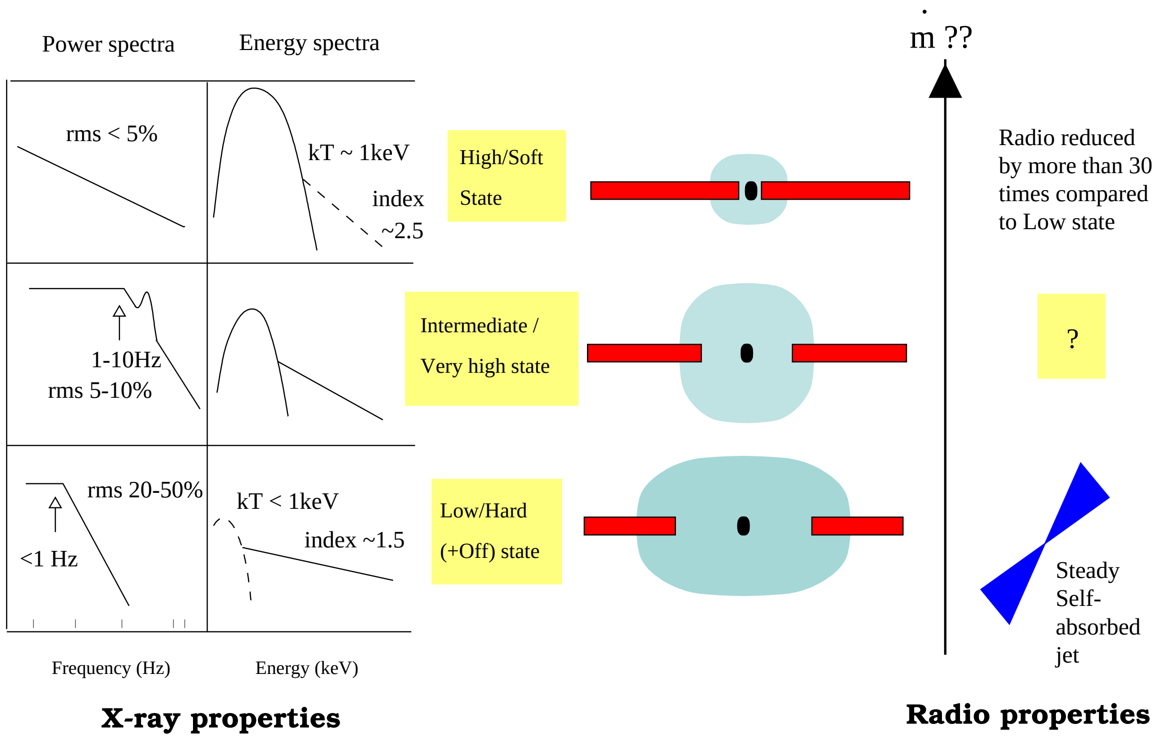

Figure 1.12: The canonical GBH states (adapted from Fender et al. 2001, Fig. 4). **Left:** Typical X-ray properties. **Middle:** Basic physical components present in each state. **Right:** Typical radio emission properties.

extreme caution must be taken when interpreting the actual radius and temperature values obtained from these fits because of the several simplifying assumptions that have been made during modeling (Merloni, Fabian & Ross 2000; Ebisawa 2000).

Hard tail

Some GBHs show a hard tail component in their X-ray spectra in the HS along with the soft component (see Fig. 1.10). The hard tail is steeper (photon index ~2.5) than the power-law spectrum in the low state, and does not show a clear thermal break up to ~1 MeV. This constitutes another fundamental difference in the states; although the power-law component does not show a break in the HS, there is a high energy cut-off for the LS indicating thermal Comptonization (Gierlinski et al. 1997; Gierliński et al. 1999; McConnell et al. 2000). Two models are proposed to explain the existence of this non-breaking power-law component, both invoking non-thermal electrons. The first model states that non-thermal Comptonization of the soft photons from the optically thick accretion disk by the infalling matter at a relativistic velocity (the bulk motion Comptonization-BMC-model) can produce a non-breaking power-law spectrum up to 511 keV (Borozdin et al. 1999, and references therein). The advocates of this model claim that a non-breaking power-law is a sign of a BH since a NS surface would thermalize the electrons before they can accelerate to relativistic speeds. However, there are arguments that BMC by infalling matter does not produce power-law spectrum (Psaltis 2001). Theoretical calculations of BMC under strong gravity is a very difficult problem, and observational tests are needed to prove their arguments (Ebisawa 2000).

The second model involves a "hybrid" Comptonization model such that thermal and non-thermal Comptonization take place at the same time in the corona, and the ratio between the thermal and non-thermal electrons dictate the resulting spectrum (Poutanen 1998, and references therein). The HS takes place when the non-thermal electrons dominate, and the hard tail is produced through Comptonization by very energetic (~several hundred keV) non-thermal electrons of the soft photons from both the accretion disk and perhaps from the Comptonized photons by less energetic (~tens keV) thermal electrons.

Other properties

The short term variability of the HS is generally much weaker than that of the hard state, it can be as low as a few percent relative rms amplitude. The typical soft state power spectrum shows an f^{-1} power-law extending down to below 0.001 Hz (see lower left panel of Fig. 1.11).

Another important property of the HS is its lack of radio emission. Observations indicate that the radio emission is quenched in this state even if the source shows strong radio emission in other states (Fender et al. 1999a; Corbel et al. 2001).

1.4.3 Low-hard state

X-ray spectrum and geometry in LS

The X-ray spectrum in the LS usually consists of a power-law with index ~1.7 and a thermal cut-off at around ~100 keV (see Fig. 1.10). Sometimes a soft excess disk component with T_{in} <1 keV is also present. This energy spectrum is consistent with thermal Comptonization, in which the plasma parameters are τ_c = 1-2 and kT_e = 100-200 keV, and the seed photons are supplied from the optically thick accretion disk whose inner radius is larger than that of the HS (see Fig. 1.12). Although the spectra, in principle, are consistent with that of thermal Comptonization, a simple cut-off power-law fit (with single coronal temperature) to the high quality data of Cyg X-1 was not successful (Gierlinski et al. 1997). Better fits were obtained when a temperature distribution is assumed in the corona (Misra, Chitnis & Melia 1998; Dove et al. 1998).

Several possible geometries for the accretion system in the LS are shown in Fig. 1.4. It has been shown that the sandwich model (middle panel) in which the hot corona is completely surrounding the optically thick disk is ruled out, since in this case the corona is cooled by the copious soft disk photons, and therefore cannot be hot enough to create the observed spectra (Dove et al. 1997). Moreover, such a large covering factor should have produced very strong reflection features (iron line and edge), but the reflection features are usually not very strong in this state. On the other hand, a corona which is patchy (covering only a certain fraction of the accretion disk) and separated from the accretion disk is more plausible (Beloborodov 1999; Malzac, Beloborodov & Poutanen 2001).

A preferred geometry is the optically thick accretion disk that does not extend down to the last stable orbit, but terminates somewhere far from the black hole. Inside of the optically thick disk inner radius, there exists a hot corona which Comptonizes soft seed photons from the disk. This is essentially the "sphere+disk" geometry shown in the bottom panel of Fig. 1.4. In this model, some of the Comptonized photons will hit the accretion disk and create the weak reflection components observed in GBHs.

Geometrically, the ADAF (section 1.3.3) model closely resembles the sphere+disk model. However, in the ADAF case, the source of the seed photons is not only the accretion disk, but also the synchrotron radiation originating inside the corona.

Other properties

The LS shows strong short term variability (see lower right panel of Fig. 1.11). Its relative rms amplitude is typically around 35%. The PSD of this hard state noise is roughly characterized by a flat top up to $\sim$0.1 Hz and a power-law decline towards higher frequencies ($\sim f^{-1.5}$). This is called the flat top (FT) model. QPOs, which manifest themselves as narrow but broadened peaks in the PSD are also observed in this state.

The LS is different from the HS not only in its X- and gamma-ray spectrum and temporal properties, but also in its radio emission properties. Several GBH sources in the LS are strong radio emitters. The radio spectrum is inverted (emissivity increases with frequency)–a sign of the moving material being optically thick to its own synchrotron radiation. Often, this is interpreted as the presence of a compact jet.

1.4.4 Other states

Intermediate and very high state

In the intermediate state (IS) as well as in the very high state (VHS) both spectral components – the accretion disk blackbody as well as the Comptonization power-law – are present in comparable strength, characterized by parameters that are intermediate between those of the hard and the soft state. As the names imply, during the VHS, the luminosity is quite high, often higher than the typical HS luminosities. On the other hand, the luminosity in the IS is lower than that of the HS, but higher than that of the LS. In both cases the PSD is roughly a FT as in the hard state but with an increased break frequency of a few Hz and low frequency noise below 10^{-3} Hz. QPOs are preferentially present during the IS and the VHS (see top panels in Fig. 1.11). The intermediate state is often observed as a "transitional state" between the hard and soft state (Belloni et al. 1996) and can be accompanied by flaring, optically thin radio emission (Corbel et al. 2000, and therein). The optically thin radio emission is generally attributed to the destruction/construction of the corona and can be explained in terms of discrete ejections of material (Fig. 1.13), however it is rarely resolved in the radio images. Although for some cases the IS is observed just before the transitions from the HS to the LS, in other cases, the source can stay in this state for an extended (weeks) amount of time, see for example sections 4.7.3 and 4.11.

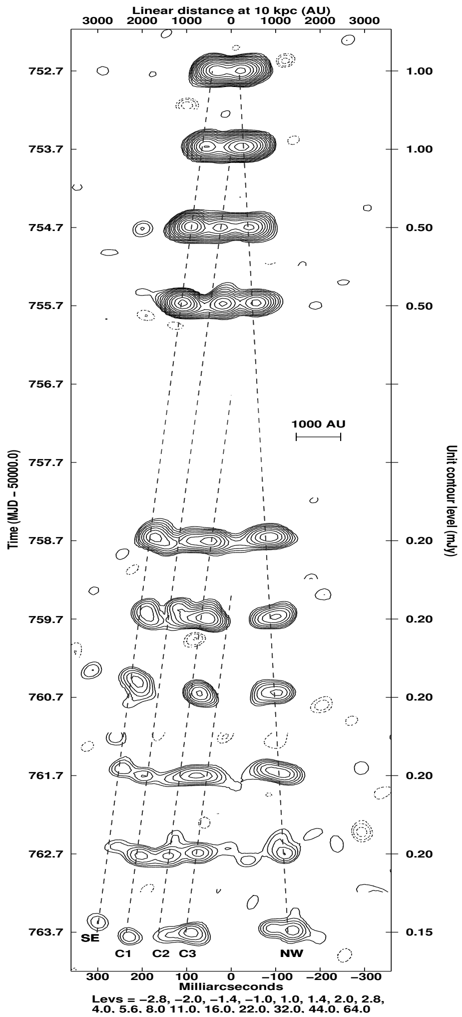

Figure 1.13: *MERLIN* observations at 5 GHz of GRS 1915+105 showing discrete ejections of material radiating at radio wavelengths and their apparent superluminal motion (Fender et al. 1999b, Fig. 2).

The quiescent state

In the quiescent or off-state of black hole transients, only very weak X-ray emission can be detected (corresponding to a luminosity of the order of $10^{30} - 10^{34}$ erg/s compared to typically $10^{36} - 10^{37}$ erg/s in the hard state). The observational properties of this state can be well explained by the ADAF model (see, e.g., Menou et al. 1999; Narayan, Garcia & McClintock 2001, and section 1.3.3). In this context, the quiescent state corresponds to an accretion rate below 1% L_{Edd} (bottom plot of Fig. 1.14). The extension of the hot plasma is large, but due to the low accretion rate, its luminosity is lower than in the hard state. The special feature of ADAF models, the fact that much of the energy of the hot plasma – the advection dominated accretion flow – is stored in the protons and not in the electrons, is of special interest in the quiescent state: since the protons are advected into the black hole without releasing their thermal energy, these flows are under-luminous, specifically as compared to the quiescent state of transient neutron star X-ray binaries, where all the residual energy of the accretion flow is transformed into radiation on the neutron star surface. Consistent with these ideas, a systematic difference in X-ray luminosity between black hole and neutron star X-ray binaries in quiescence has been observed for a small sample of sources (Narayan, Garcia & McClintock 2001; Kong et al. 2002b).

1.4.5 Spectral states and ADAF

Esin, McClintock & Narayan (1997) investigated how the various spectral states observed in GBHs can be understood in the context of the ADAF model. Fig. 1.14 summarizes the broad features of the scenario relating the ADAF, geometry, mass accretion rate[6] and the spectral states. At the lowest $\dot{M}$ ($\lesssim 10^{-2}$) the quiescent state is present, where the accretion disk is truncated at a fairly large radius and the accretion flow switches to an ADAF farther in. For LMXBs, Esin, McClintock & Narayan (1997) estimated a transition radius (where the accretion disk is truncated) of $\sim 10^4\,GM/c^2$. For $\dot{M}$ up to a critical value ($\dot{M}_{crit} \sim 0.08$) the geometry remains essentially the same as in the quiescent state, however due to increased radiative efficiency the flow becomes luminous (Narayan & Yi 1995). This is the LS. Once $\dot{M}$ exceeds $\dot{M}_{crit}$, the ADAF zone radiates too efficiently to remain advection dominated. As a result, the ADAF shrinks and the inner edge of the accretion disk moves inward. This state is identified as the IS. When the mass accretion rate increases further, the ADAF zone disappears altogether and the thin disk moves all the way to the marginally stable orbit. This is associated with the HS. Finally, at accretion rates close to the Eddington limit, the flow makes a transition to the VHS where the corona is massive and active. The VHS is identified as the least understood aspect of the ADAF scenario in Esin, McClintock & Narayan (1997).

6 The $\dot{M}$ is given Eddington units (see equation 1.7) in this section.

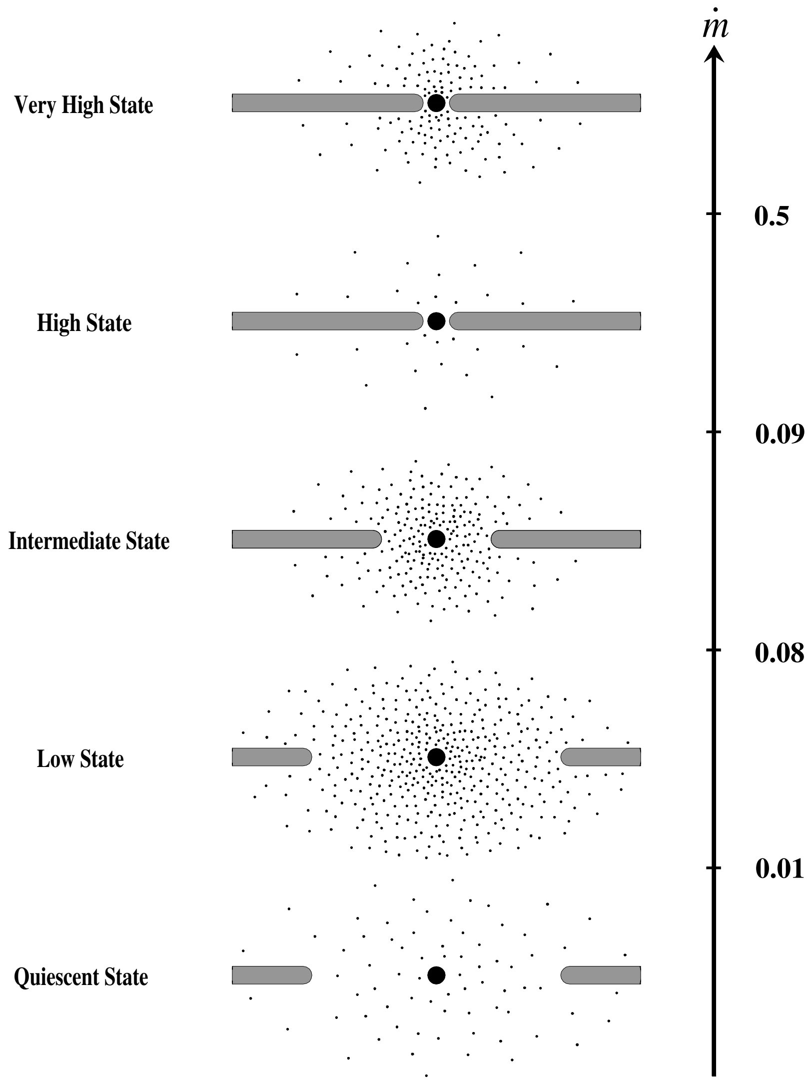

Figure 1.14: Graphic interpretation of the relative strength of the accretion disk and the Comptonizing plasma according to the ADAF model (section 1.3.3). The transition radius $r_{\rm tr}$ between both components – and thus the state – are determined by the mass accretion rate $\dot{M}$ (Esin, McClintock & Narayan 1997, Fig. 1).

1.4.6 State transitions

During the initial rise of the outburst, a GBH is usually in the LS. As the luminosity increases, it makes a transition to a softer state (either the HS or the VHS). And as the source decays towards quiescence, it makes another transition to the LS. This sequence can be clearly observed in Fig. 1.15. The BATSE instrument on *CGRO* measures hard X-ray flux that arises from the power-law component, the ASM on

RXTE measures the soft X-rays in 2–12 keV that come mainly from the disk component. This figure also shows the relation between the states and the radio emission as discussed in the previous sections. Some sources can make one or more additional transitions (i.e. VHS to HS to IS to LS). In fact, the GX 339−4 outburst shown in Fig. 1.15 starts hard, and follows the sequence of LS $\rightarrow$ VHS $\rightarrow$ HS $\rightarrow$ IS $\rightarrow$ LS $\rightarrow$ off state. In the picture described above, transitions between states appear to track the accretion rate. However, the luminosities at which these transitions occur are not fixed, and exhibit hysteresis[7] (Nowak 2002, and references therein). Moreover, XTE J1550−564 showed a very complex behavior in terms of hardness and states (Homan et al. 2001) indicating that the accretion rate may not be the sole-determinant of state transition behavior.

Here I will very briefly summarize the observational changes in temporal properties during a transition to the LS during outburst decay. A very detailed discussion of it is given in section 5.2.1. Close to the transition, as the source flux decays, the X-ray spectrum hardens and often T_{in} decreases. (This decrease in T_{in} is sometimes interpreted as the retreat of the inner disk radius.) As the transition happens, broad band variability in the PSD appears or increases significantly. Often this variability is accompanied by a QPO. For most of the sources, the temporal transition is sharp with an observation in the HS with no variability followed by an observation in the LS with strong variability only 2-3 days later. Although for some sources, a sharp transition in terms of temporal properties is accompanied by a sharp change in spectral properties, for others the spectral evolution is smoother. After the transition, the spectrum continues to harden, T_{in} continues to decrease (if the component does not disappear completely), and the characteristic frequencies of the PSD also decrease, perhaps indicating the inner disk radius retreat.

State transitions are among the most interesting phenomena of GBHs. They indicate a large geometrical and physical restructuring of the accretion system, and when closely followed, can supply valuable information about the accretion structure of GBHs. This thesis is mostly about one particular type of transition, the transition

7 The word hysteresis is used to describe the behavior such that a state tends to remain soft to lower luminosity levels, or hard to higher luminosity levels, if it began in a soft or hard state, respectively.

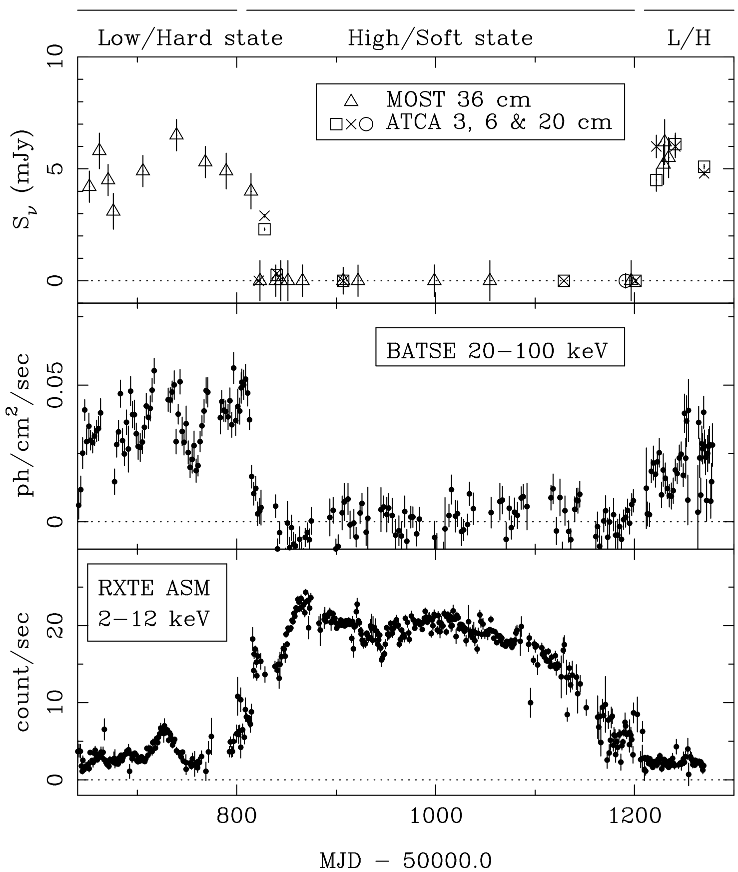

Figure 1.15: Multi-wavelength observations covering the 1998 soft state of GX 339−4 (Fender et al. 1999a, Fig. 1). **Top:** Radio light curve measured at the indicated wavelengths. **Middle:** *CGRO/BATSE* 20–100 keV hard X-ray light curve. **Bottom:** *RXTE/ASM* 2–12 keV soft X-ray light curve. Additional information (shape of the X-ray spectrum and the PSD) is required to show the presence of IS and VHS.

to the LS during the decay. This transition is very important because it involves the appearance and evolution of broad band variability. Combining the temporal evolution with the evolution of the X-ray spectrum allows us to understand their relation and helps to understand the accretion structure of the system.

1.5 Timing

Together with the X-ray spectroscopy discussed in the earlier sections, the study of rapid X-ray variability is one of the few ways to obtain valuable information about the physical environment in the vicinity of accreting compact objects. The rapid variability originates at the inner accretion flow close to the BH, and therefore some of the properties of the variability are expected to reflect the properties of the compact object. The mass and the spin of the BH are the two most important parameters that can be expected to influence the rapid X-ray variability. The temporal variability might also be affected by the mass accretion rate and the specific angular momentum of the accreting matter.

Faster the aperiodic variability is, and the larger its amplitude, the more likely that it carries information about the vicinity of the BH where the bulk of the energy is produced and the time scales are short. The dynamical time scale $t_d = 2\pi\,(r^3/GM)^{1/2}$ at the ISCO of a 10 $M_\odot$ (non-rotating) black hole is ~4.5 ms and therefore the corresponding frequency is ~220 Hz. For most of the sources discussed in this work, the temporal variability in the frequency band of 0.02 – 256 Hz was analyzed, dynamically corresponding to the vicinity of the BHs.

In this section, I introduce the general ideas about the interpretation of temporal variability in terms of the accretion structure of BHs. The details of the temporal analysis methods are given in Chapter 3.

1.5.1 Historical notes

Light curves displaying the typical LS short-term variability appear to the eye as a series of discrete, short outbursts (shots). Accordingly, "shot noise" models have been used to describe this variability (Terrell 1972; Lochner, Swank & Szymkowiak 1991). The original shot noise model for the GBH LS invoked Poisson distributed count rate flares with zero rise time and an exponential decay with a fixed relaxation time scale τ_{rel} (Papoulis 1991). Mostly these models had been evaluated by fitting shot noise PSD to the observed PSD of Cyg X-1. Since the PSD of the original shot noise model displays an asymptotic f^{-2} behavior independent of τ_{rel}, complex combinations of relaxation time scales and shot profiles have been used over the years to reproduce the observed slope of $\sim$ 1.5 ("modified shot noise models", see e.g., Weisskopf et al. 1978; Nolan et al. 1981; Lochner, Swank & Szymkowiak 1991). A summary of these attempts can be found in Pottschmidt et al. (1998).

The earlier work up to mid 1980s put strong emphasis on applying shot noise models to the data. The launch of the *EXOSAT* (1983-1986) and the *Ginga* (1987-1991) satellites with larger collecting areas and longer observation capabilities provided new information on X-ray variability of transients. A very important discovery was identifying the correlation between the variability characteristics and the accretion rate (see section 1.4). As important was the discovery of quasi-periodic-oscillations (QPOs, section 1.5.3).

With the high quality, high time-resolution data provided by *RXTE*[8] since 1996, however, it has become more and more evident that a smooth, single process PSD with an approximate $f^{-\alpha}$ shape is only a very rough description of the observed GBH LS variability: it has been shown that the hard state PSD can usually be decomposed into multiple broad components modeled with Lorentzians (Smith et al. 1997; Berger & van der Klis 1998; Nowak 2000; Belloni, Psaltis & van der Klis 2002, and this work). Therefore the emphasis in terms of understanding BH temporal variability has shifted from the shot noise models to modeling the power spectral density of these sources with multiple Lorentzians, as I will discuss in more detail in the next section.

1.5.2 Modeling of power spectra

The methods in which properties of variability can be measured using Fourier techniques are discussed in detail in van der Klis (1989) and Chapter 3. In this section, I concentrate on the physical interpretation of the modeling of the power spectral density (PSD) observed from the GBH systems. The PSD of GBHs roughly consists of a broad band noise component with power spread over a large range, usually several decades in frequency, and sometimes a well-defined resolved peak (usually modeled with a narrow Lorentzian) called a QPO. I discuss the QPOs in detail in section 1.5.3 and concentrate on the broad band variability, sometimes simply called “noise” in this section.

Shape of the PSD for different states

The PSD in the LS can be roughly described with a flat top (FT) model (see right panel in Fig. 1.16). In the FT models, below a certain frequency ν_b (usually between 0.04-0.4 Hz), the PSD is approximately flat (white noise), and above this frequency

8 Rossi X-ray Timing Explorer, see Chapter 2 for a detailed description.

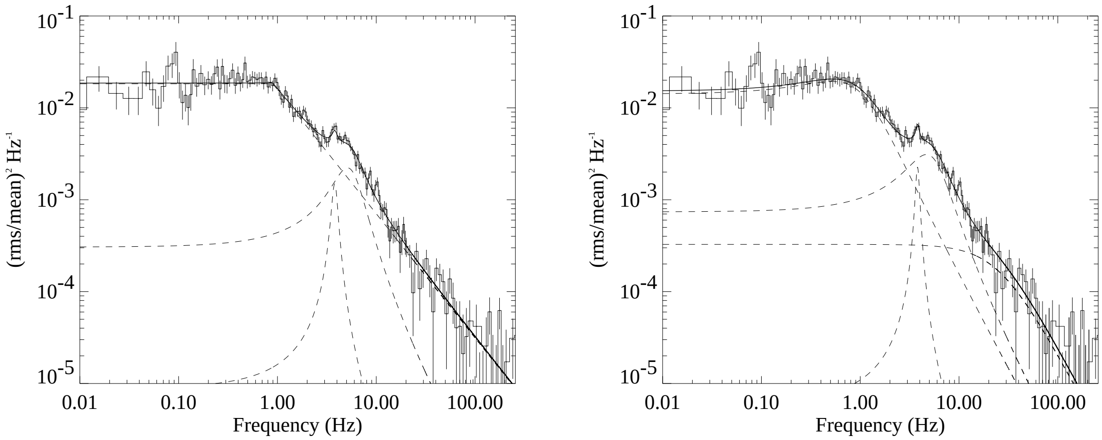

Figure 1.16: PSD of XTE J1650−500 modeled with two different models. The left panel has a FT+a broad Lorentzian and a QPO. The right panel consists of three broad Lorentzians and a QPO. This observation is representative of differences of these models. The FT usually does not require an additional Lorentzian at high frequencies. A slightly peaked Lorentzian at lower frequencies sometimes is a much better fit than a FT.

it can be described as a power law (red noise) with an index between -2 and -1. The level of the white noise can vary while the power law portion remains steady. Belloni & Hasinger (1990) noticed an interesting anti-correlation between the the white noise level and ν_b for Cyg X-1: as the white noise level drops, ν_b increases. In this state, the rms amplitude of fluctuations varies between 30% and 50%.

During a transition to the HS (or during the IS and the VHS), several changes occur. A low frequency red noise sometimes appears, the level of white noise decreases and the break frequency increases. Sometimes a QPO is also observed. During the HS, the PSD is dominated by a 1/f red noise. The PSD for different states can be seen in Fig. 1.11. Different models were proposed to explain the broad band variability with the FT model: time-variable inhomogeneities ("blobs") in the accretion disks (Bao & Ostgaard 1995; Takeuchi, Mineshige & Negoro 1995), short lived magnetic flares in the ADC (Poutanen & Fabian 1999), erratic injections of soft photons in a Comptonizing medium (Böttcher & Liang 1998; Kazanas & Hua 1999), MHD instabilities in the accretion disks (Hawley & Krolik 2001), etc.

The size of the corona and the break frequency

If one assumes that all the variability is created in the disk, then the break frequency might be an indicator of the size of the Compton corona. In the model presented by Cui (2000), the white noise is just a result of thermodynamical fluctuation in the accretion flow at the inner parts of the accretion disk. Then ν_b can be attributed to the "low-pass filtering" effects of Comptonizing processes. It is determined by the characteristic escape time of soft photons from the Comptonization region, and therefore provides a measure of this region (Cui et al. 1997a; Kazanas, Hua & Titarchuk 1997). For Cyg X-1, this would imply that the hot corona is much smaller in the HS than that of the LS, consistent with the ADAF picture presented in section 1.4.5.

Lorentzian modeling

As indicated earlier, the high quality data from the *RXTE* satellite showed that the PSD of GBHs are not smooth power-laws, but show "bumps and wiggles" (as seen in Fig. 1.16). The first attempts to model PSDs involved adding additional breaks or exponential cut-offs, or sometimes broad Lorentzians, and combinations of these approaches (Belloni, Psaltis & van der Klis 2002, and references therein). Instead of insisting on the FT and trying to modify it, some authors adapted a different approach and used only a sum of Lorentzian components, some of which are broad (Miyamoto et al. 1991; Nowak 2000; Kalemci et al. 2002; Pottschmidt et al. 2002), and demonstrated that at least phenomenologically there is no need for the FT.

The biggest difference between those models is the handling of the QPO and the broad band noise. In the FT models, the peaked components (QPOs and additional broad Lorentzians) and the broad band noise are treated *a priori* as different. On the other hand, in the Lorentzian modeling, they might have the same physical origin, with just the oscillations being more coherent for the QPO case. I have chosen Lorentzian modeling to fit all of my PSDs. This is mostly motivated by the works of Pottschmidt et al. (2002) on Cyg X-1 and Belloni, Psaltis & van der Klis (2002) on various GBH and NS binaries. They applied the Lorentzian modeling successfully and discussed several correlations among the spectral and temporal properties. By using the same fitting method, I was able to directly compare my results with theirs. For a detailed description of Lorentzian modeling see section 3.7.2.

Energy dependence of noise

Several models mentioned earlier for creating the broad band noise in the PSD also predict some form for the energy dependence of PSDs [9]. Böttcher & Liang (1998), for example, studied a thermal Comptonization model where the soft photons are either injected from a central source (like for the ADAF case) or from an external source (as in the sphere+disk case). The case with the central soft photons source predicts a steeper PSD at higher energies. In another model, Böttcher & Liang (1999) proposed that the soft photons may be injected from a cool blob spiraling into the central object. In this case the PSD becomes flatter with increasing energies. In the magnetic flare model of Poutanen & Fabian (1999), the general shape of the PSD does not change with energy, except the second break frequency is shifted to lower frequencies for higher energy bands. Note that the changes are described in terms of a FT model, but can also be interpreted in the context of the Lorentzian model (i.e., a change in the second break frequency corresponds to a change in the peak frequency of the second or third Lorentzian component). Given these predictions, it is important to study how the PSD shape depends on energy. This is one of the most important goals of this work, and I discuss this dependence for all sources.

Before this study, there have been other reports of the dependence of PSD on energy for several sources; by Belloni et al. (1997) with the *Ginga* data and by Lin et al. (2000) with the *RXTE* data. Belloni et al. (1997) found that ν_b of GS 1124−68 and GX 339−4 changes considerably with energy (from ~2 Hz in 2.3 - 4.7 keV band to ~9 Hz in 9 - 37 keV band) in the VHS. Moreover, such a shift was also observed during a transition to the LS in GS 1124−68. Lin et al. (2000) found that there is no uniform behavior for the dependence of PSD component on energy. For example, flattening was observed for Cyg X-1 for higher energies as Böttcher & Liang (1998) suggested, but three other sources that they analyzed did not show such behavior. GX 339−4 showed a decreasing rms amplitude with increasing energy, whereas GRS 1758−258

9 Energy band limited PSDs can be obtained by taking the Fourier transform of light curves in limited energy bands.

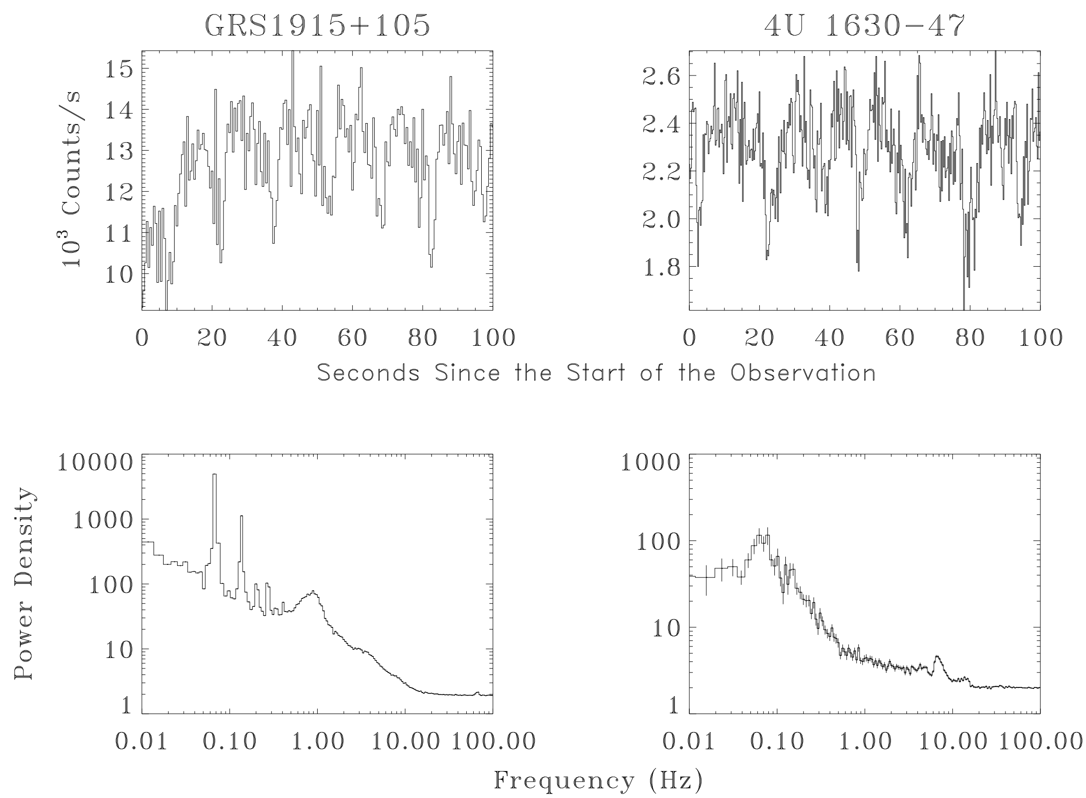

Figure 1.17: Light curves and their corresponding PSDs. The panels on the left are from microquasar GRS 1915+105. The panels on the right are from 4U 1630−47. The lowest frequency QPO corresponds to the quasi-periodic dips in the light curve for both sources. From Cui (2000). Only representative portions of the light curves are shown.

had the highest rms amplitude in the medium energy band.

1.5.3 QPOs

Phenomenology

A QPO manifests itself in a well-localized, narrow (but not infinitely narrow) peak in the PSD. Two examples are shown in Fig. 1.17. This figure also shows what kind of light curve creates strong low frequency QPOs in GBHs. Although there is no hard limit, a peak in the PSD is called a QPO when the quality value ($Q = \nu_{central}/FWHM$) is higher than 2. There is a variety of QPOs in GBHs in terms of their basic characteristics (frequency, width, rms amplitude) as well as the dependence of these characteristics on photon energy and X-ray intensity. In the extreme case of an *RXTE* observation of GRS 1915+105, a sharply peaked QPO is present at 0.067 Hz along with its 3 harmonics, a much broader QPO at 0.8 Hz along with a much weaker high frequency QPO at 67 Hz are also present (Morgan, Remillard & Greiner 1997, also shown in bottom left panel in Fig. 1.17). The frequencies of the QPO detections span 3 decades for this source. At first glance, the QPOs constitute a heterogeneous class of phenomena within a large band of frequencies, amplitudes and widths. The origin of the QPOs is believed to be the accretion disk, however in some cases the properties of QPOs seem to correlate much better with those of hard X-rays coming from the Comptonizing corona (Cui 2000).

The basic classification of QPOs in the GBHs is between the stable high frequency QPOs in 65–450 Hz range (for a recent review, see Remillard et al. 2002a) and low frequency QPOs ($<$ 20 Hz) where the central frequency varies. There is only one observation of a high frequency QPO during the outburst decay of GBHs, at 65 Hz in XTE J1550$-$564 (Kalemci et al. 2001) . The models that could create such QPO have been discussed in detail in Kalemci et al. (2001). The high frequency QPOs are out of scope of this thesis, and will not be discussed in more detail. From here on, the word QPO denotes a low frequency QPO.

A brief summary of QPO models

Two simplest models involve Keplerian motion of "blobs" inside the accretion disk. In the first case, these blobs are emitting X-rays close to the inner regions and in the second case they have high density and are absorbing X-rays at the outer regions of the accretion disk (Cui 2000; Ebisawa, Mitsuda & Inoue 1989). The second case would create harder absorption dips that have not been observed along with the low frequency QPOs. One problem with the blobs of X-ray emitting material model is the question of how they are generated in the first place. One recent model that has been proposed to explain the generation of hot spots is the "Accretion Ejection Instability" (AEI) model suggested first by Tagger & Pellat (1999). AEI is a spiral instability driven by magnetic stresses that occurs in the inner regions of the accretion disk threaded by magnetic field. The spiral extracts energy and angular momentum from the disk and stores them in a Rossby vortex (like the Giant Red Spot on Jupiter) at the co-rotation radius (Varnière, Rodriguez & Tagger 2002).

The QPOs might also be related to certain oscillation modes of long wavelength in the accretion disk (Kato 1990). The observed frequencies might be the resonant frequencies of certain modes in the disk. Note that, for low frequency QPOs, the epicyclic modes (modes due to diskoseismology, Nowak & Lehr 1998, and references therein) cannot be responsible because they predict stable frequencies like the ones observed for high frequency QPOs. It is also claimed that the QPOs are a result of the oscillation of the whole disk (Titarchuk & Osherovich 2000). Although the mode analysis results in QPO frequencies comparable to the observed ones in this model, it is not clear how the oscillations of the disk turn into the observed rms amplitudes of 10-20%.

One idea that appears to generate the right order of magnitude of frequencies is that of shocks at the inner disk and oscillation of the shock position (Molteni, Sponholz & Chakrabarti 1996). However, objections raised on the generation of such shocks (Swank 2001).

Energy dependence of QPOs, the Compton microscope model

It appears that for GBHs, most QPOs strengthen toward high energies (van der Klis 1995; Morgan, Remillard & Greiner 1997; Remillard et al. 1999b) although some follow the opposite trend (Morgan, Remillard & Greiner 1997; Rutledge et al. 1999). And indeed, some show a turnover in this relation (Tomsick & Kaaret 2000; Kalemci et al. 2001). So the energy dependence of the QPO is a complicated matter, perhaps depending on the physical properties of both the corona and the disk. A study by Lehr, Wagoner & Wilms (1999) provides one of the detailed predictions for the energy dependence of the QPO amplitude for BHCs. In their Monte Carlo simulations, Lehr, Wagoner & Wilms (1999) assume that the QPO is due to the flux modulation of soft seed photons that are subsequently Compton upscattered in a corona. The total X-ray flux emitted is the combination of the flux from regions where the QPO is active and the flux from other regions where the soft photons are unmodulated. In a given energy band the predicted QPO amplitude is given by the ratio of the flux that emerges in this energy band from the region where the QPO is active to the total flux in this energy band. If the corona has a temperature gradient and is the hottest in the region where the QPO is active, then a QPO amplitude that increases with energy is predicted because the highest energy photons come from the region where the QPO is active. However, if the QPO is active in a region where the corona is cooler, then a drop in the QPO amplitude at high energies is predicted. Within this model, observing the amplitude as a function of photon energy can be used to gain insight into where the QPO originates. If it is assumed that the electron temperature decreases with distance from the compact object (e.g., if the energy deposition in the corona becomes less efficient at larger radii), then QPOs originating in the accretion disk at a greater distance from the compact object will exhibit a larger drop in amplitude at high energies.

1.5.4 Psaltis - Norman model

The frequencies of QPOs and noise components (broad Lorentzians) in both NSs and GBHs follow similar tight correlations (see section 1.6), suggesting that all these variability components cannot directly be related to the presence of a compact object with a hard surface or large-scale magnetic field (Wijnands & van der Klis 1999; Psaltis, Belloni & van der Klis 1999). The frequencies of several QPOs observed simultaneously in NS (and corresponding QPO and Lorentzian noise components in GBHs) were shown to be nearly equal to the orbital, periastron-precession, and twice the nodal-precession frequencies of tilted test particle orbits at the inner accretion disks (Stella, Vietri & Morsink 1999). These frequencies only depend on the gravitational field and not on the accretion flow properties, and therefore can account for the tight correlations. One way to obtain these frequencies are through normal mode oscillations of the inner disk (diskoseismology, Nowak et al. 1999). Some of the modes frequencies are comparable to the orbital, periastron- and nodal-precession frequencies. Exciting and trapping these oscillations at a characteristic radius is a strong candidate for producing the modulations, especially the high frequency QPOs.

Psaltis & Norman (2000) proposed an alternative mechanism for producing high amplitude variability motivated by the similarity between the observed PSD of accreting compact objects and the response function to external perturbations of driven mechanical and electrical systems. This model studies the response of the accretion disk inside a transition radius to a broad spectrum of perturbations imposed outside

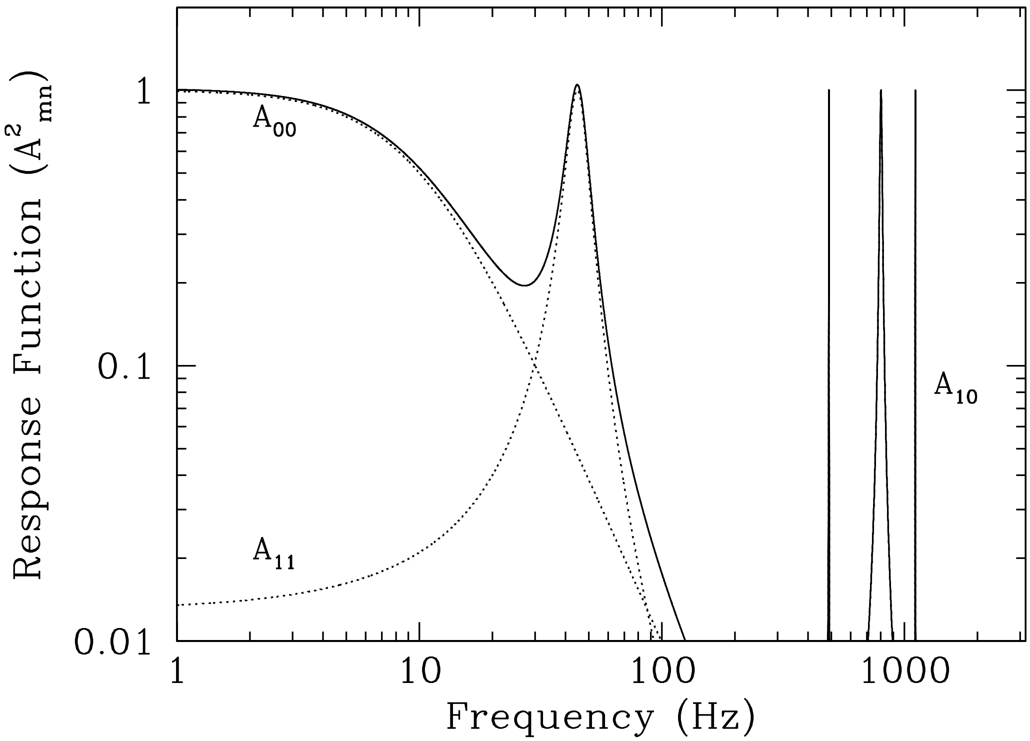

Figure 1.18: The square of the disk response function for the three lowest-order modes described in Psaltis & Norman (2000).

of it. The broad band noise is a result of broad band response of the accretion disk, whereas the QPOs are a result of resonances occurring at the normal modes of the accretion disk. The perturbations at the inner disk modulates the mass flux to the inner parts of the accretion disk and possibly loading of the hot Comptonizing corona. It has been shown that the modulation of the scattering optical depth in the ADC can produce the strong energy dependence of the observed rms amplitudes (see, Lee & Miller 1998; Miller, Lamb & Psaltis 1998), therefore it is possible that the mode frequencies also modify the radiation emerging from the system.

The details of the mode analysis are given in Psaltis & Norman (2000), and the response for the lowest three modes are illustrated in Fig. 1.18. The lowest mode is a zero-centered Lorentzian, and higher modes are in the form of peaked Lorentzians in agreement with the observations of GBH PSDs.

1.5.5 Coherence and lags

Coherence and lags are two other functions of frequency that can be obtained through Fourier analysis of light curves in different energy bands. The coherence is a measure of degree of linear correlation between X-rays at different energies such that a value of 1 means perfect linear correlation and 0 means no correlation. The Fourier time lag is a Fourier-frequency-dependent measure of the time delay between two concurrent time series (Miyamoto & Kitamoto 1989; Nowak et al. 1999). The details of how they are calculated are given in section 3.3. Here I will briefly summarize the physical interpretations and models concerning these quantities in GBHs.

It has been well established in GBHs that high energy X-ray photons systematically lag low energy photons (van der Klis 1995). In the context of Comptonization models, the hard time lags are expected, since more scattering events are required for photons to reach higher energies. However, complications arose when Miyamoto et al. (1988) computed the cross spectrum in Fourier space for Cyg X-1 and reported the strong frequency dependence of the observed lags. Examples of lag spectrum of Cyg X-1 can be seen in Fig. 1.19. It can be shown that Comptonization processes in a uniform electron gas can only produce a uniform shift between light curves in different energy bands (Miyamoto et al. 1988). This frequency dependence is probably a sign of a density (or temperature) profile for the ADC (Cui 2000). A non-uniform density profile corona was modeled quantitatively by Hua, Kazanas & Cui (1999). They showed that the HS of Cyg X-1 spectrum can be fit with a Comptonization model that has three different density profiles (uniform, $\propto 1/\mathrm{r}$, and $\propto 1/\mathrm{r}^{3/2}$) for the ADC, however only the 1/r density profile can fit the lag spectrum. The main drawback of this model is the requirement of maintaining a high temperature ($\sim$100 keV) throughout a large corona, roughly one light second across. How the energy is transported to maintain this temperature is not clear (Cui 2000).

Three other lag models were investigated in detail by Kotov, Churazov & Gilfanov (2001). Time lags due to light crossing time of the reflector (Poutanen 2001) were shown to create a feature at the iron line energy in the lag spectrum as a function of energy. This has not been observed. Time lags due to variations of the power law index require fine tuning of the parameters to explain the observed lag spectrum.

The third model they discuss, "time lags due to accretion", explains some of the observed properties of X-ray lags. In this model, perturbations introduced at a large distance from the compact object are propagated down to the region of main energy release and cause variations of the X-ray flux. The lags naturally appear in this situation if the locally emitted spectrum is a function of r. If the frequency of the perturbations decrease as a function of radius (dynamical timescale was assumed in Kotov's model) and locally emitted spectra are power laws with the photon indices smaller in the innermost region (see also Lehr model for amplifying QPO amplitudes in section 1.5.3), the time lag spectra of Cyg X-1 can be explained with reasonable model parameters. This model also accounts for the fact that the PSD at higher frequencies in the higher energy band of Cyg X-1 has a higher amplitude. (In the Lorentzian description, this would mean a higher peak frequency at higher energy.)

Analysis of the coherence function is also an important temporal tool complimenting the time lags. If the coherence function were not close to unity for the LS, it would not be interesting since numerous processes can account for the loss of coherence (Vaughan & Nowak 1997). Nevertheless, as I show in this work, they are close to 1, which put useful constraints on X-ray production mechanisms and the X-ray emitting environment. Note that it is only possible to talk about characteristic frequency dependent lags when the coherence is close to 1 (Nowak et al. 1999).

Mean coherence and lag. The Cyg X-1 case

When the shape of the frequency dependent lags and coherence are not strongly frequency dependent, or when for the same source the shape does not change but the amplitude varies, mean coherence and lag can be used to compare the strength of these quantities from observation to observation. This has been done for Cyg X-1, first by Cui et al. (1997d) and then by Pottschmidt et al. (2000). The detailed analysis of Pottschmidt et al. (2000) showed that in Cyg X-1, the mean lags do not change during the LS and the HS[10] and they have similar values, but they do increase during the state transitions, as shown both in Fig. 1.19 and Fig. 1.20. Also, during the transitions, the mean coherence decreases. This behavior was subsequently observed

10 The HS in Cyg X-1 is probably not the usual soft/high state as seen in other BHCs, but rather closer to the "very high state"

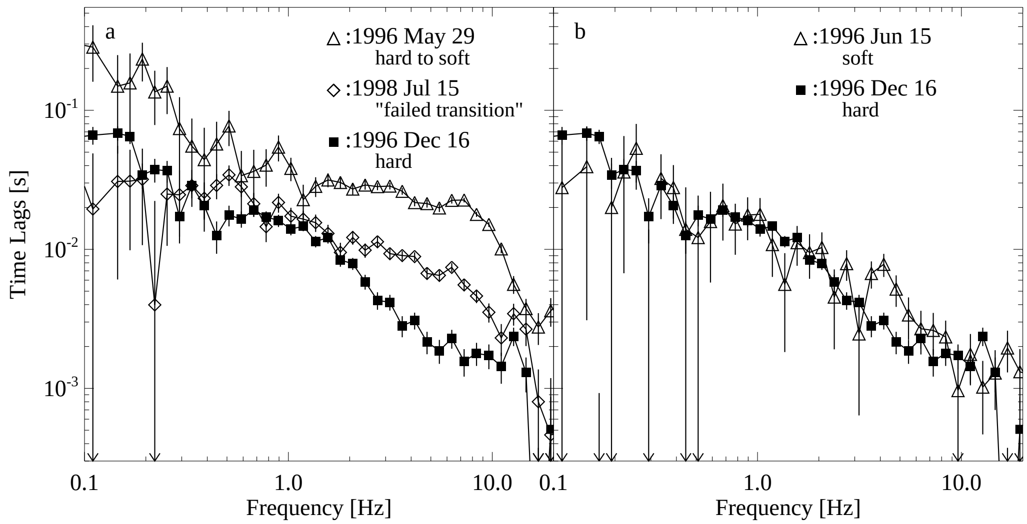

Figure 1.19: X-ray lag spectra for Cyg X-1 for different states. (a) Comparison of the lag spectrum in transition to a regular observation. (b) Comparison of the HS and LS lag spectrum for Cyg X-1. From Pottschmidt et al. (2000).

in other systems, in GX 339−4 (Nowak, Wilms & Dove 2002, and this work), and in XTE J1650−500 (Kalemci et al. 2002, and this work). Pottschmidt et al. (2000) suggested that one possible reason is the optically thin outflows during the state transition. The outflow may create an additional Comptonizing area at its base that increases the time lags and reduces the coherence due to additional scatterings. For all our observations that show a state transition I also investigated whether the mean coherence and lags change during transitions.

Lorentzians and frequency dependence of lags and coherence

In a report by Nowak, Wilms & Dove (1999), the frequency dependence of GX 339−4 was investigated in detail. They found that the coherence shows a dip of ∼0.1 near 0.5 Hz in one observation and near 2 Hz for all other observations. They realized that the dip region is exactly where their two Lorentzian components overlap in the PSD. They interpreted this result as follows: there are multiple broadband processes occurring in GX 339−4 that are individually coherent but incoherent with one another. This is also the reason why the coherence is lost at higher frequencies for all sources, multiple incoherent processes (possibly flares) feed the corona on dynamical timescales. Similarly, the overall measured time lag may in reality be a composite of

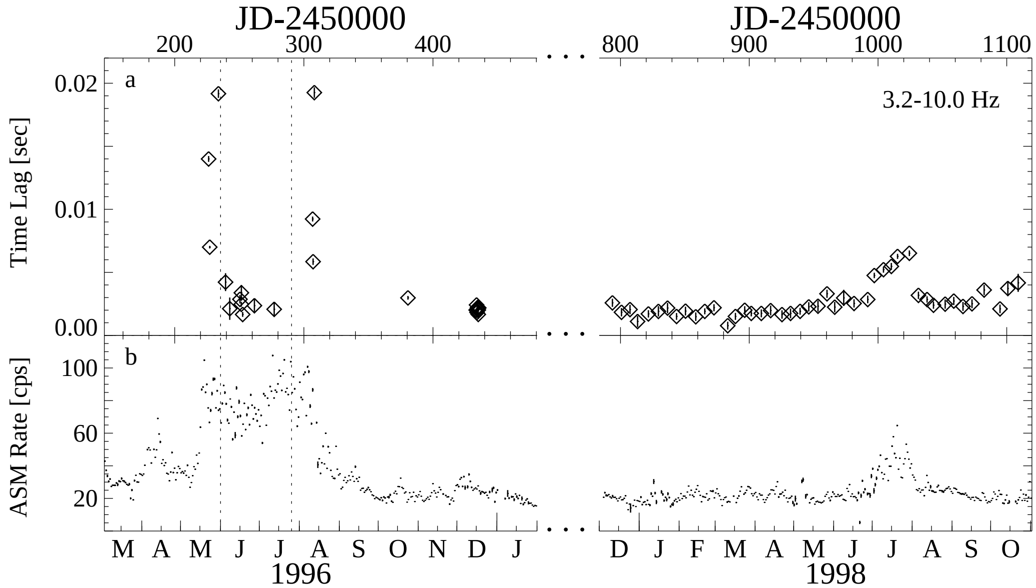

Figure 1.20: Temporal evolution of the mean lag and *RXTE* All Sky Monitor count rate for Cyg X-1 during 1996-1998. The dotted lines indicate the times for state transitions, and in between the dotted lines, Cyg X-1 is in the HS. From Pottschmidt et al. (2000).

time lags inherent to each individual Lorentzian component. Whereas the composite time lag might be fairly small, the time lags associated with the individual PSD components might be somewhat larger. The fairly long intrinsic time lags of these individual PSD components would only be revealed in the absence of the other PSD components (Nowak 2000). The reduction of the average lags during the transitions of Cyg X-1 might be due to this reason because multiple Lorentzians occupy 3–10 Hz band during the transition whereas only one Lorentzian dominates this band during the soft and hard state (Pottschmidt et al. 2002). Since I use the Lorentzians to fit the PSDs, I checked whether the coherence and lag spectrum shape depends on the position of the PSD components for all observations where it was possible to obtain frequency dependent coherence and lags.

1.6 Correlations among spectral and temporal properties

Up to this point, I have summarized the efforts to understand the physics of accretion around black holes by modeling its X-ray spectrum and temporal properties. The GBHs provide us more information than just the spectral and temporal parameters of individual observations through correlations among these parameters. One of the most important goals of this work is to find such correlations and interpret them to have a better understanding of these systems. In this section, I briefly summarize the previously reported correlations and their interpretations.

1.6.1 Correlations among spectral fit parameters

A correlation between the inner disk temperature and the spectral index was reported by Markwardt, Swank & Taam (1999) for GRS 1915+105. However, it only used the correlation to map the temporal properties (such as QPO observations) with the spectral properties, but did not discuss the reason for the correlation.

One very important correlation mentioned earlier is the one between the spectral index (Γ) and the disk solid angle[11] ($\Omega/2\pi$). A very recent work on this correlation is reported by Zdziarski et al. (2002) where they show the correlation is valid for both GBHs and AGNs. The case for the black holes is shown in Fig. 1.21. This correlation may be understood due to variation of the inner radius of the optically thick accretion disk with some overlap with the corona. Then, when the accretion disk is closer to the black hole, there will be more cooling of the hot plasma by a higher flux blackbody photons and the spectrum will be softer. The solid curve in Fig. 1.21 shows the prediction of a simple version of this model discussed in Zdziarski et al. (2002).

1.6.2 Correlations among temporal fit parameters

Wijnands & van der Klis (1999) showed a correlation between the break frequency (which roughly corresponds to smallest peak frequency in Lorentzian modeling) and

11 Disk solid angle, $\Omega/2\pi$, is the covering factor of the disk seen by the radiation source.

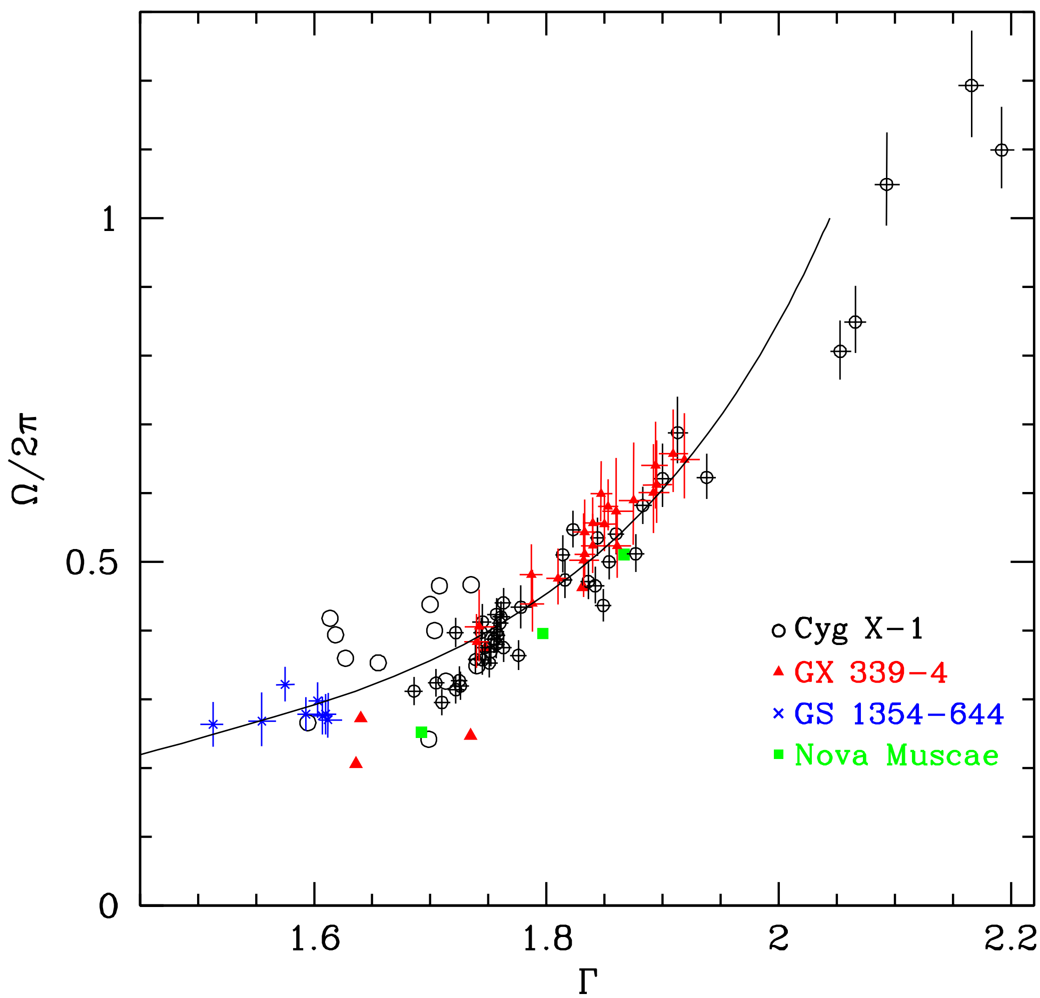

Figure 1.21: Correlation between the the strength of Compton reflection and X-ray spectral index in GBHs. From Zdziarski et al. (2002).

the QPO frequency for black hole candidates, atoll sources, a millisecond pulsar and Z sources in the LS. Later, a study by Psaltis, Belloni & van der Klis (1999) showed that a similar correlation exists between the lower “kHz” QPO frequency and the frequency of a second peaked component in the PSD for several types of X-ray binaries (Z sources, atoll sources, BHCs), as shown in Fig. 1.22. Later, Belloni, Psaltis & van der Klis (2002), adapting the Lorentzian fitting approach showed that correlations exist among the peak frequencies for six sources comprising X-ray bursters, a BHC, and a Z source. Pottschmidt et al. (2002) worked on the systematic spectral-temporal correlations of the hard state of Cyg X-1, and showed that the correlation of ν_1 and ν_2 is consistent with the correlation reported by Psaltis, Belloni & van der Klis

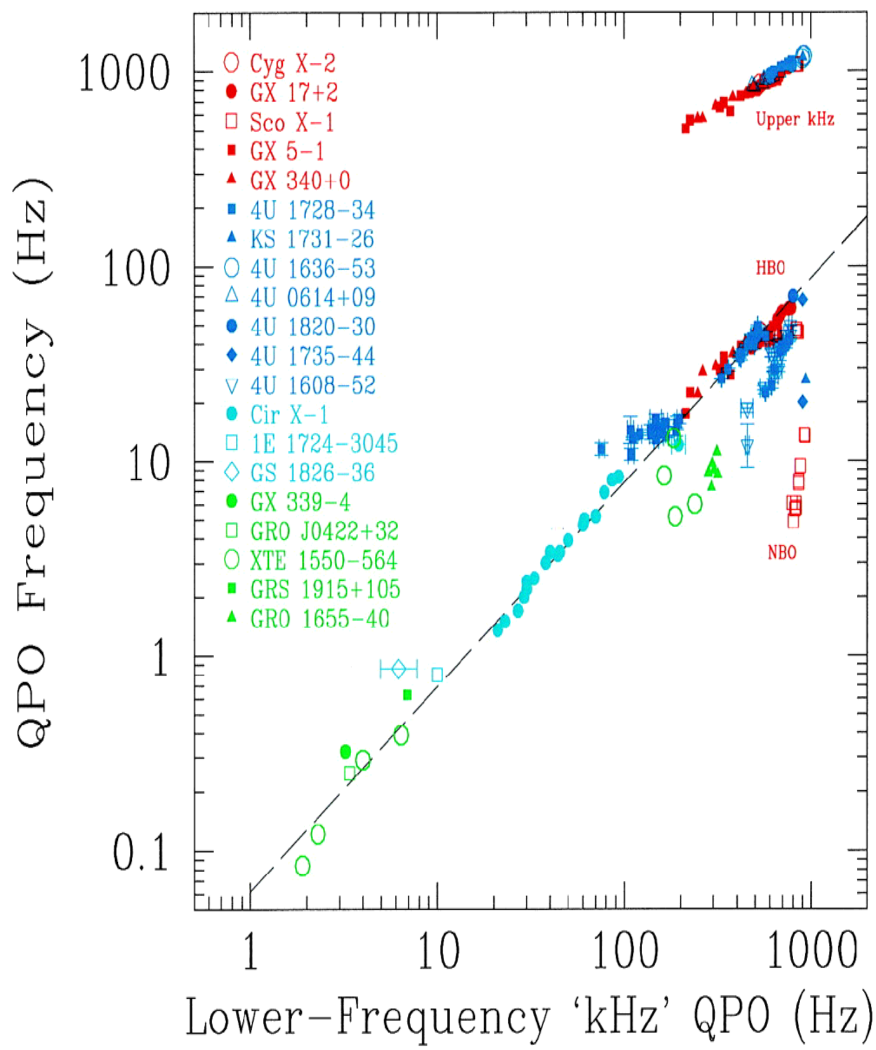

Figure 1.22: Correlations between the QPO and noise components in LMXBs including both GBHs and NSs. The dashed line is the best fit to the main correlation. From Psaltis, Belloni & van der Klis (1999).

(1999). Finally, Mauche (2002) extended the range of this correlation to much lower frequencies and showed that the correlation of Psaltis, Belloni & van der Klis (1999) is valid for some white dwarf systems also. The basic interpretation for these correlations is that the temporal variability does not depend on the presence of a hard surface or a strong magnetic field which are the parameters of the compact source, but just depends on the accretion flow around the compact object.

Apart from the correlations between the peak frequencies, Pottschmidt et al.

(2002) showed the correlations between mean lag and peak frequencies for Cyg X-1. Another well known relation is the Belloni-Hasinger relation between the flat top power level and the break frequency in PSDs of black hole systems which was first observed in Cyg X-1 (Belloni & Hasinger 1990). The flat top power level is proportional to $1/\nu_b$. This is seen in other BHCs and NS systems also (Belloni, Psaltis & van der Klis 2002, and references therein). If the PSD is modeled with a zero-centered Lorentzian, the Belloni-Hasinger relation is a natural consequence if the rms amplitude of the Lorentzian is constant. However, it is not clear why it should be constant.

1.6.3 Correlations among spectral and temporal fit paramaters

A detailed comparative study of correlations between QPO properties and spectral parameters of XTE J1550−564 and GRO J1655−40 was reported by Sobczak et al. (2000). They investigated the correlation of inner disk temperature, normalization of diskbb component, disk flux, spectral index, power-law flux and the total flux with the QPO frequency and the QPO rms amplitude for these two sources. They found that the QPO frequency and the amplitude correlates well with some of the spectral parameters, however the correlations found for XTE J1550−564 are generally opposite to those for GRO J1655−40. The only exception is the correlation between the disk flux and the QPO frequency. For both sources, the QPO frequency increases as the disk flux increases. This led to the claim that the QPOs originate at the accretion disk. This correlation, along with the correlation of the QPO frequency with the spectral index for XTE J1550−564, is shown in Fig. 1.23.

The correlation between the QPO frequency and the spectral index (with only a few sources and data points) was first reported by di Matteo & Psaltis (1999), but the discussion was limited to the implications of the limited QPO frequency band on the limited change in the inner disk radius during transitions. Again, in Sobczak et al. (2000), although the correlation between those two parameters are shown, the reason was not discussed.

In Sobczak et al. (2000) it was also shown that the QPOs appear only when the power-law flux was more than 20% of the total flux for both sources, and the rms

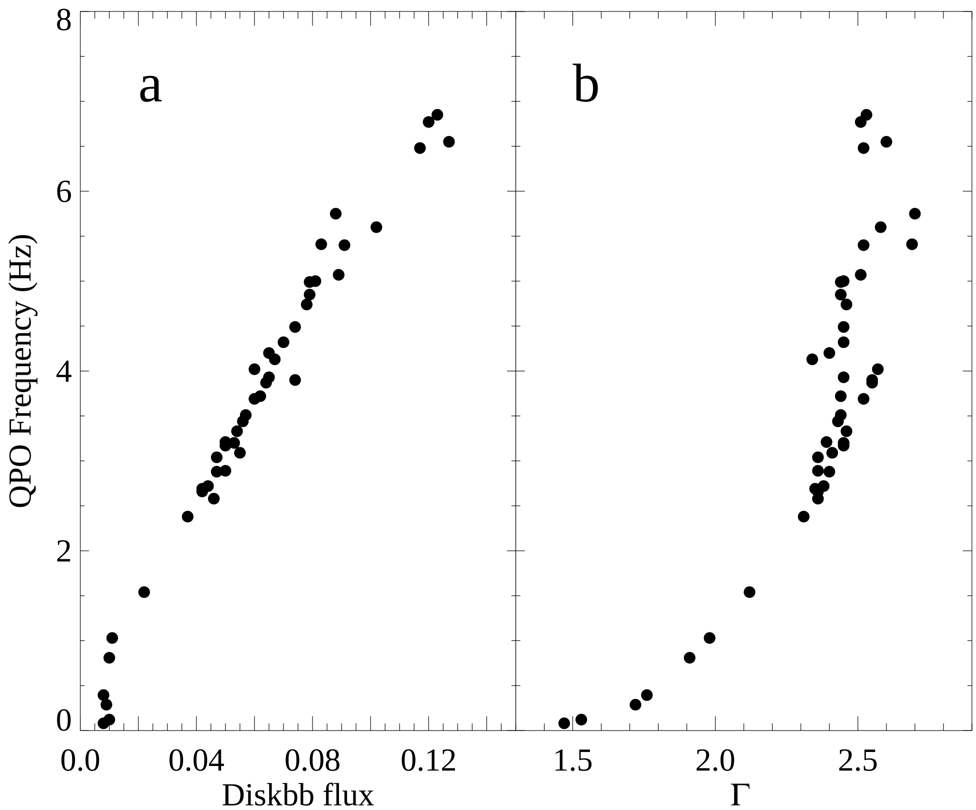

Figure 1.23: (a) Correlation between the QPO frequency and the diskbb flux for XTE J1550−564. The flux is in untis of $10^{-7}\,\mathrm{ergs\,s^{-1}\,cm^{-2}}$. (b) Correlation between the spectral index and the QPO frequency for the same source. The QPO data are from Remillard et al. (2002b) and the spectral data are from Sobczak et al. (2000).

amplitude of the QPO does not correlate well with any spectral fit parameters.

1.7 Source and method selection criteria

The object of this thesis is to understand the nature of variability and characterize the accretion geometry and physical parameters of GBHs (such as the temperature and the density) in the vicinity of the BH by modeling the X-ray energy spectra and PSDs, as well as by using other timing-related functions, such as the time lag and coherence. There are many sources with long observations and many ways to attack the problem. Thus, I need to limit the sources, observation periods and physical methods to analyze the data, yet find the best subset which would provide unreported interesting results to reach my objective.

First of all, I limited my sources to transient systems. There are two main reasons for this. First, my collaborators and I have proprietary *RXTE* data for some of these sources and a history of working on them. Second, the data are so copious from the persistent sources, it is almost impossible to combine the studies of persistent and transient sources. Thanks to my collaborator, Katja Pottschmidt, I was able to include some limited data from the persistent source Cyg X-1 during the discussion of spectral and temporal correlations.

Second, I limited my sources to the ones that were observed with the *RXTE*. The most important reasons are its large area that provides timing analysis with very good statistics and its ability to do frequent monitoring observations with good coverage. Moreover, our group and collaborators have a superior understanding of the detectors and, over time, have developed scripts to analyze both the spectral and temporal data very quickly. I participated in writing these scripts as well as writing my own scripts for modeling the temporal data. By concentrating on one instrument, I avoided problems regarding cross-calibration and other details (i.e., dead-time).

Third, I only analyzed data during the outburst decay of these sources. Most (if not all) of the GBHs show a transition to the LS during the outburst decay. The transition phenomenon is particularly interesting because it points out a large restructuring the accretion system, and provides an evolution trail of spectral and temporal properties to understand the physical changes. The LS provides very strong broad band variability and QPOs to do temporal analysis. The LS and the transition to the HS at the beginning of the outbursts are as interesting, however including them increases the amount of data significantly. Also, again I started working on the LS observations during the decay initially and we have proprietary *RXTE* data that lets me to obtain unreported results. A comparative study between the spectral and temporal parameters in the initial and final LS during an outburst is a very interesting subject and perhaps will be a future project. Note that I have not limited my sources to only ones that show state transition. There are several sources that were in the LS throughout the outburst. Since their temporal evolution at the end of the decay is similar to the evolution of the sources that show a state transition, they were also analyzed. However, the emphasis is given to the sources with state transition.

After applying the criteria outlined above, 11 sources made my list for this analysis. XTE J1650−500, GRO J1655−40, XTE J1748−288, XTE J1755−324, GX 339−4, 4U 1630−47, and XTE J1550−564 show a transition to the LS during outburst decay. 2001 and 2002 outbursts of XTE J1550−564, GRS J1737−31, GS 1354−644, XTE J118+480 are in the LS throughout the outburst. XTE J1859+226 has never shown a transition to the LS during the decay, however it shows transitions to the IS during decay, and therefore was kept in the list for some comparative studies.

Since the emphasis is on the temporal properties, I used the simplest model for the spectral analysis which consists of a diskbb component and a power law component. Sometimes additional models are also used and the details of the spectral models used and my fitting criteria are given in section 2.2.2. For PSD modeling I used Lorentzians instead of FT models, and the reason is explained in section 3.7.

For each source, first I determined the date of state transition. I characterized the evolution of spectral and temporal properties during the transition. I modeled the PSD in several energy bands and looked for systematic relations between the energy band and the rms amplitudes and peak frequencies of Lorentzian model components. When possible, for each observation, I checked whether the frequency dependent lags and coherence have a dependence on the Lorentzian fit components as proposed by Nowak, Wilms & Dove (1999). When possible, for each source, I plotted the evolution of the mean (or integrated, see section 3.7) lags and mean coherence and compared them with the behavior observed for Cyg X-1 (Pottschmidt et al. 2002). If any other analysis is performed other than the methodology presented here, it is mentioned in the "observations and analysis" section of each individual source.

Chapter 2

Instrumentation and Spectral Analysis

"John : Can you see anything?
Terminator: I see everything."

-From Terminator 2, Judgement Day

This chapter consists of two main sections. The first, entitled The *Rossi X-ray Timing Explorer*, outlines the instrument used to accumulate the temporal and spectral information from the X-ray black hole systems of interest. The second section focuses on X-ray spectral analysis, along with a brief overview of *RXTE* data selection, spectral accumulation, and instrumental calibration issues. My main emphasis in this thesis is timing, however spectral information is required to be able to interpret the results from temporal information.

2.1 The *Rossi X-ray Timing Explorer*

The *Rossi X-ray Timing Explorer* (*RXTE*) was launched on 1995 December 30 from Cape Canaveral, Florida with a Delta II rocket. It was placed into a low-Earth circular orbit with an altitude of 580 km and a 23° inclination. One of the

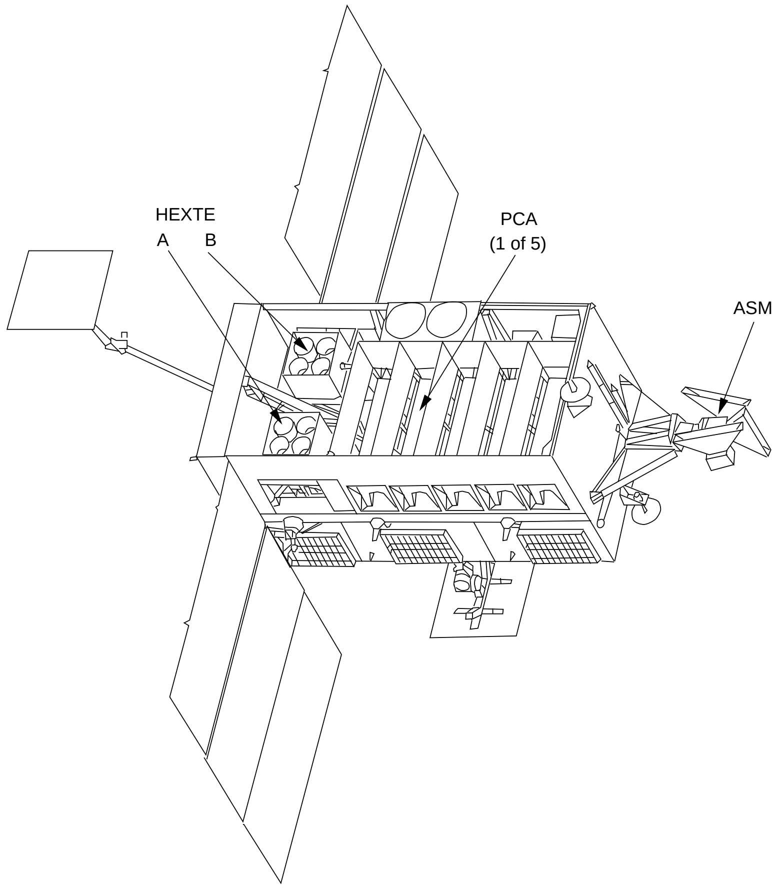

Figure 2.1: Schematic of the *RXTE* spacecraft. Observations from predominantly the two pointed instruments, the PCA and the HEXTE, were used in the thesis.

major advantages of the *RXTE* is its maneuverability. The spacecraft can slew onto a source at 6°/minute, allowing it to respond quickly to transient sources. Named after the pioneering Italian astrophysicist Bruno B. Rossi, the nominal lifetime of the mission was two years, with the goal of five years. The satellite is currently in its 7th year of operation.

A detailed technical description of the instruments is given in the *RXTE* Technical Appendix F (`http://rxte.gsfc.nasa.gov/docs/xte/appendix_f.html`), and unless otherwise noted the rest of this section is based on this publication. Unlike the current generation of soft X-ray telescopes, such as *Chandra X-ray Observatory* and *XMM-Newton*, the *RXTE* does not have focusing capabilities. Instead the spacecraft acquires a single spectrum of everything in the 1° Full Width Half Maximum (FHWM) field of view. The source density is very low at these energies and sensitivities, so

Table 2.1: *RXTE* at a glance

Instrument	Area	Energy Range	Reference	section
PCA	$6500\,\mathrm{cm}^2$	2–60 keV	Jahoda et al. (1996)	2.1.1
HEXTE	$800\,\mathrm{cm}^2$/Cluster	15–250 keV	Rothschild et al. (1998)	2.1.2
ASM	$30\,\mathrm{cm}^2$/Camera	1.5–12 keV	Levine et al. (1996)	2.1.3

source contamination other than the X-ray background is rarely a problem.

A diagram of the *RXTE* is shown in Figure 2.1, with the 3 scientific instruments (the PCA, HEXTE, and ASM, see Table 2.1 and sections 2.1.1, 2.1.2, 2.1.3 respectively) highlighted. Compared to previous missions, such as the Japanese *Ginga* satellite (Turner et al. 1989), the *RXTE* offers a much larger area and degree of flexibility in scheduling. Due to its rotating solar panels the spacecraft is able to observe almost any region of the sky, anytime of the year, although because of thermal considerations the spacecraft is not pointed within $30°$ of the sun. Also, the on board software of the *RXTE* is more intelligent than what has been flown in previous missions. For example, changing the pointing position requires only a source position (right ascension and declination) and a slewing-rate, the calculations for solar array angle and antenna pointing are done autonomously by the spacecraft.

The instruments on board *RXTE* were designed to study the temporal properties of strong X-ray sources, with moderate spectral resolution over $\sim$2 decades of energy. Simply having μs time resolution is not adequate, however, since large numbers of photons need to be collected to give adequate signal to noise in these thin time bins. Therefore the goal of high time resolution studies, especially below 1 ms, requires large areas with a high throughput as well.

In addition to the timing properties, the spectral capabilities of the *RXTE* cover the range 2–250 keV, which is over two decades of continuous coverage. This broad band spectral capability makes the *RXTE* an ideal instrument for the analysis of black holes since it is capable of detecting photons from different emitting regions (e.g. accretion disk and the corona) at the same time.

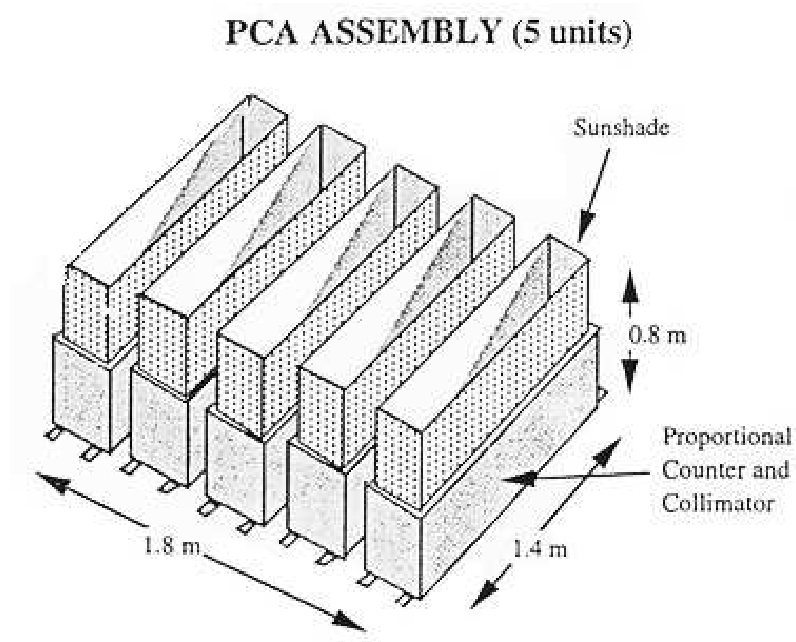

Figure 2.2: Arrangement of the 5 Proportional Counter Array Proportional Counter Units on board the *RXTE*. For the location of the PCA relative to the other instruments on the *RXTE* spacecraft, see Fig. 2.1.

2.1.1 The Proportional Counter Array

The Proportional Counter Array (PCA, see Fig. 2.2) on board the *RXTE* spacecraft was built by NASA's Goddard Space Flight Center (GSFC). It is a direct descendant of the *HEAO*–1 A–2 instrument (Rothschild et al. 1979, and references therein), only with a much larger area and much higher temporal resolution. The PCA consists of 5 nearly identical proportional counter units (PCUs) sensitive in the range 2–60 keV. In this work they will be referred to sequentially as PCUs 0–4. A diagram of a single PCU is shown in Fig. 2.3.

Proportional counters rely on the principle of gas multiplication to measure the energy of an incident X-ray photon (Knoll 1979). An X-ray photon primarily interacts with the gas through photoelectric absorption, emitting a photoelectron which creates a cloud of electron-ion pairs. If there is a voltage applied to the gas, then the electrons and ions drift to their respective electrodes. During this migration collisions occur with neutral gas molecules, but because of their low mobility the ions achieve very little average energy between collision. Free electrons, on the other hand, are

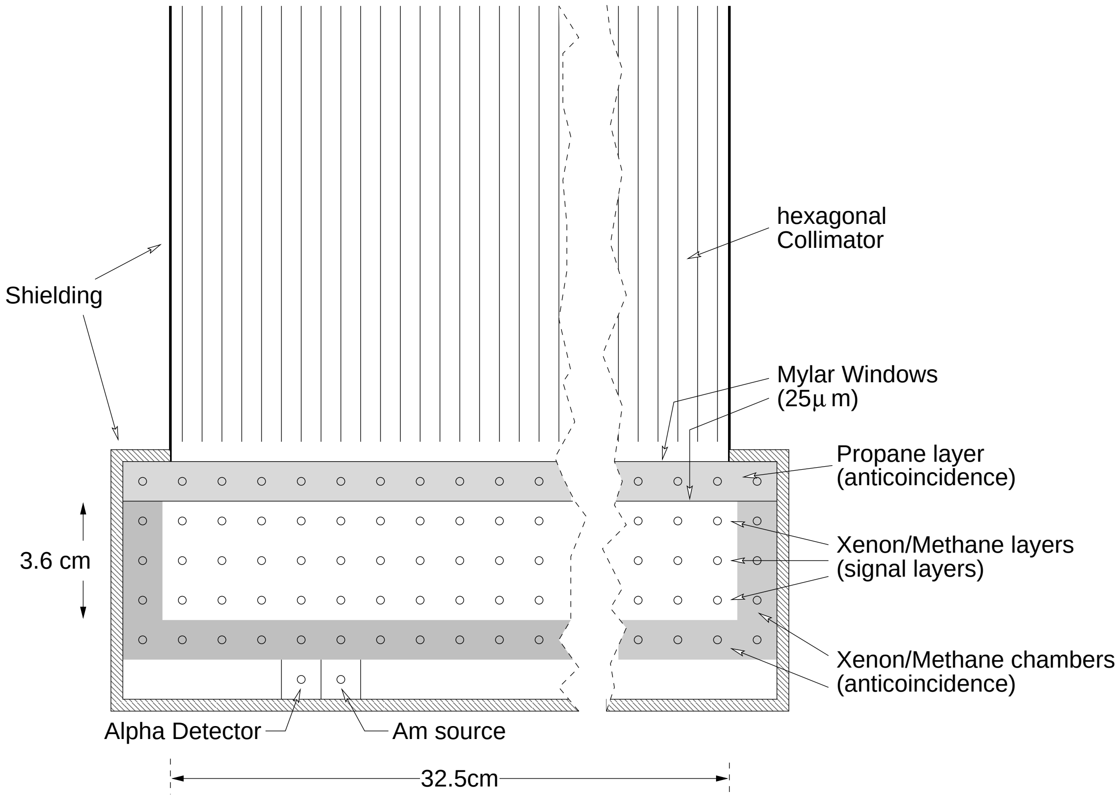

Figure 2.3: Diagram of a single proportional counter unit of the PCA. A charge pulse event is classified as a valid X-ray photon event ("good event") if none of the anti-coincidence anodes, located at the sides and bottom of the chamber, or the propane layer, are simultaneously triggered.

easily accelerated by the applied field and may have a significant kinetic energy when colliding. If this energy is greater than the ionization energy of the gas, it is possible for additional electron-ion pairs to be created in these collisions. These secondary electrons are then accelerated, undergo collisions, and create further ionizations. The gas multiplication process therefore takes the form of a cascade, known as a Townsend avalanche. Within a specific voltage range (which is a property of the material) the size of this avalanche, and therefore the amount of charge collected at the electrodes, is nearly linearly proportional to the incident photon energy. This is the region in which the PCA operates, hence the name proportional counter array.

The response of these detectors is made slightly more complex by the atomic physics of the gases used. In particular, the cross section for photoelectric absorption in Xenon increases sharply at the K-edge with increasing energy. This can be seen in

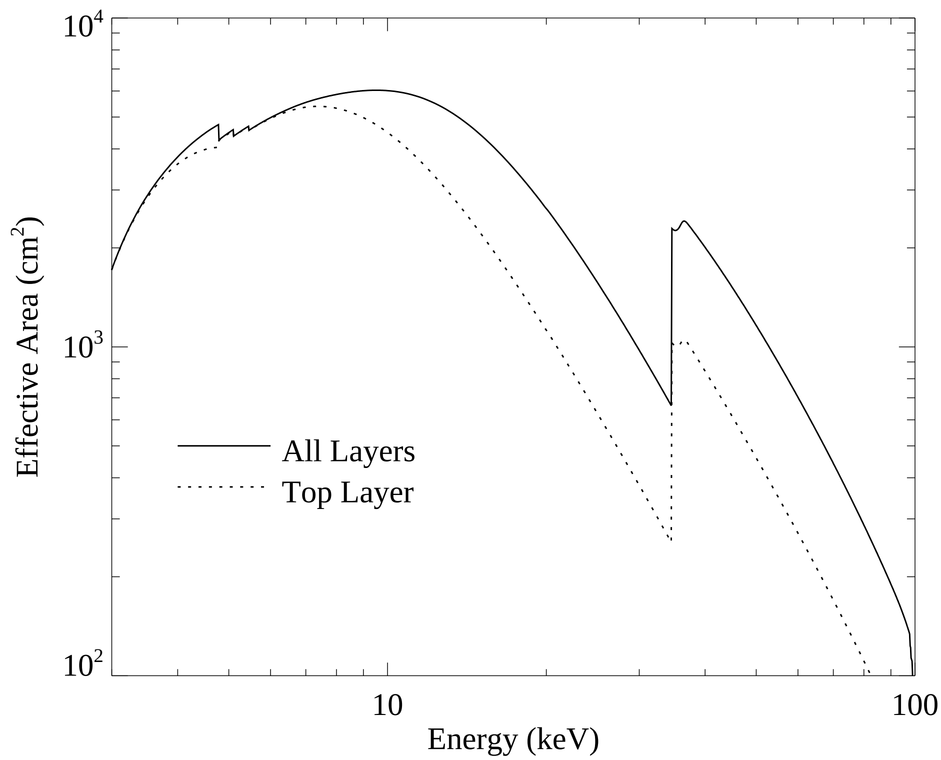

Figure 2.4: The effective area (the product of the detection efficiency with the physical collecting area) of the PCA as a function of energy with all 5 PCUs operating. The dotted line is the effective area for the top layer only. Although the area of the top layer alone is less when compared to all layers, the instrumental calibration is superior, resulting in a reduction of the systematic uncertainties in PCA spectra. The top layer alone was predominantly used for this analysis.

Fig. 2.4 as a significant increase in the PCA effective area (the product of the efficiency for the detection of a photon with the physical area of the detector) above 34.6 keV. Another complication are the L-escape photons due to the L-edges near ~ 5 keV. Again, the photoelectric cross section of Xenon drops below each of these L-edges. Photons with energies just above an edge will be photoelectrically absorbed near the surface of the detector and eject an L-shell electron. As higher-shell electrons cascade into lower levels, photons with energies below that of the L shell will be emitted. In particular, the M to L shell transition will have a much larger mean free path than the incident photon, and so there is a non-zero probability these photons will escape out the front of the detector. The effects of these edges can be seen in the instrument effective area (see Fig. 2.4).

Each PCU is collimated to a 1° FHWM field of view by a hexagonal collimator of BeCu. Behind the collimator are two mylar windows, each 1 mil thick and coated on both sides with a thin layer of aluminum. These windows are separated by 1.3 cm and contain a layer of propane used to screen out low-energy electrons ($E_{\mathrm{e}} < 2\,\mathrm{keV}$). Behind the second mylar window is the main detector volume, filled with a 90/10 Xenon/Methane mixture held at 840 torr. Inside the Xenon/Methane chamber are three layers of signal anodes which collect the charge deposited by incident X-rays, followed by a single anticoincidence anode layer at the bottom of the chamber. Side anodes provide further anticoincidence, and the detectors are passively shielded (Ta and Sn) to provide additional background reduction. The total collecting area of the 5 detectors is $\sim$6500 cm^2. The energy resolution $\Delta E/E$ of proportional counters depends mainly on the counting statistics of the number of electrons received at the anode for an X-ray photon of a given energy E, and therefore varies as $\sqrt{E}$ (Serlemitsos et al. 1976). The nominal energy resolution of the PCA is 18% at 6 keV.

The calibration is done using a tagged ^{241}Am source in each of the detectors. One of the decay channels of the ^{241}Am source, the one used for calibration, is the simultaneous emission of an α-particle with a 59.6 keV photon from the Am decay. The ^{241}Am source sits inside the gas chamber, along with an α particle detector, and photons that register simultaneously with an α particle are assumed to be from the source and are used for calibration.

Due to the large area of the instrument, the count rates can be large enough to saturate the telemetry capabilities of the satellite. In these cases the raw data has to be compressed, selecting only the information desired by the observer. This is the task of the Experiment Data System (EDS), built at the Massachusetts Institute of Technology along with the All Sky Monitor (see section 2.1.3). The EDS consists of 8 parallel, independent computers known as Event Analyzers (EAs). Six of these are dedicated to the PCA, while the remaining 2 process data from the ASM.

For the PCA, each EA can process a different observing "data mode", or prescription for compressing the data based upon time and energy information. At launch the EDS had a set of $\sim$650 available data modes, along with the ability to accept new modes uploaded while in orbit. The available PCA data modes span nearly continuously the phase space between temporal and spectral resolution. It is up the the observer to choose which combination is best for the science topic under consideration, given the constraint of maximum telemetry rate allowed. There are two main classes of modes (and therefore data). The first set are the "event" modes, where each photon collected is registered as an event. For example, the event mode designated as `E_250us_128M_18_1s` has events tagged with $250\,\mu$s time resolution, the full energy range has been compressed from the original 256 channels into 128 using the "M" rebinning scheme and starting at channel 18, and the events are read out every second.

As counting rates increase, the ability to preserve each photon individually is lost. For these sources "binned" modes are available, where histograms generated over a specific period of time instead of individual events are telemetered to the ground. These are designated in a fashion similar to the event mode data. For example, the binned mode `B_125us_4B_0_17_Q` produces a histogram every $125\,\mu$s with 4 spectral channels rebinned from the original channels 0–17 using the "B" scheme. The final "Q" denotes how many bits each histogram contains.

If the source counting rate is low enough, then there is no need for any on board data compression. For these sources the `GoodXenon` data mode is available, which preserves all information. Unlike the rest of the data modes which require a single EA, `GoodXenon` mode data requires 2. Much of the analysis for this work was done using archival *RXTE* data, and as such was limited by the principal investigator's choice of data mode.

While the EDS can accumulate 6 different modes simultaneously, 2 of these are reserved for the PCA "standard mode" data. These cannot be changed by the observer, and are available for every observation. The PCA Standard 1 data has a temporal resolution of 0.125 s, but is without any spectral information. The PCA Standard 2 data has a temporal resolution of 16 s, with 129 pulse height analyzer (PHA) channels for each layer of each PCU.

The high voltage of the PCA has been changed several times during the mission, resulting in 5 "Gain Epochs" (see Table 2.2). After launch the PCA high voltage was set to the designed value of 2000 V, and reduced to 1000 V during South Atlantic Anomaly (SAA) passages. In the SAA the Earth's magnetic field dips, allowing trapped radiation to reach much lower altitudes and greatly increase background). In mid 1996 March PCUs 3 and 4 exhibited signs of occasional breakdowns that

Table 2.2: PCA gain epoch history

Epoch	Start Date	End Date	Stop Time (UTC)
1	–	1996 Mar 21	18:33
2	1996 Mar 21	1996 Apr 15	23:05
3	1996 Apr 15	1999 Mar 22	17:57
4	1999 Mar 22	2000 May 13	00:00
5	2000 May 13	–	–

were most probably caused by sparks within the Xenon/Methane chamber followed by polymerization of the quenching gas around the anodes (Jahoda et al. 1996). On 1996 March 21 the high voltage was reduced, marking the end of PCA gain epoch 1, and the detectors began being switched off during SAA passages. Epoch 2 was short lived, however, since the high voltage was reduced again on 1996 April 15. Since the end of gain epoch 1, PCUs 3 and 4 have been switched off regularly to help extend their useful lifetime. In 1999 March PCU 1 began failing as well, and on 1999 March 22 the PCA high voltage was again reduced.

On 2000 May 12, the propane layer of PCU 0 started leaking, reaching 0 torr within a day. This led to a new epoch, since PCU 0 and the other PCUs have to be treated separately. Note that, there was no gain change between epoch 4 and epoch 5.

The PCA background consists to two main components. The first is internal to the instrument, caused by interactions of cosmic rays and their secondaries with the detector material and by short-term radioactivity produced during passages through the SAA. The second is contamination of the source spectrum due to the diffuse cosmic X-ray background, radiation thought to be produced by the superposition of many distant active galactic nuclei (Fabian & Barcons 1992, and references therein). For the PCA these background components are not observed directly, and therefore have to be modeled.

I have done all of the PCA background estimations using one of 2 background models released by the PCA instrument team. The choice of background depends on the source counting rate. The FAINT model is for source count rates below $40\,\mathrm{cts\,s^{-1}\,PCU^{-1}}$. It is based partly upon the "L7" rate, a rate indicative of charged particles made up of a combination of 7 rates in pairs of adjacent signal anodes read from standard 2 data. The FAINT model is also derived from the integrated recent particle doses during SAA passages as measured by the HEXTE particle monitor. For brighter sources the SkyVLE model was used. This model was created by using blank sky pointings to correlate the Very Large Event (VLE) count rate with the simultaneous particle background. Comparisons of the simulated and measured background spectra and light curves show that these models work quite well, especially below $\sim$25 keV where my spectral analysis is concentrated (Jahoda et al. 1996).

2.1.2 The High Energy X-ray Timing Experiment

The High Energy X-ray Timing Experiment (HEXTE) instrument on the *RXTE* was designed and built at UC San Diego by the High Energy Astrophysics (HEA) group at the Center for Astrophysics and Space Sciences (CASS). and is a direct descendant of the *HEAO*–A4 detector (Matteson 1978). The HEXTE consists of two assemblies of four NaI(Tl)/CsI(Na) phoswich scintillation counters, named clusters "A" and "B" respectively. A diagram of the entire HEXTE assembly is given in Fig. 2.5, while a cutaway illustration of 1 detector assembly is shown in Fig. 2.6. The HEXTE instrument is described in detail in Rothschild et al. (1998).

The detectors are collimated to 1° FHWM using a lead honeycomb and are co-aligned to the same source pointing field of view as the PCA. The nominal area of each cluster is 800 cm^2, and the HEXTE has a maximum time resolution of 8 μs. On 1996 March 21 one of the pulse height analyzers in cluster B failed, effectively reducing the area of that cluster by 25%. Unless noted otherwise, the observations analyzed here were made after the loss of that detector. The current effective area of each cluster as a function of energy is plotted in Fig. 2.7.

The HEXTE detectors are based upon the process of scintillation by energetic particles. The incident photons are photoelectrically absorbed by the crystals. Through interactions with the crystal lattice of the detector material, the energy of these photoelectrons is converted to a shower of UV/optical photons. The intensity of this "scintillation" of light is nearly proportional to the energy deposited in the the crystal. Behind the NaI(Tl) crystal is a window of quartz glass which optically couples the detector crystals to a photomultiplier tube (PMT). The PMT in turn converts the scintillation pulse into an electronic signal whose magnitude is approximately

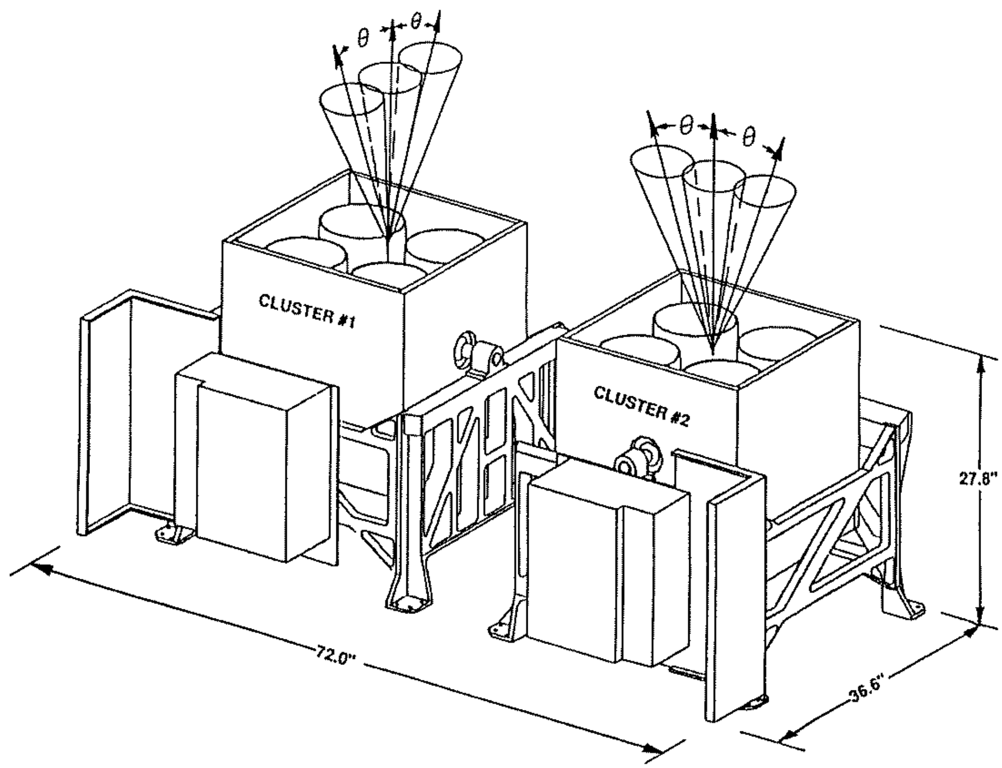

Figure 2.5: Arrangement of the two HEXTE clusters on board the *RXTE*. For the location of the PCA relative to the other instruments on the *RXTE* spacecraft, see Fig. 2.1.

proportional to the energy of the incident X-ray photon. The energy resolution is nearly proportional to $E^{-1/2}$, and is 16% at 60 keV.

In each phoswich, the light emitted by the thallium doped NaI(Tl) crystals has a characteristic decay time of 0.25 μs, while the decay times of the sodium doped CsI(Na) crystals is much slower (0.63 μs). This allows for the rejection of CsI(Na) events via a measurement of the decay time, or pulse shape. An event is accepted by the HEXTE electronics if the decay time is indicative of a NaI(Tl) event, and there is no anticoincidence signal from the shields. The CsI(Na) crystals are used to suppress the instrumental background in the detectors (see below).

Much like at the PCA edges, the HEXTE detectors suffer from a loss of response due to the K-edge of Iodine at 33.17 keV. Photons with energies just above the K-edge will be photoelectrically absorbed relatively near the surface of the detector, ejecting a K-shell photoelectron in the process. As higher-shell electrons cascade

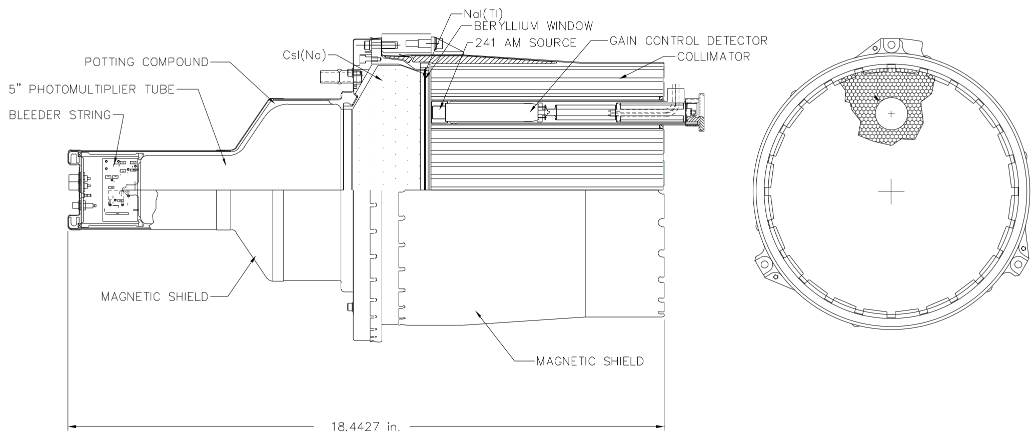

Figure 2.6: Cutaway schematic of a single HEXTE phoswich detector unit, consisting of a photomultiplier tube, scintillation crystals, and collimator assembly. The front view on the right shows the placement of the automatic gain control ^{241}Am source in the collimator and shows a portion of the collimator honeycomb.

into the lower levels, photons with energies below the K-shell will be emitted. In particular, the L to K-shell transition will produce a photon with an energy below K edge, where the cross section is lower and the mean free path in the crystal larger than for the incident photon. Because of this there is a probability these photons will escape out the front of the detector, effectively reducing the energy of detected photons just above the K-edge. This can be seen as a "dip" in the effective area of the instrument above 33 keV (see Fig. 2.7). In the HEXTE detectors this feature is well understood and calibrated.

Gain control and calibration in the HEXTE are done using a radioactive ^{241}Am source mounted into the collimator of each phoswich (see Fig. 2.6) that emits an α particle coincident with a 59.6 keV photon. Photons that register simultaneously with the detection of an α particle are used to perform continuous automatic gain control (Pelling et al. 1991).

Compared with the PCA, the HEXTE has far fewer data modes available. But due the the smaller area of the instrument, coupled with the fact that most sources have a lower luminosity in the HEXTE energy range, there is less of a requirement on the telemetry. Therefore nearly all observation made with the HEXTE are able to

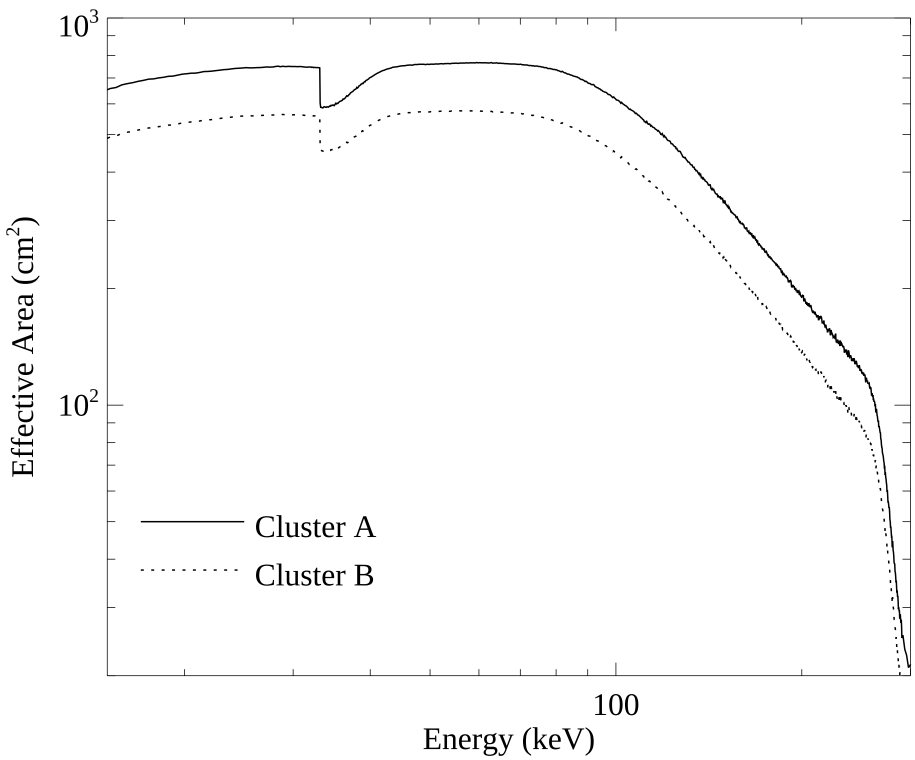

Figure 2.7: The effective area of the two HEXTE clusters. Cluster B has a slightly lower effective area due to the loss of the phoswich early in the mission. Before 1996 March 6 the area of the two clusters was nearly identical. The reduction at lower energies is due to the housing of the detector, while the reduction at higher energies is doe the the finite thickness of the detector. The sharp drop 30 keV is due to the change in the photoelectric cross section at the K-edge of Iodine and the onset of K-escape photons.

preserve full time and spectral information without the need for compression on the spacecraft.

After launch, it was found that the HEXTE electronics experienced a deadtime which was much larger than the prelaunch expectations. This increase is believed to be due to the saturation of the pulse shape circuitry for a period of time larger than specified due to large cosmic-ray energy loss events in the NaI(Tl) crystals. This reduced the livetime accumulated during each observation by an appreciable fraction, on average $\sim$40%. A detailed description of this effect is given by Rothschild et al. (1998). The correct livetime for each observation has to be modeled as part of the HEXTE data analysis procedure, using software released by the HEXTE instrument team. For timing analysis, the deadtime causes additional noise in the power spectral density. This effect will be discussed extensively in Chapter 3.

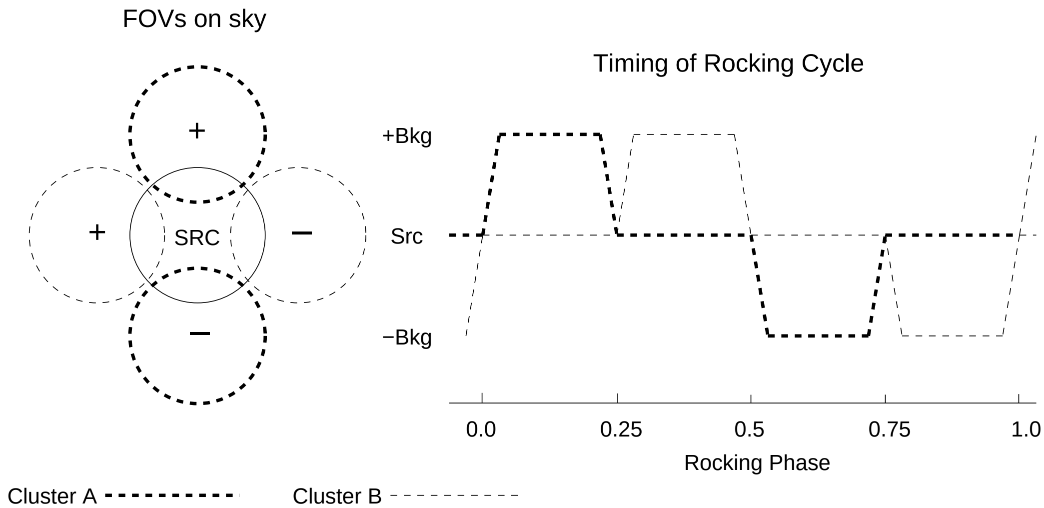

Figure 2.8: Left: The various background pointing positions on the sky with respect to to the source position. The 2° full width zero maximum (FWZM) fields are shown. Right: The timing diagram for the rocking cycle. The duration of each single on-source pointing (with 4/cycle) is a multiple of 16 s. Notice that one of the clusters is always pointing in the source direction, while the background pointings are shorter by 4 seconds irrespective of rocking period.

The HEXTE background consists of both internal background and that from the cosmic diffuse X-ray background, much like the PCA. As mentioned previously, the internal background in the detectors is reduced by using pulse shape discrimination to select only events from the NaI(Tl) crystal (Rothschild et al. 1998). The benefit of the CsI(Na) crystal is to provide active anticoincidence shielding from both X-rays from outside the filed of view, and from events that result in only a partial energy loss in the NaI(Tl) crystal. Plastic anticoincidence detectors around each cluster perform additional background rejection. The resulting instrumental background is reduced to $\sim$100 $\mathrm{cts\,s^{-1}}$ by these procedures.

To estimate the remaining background, the HEXTE clusters "rock" on and off source, where each of the clusters can be displaced by 1°.5 or 3° from the central pointing position. When the HEXTE is in rocking mode (as opposed to "staring," where no background is measured) one cluster observes the source while the other observes a background field. Source and background swapping is done every 16 s (or multiple of 16 s), with one and only one cluster always pointing in the source direction. The HEXTE source and background fields of view, as wells as the rocking scheme, can be seen in Fig. 2.8. Because of the near simultaneous measurement of source and background for each cluster, the background estimation in HEXTE does not require modeling.

2.1.3 The All Sky Monitor

The third instrument on the *RXTE* is the All Sky Monitor (ASM), built by the Center for Space Research at the Massachusetts Institute of Technology. The ASM was designed to monitor the fluxes of many discrete sources simultaneously (Levine et al. 1996). Although data from the ASM was not analyzed extensively for this research, they were very useful for monitoring the flux of sources between pointed observations. Also, the ASM has been vital in identifying and monitoring outbursts from transient accreting X-ray black holes.

The ASM consists of 3 Scanning Shadow Cameras (SSCs), each operating in the 1.5–12 keV energy range. The field of view of each SSC is collimated to a $6^\circ \times 90^\circ$ FHWM; the detectors have a spatial resolution of $3' \times 15'$ (see Fig. 2.9). The shadow mask on each of the SSCs is a thin aluminum sheet subdivided into $6{\times}2$ subsections. Each of the 12 subsections contains $\sim$15 open and $\sim$16 closed slit elements arranged in 1 of 6 carefully chosen pseudo-random patterns. The SSC detector plane contains a Position-Sensitive Proportional Counter (PSPC) with an effective area of $\sim$30 cm^2. The PSPCs are used to measure the displacements and strengths of the shadow patterns cast by X-ray sources within the field of view, and thereby allowing source intensities and directions to be inferred.

The cameras are mounted to a platform at one end of the spacecraft (see Fig. 2.1), and operates independently of the other two instruments while the spacecraft conducts pointed observations. The platform is rotated about its axis, dwelling at each sky position for 90 s. In this way $\sim$80% of the sky passes through the ASM field of view during each spacecraft orbit. This allows the ASM to monitor the 1.5–12 keV intensity of the $\sim$150 brightest X-ray sources in the sky. This data is made available to the public via the World Wide Web, usually within 24 hours, allowing for near realtime monitoring of source intensities. Due to the variability of the X-ray sky, the ASM a powerful tool for identifying when transient sources, both known and previously undiscovered, have gone into outburst.

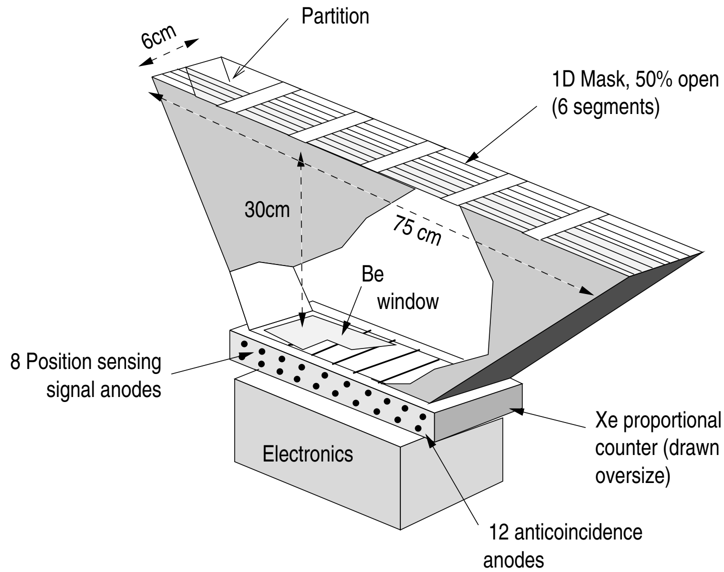

Figure 2.9: Diagram of a single ASM shadow camera. Note that this is *not* drawn to scale; each segment of the shadow mask is the size of the detector window, allowing for a full reconstruction of the shadow pattern.

2.2 Data accumulation and spectral analysis

Along with timing, one of the primary uses of the *RXTE* is to measure the spectra of bright X-ray sources. The distribution of emitted photon energies from a source is called the source *photon spectrum*, or often simply just the source spectrum. Unfortunately this cannot be measured directly. In general, the measured spectral shape is influenced by the effects of the instrumental response, such as the effective area (see Figs. 2.4 and 2.7) and energy resolution, as well as photon counting statistics. Therefore what is actually measured is referred to as the *counts spectrum*. Since this is what is measured by the *RXTE* instruments, unless otherwise noted when I refer to a spectrum , it will be a counts spectrum.

The observed counts spectrum $C(I)$ is represented by (Arnaud 1996):

$$C(I) = \int_0^\infty F(E)R(I,E)dE + N(I) \tag{2.1}$$

where I represents the detector channel number and E photon energy, $F(I)$ is the incident photon spectrum, $N(I)$ the additive noise component, and $R(I,E)$ the detector *response matrix*. The response matrix is the mathematical function that relates the observed counts spectrum to the "true" incident photon spectrum. Along with the determination of the noise component $N(I)$, the response matrix can be a major source of systematic uncertainties in the inference of the source spectrum. In practice, the response matrix is determined through a combination of Monte Carlo simulations, observations of calibration sources with known spectra, and observations of the "standard" X-ray source the Crab Nebula/Pulsar. The understanding of the response matrix, along with its limitations and features, is vital to the interpretation of X-ray spectra.

Although a direct inversion of Eq. 2.1 would be ideal, it is unfortunately not practical. The response matrices of real detectors are often non-linear and have off-diagonal elements, making the inversion non-unique and often simply impossible. Since the measured counts spectrum $C(I)$ cannot be converted into the incident photon spectrum $F(E)$ directly, an indirect fitting method must be used. Starting with an *a priori* model, it is folded forward through the response matrix to get the predicted counts. These are then compared to what was measured using the χ^2 statistic. By doing a number of iterations of the model fit parameters, a minimum in χ^2 can be found, thus giving the best fit for that model.

2.2.1 Data accumulation

The first step in the analysis procedure is the conversion of PCA and HEXTE raw data files provided by the *RXTE* Guest Observer Facility (GOF) into meaningful X-ray counts spectra and light curves. This is done in a straightforward manor using the NASA released `HEASoft` analysis tools[1]. The `HEASoft` consists of two main packages, the `FTOOLs` data accumulation software and the `XANADU` spectral, timing, and image analysis software. The entire process of accumulating data using the `FTOOLs` is outlined in "The RXTE Cook Book: Recipes for Data Analysis and Reduction," provided by the High Energy Astrophysics Science Archive Research Center (HEASARC) and is available via the world wide web at the *RXTE* GOF. Further information is available in "The ABC of XTE" guide, also available at the *RXTE* Guest Observer web site. A flow diagram of the basic procedure is given in Fig 2.10.

When determining source "goodtime" intervals, times from which to allow the

1 see `http://heasarc.gsfc.nasa.gov/` on the world wide web

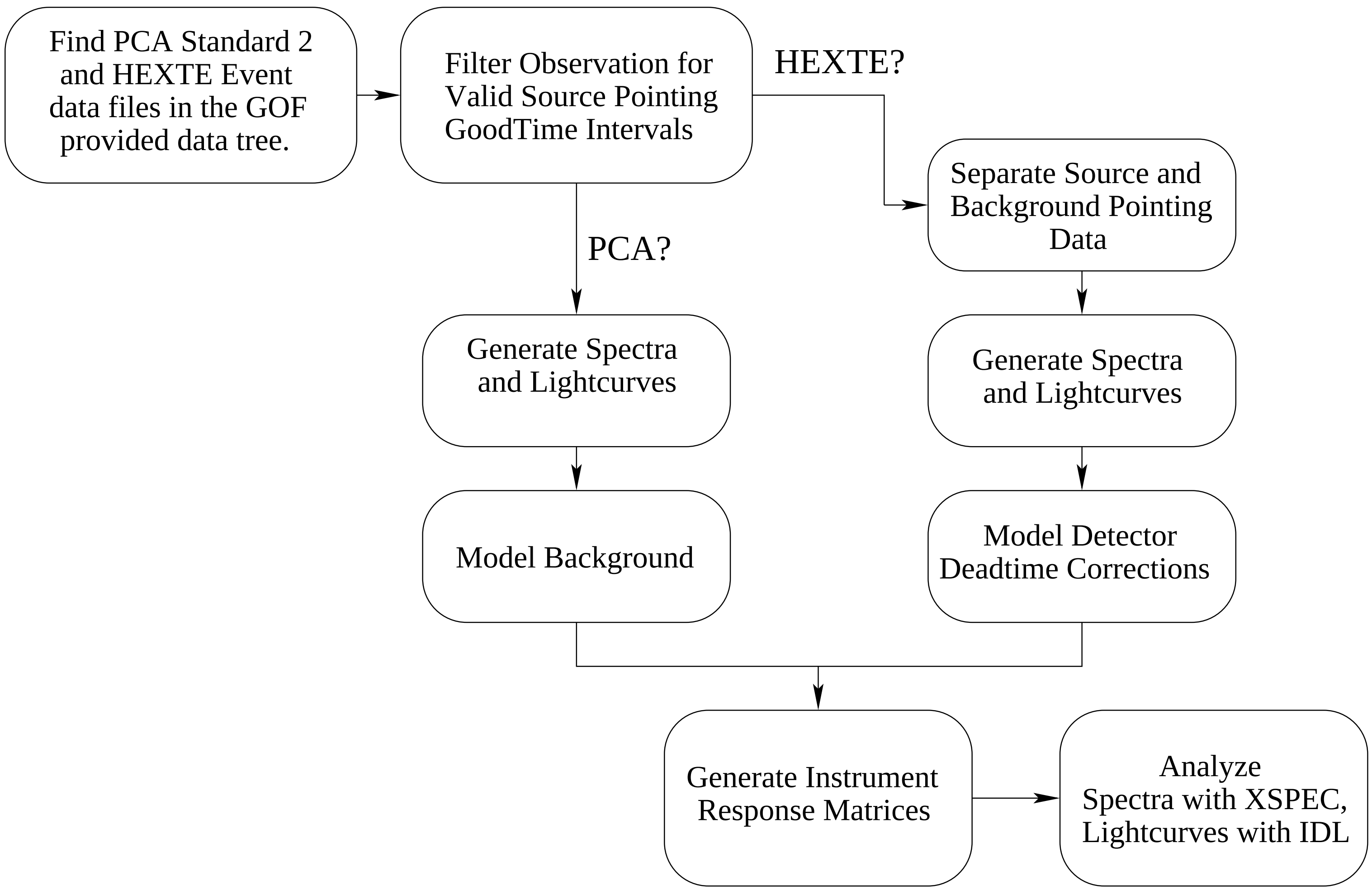

Figure 2.10: Flow diagram of the steps taken to properly accumulate *RXTE* spectra and light curves. The entire process is detailed at the *RXTE* Guest Observer Facility website, `http://heasarc.gsfc.nasa.gov/docs/xte/xtegof.html`

extraction of source (or background) counts, I used the following data selection criteria. To avoid possible contamination from X-rays from the Earth's limb, data was accumulated only when the satellite was pointing more than 10° above the horizon. To avoid possible contamination from activation in the detectors due to the high particle rates associated with SAA passages, I rejected data from a 30 minute interval beginning with the satellite entering the SAA. I also required that the satellite be pointing to within 0°.01 of the source position. Lastly, for faint sources and with the PCA instrument only, the electron ratio in each of the accumulated PCUs was required to be less than 0.10.

All other data accumulation steps, such as the modeling of the PCA background, modeling HEXTE deadtime corrections, and generating response matrices, was done using the released `HEASoft FTOOL` appropriate for the task. Since the procedure to generate spectra and light curves has many discrete steps and uses a variety of different `FTOOLs`, I wrote and developed several shell scripts to automate the process. As a user I have also been active in identifying and reporting problems with the software to the *RXTE* GOF. For spectral analysis I used the `XSPEC` fitting package, released as part of `XANADU` in the `HEASoft` tools. I used version 11.0.1 (Arnaud 1996).

2.2.2 Data analysis and models

The emphasis of this thesis is on timing. I used spectral analysis to relate my timing results to the physical environment defined by them. I also looked for certain correlations that were reported between spectral and temporal fit parameters. It is a daunting task to fit both the X-ray energy spectrum and the power spectrum of all the BHC outburst decay observations, and instead, I used energy spectral fit values published by other scientists when possible. For some observations, the spectral analysis had not been done before, and I performed this analysis. Here, I explain the methods I used for the analysis and summarize the XSPEC fit models I used.

Energy spectral analysis

For most of my spectral analysis, I only used the PCA data due to the low statistical significance of data from HEXTE when observations were short and fluxes were low. After I extract the spectrum as explained in section 2.2.1, I added 1% systematic error. I fit the data in the 3–25 keV band using the response matrix and the background model created using the standard FTOOLS programs. I tested multi-component spectral models until a reduced χ^2 between 0.5 and 1.5 is obtained. Unless otherwise mentioned, I report 68% (1σ) confidence error limits on all my spectral fit parameters.

For some cases I did simultaneous PCA and HEXTE fits. For HEXTE, I combined Cluster A and B spectra, and used the same good time intervals that I used for PCA. The relative normalization was kept floating.

A study with emphasis on X-ray spectrum would have required a more through analysis. For example, HEXTE spectra might be included for all observations and the systematic errors for the PCA might be determined by fitting the Crab spectrum (for a full prescription, see Wilms et al. 1999). However, my interest is more on trends, correlations and big changes (for example during a state transition) of these parameters rather than the correct absolute values. Nevertheless, to be sure that my simple approach does not result in unacceptable fit parameters and to estimate my systematic errors, I conducted a test by comparing the results of a spectral fit which was done by following the optimal prescription and my method. I computed the energy spectra for an observation of XTE J1550$-$564 during the decay of the 2000 outburst and fitted with a model consisting of [**wabs smedge (diskbb+power+gauss)**] (see below for a description of these models) and compared the fit results with the ones reported by Tomsick, Corbel & Kaaret (2001). The fitted parameters differ by $\sim$5% or less, which is approximately my true systematic error for the fit parameters. In Fig. 2.11, I showed this spectrum and my fit along with the residuals in χ^2 units. The reduced χ^2 is 0.61. I usually obtained low χ^2 values, and it is most likely due to 1% systematic error I applied to the data, which is an overestimate.

Summary of models

In this section, I summarize the XSPEC models that I use in my fits, or the models that has been used in other papers that I reported here.

phabs:

This multiplicative model is used to calculate the absorption of X-rays by the inter-

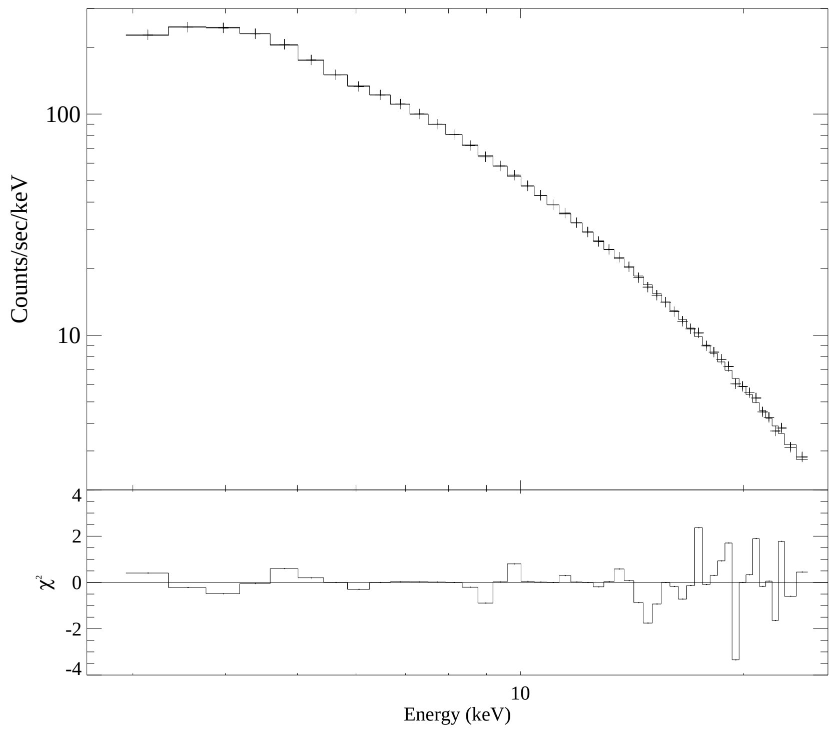

Figure 2.11: Upper panel: Fit to the test spectrum with the model [**phabs smedge (power+diskbb+gauss)**]. The crosses are the data points and the solid line is the overall fit. (See Fig. 2.12 for the contribution of individual fit model components.) Lower panel: Residuals in χ^2 units. This is an excellent fit with a reduced χ^2 of 0.61 with 42 degrees of freedom.

stellar medium (ISM) and defined as

$$M(E) = e^{(-par_1\ \sigma(E))} \tag{2.2}$$

where E is the energy and par_1 is the equivalent hydrogen column (in units of $10^{22}\,\text{atoms/cm}^2$). $\sigma(E)$ is the photoelectric cross-section from Balucinska-Church & McCammon (1992). Although currently **phabs** is the more popular absorption model, some older papers that I reported results from used an absorption model called **wabs**. For **wabs**, the cross sections are from Morrison & McCammon (1983).

power:

This additive model is the simple photon power-law, defined as:

$$A(E) = K\,(E/1\,keV)^{-par_1} \tag{2.3}$$

where K is the normalization (photons/keV/cm^2/s at 1 keV) and par_1 is the photon index of power law.

cutoffpl (cut-off power-law):
In this case, there is an exponential high energy cutoff for the power law. It is defined as:

$$A(E) = K\,(E/\,1keV)^{-par_1}\,e^{(-E/par_2)} \tag{2.4}$$

where K and par_1 are defined the same as in powerlaw, and par_2 is the cutoff energy of exponential cutoff (in keV). Both **power** and **cutoffpl** phenomenologically represent Compton upscattering as discussed in section 1.3.2.

diskbb (multi-color disk blackbody):
It describes optically thick radiation from a standard, geometrically thin accretion disk around a compact object (Makishima et al. 1986). A brief physical description is given in Makishima et al. (1986), and the diskbb spectrum is expressed as:

$$A(E) = \frac{8\pi}{3}\,r_{in}^2\,\cos(i)\int_{T_{out}}^{T_{in}}(T/T_{in})^{-11/3}\,B(E,T)\,dT/T_{in} \tag{2.5}$$

where $T_{in} = T(r_{in})$ and $T_{out} = T(r_{out})$ are the innermost and the outermost disk temperatures respectively, $B(E,T)$ is the blackbody photon flux per unit photon energy from a surface area of temperature T, and i is the inclination angle. XSPEC uses two parameters for this model, T_{in} and and a normalization which is equal to $((r_{in}/\mathrm{km})/(D/10\,\mathrm{kpc}))^2\;\cos(i)$. Here, r_{in} is the inner disk radius in units of km, and D is the distance to the source in units of 10 kpc. T_{out} is well below the energy range of interest, and therefore is not a parameter.

Note that, although the normalization is given in terms of "measurable" physical quantities, due to the relativistic corrections and other factors close to the black hole, the actual numbers obtained from these fits should be considered with extreme caution (Merloni, Fabian & Ross 2000). Although the actual numbers might not reflect the exact physical quantities, it is generally accepted that the trends of the fit parameters are real. For example, an increasing normalization corresponds to an increasing inner disk radius.

smedge (smeared iron edge):
For some black hole systems, especially in the LS, the energy spectra show a significant

local absorption structure above $\sim$ 7 keV, which may be due to iron K-absorption (Ebisawa et al. 1994). However, the structure is broader and shallower than a simple edge, therefore a modified iron K-absorption structure is proposed, which is denoted the "smeared edge model" (Ebisawa et al. 1994). Since this edge is due to absorption by iron K-absorption, it is a multiplicative model, and is defined in XSPEC as:

$$M(E) = \begin{cases} 1. & \text{for} E < par_1, \\ \exp(-par_2\,(\frac{E}{par_1})^{par_3}\,(1 - e^{\frac{par_1 - E}{par_4}})) & \text{for} E > par_1. \end{cases} \tag{2.6}$$

where par_1 is the threshold energy in keV, par_2 is the maximum absorption factor at threshold, par_3 is the index for photoelectric cross-section (normally -2.67), and par_4 is the smearing width in keV. I often fixed the width to 7 keV following Sobczak et al. (2000) and Tomsick, Corbel & Kaaret (2001) to avoid non-physical fit parameters. The index was always kept at -2.67.

gaussian (iron line):

For the excess around 6.5 keV often observed in black hole systems and interpreted as iron line I used a simple gaussian line profile. It is additive model obviously called **gaussian** in XSPEC and defined as:

$$A(E) = \frac{K}{\sqrt{2\,\pi\,par_2^2}}\; e^{(-0.5(\frac{E - par_1}{par_2})^2)} \tag{2.7}$$

where par_1 is the line energy in keV, par_2 is the line width σ in keV, and K (normalization) is the total photons/cm^2/s in the line. If the width is =<0, then it is treated as a delta function. In my fits, I started with an initial value of 6.5 as line energy and 0.5 keV as the width, and I fixed first the width to 0.5 and then the energy to 6.5, in case unphysical fit parameters were obtained if they are kept as free parameters. The interpretation of the iron line fit parameters are beyond the scope of this thesis, and therefore not reported. Likewise, the **smedge** model is treated as completely phenomenological and used to get acceptable χ^2 values to the fits, and also to be consistent with the published results. Therefore, the fit parameters of this model are not reported either. Finally, in Fig. 2.12, I show the individual model components that fits the spectrum that was discussed earlier in this section and shown in Fig. 2.11.

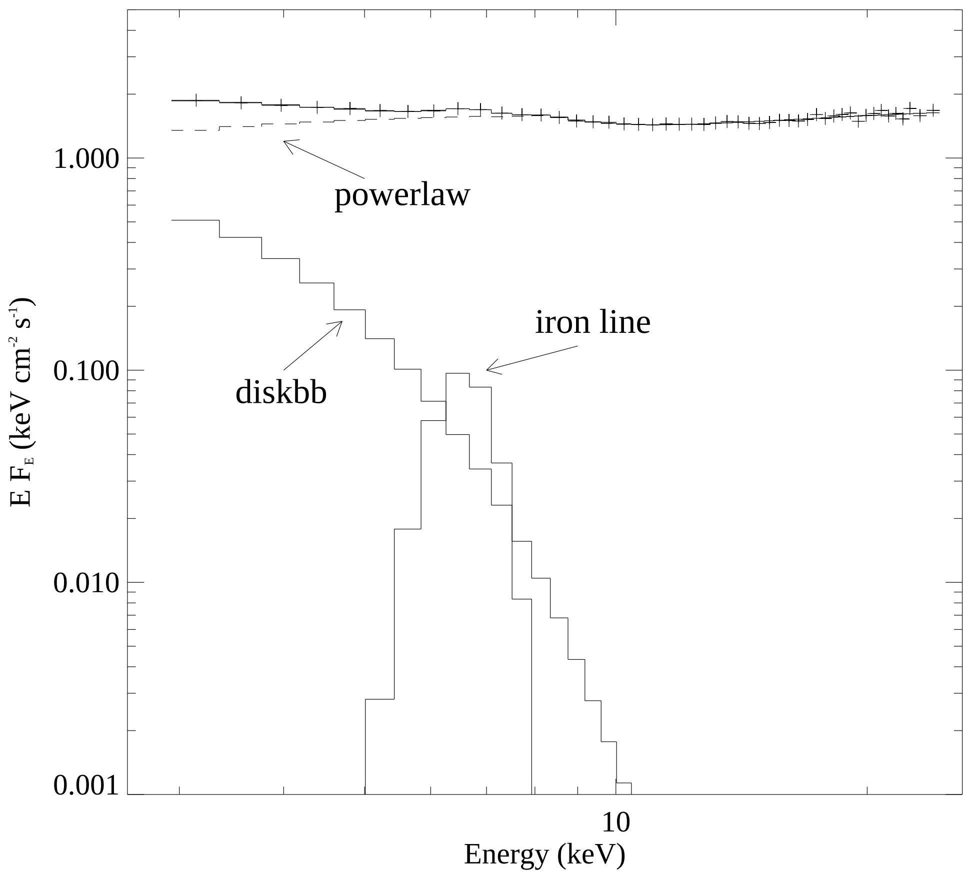

Figure 2.12: The individual model components of the test spectrum. The data points are shown with crosses, and the solid line going through the data points is the overall fit. The model is [**phabs smedge (power+diskbb+gauss)**]. The dashed line show the power law component, which dominates the spectrum above 8 keV. The plot is in energy times flux units.

Chapter 3

Temporal analysis

> "I have heard it said that, in real estate, the three most important things are location, location, location. I believe that in everything else, including life, the three most important things are timing, timing, timing."
>
> \- Arnold Pulda

In this chapter I summarize the mathematical formulation of the Fourier quantities which I use in Chapter 4 to evaluate the short term variability in the light curves of black hole systems. The calculation of the Fourier frequency dependent PSD, the coherence function, and the time lags as well as their uncertainties and noise components are described. Due to the binned nature of measured light curve data used in this work, the discrete formulation is selected and the usual procedure to enhance the signal-to-noise-ratio of the measured quantities – averaging them over many light curve segments and Fourier frequencies – is also included. A review of Fourier analyses of astronomical time series concentrating on the PSD is given by (van der Klis 1989). Most of the equations presented here, especially those associated with the coherence and the time lags, can be found in (Vaughan & Nowak 1997) and (Nowak et al. 1999).

3.1 The discrete Fourier transform

The variability of astronomical sources is usually expressed as a time series, x_h, of observed count rates in a certain energy band, where h denotes the number of the time bin during which the count rate was measured. In the following, it is assumed that x_h consists of m evenly spaced time bins of length Δt. The basis of many powerful analysis techniques to evaluate the properties of x_h is its discrete Fourier transform X_j:

$$X_j = \sum_{h=0}^{n-1} x_h e^{2\pi \mathrm{i} jh/m} \tag{3.1}$$

where $\mathrm{i} = \sqrt{-1}$. Independent values for this complex quantity are obtained for the Fourier frequencies:

$$f_j = \frac{j}{T} = \frac{j}{m\Delta t} \tag{3.2}$$

Here $T = m\Delta t$ is the length of the light curve. Formally the Fourier frequencies are defined in $j \in [-m/2, m/2]$, but for the analysis of measured light curves the minimally accessible frequency is given by the duration of the observation: $j_{\mathrm{min}} = 1$, i.e., $f_{\mathrm{min}} = 1/T$. The maximally accessible frequency, the Nyquist frequency, is given by the bin time: $j_{\mathrm{max}} = m/2$, i.e., $f_{\mathrm{max}} = 1/(2\Delta t)$. Also, measured light curves always contain noise, for X-ray light curves this is mainly counting, i.e., Poisson, noise (section 3.2.4). Since the lightcurve ideally can be split into an independent signal component s_h and an independent noise component n_h, i.e., $x_h = s_h + n_h$, this is also true for their discrete Fourier transforms:

$$X_j = S_j + N_j \tag{3.3}$$

In the following sections I describe the PSD (section 3.2), which is constructed from the Fourier transform of one light curve and the cross spectral density (section 3.3), which is derived from the Fourier transforms of two light curves, e.g., measured simultaneously in two different energy bands. The latter is the basis of the coherence function (section 3.4) and of the time lags (section 3.5).

3.2 The power spectral density (PSD)

3.2.1 Calculating and averaging the PSD

The PSD is a non-complex quantity obtained by multiplying the discrete Fourier transform and its complex conjugated quantity, i.e., the PSD is the squared magnitude of the complex Fourier transform.

$$P_j = X_j^* X_j = |X_j|^2 \tag{3.4}$$

The power spectral density is directly related to the variance of the light curve in the sense that P_j gives the fraction of the total light curve variance that is due to variability characterized by the frequency f_j. For practical use, several different normalizations of Eq. (3.4) exist. Periodic variability, e.g., sinusoidal with a single frequency, $x_h = \sin(2\pi f^* h\Delta t)$, produces a δ-peak in the PSD located at this frequency, f^*. While the PSD is thus mainly used to conduct searches for periodic signals in light curves, it is clear that it can also be used to evaluate variability characterized by a continuous distribution of frequencies.

The statistical uncertainty of the individual, non-averaged PSD is of the order of the PSD itself, and by averaging, it can be reduced by the square root of the averaged independent measurements, as seen in Eq. (3.11) below. Therefore averaging of PSD plays an important role in the analysis of measured power spectra in order to achieve better signal-to-noise ratios (SNRs). Two different kinds of averaging can be applied: the Fourier frequencies and their corresponding PSD values can be rebinned to a new frequency grid ($f_j \to f_k$) and/or the final PSD can be obtained by averaging individual PSDs each corresponding to a segment of given length of the original light curve. In the former case the frequency resolution is reduced, while in the latter case the minimum accessible frequency is constrained to $1/T_{\text{seg}}$ instead of extending down to $1/T$. Usually, both methods are applied simultaneously. In the following, angle brackets are used to denote an average over a finite number, M, of independent measurements:

$$P_k = \langle P_j \rangle = \langle P \rangle \tag{3.5}$$

In this nomenclature M is the product of M_{seg} light curve segments and M_f Fourier frequencies used to obtain a given $\langle P \rangle$ value:

$$M = M_{\mathrm{seg}} \times M_f \tag{3.6}$$

The number of averaged light curve segments can vary depending on the frequency range under consideration: a few long segments can be produced to reach low frequencies, while PSDs from many short segments can be averaged for maximum SNR at high frequencies. The number of averaged Fourier frequencies can also vary depending on which frequency bin f_k is considered. For the broad band power spectra studied in this work a logarithmic frequency rebinning ($\Delta f/f = \mathrm{constant}$) has proven to be useful.

3.2.2 Normalizing PSD values, background correction

In X-ray astronomy applications, several different normalizations of the PSD are useful. They are obtained by multiplying the original PSD by a normalization factor A:

$$\langle P_{\mathrm{norm}} \rangle = A \, \langle P \rangle \tag{3.7}$$

The most important definitions of A are the following:

$$A = \begin{cases} 1 & \text{unnormalized} \\ \frac{2}{TR} & \text{for Leahy et al. (1983) normalization} \\ \frac{2}{TR_{\mathrm{sig}}R_{\mathrm{sig}}} & \text{for Miyamoto \& Kitamoto (1989) normalization} \end{cases} \tag{3.8}$$

Above, the distinction between the total time-averaged count rate $R = \langle x_h \rangle$ of the light curve and the average signal count rate R_{sig} is made. The latter is obtained by subtracting the average count rate due to the X-ray background level present in measured light curves, R_{bkg}:

$$R_{\mathrm{sig}} = R - R_{\mathrm{bkg}} \tag{3.9}$$

Only the "Miyamoto" normalization takes the background into account.

The unnormalized PSD is required to calculate higher order Fourier quantities like the coherence function (section 3.4). In "Leahy" normalization the PSD delivers the light curve variance or the squared root mean square variability, rms^2, per frequency interval. In this case Parseval's theorem can be written in the following simple form:

$$\mathrm{rms}^2 = \left\langle x_h^2 \right\rangle - \left\langle x_h \right\rangle^2 = \sum_k \frac{2}{T \left\langle x_h \right\rangle} \left\langle P \right\rangle \Delta f_k \tag{3.10}$$

In this normalization the Poisson noise level is to be found at the value of 2, independent of the source count rate. The "Miyamoto" normalization gives the PSD in units of the squared *fractional* rms variability per frequency interval, i.e., the variance that each frequency contributes in units of the average signal count rate R_{sig} of the source. This normalization is usually given in units of $(\mathrm{rms}/R_{\mathrm{sig}})^2/\mathrm{Hz}$. While the Miyamoto normalization allows a better comparison of systematic brightness-independent similarities between different PSDs (shape, fractional variance) and is therefore most often used, the effects of varying source brightness which might be of interest, e.g, when comparing PSDs from two different BHCs or from one BHC in different states, are only apparent in the Leahy normalization. Note that the expression "squared rms" (or "rms amplitude" or "rms variability") which has been used in the absolute sense of Eq. (3.10) in this section is often also used for the fractional variability, i.e., meaning $(\mathrm{rms}/R_{\mathrm{sig}})^2$.

Background correction after the loss of propane layer

I continued to use PCU 0 even after the loss of the propane layer, since at low count rates, it is essential to get all the source counts possible. As mentioned earlier, background count rate is required to calculate the Miyamoto normalized PSDs. I analyzed several observations before the release of the new background files. I dealt with the additional background by assuming that PCU 0 and PCU 2 are identical and that the difference in the count rates between the two is the excess background from PCU 0. This excess background is added to the background obtained by using the FTOOL "pcabackest".

3.2.3 Statistical uncertainty of the averaged PSD values

If x_h is assumed to be approximately normally distributed (e.g., for large m, "central limit theorem") which is generally the case, then the PSD values are χ^2 distributed with two degrees of freedom (van der Klis 1989). For Poisson noise, the 1σ uncertainty of an individual unrebinned PSD value can be shown to be of the order of the intrinsic noise PSD value itself. In Leahy normalization, the Poisson noise has a mean value of 2, independent of frequency ("white noise"). Its uncertainty, being χ^2 distributed with two degrees of freedom, amounts to $\sigma(|N_{\mathrm{poisson},j}|^2) = \sqrt{\mathrm{var}(|N_{\mathrm{poisson},j}|^2)} = \sqrt{4} = 2$. Rebinning reduces σ to $2/\sqrt{M}$ and approximates a Gaussian distribution again. The corresponding statistical arguments can be adopted for the signal component of the PSD, allowing one to express the uncertainty of the measured PSD values as (van der Klis 1989):

$$\sigma \langle P \rangle = \frac{\langle P \rangle}{\sqrt{M}} \tag{3.11}$$

The same normalization factor as chosen for $\langle P_{\mathrm{norm}} \rangle$ must also be applied to the PSD uncertainty:

$$\sigma \langle P_{\mathrm{norm}} \rangle = A \sigma \langle P \rangle \tag{3.12}$$

3.2.4 Noise component of the PSD and its deadtime correction

In order to use the measured PSD to evaluate and model the source variability, the variability contributed by non-source related noise, $\langle |N|^2 \rangle$, has to be determined and removed. From $S_j = X_j - N_j$ (Eq. 3.3) the unnormalized signal component of the PSD, $\langle |S|^2 \rangle$, can be determined as:

$$\langle |S|^2 \rangle = \langle P \rangle - \langle |N|^2 \rangle \tag{3.13}$$

It is safe to assume X_j and N_j are uncorrelated, and therefore their averaged cross terms will tend to average out to zero (van der Klis 1989). Equivalent formulae are valid for all normalizations. Due to the statistical uncertainty of the observed noise component, a PSD from which the theoretical noise level has been subtracted still shows deviations from the signal component. These deviations can be represented by an "effective noise level", E:

$$E = \frac{1}{\sqrt{M}} \langle |N|^2 \rangle \tag{3.14}$$

As already mentioned, the noise in black hole candidate X-ray light curves is mainly counting noise. In the different normalizations introduced in section 3.2.2, the frequency-independent Poisson noise level amounts to the following values:

$$\left\langle |N_{\text{Poisson}}|^2 \right\rangle = |N_{\text{Poisson}}|^2 = \begin{cases} TR & \text{unnormalized} \\ 2 & \text{for Leahy et al. (1983) normalization} \\ \frac{2}{R_{\text{sig}}} & \text{for Miyamoto \& Kitamoto (1989) normalization} \end{cases} \tag{3.15}$$

However, this noise component is modified by the occurrence of deadtime in X-ray detectors, i.e. the time after an X-ray photon triggered the detector during which it cannot register any further photons.

Deadtime in PCA

For proportional counters like the *RXTE/PCA* instrument, the deadtime is the time elapsed until the electrons generated by an X-ray photon in the detector gas are transported to the anode wires and the detector gas is neutral again. The influence of the deadtime on the counting noise is frequency-dependent (see Eqs 3.16–3.19 below). It has to be taken into account in terms of a correction of the Poisson noise level that is to be removed from the measured PSD. For an individual noise measurement in full Fourier frequency resolution this corrected noise component $|N_j|^2$ can be written as:

$$|N_j|^2 = |N_{\text{Poisson}}|^2 \left(1 + K_{\text{dead},j} + K_{\text{instr},j}\right) \tag{3.16}$$

As reflected by this equation, the deadtime correction of $|N_{\text{Poisson}}|^2$ can generally be divided into two parts: a functionally instrument-independent contribution, $K_{\text{dead},j}$, which is caused by the incident X-ray photons[1]. This means that observed photons outside the considered energy range or, e.g., from coincident events, although they are causing the same amount of deadtime, do not have to be considered in the noise correction. There is also an additional, instrument-dependent contribution, $K_{\text{instr},j}$. In case of the *RXTE/PCA* instrument, e.g., "very large events" cause a different kind of deadtime since they appear as "anti-shots" in the light curves. They are not included in the measured light curve count rates since they are known to be caused by energetic cosmic rays. A measure of these events is provided by the very large event

1 More precisely, by those incident X-ray photons that are taken into account in the light curve that is Fourier transformed (Zhang et al. 1996)

(VLE) count rate, counting cosmic ray events depositing more than a predefined threshold energy in the detector. The measured VLE rate is delivered with each *RXTE/PCA* observation. Thus their deadtime influence can also be corrected. For the following I set

$$K_{\mathrm{instr},j} = K_{\mathrm{vle},j} \tag{3.17}$$

specializing on the *RXTE/PCA* instrument for describing the instrument-dependent part of the deadtime correction.

Analytically, the expectation value of the general (instrument-independent) deadtime modification of the Poisson noise has been thoroughly studied by Zhang et al. (1995). They discriminate between two possible kinds of deadtime, the paralyzable type (every incident event causes deadtime) and the non-paralyzable type (only detected events cause deadtime). This distinction is insignificant below 10 kHz, and therefore not relevant for analyzing BHC PSDs (Jernigan, Klein & Arons 2000). In practical applications, both types, the paralyzable (Jernigan, Klein & Arons 2000) as well as the non-paralyzable (Zhang et al. 1996) deadtime correction have been used to correct *PCA* PSDs. Jernigan, Klein & Arons (2000) showed that the description of $K_{\mathrm{dead},j}$ as paralyzable deadtime influence in its basic form – i.e., not taking binning effects into account – is well suited for *PCA* observations comparable to our observations:

$$K_{\mathrm{dead},j} = 2R_{\mathrm{pcu}} \left[\frac{\sin\left(2\pi\tau_{\mathrm{d}} f_j\right)}{2\pi f_j}\right] \tag{3.18}$$

In this equation R_{pcu} is the observed count rate *per PCU* and τ_{d} is the detector deadtime (which accounts for collection time and event processing) which nominally amounts to $10\,\mu$s for the *PCA*. Note again that in case of correcting PSDs from selected energy bands, R_{pcu} consists only of those events that are part of the discrete Fourier transform, i.e., R_{pcu} is the count rate in the selected energy band.

The deadtime correction due to very large events in the *PCA*, $K_{\mathrm{vle},j}$, can be calculated by (Zhang et al. 1996; Jernigan, Klein & Arons 2000):

$$K_{\mathrm{vle},j} = R_{\mathrm{pcu}} R_{\mathrm{vle}} \left[\frac{\sin\left(\pi\tau_{\mathrm{vle}} f_j\right)}{\pi f_j}\right]^2 \tag{3.19}$$

Here R_{vle} is the VLE count rate *per PCU* and τ_{vle} is the deadtime caused by each very large event. The latter depends on the energy threshold that has been set for the observation in question. According to the "*RXTE* Cook Book", four different settings are possible; the threshold of 75 keV, e.g., corresponds to $\tau_{\mathrm{vle}} \sim 170\,\mu$s (Zhang et al. 1996).

Eqs (3.18) and (3.19) have been tested by Jernigan, Klein & Arons (2000) using PSDs observed for the neutron star XRBs GX 17+1 and for Cyg X-1. They model the noise dominated high frequency part of the observed PSDs according to Eqs (3.16)–(3.19) [2] finding good agreement. Therefore, this is the description that was used for noise-subtracting most of the PSDs. For the more recent observations no usable VLE count rates were available, thus they were corrected taking only K_{dead} into account. In this case Eq. (24) of Zhang et al. (1995) – which also takes binning effects into account – was used. However, for BHC PSDs, there is no detectable difference to simply using Eq. (3.18) – which does not take binning into account.

Fig. 3.1 illustrates the magnitude of the different noise corrections for parameters typical for a BHC in the frequency range relevant for this work, i.e., below 100 Hz: The deadtime correction reduces the noise level by ~2% (Fig. 3.1a). The VLE correction only slightly increases the noise level again. This increase amounts to ~ 0.03% of the noise level (Fig. 3.1b) and its omission does not significantly influence the PSD analyses presented in this work. The difference in the general deadtime correction according to Eq. (24) of Zhang et al. (1995) and Eq. (3.18) is even smaller (Fig. 3.1b).

3.2.5 Deadtime in HEXTE

The HEXTE is designed to provide a measurement of deadtime by gating an internal clock to count whenever the system was unable to accept a new event. Three examples enabling this clock are: (1) an X-ray event which is currently processed by the PSA/PHA system, (2) a vetoed event due to a high energy particle in the CsI shield crystal, and (3) congestion in the event processing system which might occur at very high rates. It was discovered soon after the launch that the system did not function entirely as intended due to a subtle problem in the preamplifier baseline control during recovery from very large energy losses. The effect of this flaw is to introduce an additional component of deadtime the magnitude of which depends on

2 Their model formally includes another empirical additive noise correction, however, it is consistent with zero for those two sources.

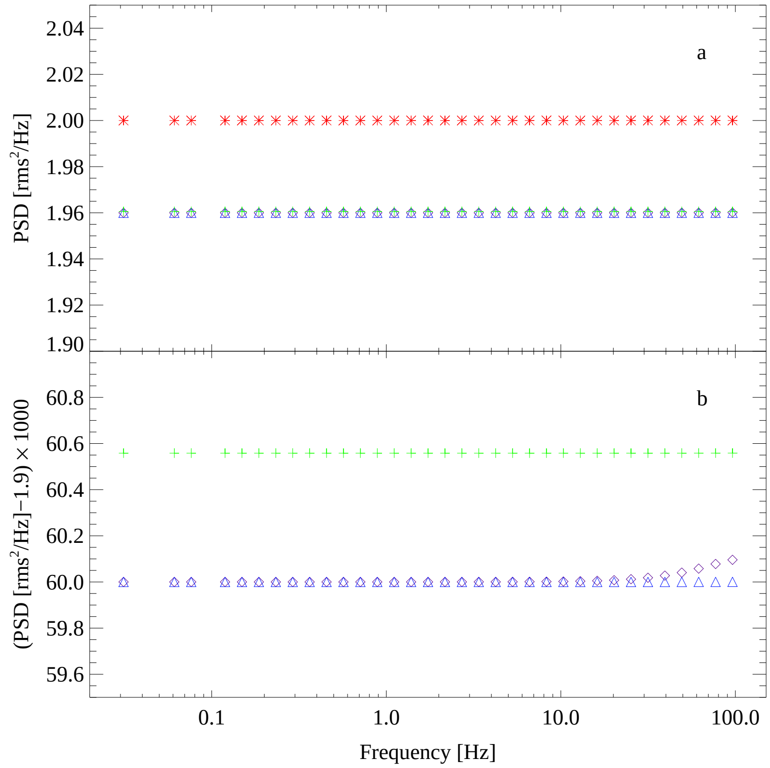

Figure 3.1: **a stars:** Pure Poisson noise in Leahy normalization. **Diamonds:** Poisson noise with general deadtime correction; paralyzable with binning effects; Eq. 24 of Zhang et al. (1995); with $R_{\rm pcu} = 1000\,{\rm cps}$, $\tau_{\rm d} = 10\,\mu{\rm s}$, $\Delta t = 2^{-8}\,{\rm s}$, and $m = 8192$. **Triangles:** Poisson noise with general deadtime correction; paralyzable without binning effects; Eq. (3.18); with $R_{\rm pcu} = 1000\,{\rm cps}$, and $\tau_{\rm d} = 10\,\mu{\rm s}$. **Crosses:** Same as blue triangles plus additional VLE correction; Eq. (3.19); with the additional parameters $R_{\rm vle} = 75\,{\rm cps}$, and $\tau_{\rm vle} = 61\,\mu{\rm s}$. **b** Same quantities as shown above but with the y-scale adjusted to emphasize the (small) differences between the noise corrections. The pure Poisson noise is off the scale in this panel. In both panels all noise spectra have been frequency-rebinned to a logarithmically equidistant grid for reasons of clarity.

the size of the energy loss.

The Ftool "hxtdead" corrects a HEXTE spectral or light curve FITS file for detector deadtime. However, the only effect of this program is multiplication of rates by a factor depending on deadtime which does not affect the shape of the power spectrum. Additional modeling is required to understand the effects of deadtime on the PSD shape.

From the three reasons listed above, high energy particles are the ones which cause the majority of the deadtime. There are two discriminator levels in HEXTE electronics which classify the energy loss in the detectors. The Upper Level Discriminator

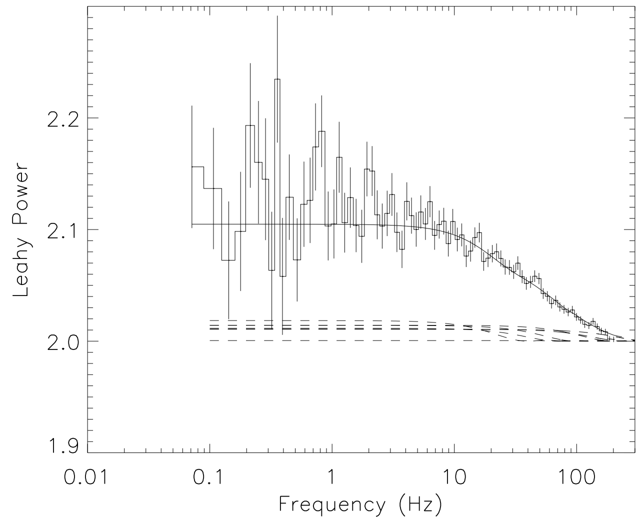

Fit Parameters

R_p (cts/s)	55.	22.	19.	7.6	4.6	1.9	0.96	0.36
τ (ms)	2.5	4	5	7	10	14	25	35

Figure 3.2: Leahy normalized power spectrum of a blank sky observation by HEXTE Cluster A. The solid line is the fit to data by the function given in the text and with the parameters seen above. The dashed lines correspond to contribution from each term from the fit parameters.

(ULD) counts the events which leave greater than 0.25 MeV and the eXtra Upper Level Discriminator (XULD) counts those leaving more than 20 MeV. The electronics are adjusted such that each XULD event causes a minimum of 2.5 ms deadtime. The XULD rate is ~100 cts/s, and the ULD rate is ~700 cts/s. The cumulative dead-time effect can be as high as 40%. Both ULD and XULD rates for each 16 s interval can be obtained from the HEXTE housekeeping files.

I investigated the effects of deadtime on the background power spectra of HEXTE. When Leahy (Leahy et al. 1983) normalized, the background power, dominated by the counting statistics, must be at the constant level of two. However, due to the effects of deadtime there is a small, frequency dependent excess especially towards lower frequencies as seen in Fig. 3.2.

A similar effect is observed in the PCA power spectra also, but the impact is much less severe since the deadtime per particle is small and constant. The power spectra of PCA is corrected by subtracting a frequency dependent function as described in Zhang et al. (1996), and in previous section. I modified this function to accommodate different deadtimes and rates and was able to fit the Leahy normalized HEXTE background power spectrum (from blank sky observation). The formula is given below, R_x is the X-ray rate per detector and $R_p(i)$ is the rate of particles which cause a deadtime of $\tau(i)$.

$$P(f) \;=\; 2 \,+\, 2\, R_x \sum_i R_p(i)\, \frac{\mathrm{Sin}^2(\pi\, \tau(i)\, f)}{\pi^2(i)\; f^2}$$

The fit parameters are found as follows: I only considered very high energy particles (XULD), where the minimum dead time is 2.5 ms. I obtained deadtime as a function of energy loss up to 300 MeV by using atmospheric muons and the HEXTE engineering module. Particles leaving more than 100 MeV cause deadtimes more than 2.5 ms (See Fig. 3.3). I estimated the energy loss spectrum by using the cosmic particle rates above the atmosphere, orbit parameters and the HEXTE material properties and geometry. From the energy loss spectrum I obtained an initial estimate of parameters for the fitting process. During the fit, deadtimes were frozen and the rates corresponding to each deadtime were free. I then compared the total R_p with the observed XULD rate for consistency.

I have applied some tests to validate this correction. First, I applied the formula to a power spectrum of the same blank sky observation but with a different energy range such that the composition of high energy particles remained constant but the X-ray rate per detector is changed. The function fit the resulting power spectrum reasonably well. I then applied the formula to a different observation with a different average XULD rate and again obtained a reasonably good fit.

To test this correction further, I analyzed power spectra from one observation of XTE J1550−564 in the 15-30 keV range using both HEXTE and PCA. Without the correction, the PCA and HEXTE power spectra are significantly different. With the deadtime correction good agreement between PCA and HEXTE is obtained. (Fig. 3.4) I feel this confirms our parametrization of the HEXTE deadtime correction for power spectra (Kalemci, Tomsick & Rothschild 2000).

One assumption I made is that the spectrum of cosmic-rays varies little with

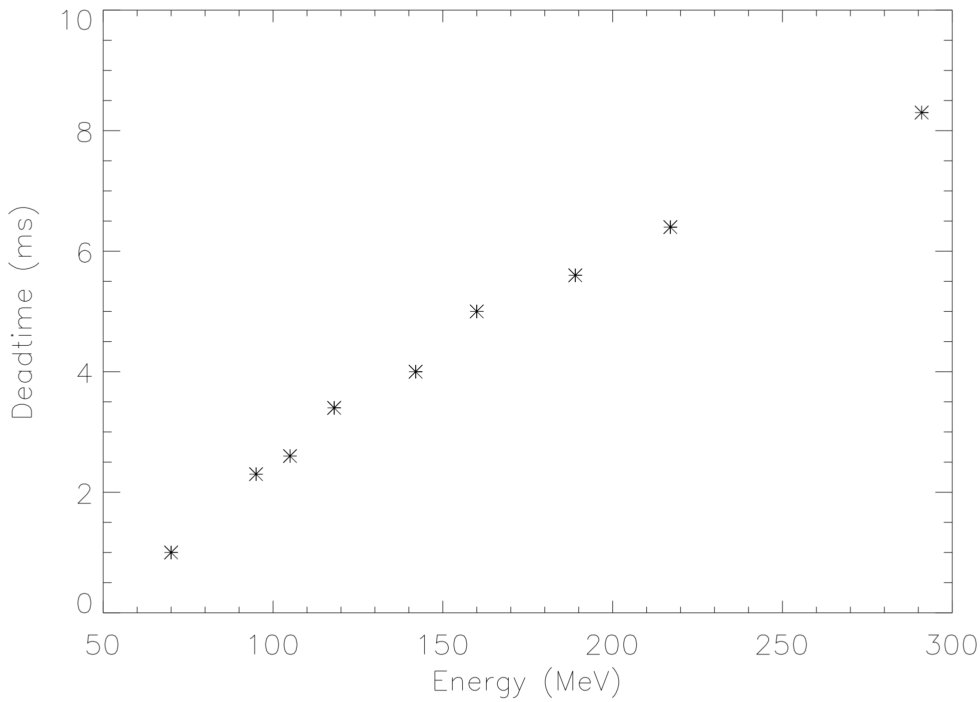

Figure 3.3: Deadtime versus energy loss in HEXTE.

orbit, but the overall normalization changes with the XULD rate. The fit parameters were obtained for an average XULD rate of 85 cts/s, and for other observations, I multiplied the deadtime correction with the observed XULD rate divided by 85. This might not be a very good assumption since, depending on the orbit, due to changes in rigidity, the energy spectrum of particles can change. A next generation deadtime model might fit the power spectrum of background data from the observation under investigation with the function given in this report. Then one can use the resulting parameters to correct the on-source data power spectrum. However, this is applicable only for sufficiently long observations.

This analysis has been done for both HEXTE Cluster A and B, and no difference in fit parameters was found between clusters. There is a 15% discrepancy between the fitted particle rate and the total XULD rate. I believe this occurs because I have not taken into account the deadtime from the ULD events.

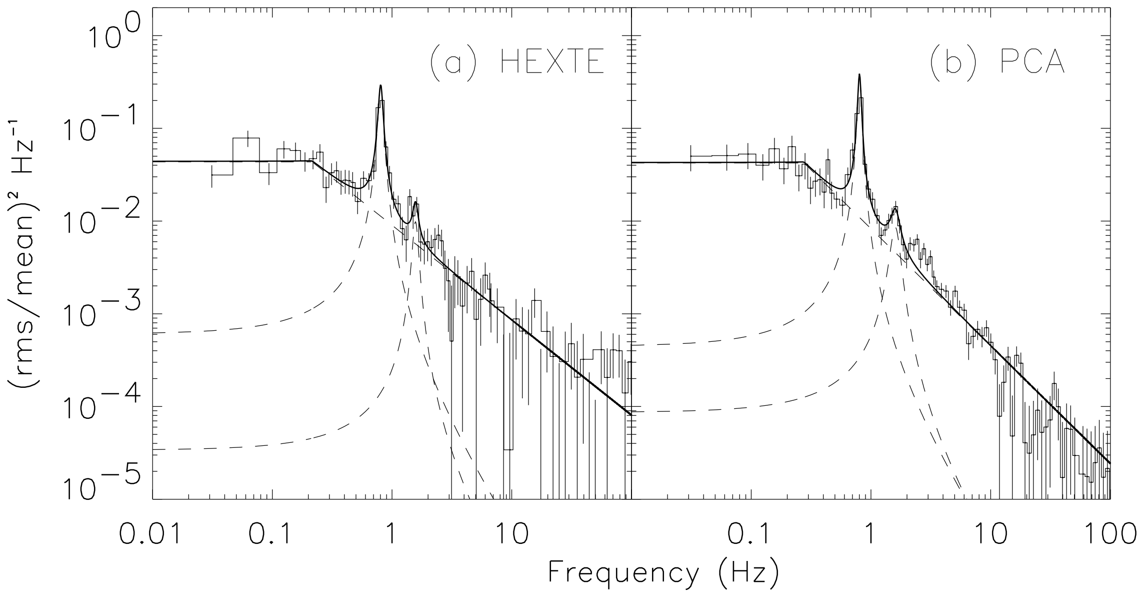

Figure 3.4: XTE J1550-564 power spectrum in the 15-30 keV range. Both HEXTE (Cluster A) and PCA show the fundamental QPO (0.8 Hz) and its harmonic (1.6 Hz). The RMS values of the fundamental are 18.1% $\pm$ 1.1% and 18.1% $\pm$ 1.4% respectively.

3.3 The cross power density (CPD)

3.3.1 Calculating and averaging the CPD

Let $x_{1,h}$ and $x_{2,h}$ be two light curves with identical temporal binning, such as the X-ray fluxes observed simultaneously in two different energy ranges for the same source. The cross power density (CPD) is a complex quantity obtained by multiplying the discrete Fourier transforms of the two light curves:

$$C_j = X_{1,j}^* X_{2,j} \tag{3.20}$$

As in case of the PSD, an average over light curve segments and, if desired, over a frequency band can be calculated for practical applications:

$$C_k = \langle C_j \rangle = \langle C \rangle \tag{3.21}$$

Contrary to $\langle P \rangle$, $\langle C \rangle$ is generally a complex quantity. To illustrate this I plot vector representations of $\sum C_j = M \langle C \rangle$ in Fig. 3.5. The magnitude as well as the phase of this complex quantity can be used for timing analysis, leading to the coherence

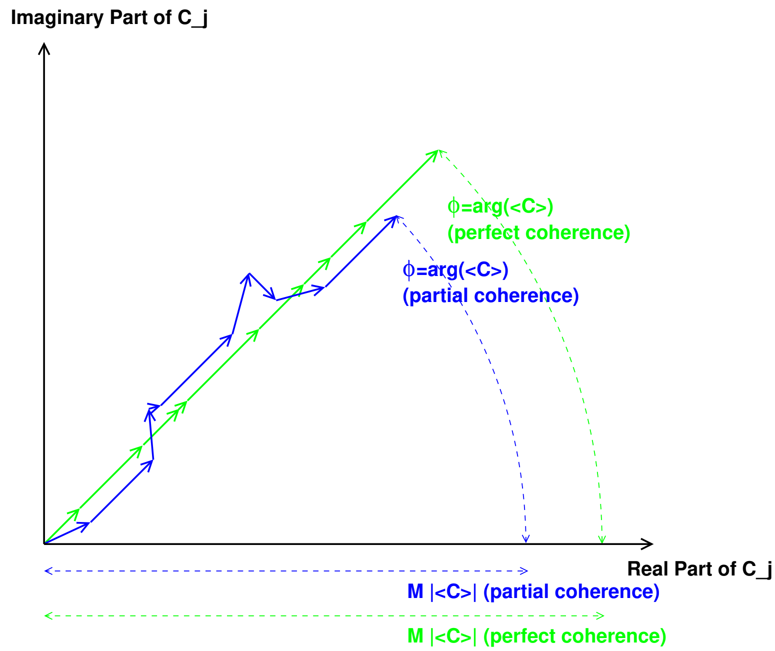

Figure 3.5: Vector representation of the CPD. The average CPD or, more precisely, $M\langle C\rangle$, observed for a certain frequency bin f_k is calculated by summing $M = M_{\rm seg} \times M_f$ individual C_j vectors. The case of perfect coherence (light, $\gamma_k^2 = 1$), is compared to the case of partial coherence (dark, $\gamma_k^2 < 1$). For partial coherence a decreased CPD magnitude, $M|\langle C\rangle|$, is observed and an uncertainty in CPD phase, $\arg(\langle C\rangle)$, is introduced, leading to decreased coherence values and to time lag uncertainties.

function and the time lag spectrum, respectively. Both allow one to compare the short term variations produced in two different energy bands, i.e., to perform combined spectro-temporal analyses.

3.4 The coherence function

3.4.1 Calculating the coherence function

The coherence function is calculated by dividing the observed squared magnitude of the average CPD, $|\langle C\rangle|^2$, by the *signal* PSDs, $\langle|S_1|^2\rangle$ and $\langle|S_2|^2\rangle$, of the two light curves:

$$\gamma_k^2 = \frac{|\langle C\rangle|^2}{\langle|S_1|^2\rangle\,\langle|S_2|^2\rangle} \tag{3.22}$$

This means that $|\langle C\rangle|^2$ is compared to its maximal possible value which could be reached in case of a noiseless signal for constant phase values for all C_j (Fig. 3.5, green vectors), i.e., perfect intrinsic coherence. If the measured C_j were indeed noiseless (Fig. 3.5, blue vectors) γ_k^2 can assume values between 0 and 1. In reality, counting noise causes a comparatively larger squared *magnitude* $|\langle C\rangle|^2$ and thus $\gamma_k^2 > 1$ is possible. This is true even though the random *phase* of counting noise reduces coherence. If the noise is also taken into account in the denominator (Eq. 3.33), then 1 is again the maximum possible value. The coherence is a measure of the degree of linear correlation, in the fractional mean-squared sense, between the two measured light curves in a given frequency bin f_k (Nowak et al. 1999). A mathematical description of such correlations based on transfer functions can be found in Vaughan & Nowak (1997).

3.4.2 Noise component of the coherence

In order to perform a noise correction for γ_k^2, the squared magnitude of the observed average CPD has to be noise-corrected. In terms of signal and noise Fourier transforms of the two light curves, $|\langle C\rangle|^2$ can be written as:

$$\begin{aligned} |\langle C\rangle|^2 &= |\langle X_1^* X_2\rangle|^2 \\ &= \left|\left\langle (S_1^* + N_1^*)(S_2 + N_2)\right\rangle\right|^2 \\ &= |\langle S_1^* S_2\rangle + \langle S_1^* N_2\rangle + \langle N_1^* S_2\rangle + \langle N_1^* N_2\rangle|^2 \end{aligned} \tag{3.23}$$

Instead of being based on $|\langle X_1^* X_2\rangle|^2$ – like the observed coherence γ_k^2 – the noise-corrected signal coherence $\gamma_{\mathrm{sig},k}^2$ is based on $|\langle S_1^* S_2\rangle|^2$. This quantity has therefore to be extracted from Eq. (3.23). Vaughan & Nowak (1997) demonstrate how this can be achieved under certain conditions by defining the auxiliary quantity q_k^2:

$$q_k^2 = \frac{1}{M}\left(\langle|S_1|^2\rangle\langle|N_2|^2\rangle + \langle|N_1|^2\rangle\langle|S_2|^2\rangle + \langle|N_1|^2\rangle\langle|N_2|^2\rangle\right) \tag{3.24}$$

In the following the approximate noise correction for the case of high powers and high measured coherence, as appropriate for most black hole candidates at high enough count rates in the LS, over a large frequency range is given. The conditions of high powers and high measured coherence translate into:

$$\frac{\langle|S_{1,2}|^2\rangle}{\langle|N_{1,2}|^2\rangle} > \frac{B}{\sqrt{M}} \qquad \text{and} \qquad \gamma_k^2 > \frac{B q_k^2}{\langle|S_1|^2\rangle\langle|S_2|^2\rangle} \tag{3.25}$$

If B is of the order of a few or larger, the separation of Eq. (3.24) is possible:

$$|\langle C\rangle|^2 = |\langle S_1^* S_2\rangle|^2 + q_k^2 \tag{3.26}$$

In this case, the noise-corrected signal coherence can be written as:

$$\gamma^2_{\mathrm{sig},k} = \frac{|\langle C\rangle|^2}{\langle|S_1|^2\rangle\langle|S_2|^2\rangle} - \frac{q_k^2}{\langle|S_1|^2\rangle\langle|S_2|^2\rangle} = \frac{|\langle C\rangle|^2 - q_k^2}{\langle|S_1|^2\rangle\langle|S_2|^2\rangle} \tag{3.27}$$

3.4.3 Statistical uncertainty of the coherence values

The interesting uncertainty for the analysis of source variability is the uncertainty of $\gamma^2_{\mathrm{sig},k}$, the noise-corrected signal coherence. Like the uncertainty of the *noise-corrected* signal PSD[3], $\langle|S|^2\rangle$, which can be given as $\langle P\rangle/\sqrt{M} = (\langle|S|^2\rangle + \langle|N|^2\rangle)/\sqrt{M}$, this uncertainty consists of an intrinsic contribution sufficient only for a *noiseless* signal determination and of a noise contribution. The intrinsic coherence uncertainty is given by Bendat & Piersol (1986) as:

$$\sigma\gamma^2_{\mathrm{int},k} = \left(\frac{2}{M}\right)^{1/2} \frac{1-\gamma^2_{\mathrm{sig},k}}{|\gamma_{\mathrm{sig},k}|} \tag{3.28}$$

In the case of high powers and high measured coherence, the uncertainty of the *noise-corrected* signal coherence, $\sigma\gamma^2_{\mathrm{sig},k}$, can be approximated by the sum of the uncertainty of *noiseless* signal coherence measurements, $\sigma\gamma^2_{\mathrm{int},k}$, plus additional terms due to Poisson noise (Vaughan & Nowak 1997):

$$\sigma\gamma^2_{\mathrm{sig},k} = \frac{\gamma^2_{\mathrm{sig},k}}{\sqrt{M}}\left[\frac{2q_k^4 M}{(|\langle C\rangle|^2 - q_k^2)^2} + \frac{\langle|N_1|^2\rangle^2}{\langle|S_1|^2\rangle^2} + \frac{\langle|N_2|^2\rangle^2}{\langle|S_2|^2\rangle^2} + \frac{M(\sigma\gamma^2_{\mathrm{int},k})^2}{(\gamma^2_{\mathrm{sig},k})^2}\right]^{1/2} \tag{3.29}$$

Vaughan & Nowak (1997) also present equivalent formulae for $\gamma^2_{\mathrm{sig},k}$ and $\sigma\gamma^2_{\mathrm{sig},k}$ in the case of high powers and low measured coherence.

3.5 The lag spectrum

3.5.1 Calculating the phase- and time lags

The argument of the cross power density C_j is the phase difference between $X_{1,j}$ and $X_{2,j}$, i.e, between intensity fluctuations in the two energy bands at frequency f_j.

3 This is the same uncertainty as for the non-noise-corrected quantity, $\langle P\rangle$, itself (Eq. 3.11). Note, however, the presence of the effective noise level after noise correction (Eq. 3.14).

In its averaged form (see Fig. 3.5) the phase lag is given by:

$$\phi_k = \arg(\langle C \rangle) \tag{3.30}$$

By relating the phase lag to its associated frequency, f_k, it can be converted into a time delay:

$$\delta t_k = \frac{\phi_k}{2\pi f_k} \tag{3.31}$$

Both forms, the phase lag and time lag, have been presented in analyses of the short term variability of BHCs. In this work I concentrate on the time lag, therefore the remaining equations of this chapter are given in time lag notation. Note that for practical applications $X_{1,j}$ is associated with the softer energy band and $X_{2,j}$ with the harder energy band. Thus a positive time lag is measured when the fluctuations in the hard emission are delayed with respect to those in the soft band and vice versa.

3.5.2 Noise estimation

While measurement noise changes the expectation value of PSD as well as of coherence, its contribution to the phase of the CPD is completely random (Nowak et al. 1999). It does not change the expectation value of the phase but enhances its uncertainty (see next section). Based on Poisson noise and an $A^2 f_k^{2\alpha}$ power law PSD, Nowak et al. (1999) develop an approximation of the noise related uncertainty that is depending on source parameters, the amount of logarithmic frequency rebinning, and the total exposure time:

$$\sigma(\delta t_k) \approx \frac{\pi^{-1}|A|^{-1}}{\sqrt{R\gamma_k^2 d \times T}} f_k^{\alpha-3/2} \tag{3.32}$$

3.5.3 Statistical uncertainty of the time lags

An uncertainty in the phase is introduced whenever there is a deviation from perfect coherence either due to partial intrinsic coherence as illustrated in Fig. 3.5 and/or due to measurement noise. The latter is providing random phase contributions to the CPD vector sum. In contrast to the situation shown in Fig. 3.5, however, measurement noise also introduces a change in the *magnitude* of the cross power density (making the noise correction of γ_k^2 necessary, Eq. (3.29)). This has to be taken into account in the determination of the phase lag uncertainty. The definition of perfect coherence in this case includes the noise terms: the magnitude of the cross power density is compared to its *overall* maximum value $\langle P_1\rangle\langle P_2\rangle$ (and not to $\langle|S_1|^2\rangle\langle|S_1|^2\rangle$). The uncertainty of the time delay is thus based on g_k^2, a quantity closely related to the coherence function γ_k^2:

$$\sigma(\delta t_k) = \frac{1}{\sqrt{M}2\pi f_k}\sqrt{\frac{1-g_k^2}{2g_k^2}} \qquad \text{where} \qquad g_k^2 = \frac{|\langle C\rangle|^2}{\langle P_1\rangle\langle P_2\rangle} \tag{3.33}$$

3.6 IDL tools

In order to analyze more than 100 *RXTE* observations in multiple energy bands, I used and helped develop a set of programs using the "Interactive Data Language" environment (IDL 5.1). These programs are mostly developed by Dr. Katja Pottschmidt at University Tübingen. All the Fourier analysis tools used in the following are available in electronic form (`http://astro.uni-tuebingen.de/software/idl/aitlib`). The most important features of these tools are:

- Simultaneous observation times are selected from all energy bands for which light curves have been extracted. From the resulting light curves, equally-binned light curve segments (= with no gaps) are created.

- Averaged (over light curve segments and frequencies) power spectra, time lags, coherence functions are calculated in several energy bands, together with their uncertainties and noise components. In case of the PSD, a complex deadtime correction of the noise component can be performed, where additional PCA or HEXTE deadtime effects can be included.

- All data products are stored in a standard binary data format ("xdr"), and are thus portable between machines with a different floating point representation.

- The analysis can be performed automatically for a large set of *RXTE* observations.

- The individual steps in the automatic analysis (e.g., the light curve segmenting or the PSD deadtime correction) correspond to modular tools. Many are instrument independent, i.e., they can also be used for light curve data from instruments other than *RXTE*.

In addition, I wrote χ^2 fitting algorithms in IDL for various fitting functions (Lorentzian, flat top), and other IDL programs to read and process the results of fitting scripts. In the next section, I will describe my temporal analysis in more detail.

3.7 Details of temporal analysis used in this work

3.7.1 Choice of energy bands, time resolution and light curve segmentation

The first step of timing analysis is obtaining light curves in the desired energy bands with the desired time resolution and light curve segmentation. I tried to be as uniform as possible in terms of choosing my bands, resolution and segmentation for all of my sources. Unfortunately, since some of this work is based on the analysis of the archival data, I was limited to the choice of data modes by the PI of the original proposal. As explained in section 2.1.1, energy bands of the binned modes are set by the original PI and cannot be changed. It turned out that for most of the observations for which the event mode is binned, the energy band choices are 0–13 and 14–35 in absolute channels. These bands are called E1 and E2 respectively. For almost all observations, after channel 36, the observations were made in the event mode where I was free to choose the energy band. For most of the observations, I chose the third band as 36–71 (called E3 hereafter). Due to gain changes during the lifetime of PCA (which corresponds to different epochs, see Table 2.2 and `http://heasarc.gsfc.nasa.gov/docs/xte/e-c_table.html`) these channel bands correspond to slightly different energy bands for each epoch. For example for epoch 3, E1, E2, and E3 correspond to 2–5, 5–13, 13–26 keV respectively, whereas for epoch 4 they correspond to 2–6, 6–15 and 15–30 keV. Although those are the bands I used for most of my observations, for some rare cases I had to use different bands (I tried to be as close as possible to E1, E2 and E3). For such cases, this discrepancy is mentioned in "Observations and Analysis" section of the particular observation.

The maximum frequency of a PSD is the Nyquist frequency and it is set by the time resolution of the light curve (see Section 3.1). Although some PCA modes provide power spectra up to 4096 Hz, frequencies higher than 512 Hz do not provide measurable power above the noise level for most black hole systems in the LS. Therefore, I selected a time resolution of $\sim$1 ms. My approach to determine the highest frequency is as follows. First I calculate the PSD for the highest count rate observation with a Nyquist frequency of 512 Hz. Then, comparing this PSD with the expected noise level (see section 3.2.4), I choose the highest frequency for all the observations for the particular source for the particular outburst This is done to save computing resources, since doing the analysis with 128 Hz Nyquist frequency instead of 512 Hz is four times faster and requires four times less disk space.

The minimum frequency of a PSD is determined by the size of the light curve segments that are averaged to obtain the final PSD (see Section 3.1). A typical monitoring observation is usually less than 2 ks, which corresponds to a minimum frequency of 0.0005 Hz. On the other hand, using the whole segment results in very large error bars for the lowest frequencies making them practically useless. For most of my analysis, I used 256 s light curve segments which resulted in good statistics without the loss of interesting information. This corresponds to $\sim$0.004 Hz. For some rare cases (for example if a very low frequency QPO was present), I used longer segments, and these cases are mentioned again in "Observations and Analysis" section of the particular observation.

3.7.2 Lorentzian fit function

Historically, the PSD of BHCs during the low state has been modeled by a broken power-law (or power-laws with more than one break) plus narrow Lorentzians to fit the QPOs (Nowak et al. 1999; Tomsick & Kaaret 2000). However, recent papers successfully fit several BHC and neutron star PSDs with broad Lorentzians for the continuum and narrow Lorentzians for the QPOs (van Straaten et al. 2002; Pottschmidt et al. 2002; Belloni, Psaltis & van der Klis 2002). When I fit the data with broad and narrow Lorentzians I see that this modeling represents the PSDs as well as or better than the broken power law in terms of χ^2 statistics. I did both kinds of fitting for some representative PSD, and decided to use the Lorentzian fits. The major advantage of using Lorentzian is that it allows for an easier comparison to recent work, for example on Cyg X-1 by Pottschmidt et al. (2002).

I fit all the PSDs with Lorentzians of the form

$$L_i(f) \;=\; \frac{R_i^2\,\Delta_i}{2\,\pi\,[(f-f_i)^2+(\frac{1}{2}\,\Delta_i)^2]} \tag{3.34}$$

where subscript i denotes each Lorentzian component in the fit, R_i is the rms amplitude of the Lorentzian (if integrated from -∞ to +∞), Δ_i is the full-width-half-maximum, and f_i is the resonance frequency. A useful quantity of the Lorentzian is the frequency at which its contribution to the total rms variability is maximum (hereafter peak frequency):

$$\nu_i \;=\; f_i\,\left(\frac{\Delta_i^2}{4\,f_i^2}+1\right)^{1/2} \tag{3.35}$$

In Fig. 3.6, I plot an example power spectrum in the form of PSD $\times$ frequency and over-plot the Lorentzian fits. In this figure, the Lorentzians peak at ν_i not at f_i. In this work, including the tables, Lorentzian frequency means the peak frequency, not the resonance frequency. Most of the observations contain a Lorentzian that is narrow (with a quality factor $Q_i = (f_i/\Delta_i > 2$, as compared to $Q < 1$ for broad Lorentzians) which I denote a QPO. The QPO frequencies reported in this work are the resonance frequencies to make them easier to be compared to previous reports, though the peak and resonance frequency of a high Q Lorentzian are not very different. I call the broad Lorentzians in the fit L_i, where i=1 is the lowest frequency peak Lorentzian. The QPO is not counted and always referred as the QPO throughout this work.

The rms amplitude of a Lorentzian in the frequency band of 0 to ∞ is given as:

$$\mathrm{rms}_i = R_i\left(\frac{1}{2}-\frac{\tan^{-1}(-2\,Q_i)}{\pi}\right)^{1/2} \tag{3.36}$$

Often, the PSD statistics were poor at frequencies higher than 20 Hz, as can be seen in Fig. 3.6. The Lorentzian fit covering these frequencies sometimes results in unphysical fit parameters. For some cases, it might become too broad and very high

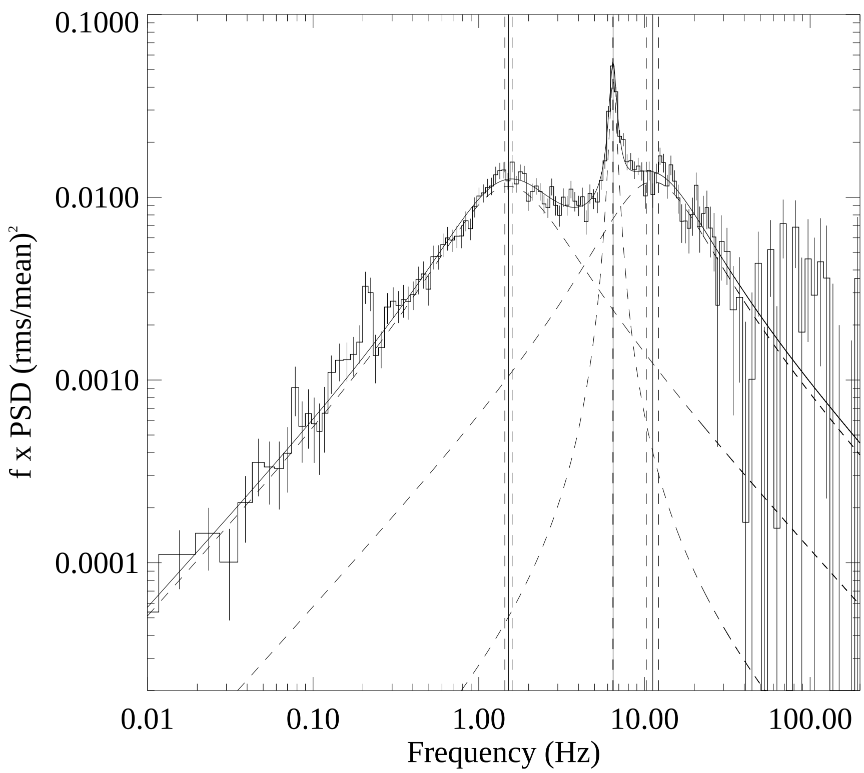

Figure 3.6: Lorentzian fit to a typical BHC PSD in LS. The dashed Lorentzians are individual components and the solid line is the overall fit. The solid vertical lines indicate the peak frequencies and dashed vertical lines are their errors. The Lorentzian that peaks at 1.5 Hz is called L_1, and the Lorentzian that peaks at 11.2 Hz is called L_2. The narrow Lorentzian is a QPO at 6.5 Hz. The error bars on the QPO frequency are so small that it they are unidentifiable from the peak frequency.

rms amplitudes with large error bars are obtained. To avoid this, sometimes rms amplitudes in a restricted frequency band are calculated by numerically integrating the Lorentzian. If this is done, it is mentioned in the "Observations and Analysis" section of the particular source. Otherwise, reported rms amplitudes are over a frequency band from 0 to ∞.

3.7.3 Coherence and lags

I worked on two aspects of coherence and lag analysis. The first one is the frequency dependent lags and coherence, and the comparison to the Lorentzian PSD fit. To do that, I use figures such as shown in Fig. 3.7 where PSD, Lorentzian fits,

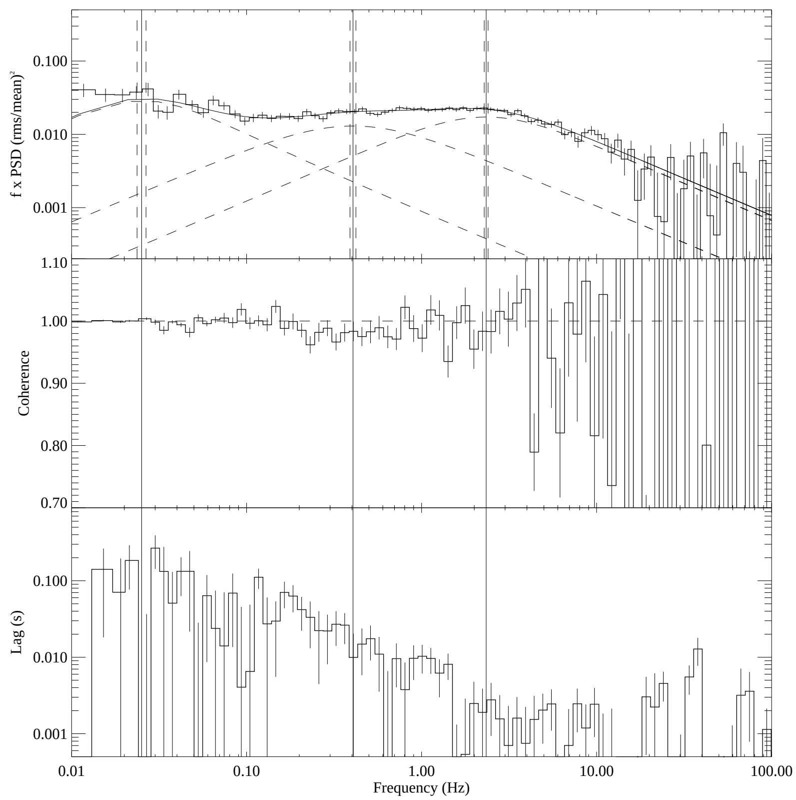

Figure 3.7: The top panel is the PSD with its Lorentzian components. The middle panel is frequency dependent coherence. The horizontal dashed line is the unity coherence. The bottom panel is the lag spectrum. The solid vertical lines show the peak frequencies.

peak frequencies, coherence and lags can all be seen together. In these figures, the top panel is the PSD, which has the same structure as in Fig. 3.6. If the statistics are good enough, both coherence and lag spectra are shown. The peak frequencies of the Lorentzian components are drawn for all panels for guiding the eye. If the statistics are poor, only coherence is shown. Unless otherwise stated, the coherence and lag is calculated between E1 and E2.

The second aspect is the evolution of the averaged (or integrated) components over a frequency band. For coherence, I only used the weighted mean in a band where the coherence has small errors. For the observation shown in Fig. 3.7, 0.01–10 Hz can be used to calculate the mean coherence. Although I started calculating the weighted mean lags over a frequency range, I quickly realized that the mean is very strongly determined by the highest frequency bins with smaller error bars. Moreover, the strong frequency dependence and logarithmic rebinning also complicates the interpretation. Therefore I decided to integrate the lag in the given frequency band. Although this has no physical meaning, it is more useful in comparing the magnitude of lags for different observations in a given frequency band. Again, unless otherwise stated, the weighted mean or integrated values are calculated for lags and coherence between E1 and E2. Rarely, for high count rate observations, coherence and lags between E1 and E3 are also reported to see if magnitude of lags increase with energy as predicted for thermal Comptonization.

Chapter 4

Results

"Is it still there?"

- Bug Eyed Earl

4.1 XTE J1650−500

XTE J1650−500 was first detected by the ASM on board *RXTE* in September, 2001 (Remillard 2001). The optical and radio counterparts were identified by Castro-Tirado et al. (2001) and Groot et al. (2001), respectively. Augusteijn, Coe & Groot (2001) suggest a long orbital period and a low-mass secondary. Pointed X-ray observations by *RXTE* show strong low frequency QPOs and band limited timing noise (Wijnands, Miller & Lewin 2001), while *Chandra* revealed ionized iron absorption lines (Miller et al. 2002b). The X-ray flux started to decay 45 days after the beginning of the outburst, and a transition to the hard state occurred (see Fig. 4.1 for the ASM + PCA light curve for the whole outburst). During the hard state, additional radio measurements were made and an inverted spectrum indicative of a compact jet was observed (S. Corbel, private communication). Around 10 days after the state transition, the source was unobservable due to the proximity of the Sun. After the Sun gap, the X-ray flux showed a modulation with a ∼14 day period (Tomsick et al. 2002b). The mass function has very recently been measured to be 0.064 ± 0.03 (Sanchez-Fernandez et al. 2002). Both the X-ray spectra, and the temporal properties are similar to the known BHCs. Moreover, a recent *XMM-Newton* analysis of the broad iron line feature suggests that XTE J1650−500 is a rapidly rotating black hole (Miller et al. 2002a). The low mass function indicates an inclination less than 40° if indeed XTE J1650−500 is a BH.

4.1.1 Observations and analysis

The spectral data from the decay observations were analyzed by Tomsick et al. (2002a) using a model consisting of a diskbb, smedge, power law, iron line and absorption.

I analyzed the temporal data from the start of the decay (∼MJD 52218) until the source was close to the sun between MJD 52240 and MJD 52266 (proposal ids P60118, P70124). When it was observable again, the flux had decayed significantly. Until MJD 52230 the X-ray energy spectrum was typical of a HS black hole spectrum. Between MJD 52230 and MJD 52232 (around the dashed line in Fig. 4.2) the energy spectrum hardened. For the observation at MJD 52232, both the energy

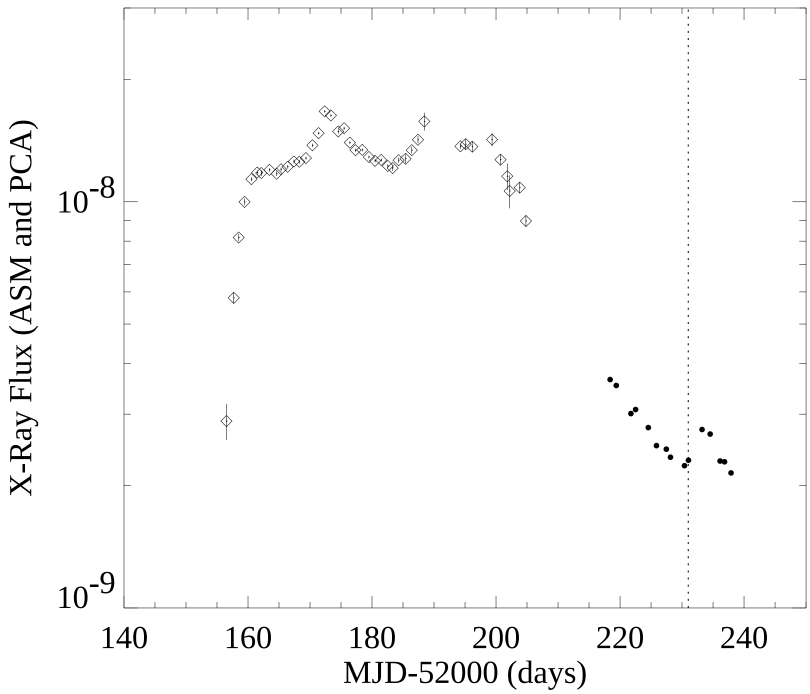

Figure 4.1: Combined ASM and PCA light curve of XTE J1650−500 in 2 – 12 keV band. The dashed line represents the time when the state transition occurred. The observations represented by diamonds are ASM points and the dots are PCA pointings.

spectrum and the power spectrum showed significant changes and a transition to the hard state occurred (the first observation after the dashed line in Fig. 4.2). I call this observation 1, and number the following observations according to their date of observation. Before the transition, the variability was very weak and the power spectrum was not above the noise level. I obtained a PSD by combining light curves from the 10 observations in the HS and fitted it with a Lorentzian, which resulted in a 95% confidence rms amplitude upper limit of 4%. The rms amplitude jumped to 17% for Obs 1, and a weak QPO at 8.71 Hz is observed for observation 2. For the following observations until the sun gap, both the energy spectrum and the power spectrum showed characteristics of a typical hard state (see Fig. 4.3). In this section, I focus on the seven observations after the state transition and before the sun gap. Due to the drastic change in the flux and the low quality of the temporal data, the observations after the sun gap are not included in this work.

For each observation, I computed the power spectra and cross spectra for three

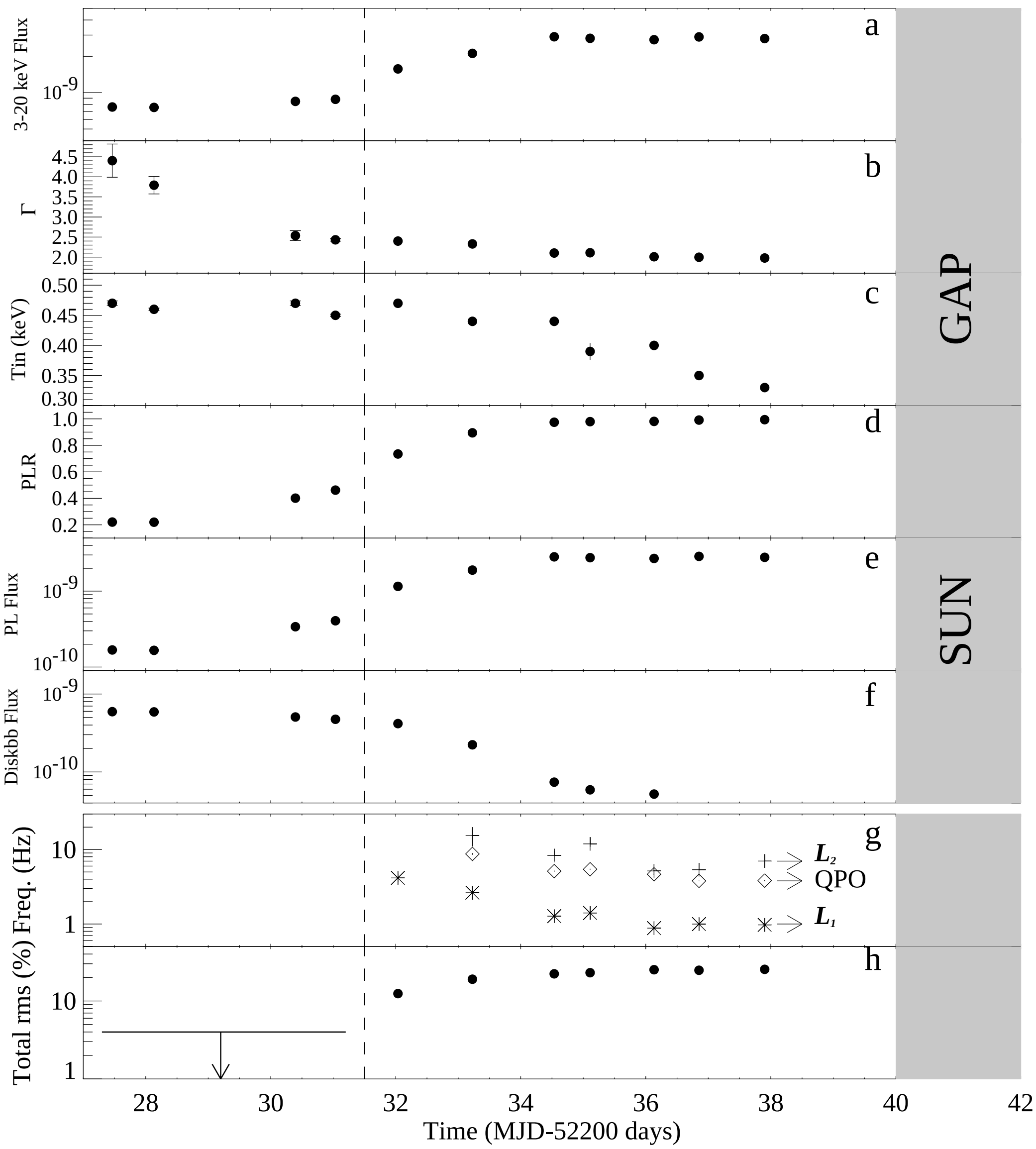

Figure 4.2: Spectral and temporal evolution of XTE J1650−500 during and after the state transition. (a) PCA light curve. (b) Power law index. (c) Inner disk temperature. (d) PLR, ratio of the power-law flux to the total flux. (e) Power-law flux. (f) Diskbb flux. All flux measurements are in 3–25 keV band. (g) Peak frequencies of the Lorentzians and the central frequency of the QPO. The crosses are for L_2, the diamonds are for QPOs and the stars are for L_1. (h) Rms amplitude in 0.08–20 Hz band for 2–30 keV PSD. The dashed line represents the line when the state transition occurred. The gray area is the time when the source is close to the sun and unobservable.

energy bands, 3 – 6 keV (E1), 6 – 15 keV (E2), and 15 – 30 keV (E3) and the combined band of 2 – 30 keV. Above 30 keV, the source is not significantly above the background. Using 128 second time segments, I investigated the QPOs and the timing properties of the continuum up to 256 Hz. I also analyzed the time lags and coherence function between E1 and E2 energy band light curves.

4.1.2 Spectral and temporal evolution

Fig. 4.2 summarizes the changes in spectral and temporal properties of XTE J1650−500 during the state transition. In this figure, the dashed line represents the time when most significant changes in terms of temporal properties occurred and hence the state transition. The flux (a) increases during the state transition, which is possibly due to the hardening of the spectrum which results in more photons in the PCA energy band. A significant spectral change, the hardening of the power law index (b), happened around three days before the transition. It gradually continued to harden. The inner disk temperature (c) was constant at around 0.45 keV until the state transition, and then started to decrease, possibly indicating the inner disk retreating. Supporting this claim is the overall decrease of the peak and QPO frequencies (g) after the state transition as the transition progresses. The PLR (d), ratio of the power-law flux to the total flux in 3–25 keV band started to increase 3 days before the transition and showed a jump at the transition. This jump is caused by both the increase in the power-law flux (e) and a decrease in the diskbb flux (f). Finally, the rms amplitude (h) increased, and then leveled off (with the PLR).

4.1.3 Lorentzian fits

In Fig. 4.3, I plot the power spectra in the form of PSD $\times$ frequency and overplot the Lorentzian fits. As seen in Fig. 4.3, except for the first observation, each observation requires at least two broad Lorentzians to fit the continuum, and a QPO (see Table 4.1 for the fit parameters). For observation 1, the 95% confidence upper limit on the rms amplitude of a QPO in 0.1 - 20 Hz range with a $Q = 6$ is 2.8%. The QPO is always the second peaked component in the PSD. Although the second peaked component in observation 4 has a quality value of $\sim$1.5, it is still quoted as a QPO for consistency. Since they are narrow, the quoted resonance frequencies are

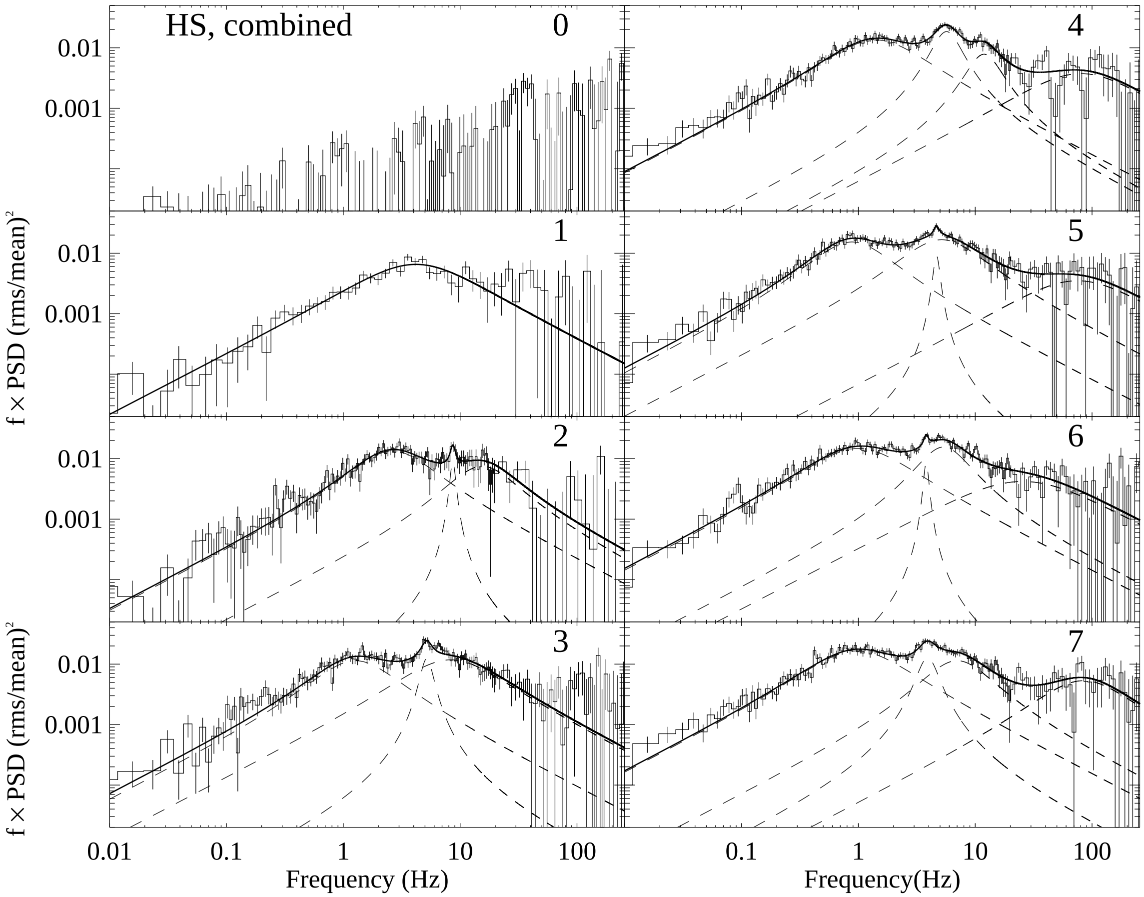

Figure 4.3: Power spectra and Lorentzian fits. The panel indicated by "0" is the power spectrum from the combined light curves in the HS. Except for the HS power spectrum, the solid line represents the overall fit and the dashed lines represent each component.

very close to the peak frequencies[1].

There is an overall shift to lower frequencies with time for both the wide Lorentzians and the QPOs (see Fig. 4.2d). The overall rms amplitude increases with time, and settles at around 30% after observation 5 as seen in Fig. 4.2e. The rms amplitudes of individual Lorentzian components do not show a regular trend and can be found in Table 4.1.

I also study the dependence of temporal properties on energy. I fit the PSDs from two energy band light curves, E1 and E2, and study the evolution of the peak

1 The peak frequency and the resonance frequency of the QPO differ by 5% for the worst case of observation 4.

Table 4.1: Lorentzian Fit Parameters

Obs.	1	2	3	4	5	6	7
Date (MJD)[a]	52232.0	52233.2	52234.5	52235.1	52236.1	52236.9	52237.9
Flux[b]	1.57	2.12	2.91	2.82	2.75	2.91	2.81
Int. time[c]	1224	1488	1152	2000	1664	1824	1904
ν_1	4.18 ± 0.51	2.65 ± 0.19	1.28 ± 0.12	1.41 ± 0.09	0.88 ± 0.05	1.00 ± 0.03	0.97 ± 0.07
L_1 rms[d]	12.42 ± 0.55	16.20 ± 0.79	15.04 ± 1.03	17.40 ± 0.45	17.25 ± 0.61	18.53 ± 0.16	19.61 ± 0.72
ν_2	-	15.41 ± 4.08	8.31 ± 1.29	11.91 ± 1.01	5.16 ± 0.57	4.68 ± 0.08	6.85 ± 1.30
L_2 rms	-	9.126 ± 1.64	14.92 ± 1.46	8.06 ± 1.16	17.40 ± 1.06	14.14 ± 0.17	13.15 ± 2.23
ν_3	-	-	-	80.5 ± 40.7	85.7 ± 30.6	25.5 ± 2.8	85.0 ± 37.3
L_3 rms	-	-	-	3.63 ± 0.77	3.78 ± 1.76	7.46 ± 0.23	3.42 ± 0.63
QPO freq.[e]	0.1-20[f]	8.64 ± 0.16	5.13 ± 0.09	5.44 ± 0.09	4.66 ± 0.07	3.80 ± 0.03	3.84 ± 0.08
QPO rms	<2.8[g]	3.98 ± 1.06	7.10 ± 1.12	13.12 ± 0.80	4.36 ± 0.94	3.72 ± 0.27	8.83 ± 2.09
QPO fwhm	$0.167 \times$ freq.[h]	0.98 ± 0.56	1.34 ± 0.39	3.29 ± 0.38	0.62 ± 0.27	0.39 ± 0.08	1.57 ± 0.48
χ^2/DOF	56.0/67	144.1/144	153.6/144	166.8/152	125.5/141	182.7/141	137.6/141

a MJD at the beginning of the observation.
b Flux in 3–25 keV range, in units of $10^{-9}\,\mathrm{ergs\,cm^{-2}\,s^{-1}}$.
c Integration time in seconds.
d All rms amplitudes are in 0.08–20 Hz band
e This is the resonance frequency, not the peak frequency
f Frequency range searched.
g 95% confidence upper limit.
h The width is fixed to $0.167 \times$ QPO frequency ($Q = 6$).

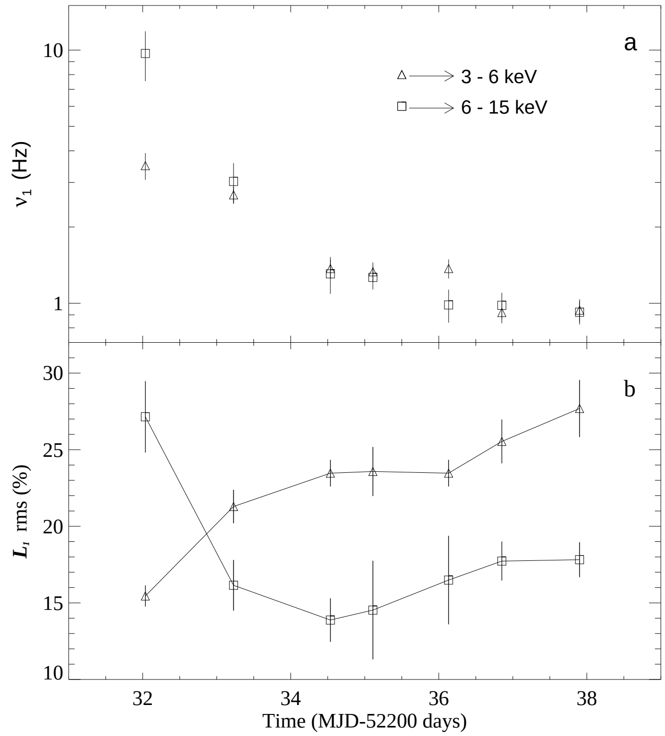

Figure 4.4: Energy dependence of PSD fit parameters: (a) Peak frequencies of L_1. Squares represent E2, and triangles represent E1. The E2 peak frequency for the first observation is clearly higher than that of E1. For the remaining observations, the peak frequencies are the same for both energy bands within 1-σ error. (b) Rms amplitude in the two energy bands mentioned.

frequencies and the rms amplitudes of Lorentzian components. Fig. 4.4 summarizes my efforts, where I plot the peak frequencies and the rms amplitudes of L_1 in the two energy bands mentioned. For observation 1, during the state transition, there is a clear shift with energy in the peak frequency of L_1, the only component in the PSD fit as seen in Fig. 4.5. The E2 L_1 peaks at 3.50 ± 0.42 Hz, whereas the E1 L_1 peaks at 9.70 ± 2.16 Hz. Moreover, the E2 rms amplitude is higher than the E1 amplitude. For the remaining observations, the E1 rms amplitude is higher, and the Lorentzians peak at the same frequency (within 1σ uncertainty).

4.1.4 Lags and coherence

Fig. 4.6 shows the evolution of mean coherence and integrated time lag in 1 – 10 Hz band where they are least affected by the Poisson noise. The integrated lag de-

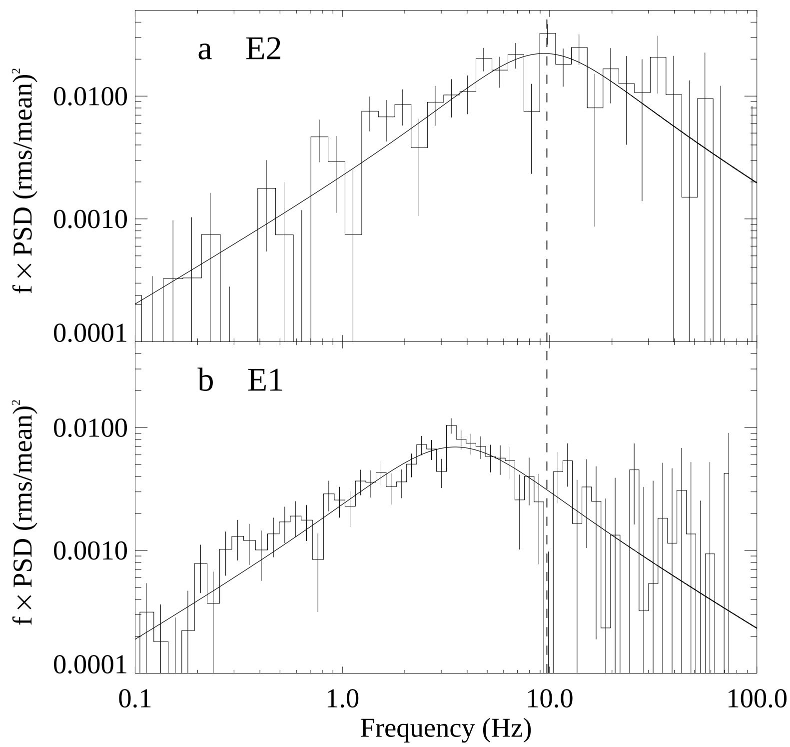

Figure 4.5: Fits to the power spectra of observation 1 in two energy bands: (a) E2, (b) E1. As clearly seen, the E2 Lorentzian peaks at a higher frequency and has higher rms amplitude for this observation. The dashed line is the peak frequency of the E1 Lorentzian.

creases whereas the coherence function increases with time, and they both approach an asymptotic value. The time lag decays from 0.20 to around 0.05, and the coherence increases from 0.6 to unity. Note that during the HS, the average coherence is consistent with being zero, therefore time lags have no physical meaning (Nowak et al. 1999). This is the third source after Cyg X-1 and GX 339−4 to show enhanced lags during the state transition. I also added the evolution of the spectral index in Fig. 4.6. Spectral index and average lag have been shown to correlate for Cyg X-1 (Pottschmidt et al. 2002) and GX 339−4 (Nowak, Wilms & Dove 2002), and this correlation holds for XTE J1650−500 also. Since the first two observations during the transition showed different PSD, coherence and lag characteristics, they are classified as “transitional state” (TS) observations in the Discussion chapter.

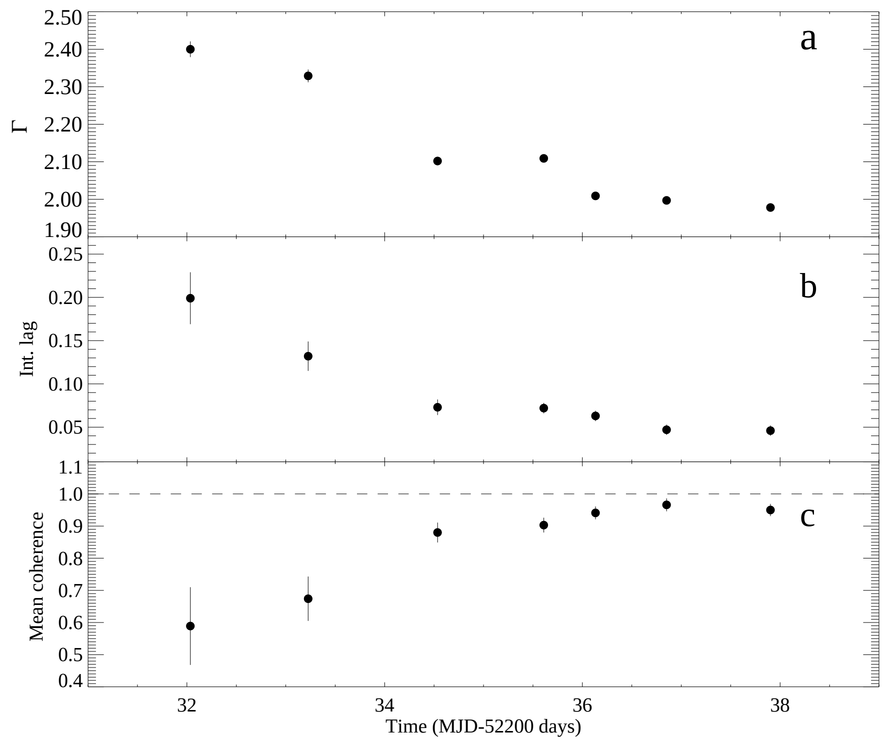

Figure 4.6: (a) Spectral power law index. (b) Integrated lag between E1 and E2. (c) Mean coherence between E1 and E2. The frequency band is 1–10 Hz where the measurements are well above the noise level. For observation 1 and 2, the lags are significantly longer compared to the following observations. The dashed line indicates the unity coherence.

4.1.5 Summary

The similarity of the evolution of temporal properties to those of other known black hole systems suggest that XTE J1650−500 is also a black hole system. The largest change in the power law index occurred 3 days before the change in temporal properties. The consequent evolution of the spectral parameters were smooth and similar to other black hole systems. The state transition is sharp in terms of the temporal properties with the appearance of band limited noise in the PSD. The rms amplitude increases from 4% upper limit in HS to ∼16% during observation 1. The last HS observation and observation 1 are only one day apart. The PSD can be characterized by broad Lorentzians and QPOs. The characteristic frequencies of these components decrease after the transition to the LS occurs, which can be interpreted as retreating of the inner disk radius as discussed in di Matteo & Psaltis (1999)

Table 4.2: XTE J1650−500

Name :	XTE J1650−500
Mass :	-
Distance :	-
Gal. Coord. :	336.70, -3.44
N_H :	$0.57 \times 10^{22}\,\mathrm{cm}^{-2}$ [a]
Peak Flux[b] :	16.8
Peak Luminosity :	-
At the state transition:	
Flux :	3.5
Luminosity :	-
Γ_{trans} :	2.4
T_{in} :	0.46 keV
Power-law flux :	1.22

a From Tomsick et al. (2002a).
b All fluxes in this table are in 1.5-12 keV band, in units of $10^{-9}\,\mathrm{ergs\,cm^{-2}\,s^{-1}}$

for other BHCs. The total rms amplitude increases during this time. The integrated lags are higher during the first two observations than the remaining observations. The coherence function anti-correlates with integrated lag, increases during the transition, and becomes unity coherence for the last two observations. L_1 peaks at different frequencies for different energy bands during observation 1. After this observation this shift disappears. Also, the rms amplitude of L_1 increases with energy only for the first observation whereas it decreases with energy for the remaining observations. The shift can be a sign of temperature gradient at the base of a jet as will be discussed in section 5.6.

Table 4.2 characterizes the physical properties of XTE J1650−500 during the state transition.

This section, in part, is a reprint of the material that has been submitted to *The Astrophysical Journal* as "X-ray Temporal properties of XTE J1650−500 During Outburst Decay", Kalemci, E., Tomsick, J. A., Rothschild, R. E., Pottschmidt, K., Corbel, S., Wijnands, R., Miller, J. M., Kaaret, P., 2002.

4.2 GRO J1655−40

GRO J1655−40 was discovered with BATSE on *CGRO* on July 27, 1994 and since then irregular outburst activity has been observed (Sobczak et al. 2000). It has a well determined dynamical mass of 7.02 ± 0.22 $M_\odot$ (Orosz & Bailyn 1997), and distance of 3.2 ± 0.2 kpc (Hjellming & Rupen 1995). This source is a microquasar with superluminal radio jets for which there is a clear understanding of the masses and dimensions of the binary system. The X-ray spectrum of GRO J1655−40 has been also detected with *OSSE* to photon energies near 1 MeV (Tomsick et al. 1999). Above 50 keV, the X-ray spectrum is consistent with power-law of index 2.4 – 2.8. Soft X-ray observations with *ROSAT* and *ASCA* found that below 10 keV, the spectrum is dominated by the multicolor disk component (Remillard et al. 1999b, and references therein).

A second outburst was discovered on April 25, 1996 by ASM on *RXTE* (Remillard et al. 1996) and continued for 16 months (see Fig. 4.7). There was intensive observing campaign with *RXTE* during this period.

GRO J1655−40 exhibits four types of QPOs between 0.1 Hz and 450 Hz (Remillard et al. 1999b; Strohmayer 2001a). It exhibits a high frequency QPO pair at 300 Hz and 450 Hz (Strohmayer 2001b). The low frequency QPOs (QPO from here on) are narrow and strong, and carry similar characteristics of the QPOs found in XTE J1550−564 (Sobczak et al. 2000). These strong QPOs are observed during the outburst rise and also in the decay, when the source was in the LS (Remillard et al. 1999b). The X-ray spectrum is typical of black hole systems, and modeled with a soft multicolor disk and a hard power-law component.

The outburst started to decay at the end of May 1997 (MJD 50600) and a transition to the LS happened sometime before August 14, 1997 (Méndez, Belloni & van der Klis 1998). The coverage is very sparse. The analysis of spectral and temporal properties during the decay was done by Méndez, Belloni & van der Klis (1998), therefore, I only did time lag and coherence analysis and characterized the energy dependence of the PSD and QPOs.

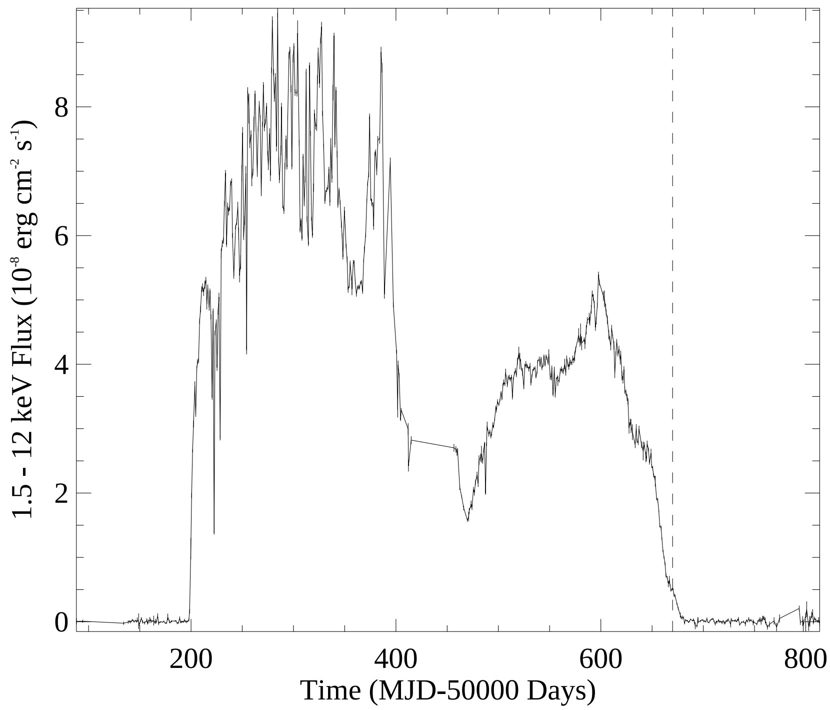

Figure 4.7: ASM light curve of GRO J1655−40. The dashed line indicates the approximate time of state transition.

4.2.1 Observations and analysis

I analyzed the data from 5 observations at the end of the decay as the source was going into quiescence (proposal id P20402). For spectral data, I used the values given in Méndez, Belloni & van der Klis (1998). When there is significant variability, I did the temporal analysis, including lags and coherence. I used three energy bands, approximately corresponding to 2–5 keV (E1), 5–13 keV (E2) and 13–26 keV (E3).

4.2.2 Results

The spectral and temporal evolution of the source at the end of decay is summarized in Fig. 4.8. For observations on MJD 50658.4 and MJD 50663.7, the source was in the HS. During these observations, the disk component dominated the X-ray spectrum, as could be understood from the low values of PLR (ratio of power-law flux to diskbb flux in 2–10 keV band), and the variability (less than 2% rms am-

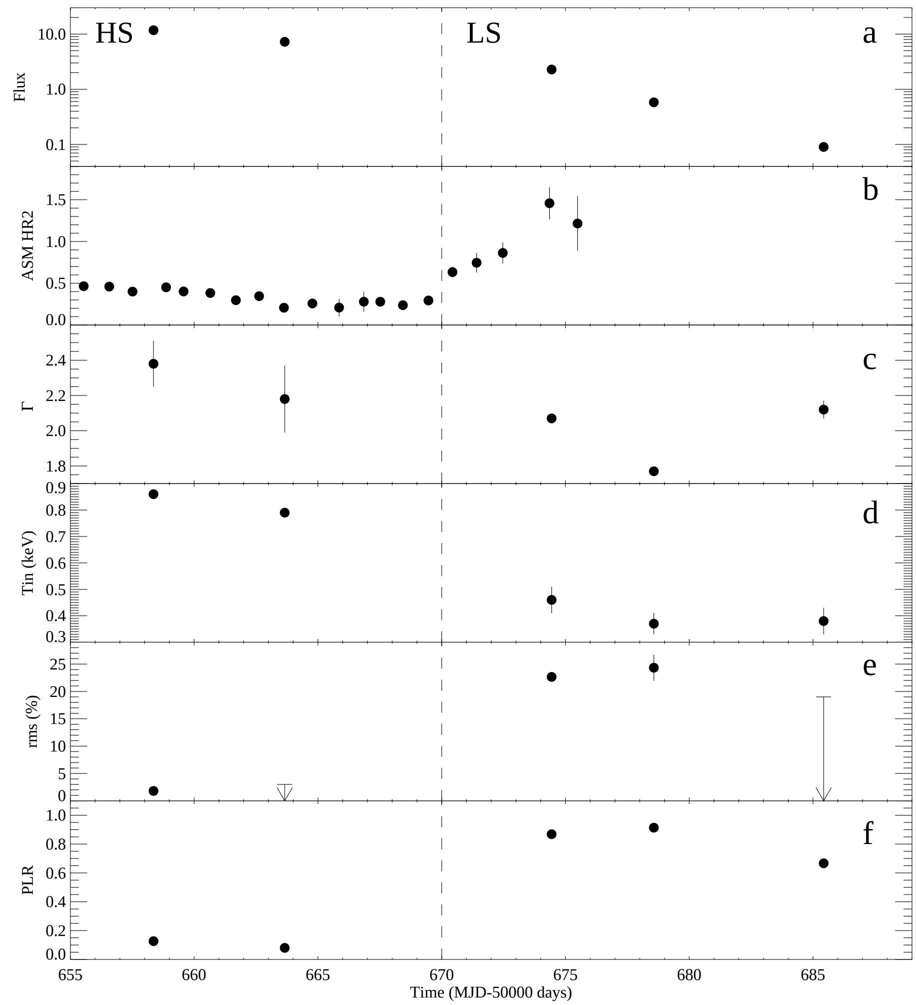

Figure 4.8: Spectral and temporal evolution of GRO J1655−40. (a) Flux in 2–10 keV band in units of $10^{-9}\,\mathrm{ergs\,cm^{-2}\,s^{-1}}$. (b) ASM hardness ratio 2, the ratio of 5–12 keV band count rate to 1.5–3 keV band count rate. (c) Power-law index. (d) Inner disk temperature. (e) Total rms amplitude in 1–30 keV band in 0.01–100 Hz band. (f) PLR, hardness ratio, ratio of power-law flux to total flux in 2–10 keV band. All values except ASM hardness ratios are from Table 1 of Méndez, Belloni & van der Klis (1998).

plitude). On MJD 50674.4, the source was found to be in the LS. The strength of variability jumped to ∼20%, the inner disk temperature decreased significantly, and the power-law flux dominated the X-ray spectrum. An analysis of the ASM hardness ratio indicates that the state transition has started on ∼MJD 50670. The change in the power law index was not significant, although error bars shrunk considerably after the transition due to much stronger power-law flux. A QPO appeared at 6.5 Hz on MJD 50674.4, and then its frequency moved down to 0.8 Hz during the observation

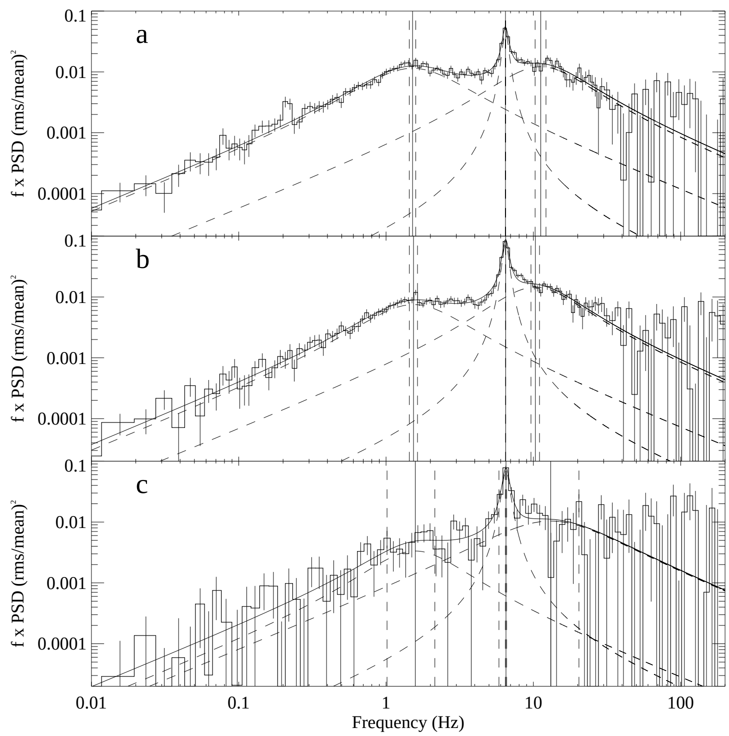

Figure 4.9: Fits to observation 1 for different energy bands. (a) E1. (b) E2. (c) E3. The dashed Lorentzians are individual components and the solid line is the overall fit. The solid vertical lines indicate the peak frequencies and dashed vertical lines are their errors.

on MJD 50678.6. The flux level was too low for the final observation to do timing analysis.

Temporal fits

I fitted the power spectra of the first two observations after the dashed line in Fig. 4.8 that show variability with broad Lorentzians for the continuum and a narrow Lorentzian for the QPO in three energy bands. These fits can be seen in Fig. 4.9 and Fig. 4.10. The parameters of the fits can be found in Table 4.3.

All three bands require two broad Lorentzians and a QPO to fit the PSD and the characteristic frequencies are remarkably similar in different bands. The rms amplitudes are a different story. For observation 1, the rms amplitude of the low frequency Lorentzian decreases with energy. On the other hand, the rms amplitude of the QPO increases with energy. The higher frequency Lorentzian and all Lorentzians

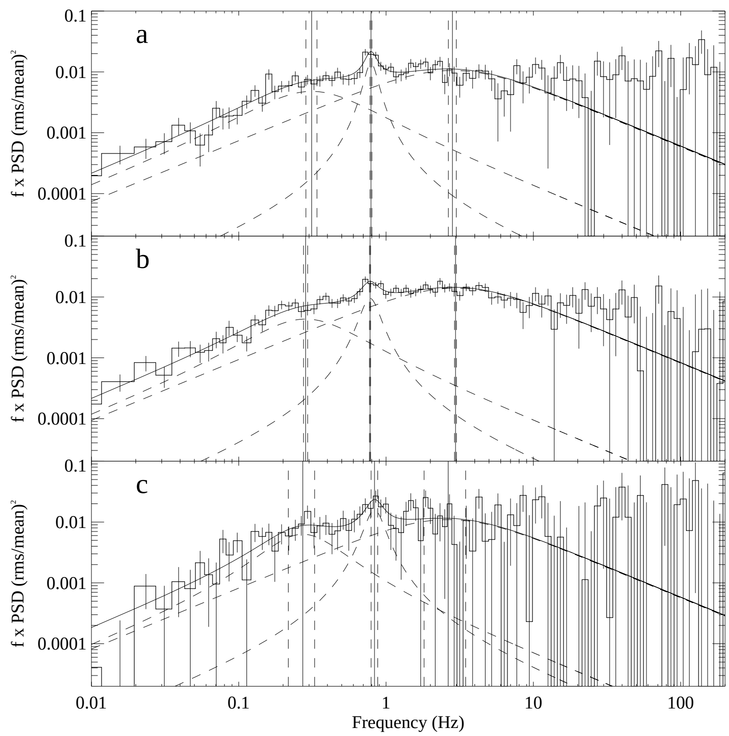

Figure 4.10: Fits to observation 2 for different energy bands. (a) 2–5 keV. (b) 5–13 keV. (c) 13–27 keV. The dashed Lorentzians are individual components and the solid line is the overall fit. The solid vertical lines indicate the peak frequencies and dashed vertical lines are their errors.

in observation 2 do not show any dependence on energy.

Like the other black hole transients during decay, the characteristic frequencies of the PSD components show a decreasing evolution. The QPO frequency decreased from 6.5 Hz to 0.8 Hz. The peak frequency of the lower frequency Lorentzian (ν_1) decreased from 1.5 Hz to 0.3 Hz, and likewise the peak frequency of the higher frequency Lorentzian (ν_2) decreased from 11.2 Hz to 2.9 Hz (see Table 4.3).

Coherence and lags

Observation 1 has high enough statistical quality to do frequency dependent lag and coherence analysis. In Fig. 4.11 we show the results of this analysis. The lag and coherence are calculated between E1 and E2. This figure suggests that the coherence slightly increases at the QPO frequency. Also, at frequencies where both the low frequency Lorentzian and the QPO is contributing strongly to the PSD (between 2

Table 4.3: Temporal fit parameters

Obs. 1 (MJD50674.4)	2–5 keV	5–13 keV	13–27 keV
$\nu_1{}^a$	1.514 ± 0.077	1.537 ± 0.098	1.579 ± 0.564
rms 1	15.53 ± 0.59	12.01 ± 0.63	7.90 ± 1.61
QPO freq. (Hz)	6.457 ± 0.020	6.475 ± 0.032	6.506 ± 0.079
QPO fwhm (Hz)	0.696 ± 0.063	0.703 ± 0.054	0.790 ± 0.106
QPO rms (%)	8.62 ± 0.31	11.40 ± 0.29	11.47 ± 0.79
$\nu_2{}^b$	11.225 ± 0.952	10.321 ± 0.688	13.115 ± 7.277
rms 2	14.86 ± 1.02	16.08 ± 0.87	15.90 ± 4.26
Obs. 2 (MJD50678.6)			
ν_1	0.313 ± 0.027	0.284 ± 0.009	0.272 ± 0.055
rms 1	10.50 ± 0.44	9.65 ± 0.12	10.22 ± 0.89
QPO freq. (Hz)	0.785 ± 0.011	0.768 ± 0.006	0.824 ± 0.035
QPO fwhm (Hz)	0.177 ± 0.022	0.249 ± 0.013	0.269 ± 0.106
QPO rms (%)	6.85 ± 0.33	6.73 ± 0.12	8.74 ± 1.59
ν_2	2.822 ± 0.175	2.961 ± 0.046	2.641 ± 0.829
rms 2	18.18 ± 0.72	20.92 ± 0.19	18.52 ± 2.67

^{a} Peak frequency of the lower frequency Lorentzian
^{b} Peak frequency of the higher frequency Lorentzian

and 5 Hz) the coherence is lower. Again, in this frequency range, the lags seem to be lower.

4.2.3 Summary

This is a very important source since the mass and the distance are precisely known. Unfortunately, the *RXTE* observations were sparse, and therefore I could not follow the evolution of the state transition in detail. The observations I analyzed indicate that the evolution is similar to other sources; the inner disk temperature decreased, the power law index hardened and the peak frequencies decreased after the transition.

The coherence increases at the QPO frequency, and the coherence and lag seems lower around the frequency region where the Lorentzian components in the PSD meet.

Table 4.4 characterizes the physical properties of GRO J1655−40 during the state transition.

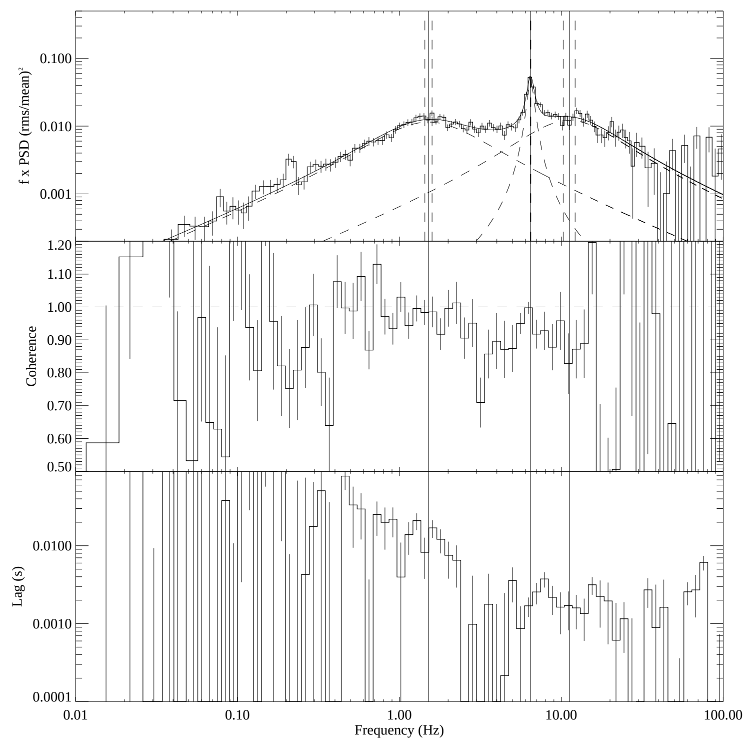

Figure 4.11: Frequency dependent coherence and lags. The top panel is the PSD in E1. The middle panel is the coherence function and the bottom panel is the lag. The vertical solid lines are the peak frequencies and the dashed lines are the errors in peak frequencies. The horizontal dashed line in the middle panel indicates the unity coherence.

Table 4.4: GRO J1655−40

Name :	GRO J1655−40
Mass :	7.02 ± 0.22 $M_\odot$
Distance :	3.2 ± 0.2 kpc
Peak Flux[a] :	80.
Peak Luminosity :	9.83[b]
Gal. Coord. :	345.0, +2.5
N_H :	$0.67 \times 10^{22}\,\mathrm{cm}^{-2}$ [c]
At the state transition:	
Flux :	3.37
Luminosity :	0.41
Γ_{trans} :	2.07
T_{in} :	0.46 keV
Power-law flux :	2.68

a All fluxes in this table are in 1.5-12 keV band, in units of $10^{-9}\,\mathrm{ergs\,cm^{-2}\,s^{-1}}$.

b All luminosities in this table are in 1.5-12 keV band, in units of $10^{37}\,\mathrm{ergs\,cm^{-2}\,s^{-1}}$.

c From Méndez, Belloni & van der Klis (1998).

4.3 XTE J1748−288

XTE J1748−288 was discovered by ASM on *RXTE* on June 4, 1998 (Smith, Levine & Wood 1998). The ASM light curve of the source during the 1998 outburst is shown in Fig. 4.12. Preliminary *VLA* observations revealed an unresolved radio source with position coincident to that of the X-ray source (Hjellming et al. 1998a). Subsequently, the radio source was resolved (Rupen, Hjellming & Mioduszewski 1998). Based on a 21 cm Hydrogen absorption measurement, the distance to the source was estimated to be ≥8 kpc, implying an intrinsic jet velocity higher than 0.93 c (Hjellming et al. 1998b), and therefore this source is a microquasar.

Two QPOs with central frequencies ∼0.5 and ∼32 Hz were found with the PCA on June 6 1998 (Fox & Lewin 1998). The source was observed with *RXTE* quasi-evenly from June until September 1998, obtaining a good coverage of the outburst. Timing and spectral results from these observations were presented by Revnivtsev, Trudolyubov & Borozdin (2000). A more detailed spectral analysis of the same observations to investigate the relativistic iron emission from this source was presented by Miller et al. (2001).

The X-ray energy spectrum fits by Revnivtsev, Trudolyubov & Borozdin (2000) include a diskbb component and a power law with absorption. Their temporal analysis, along with the spectral results yield that the source was in the VHS in the beginning of the outburst, made a transition to the HS, and later during the decay, the transition to the LS happened on MJD 51012. The VHS PSD showed a QPO in 21–32 Hz range and total rms amplitude variability of around 13%. The combined HS observations showed a PSD that can be characterized by a power law shape with a total rms amplitude of ∼1%.

4.3.1 Observations and analysis

I did the analysis of temporal properties of LS observations, and three observations before the transition (proposal id P30185). For spectral results, I used the results from Revnivtsev, Trudolyubov & Borozdin (2000). As usual, the PSD and cross spectral analysis were done in three energy bands, 2–5 keV (E1), 5–13 keV (E2), 13–27 keV (E3) as permitted by the data modes. For the LS observations, a time resolution of

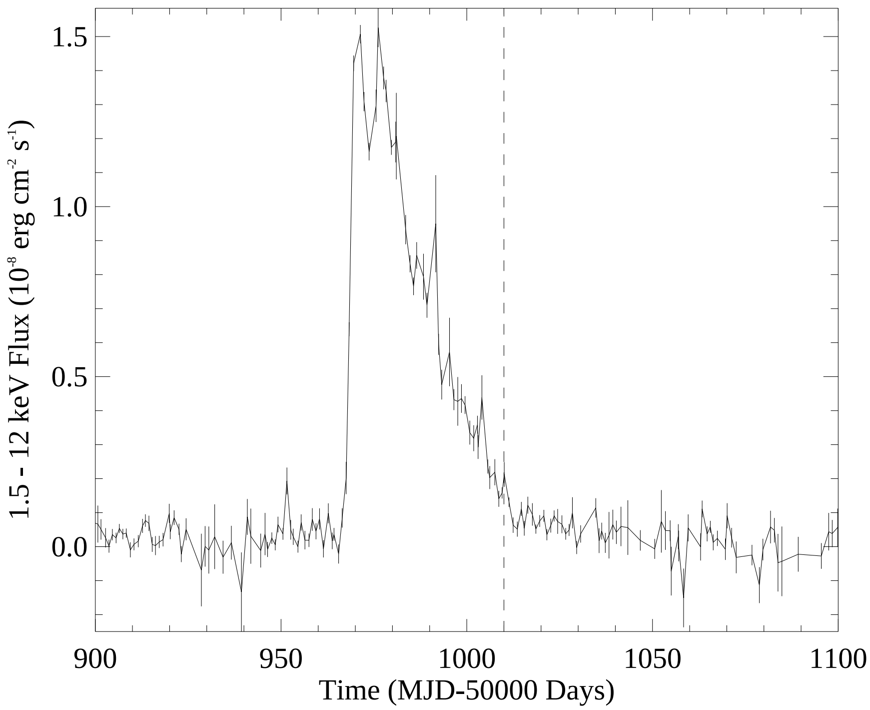

Figure 4.12: ASM light curve of XTE J1748−288 during the 1998 outburst. The dashed line indicates the time of transition to the LS.

2^{-8}s was used.

4.3.2 Spectral and temporal evolution

Fig. 4.13 shows the spectral and temporal evolution of XTE J1748−288 during the decay. The dashed line in this figure separates the HS and LS observations. The overall flux (a) showed a smooth decay. The PLR (b), ratio of the power-law flux to the total flux increased substantially just before the transition, and was unity after the transition. The spectral index (c) showed a smooth decay to the transition, and a sharper drop at the transition. After the transition, the index increased slightly. T_{in} (d) showed a big drop at the transition. The power-law flux (e) increased considerably around a week before the transition, and decreased smoothly after the transition. At the same time that the power-law flux increased, the diskbb flux (f) decreased, and cannot be observed after the state transition. It is possible that the transition had begun 3-5 days before the large temporal changes in the PSD, since this is the time

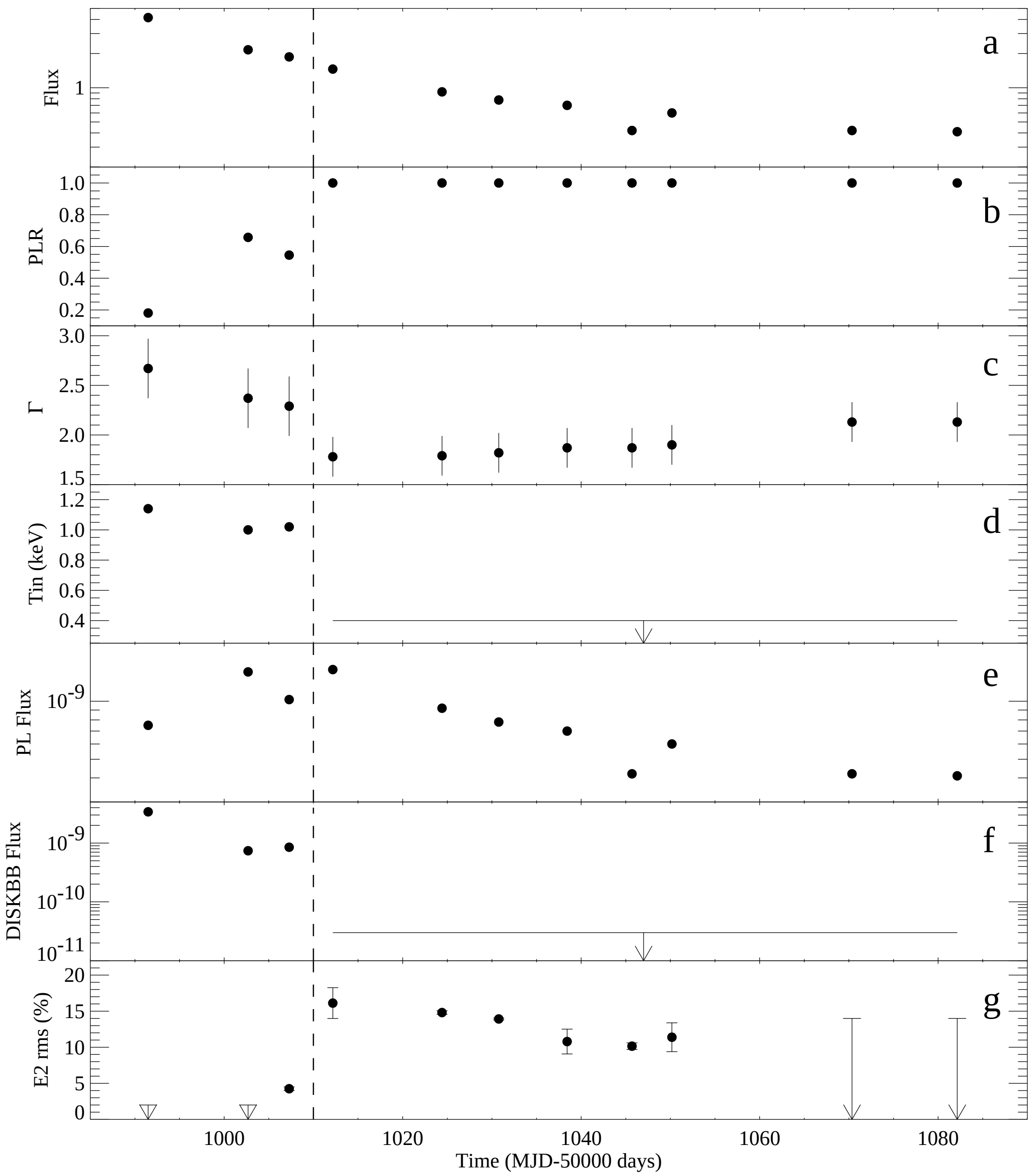

Figure 4.13: The spectral and temporal evolution of XTE J1748−288 during the 1998 outburst decay. (a) Flux in 3 – 25 keV band. (b) PLR, ratio of power-law flux to total flux in 3–25 keV band (c) Spectral index. (d) Inner disk temperature. (e) Power-law flux. (f) Diskbb flux. (g) E2 rms amplitude. The spectral parameters are from Revnivtsev, Trudolyubov & Borozdin (2000), except the upper limits for T_{in} and the diskbb flux in the LS are from Miller et al. (2001). The dashed line separates low and high state observations, the left hand side is the HS. The upper limits are 90% confidence limits.

when PLR first increased, and a very low frequency, weak (∼4%) noise component appeared in PSD. For the remaining observations, the rms amplitude (g) of variability

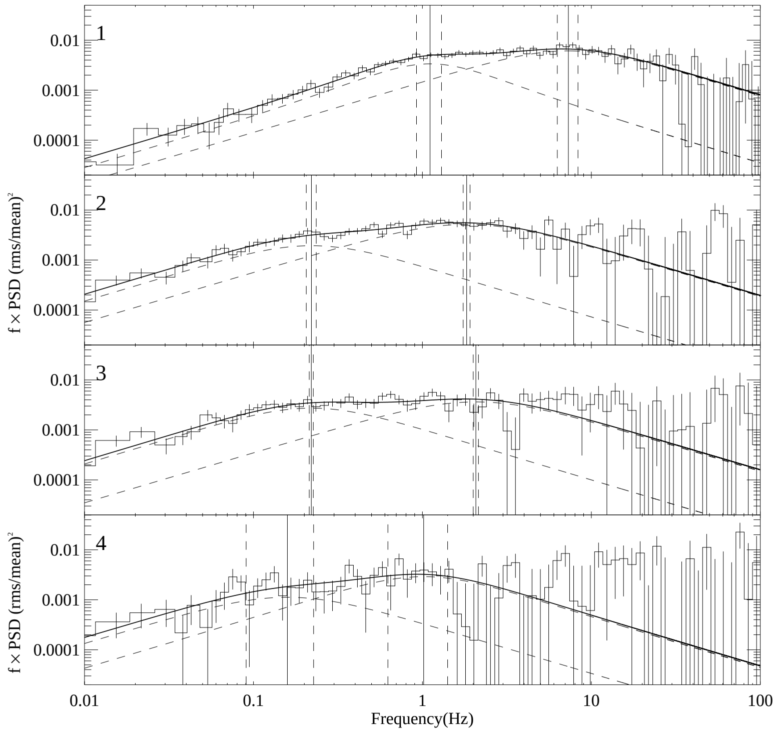

Figure 4.14: Lorentzian fits to the first four observations in E2 in LS of XTE J1748−288. The dashed curves are individual PSD components and the solid curve is the overall fit. The solid vertical lines are the peak frequencies and the dashed vertical lines are the errors in peak frequencies. The peak frequencies shift to lower values from observation 1 to 2.

was on the order of 20%. For the last two observations, the flux was too low, and only a 90% confidence upper limit of 14% rms amplitude could be placed on variability.

I fit the PSD with Lorentzians in three energy bands. The results are presented in Table 4.5. I also plot the E2 PSDs for the first four observations in the LS and their Lorentzian fits in Fig. 4.14. The remaining observations are not shown in this figure since the PSDs are noisy and peak frequencies are not well constrained due to low statistics (see Table 4.5). As can be seen, two Lorentzians adequately describe the PSDs. There is a drop in peak frequencies from the first observation to the second, however it is not clear if this drop continues for the remaining observations. The rms amplitude generally increases with energy for both individual Lorentzian cases and overall. E3 band PSDs do not have good statistics, and although I reported the peak frequencies in Table 4.5, claiming that the peak frequencies change with energy based on E3 data would be a strong statement.

The statistics was not good enough to do frequency dependent coherence and lag studies. For the longest observations with higher flux levels (observations 1 and 2), I was able to calculate the mean coherence in 0.1 – 1. Hz range. Between E1 and E2, the mean coherence was 0.882 ± 0.075 and 0.932 ± 0.112 respectively. I obtained similar numbers for the coherence between E1 and E3. The frequency dependent time lags were very noisy.

4.3.3 Summary

This is a source with a moderate strength outburst showing the usual evolution to the LS during outburst decay. The transition is sharp, and occurs within 3 days as the power-law index hardens considerably and the PSD shows strong variability. After the transition, the peak frequencies decrease. Contrary to the most of the other sources, the rms amplitudes decrease instead of increasing as the source evolves after the transition. The energy dependent PSD analysis indicates that the rms amplitudes generally increase with energy for the individual Lorentzian components and overall. The statistics were not good enough to do frequency dependent coherence and lag analysis.

Table 4.6 characterizes the physical properties of XTE J1748−288 during the state transition.

Table 4.5: Temporal fit parameters of XTE J1748−288

Obs/Band[a]	Date[b]	ν_1 (Hz)	rms 1 (%)	ν_2 (Hz)	rms 2 (%)	Total rms
1/E1	1012.17	0.813 ± 0.159	5.24 ± 0.46	5.583 ± 0.918	11.57 ± 0.85	12.71 ± 0.97
1/E2		1.104 ± 0.186	8.85 ± 0.96	7.283 ± 1.015	13.47 ± 1.92	16.12 ± 2.13
1/E3		1.422 ± 0.479	11.11 ± 1.36	7.146 ± 1.198	12.72 ± 1.19	16.90 ± 1.79
2/E1	1024.41	0.300 ± 0.020	5.97 ± 0.10	2.402 ± 0.125	10.20 ± 0.18	11.81 ± 0.21
2/E2		0.220 ± 0.014	7.57 ± 0.17	1.827 ± 0.085	12.73 ± 0.20	14.81 ± 0.25
2/E3		0.323 ± 0.027	14.63 ± 0.46	2.503 ± 0.333	18.02 ± 0.81	23.22 ± 0.92
3/E1	1030.77	0.214 ± 0.004	6.42 ± 0.04	1.712 ± 0.073	7.205 ± 0.08	9.65 ± 0.09
3/E2		0.219 ± 0.006	8.94 ± 0.07	2.072 ± 0.073	10.66 ± 0.12	13.92 ± 0.13
3/E3		0.263 ± 0.026	15.71 ± 0.59	2.266 ± 0.442	17.76 ± 1.16	23.71 ± 1.27
4/E1	1038.43	-	-	-	-	$< 15.27^{c}$
4/E2		0.158 ± 0.068	5.88 ± 1.30	1.017 ± 0.392	9.051 ± 1.20	10.79 ± 1.72
4/E3		0.986 ± 0.069	21.33 ± 0.52	-	-	21.33 ± 0.52
5/E1	1045.70	-	-	-	-	< 9.61
5/E2		0.459 ± 0.058	10.15 ± 0.46	-	-	10.15 ± 0.46
5/E3		-	-	-	-	< 12.31
6/E1	1050.17	-	-	-	-	< 8.05
6/E2		0.099 ± 0.032	5.93 ± 0.82	1.251 ± 0.733	9.72 ± 1.84	11.39 ± 2.00
6/E3		-	-	-	-	< 17.22

a Numbering starts after the dashed line in Fig. 4.13.
b MJD-50000 days
c All upper limits are in 90% confidence

Table 4.6: XTE J1748−288

Name :	XTE J1748−288
Mass :	-
Distance :	> 8 kpc
Gal. Coord. :	0.7, -0.21
N_H :	$7.5 \times 10^{22}\,\mathrm{cm}^{2\,a}$
Peak Flux[b] :	15.
Peak Luminosity :	> 11.5 [c]
At the state transition:	
Flux :	1.24
Luminosity :	>0.95
Γ_{trans} :	1.86
T_{in} :	0.42 keV
Power-law flux :	1.24

a From Miller et al. (2001)
b All fluxes in this table are in 1.5-12 keV band, in units of $10^{-9}\,\mathrm{ergs\,cm^{-2}\,s^{-1}}$
c All luminosities in this table are in 1.5-12 keV band, in units of $10^{37}\,\mathrm{ergs\,s^{-1}}$

4.4 XTE J1755−324

XTE J1755−324 was discovered by the ASM on *RXTE* on July 25, 1997 (Remillard et al. 1997). The ASM light curve (as seen in Fig. 4.15) is typical of black hole transient light curves, and shows a fast rise and an exponential decay. Radio observations at August 18, 1997 did not reveal significant radio flux (Ogley, Ash & Fender 1997). The optical extinction in the direction of the source indicates $N_H \sim 3.7 \times 10^{21}\,\mathrm{cm}^{-2}$. No optical counterpart has been detected. At the peak of the outburst, the X-ray spectrum indicated that the source was in the VHS, however no short term variability was detected (Revnivtsev, Gilfanov & Churazov 1998).

The *RXTE* observations were very sparse, and on MJD 50758, the source was found in the LS. The rms amplitude of variability jumped from 1.5% to 24% for the last two observations. The energy spectrum in this state had a power-law and an iron line component, and it did not require a diskbb component which was present in the earlier observations (Revnivtsev, Gilfanov & Churazov 1998).

4.4.1 Observations and analysis

I analyzed the data from the last two observations at the end of the decay as the source was going into quiescence (proposal id P20425). For spectral data, I used the values given in Revnivtsev, Gilfanov & Churazov (1998). I used two energy bands, approximately corresponding to 2–5 keV (E1) and 5–13 keV (E2) for temporal analysis.

4.4.2 Results

The spectral and temporal data of the source is summarized in Table 4.7. The coverage is very sparse, and it only shows that the source transited into LS sometime between MJD 50661 and MJD 50758. Moreover, observation 3 on MJD 50758 was a scanning observation with a small PCA livetime (∼300 s) and had low count rate, and therefore the PSD is very noisy.

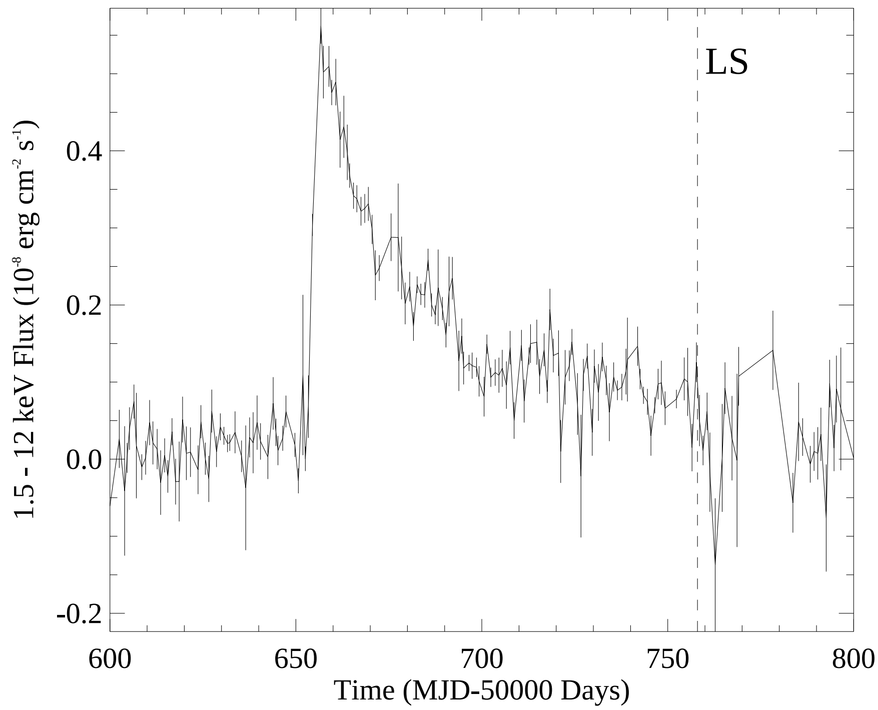

Figure 4.15: ASM light curve of XTE J1755−324. The dashed line corresponds the PCA observation in the LS. The observations were very sparse, and it is not clear when the state transition has happened.

Temporal fits

I fitted the power spectra of two observations that show variability with one Lorentzian. The fits in different energy bands can be seen in Fig. 4.16, and the parameters of the fits can be found in Table 4.7.

Due to the short livetime, the fit parameters of observation 3 are not well determined. Observation 4 PSDs show no dependence on energy and the peak frequencies and rms values are equal in two energy bands within 1σ uncertainty.

Coherence and lags

Neither of the observations have enough statistics to do frequency dependent time lag and coherence studies. The short livetime of observation 3 does not allow me to obtain any information on the cross spectrum. For observation 4, the mean coherence in 0.1 – 1 Hz range is 0.911 ± 0.084. The lag spectrum is not above the noise level

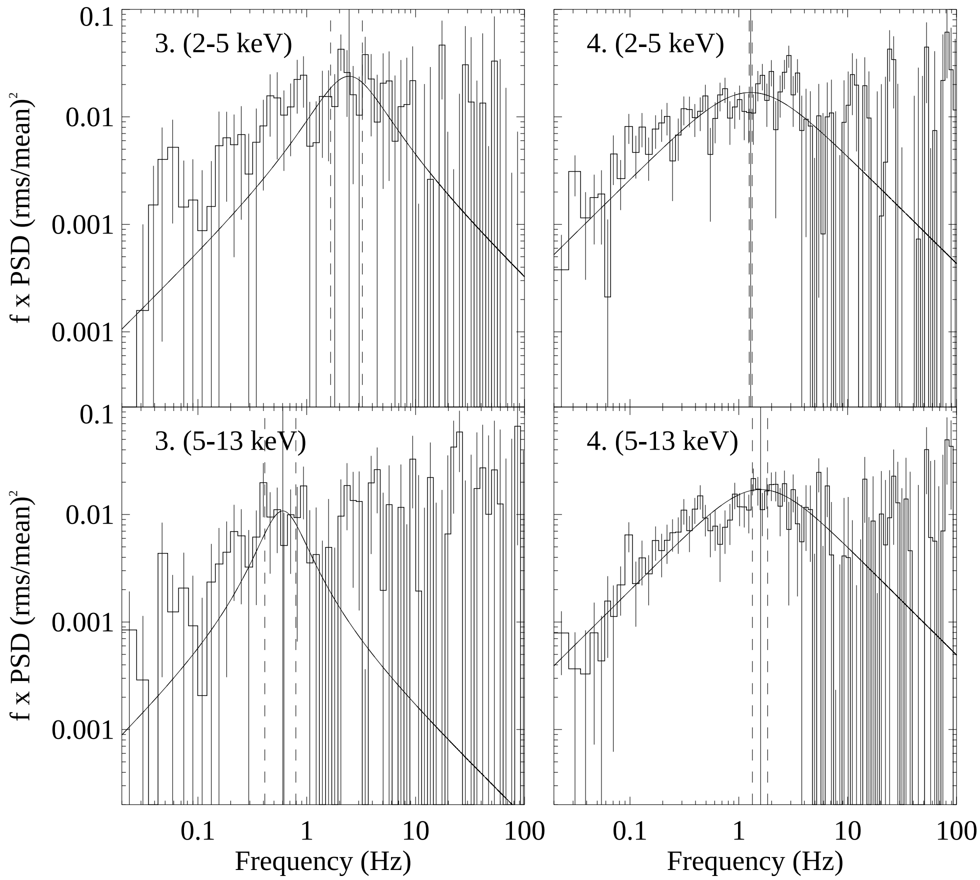

Figure 4.16: Fits to LS PSDs in different energy bands. The upper panels are for PSDs in E1 and lower panels in E2. The left hand side is for observation 3 and right hand side is for 4. The solid line is the Lorentzian fit. The solid vertical lines indicate the peak frequencies and dashed vertical lines are their errors.

and the mean in 0.1 – 1 Hz range is consistent with zero.

4.4.3 Summary

Not much is known about this source, and the *RXTE* coverage is very sparse. The outburst was weak. The source was in the VHS during the rise and found to be in in the LS during the decay. The energy dependent analysis did not show any particular dependence of temporal fit parameters with energy. The statistics were not good enough to do cross spectral analysis.

Table 4.8 characterizes the known physical properties of XTE J1755−324.

Table 4.7: Temporal and spectral fit parameters

Obs	Date[a]	Flux[b]	Γ[c]	E1 f_{peak} (Hz)	E1 rms (%)	E2 f_{peak} (Hz)	E2 rms (%)
1	658.00	1.72 ± 0.08	2.30 ± 0.34	-	<2%[d]	-	<2%
2	661.00	1.59 ± 0.07	1.83 ± 0.10	-	< 2%	-	<2%
3	758.67	0.48 ± 0.01	1.96 ± 0.01	2.450 ± 0.793	21.24 ± 2.06	0.603 ± 0.192	11.95 ± 1.41
4	764.67	0.40 ± 0.01	1.87 ± 0.01	1.285 ± 0.040	23.00 ± 0.23	1.586 ± 0.254	22.76 ± 1.83

a MJD - 50000 days

b 3 - 30 keV in units of $10^{-9}\,\mathrm{ergs\,cm^{-2}\,s^{-1}}$, from Revnivtsev, Gilfanov & Churazov (1998).

c From Revnivtsev, Gilfanov & Churazov (1998).

d The rms amplitudes for the first two observations have an upper limit of 2% (Revnivtsev, Gilfanov & Churazov 1998).

Table 4.8: XTE J1755−324

Name :	XTE J1755−324
Mass :	-
Distance :	-
Gal. Coord. :	358.0, -3.6
N_H :	3.7×10^{21} cm^{-2} [a]
Peak Flux[b] :	5.2
Peak Luminosity :	
At the state transition:[c]	
Flux :	0.45
Luminosity :	-
Γ_{trans} :	1.96
T_{in} :	-
Power-law flux :	0.45 keV

a From Revnivtsev, Gilfanov & Churazov (1998)
b All fluxes in this table are in 1.5-12 keV band, in units of $10^{-9}\,\mathrm{ergs\,cm^{-2}\,s^{-1}}$
c During the first LS observation.

4.5 GX 339−4

GX 339−4 was discovered with the *OSO-7* satellite in 1973, and was classified as a black hole candidate due to its similarity in X-ray behavior to Cyg X-1 (Markert et al. 1973). Although GX 339−4 could be classified as a transient source with very long outbursts, it spends most of the time in LS like a faint persistent source (Kong et al. 2002a). During the LS, the energy spectrum can be described as a power-law with an index of ∼1.5-2. During the HS, it exhibits a diskbb and a steeper power-law (Grebenev et al. 1991; Belloni et al. 1999). This source also exhibits VHS (Miyamoto et al. 1991; Smith et al. 2002) with a PSD showing 1% - 15% rms amplitude variability and IS (Méndez & van der Klis 1997) with similar variability properties as the VHS but with much lower luminosity. It rarely enters an off state with spectral shape and temporal properties consistent with the LS, except that the flux is ∼10 times lower (Kong et al. 2002a).

It is optically identified (Doxsey et al. 1979) with an ∼15 hr period interpreted as the orbital period (Callanan et al. 1992). It has been hypothesized that the optical emission is dominated by the accretion disk, which made it difficult to obtain a good distance measurement and mass function (Wilms et al. 1999). A careful study of the distance estimates led Zdziarski et al. (1998) to argue for a distance of ∼4 kpc.

GX 339−4 has also been detected in radio (Sood & Campbell-Wilson 1994), and a possible extended emission was reported by (Fender et al. 1997a). During the LS, the radio spectrum is flat/inverted indicative of a compact jet (Fender et al. 1997a). Furthermore, in this state the radio flux is correlated with the X-ray and gamma-ray fluxes (Hannikainen et al. 1998). Recently, a long term campaign of radio, soft and hard X-ray observations of GX 339−4 revealed a strong 3-way linear correlation between soft and hard X-rays and radio emission in the LS (Corbel et al. 2000) similar to the report of Hannikainen et al. (1998). Note that, this correlation between X-ray and radio was interpreted such that the synchrotron emission in the jet may be responsible for both the X-ray and radio emission (S. Corbel, private communication). In LS, the radio emission is linearly polarized which is indicative of a favored axis in the system probably related to the compact jet and/or black hole spin axis. In the HS, the radio emission is quenched. It is also noted that the transitions between

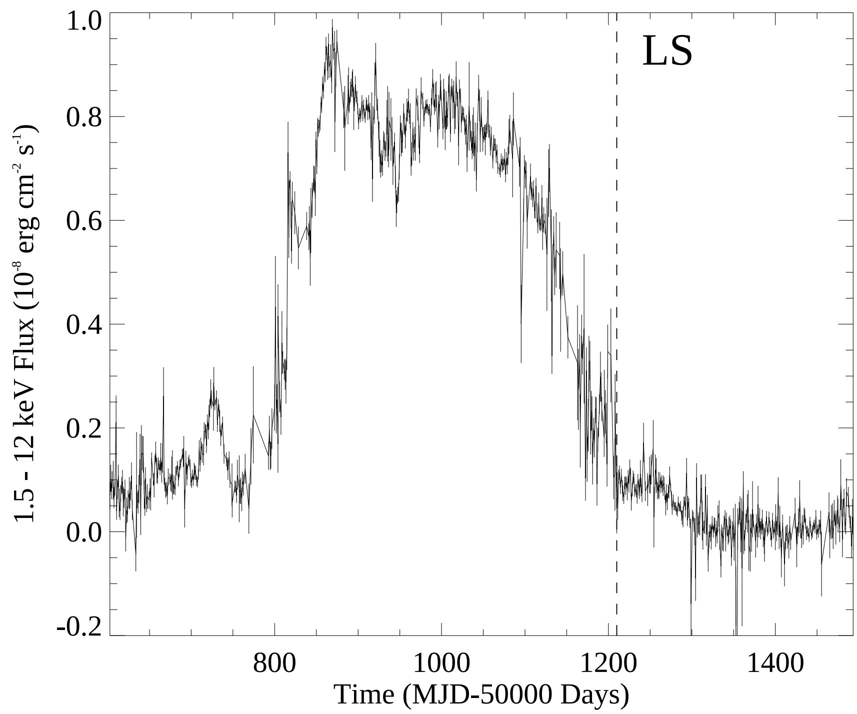

Figure 4.17: ASM light curve of GX 339−4. The dashed line marks the transition to the LS.

LS and HS are possibly associated with discrete ejections of expanding relativistic plasma (Corbel et al. 2000).

In the beginning of January 1998, the ASM on *RXTE* showed a sharp increase in emission coming from GX 339−4 (see Fig. 4.17). Although the outburst rise was fast, similar to the rise of usual FRED type outburst light curves, the flux remained constant for around ∼150 days before starting to decay. The source was in the HS during the outburst maximum (Belloni et al. 1997). Observations at the end of the decay showed that the source made a transition to the LS before ∼MJD 51220 (Nowak, Wilms & Dove 2002), as indicated by the dashed line in Fig. 4.17. The spectral and temporal properties during the LS were reported by Nowak, Wilms & Dove (2002).

4.5.1 Observations and analysis

I analyzed the data from 6 observations at the end of the decay as the source was going into quiescence in 1999 (proposal id P40108). For spectral analysis, I used both the PCA and the HEXTE data. The timing analysis is done in three energy bands when possible. Due to the change in gain epoch in the middle of observations, my approximate energy bands also changed since the channel boundaries were set by the event mode. Therefore, for the first four observations during epoch 3, my energy bands are 2–5 keV, 5–13 keV and 13–26 keV. For the last two observations during epoch 4, they moved to 2–6 keV, 6–15 keV and 15–30 keV. Those bands are called E1, E2 and E3 respectively. For the first two observations, only the E1 and E2 PSD were above the noise level. I studied the evolution of spectral and temporal properties during the decay, including lags and coherence among the given energy bands.

4.5.2 Results

Spectral and temporal evolution

I fit the X-ray spectrum with a model consisting of diskbb, power-law, a smeared edge (smedge) and absorption where I fixed the hydrogen column density to $6 \times 10^{21}\,\mathrm{cm}^{-2}$ following Nowak, Wilms & Dove (2002). The results are summarized in Table 4.9. For the first two observations diskbb is required, however only the power-law component remains after the second observation. At this point the source is in the LS. The temporal properties, which will be discussed in the next section in more detail, also confirm that the source is already in the LS.

The spectral and temporal evolution can be followed better in Fig. 4.18. For the first two observations, there is significant variability (8%–12% rms amplitude) along with the soft component, which is typical of IS state observations. These observations were claimed to be in the HS by Nowak, Wilms & Dove (2002). In this work the observations right at the transition which show large PSD changes are called the "transitional state" (TS) observations. These two observations also belong to this class. After the state transition, the soft component disappears, the rms amplitude increases and the peak frequencies decreases, which are typical properties of LS.

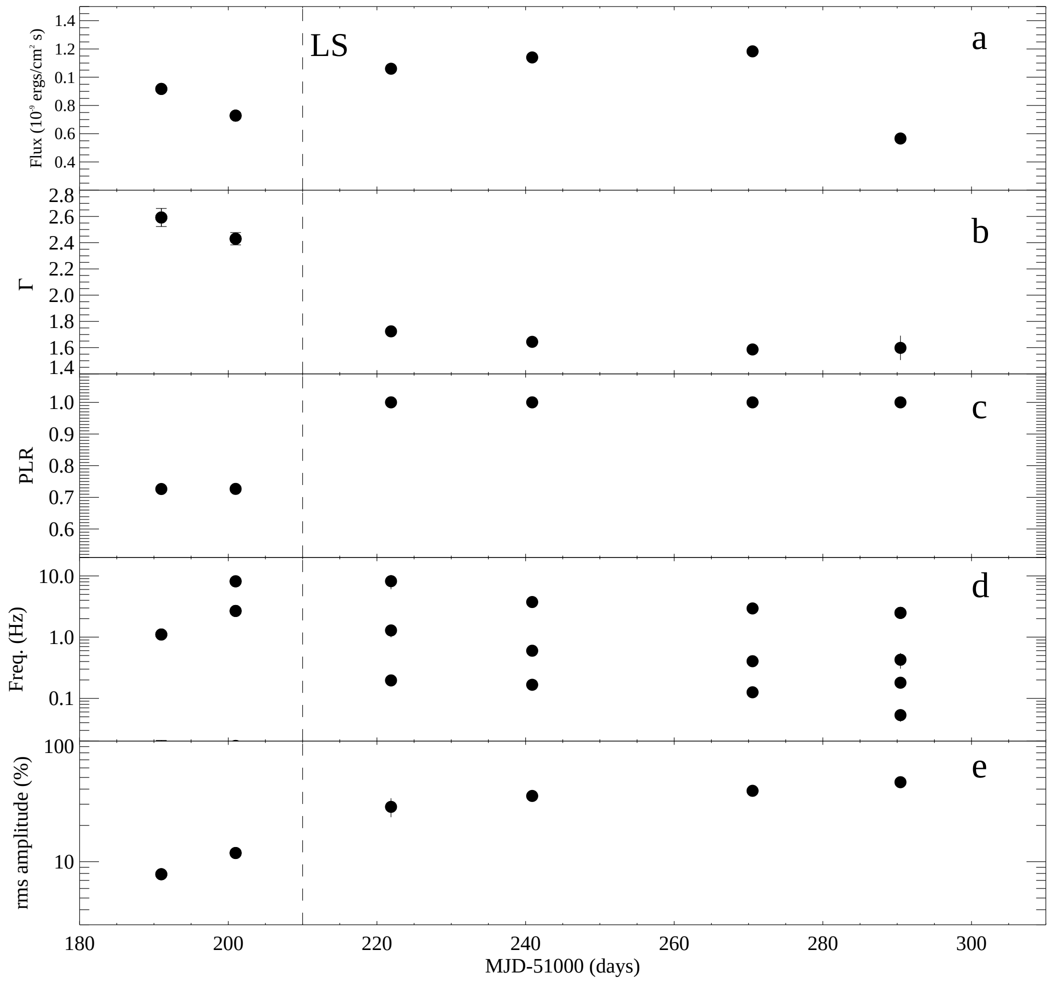

Figure 4.18: Spectral and temporal evolution of GX 339−4. (a) Flux in 3–25 keV band in units of $10^{-9}\,\mathrm{ergs\,cm^{-2}\,s^{-1}}$. (b) power-law index. (c) PLR, hardness ratio, ratio of power-law flux to total flux in 3–25 keV band. (d) Peak frequencies of Lorentzians (e) Total rms amplitude in 2–15 keV band. The dashed line separates the LS and TS (or intermediate state) observations. The placement of this line is consistent with the increased hardness in the ASM hardness ratio.

Temporal fits

I first combined E1 and E2 light curves and analyzed the evolution of the PSDs in this combined band. Fig. 4.19 shows all the PSDs in this combined band also the Lorentzian fits. The fit parameters are given in Table 4.10. The TS observations require two Lorentzians, and the first three observations in the LS require three Lorentzians to fit the PSD continuum. The last observation on the other hand needs four Lorentzians. As discussed earlier, the overall trend in peak frequencies

Table 4.9: Spectral fit values of GX 339−4.

Obs	Date[a]	Γ	T_{in} keV	power-law flux [b]	Total flux[c]
1	190.9	2.592 ± 0.069	0.519 ± 0.006	0.666	1.181
2	200.9	2.430 ± 0.047	0.518 ± 0.006	0.529	0.922
3	221.8	1.724 ± 0.008	-	1.060	1.060
4	240.8	1.644 ± 0.007	-	1.140	1.140
5	270.5	1.586 ± 0.012	-	1.183	1.183
6	290.4	1.598 ± 0.093	-	0.566	0.566

a MJD-50000 days
b PCA, 3–25 keV band, unabsorbed, in units of $10^{-9}\,\mathrm{ergs\,cm^{-2}\,s^{-1}}$
c Same as above.

of Lorentzian components is a decreasing one after the state transition, however the behavior of rms amplitudes is not as clear. The requirement of the 4th Lorentzian in observation 6 complicates the matter further.

As can be seen in Fig. 4.19, observations 2, 3 and 5 need narrow Lorentzians (QPOs) in order to obtain acceptable fits. The parameters for these QPOs are given separately in Table 4.10. The QPOs in the low state are weak, sharp features ($Q \gtrsim 10$) which can only be detected in the combined band. The pairs might possibly be related harmonically, especially the one in observation 3. The QPO in the TS on the other hand has a very strong energy dependence and detected strongly in E2.

Energy dependence of PSD components

As I did for other sources, I also analyzed the energy dependence of the PSD fit parameters. The fit results are given in Table 4.11. I also show the fits in two energy bands for the TS observations in Fig. 4.20 and three energy bands for two representative LS observations (3 and 5) in Fig. 4.21.

Both observation 1 and 2 carry a red noise-like component at low frequencies. Although it could be fitted with a Lorentzian for the combined band, for the energy dependent analysis, its properties are not well constrained with a Lorentzian. The second component, on the other hand is well constrained for both observations. Its frequency does not change with energy (see Fig. 4.20), however the rms amplitude increases substantially with energy, which is usual for TS observations. The observa-

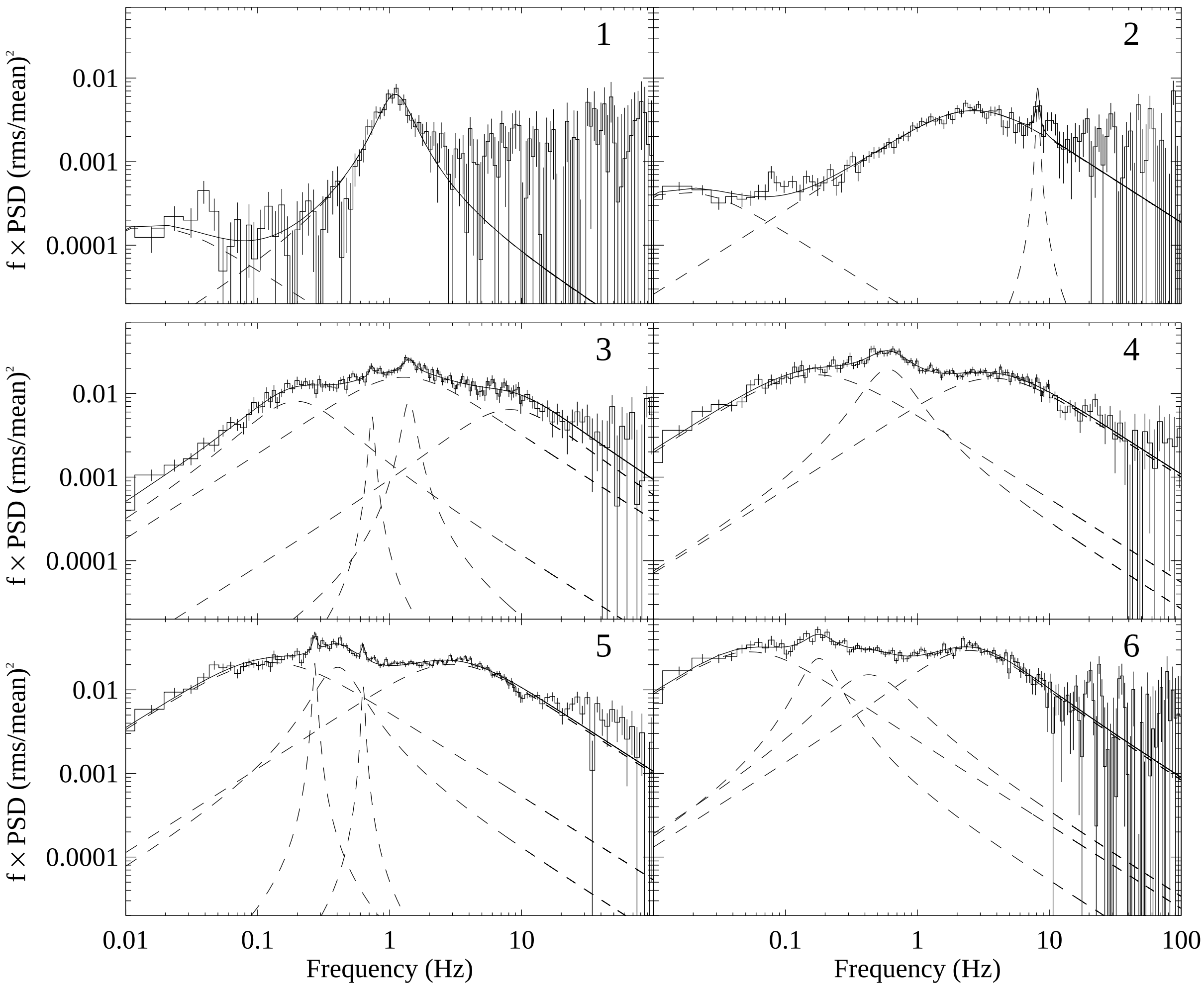

Figure 4.19: Evolution of PSD in GX 339−4. The upper two panels are TS observations and the remaining four observations are the LS observations. The solid curves are the overall fit with Lorentzians, while the dashed curves are the individual components. The solid vertical lines are the peak frequencies and the dashed vertical lines are their errors.

tion 2 PSD is significantly energy dependent since it shows a low frequency QPO in E1, which is not statistically significant in E2, and a higher frequency QPO in E2, which is not statistically significant in E1. The QPO in E1 is at 0.087 ± 0.001 Hz, has an rms amplitude of 1.45 ± 0.05 % and its FWHM is 0.035 ± 0.003 Hz. The QPO in E2 is at 7.847 ± 0.013 Hz, has an rms amplitude of 6.70 ± 0.08 % and its FWHM is 1.509 ± 0.027 Hz.

Although the combined band PSD in observation 6 requires four Lorentzians, the individual bands, probably due to lack of statistics, require 3 Lorentzians for

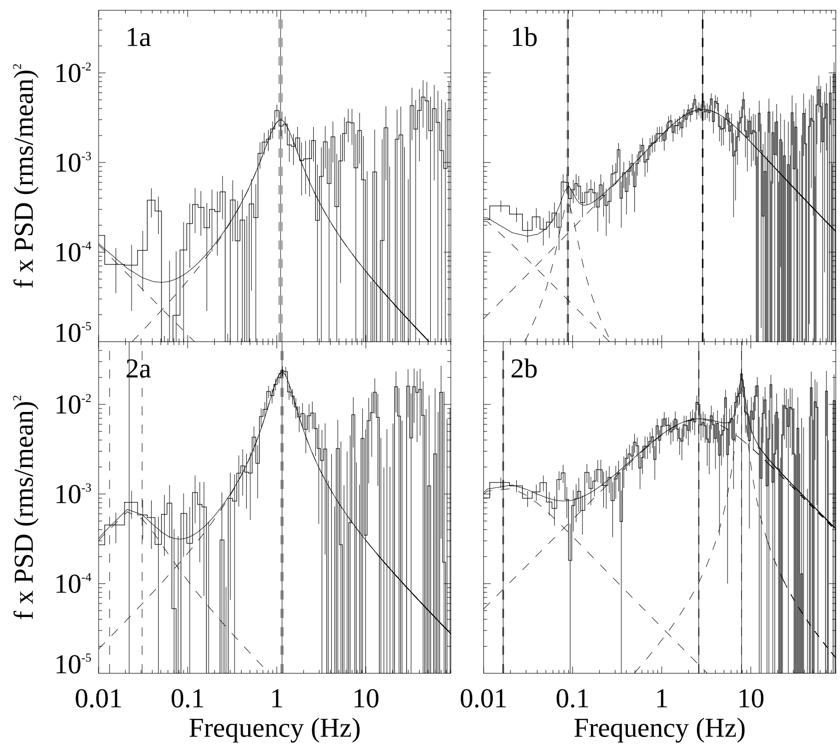

Figure 4.20: Energy dependent PSD fits for TS observations of GX 339−4. (1a) E1 PSD of observation 1. (1b) E2 PSD of observation 1. (2a) E1 PSD of observation 2. (2b) E2 PSD of observation 2. The solid curve is the overall fit with Lorentzians and the dashed curves are individual components. The solid vertical lines are peak frequencies and the dashed vertical lines are corresponding errors.

all observations including observation 6. The total rms amplitude in E3 is ~64%, highest I have ever observed during the LS. The peak frequencies do not change with energy, neither in the TS state nor in the LS (disregarding the poorly constrained first Lorentzian in the TS). The rms amplitudes are a different story. The total rms increases with energy in the TS. In the LS, it decreases for observation 3, stays constant for observations 4 and 5, and stays constant and then increases substantially for observation 6. These changes are not driven particularly by Lorentzian 1,2 or 3, but they are due to a combination of those.

Coherence and lags

I also analyzed the lag and coherence behavior of GX 339−4 during the decay. The frequency dependent analysis was only possible for LS observations, however the

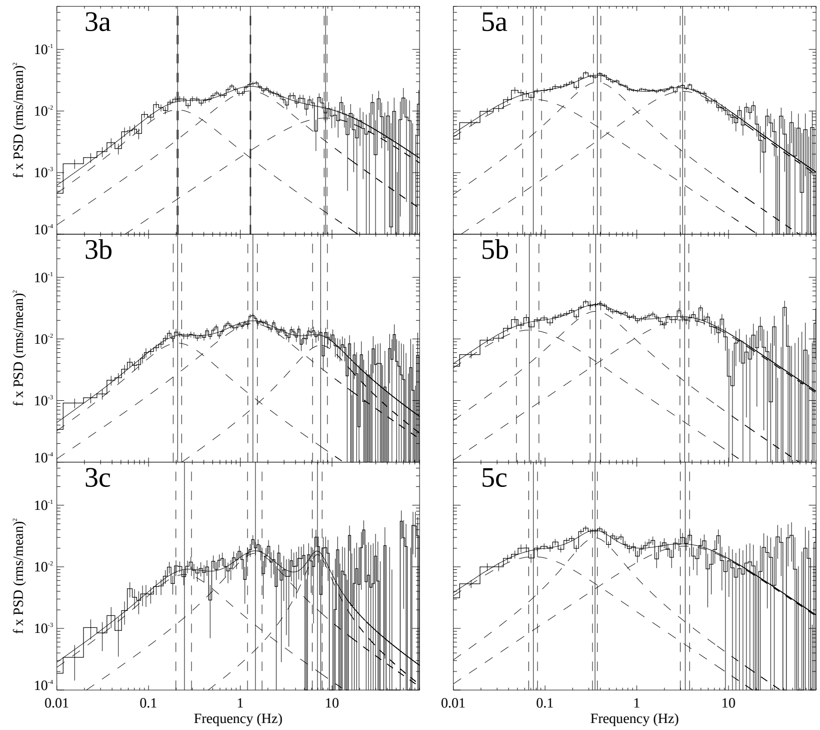

Figure 4.21: Energy dependent PSD fits for LS observations of GX 339−4. (3a) E1 PSD of observation 3. (3b) E2 PSD of observation 3. (3c) E3 PSD of observation 3. (5a) E1 PSD of observation 5. (5b) E2 PSD of observation 5. (5c) E3 PSD of observation 5. The solid curve is the overall fit with Lorentzians and the dashed curves are individual components. The solid vertical lines are peak frequencies and the dashed vertical lines are corresponding errors.

analysis of the average properties were done for all observations. The frequency dependent analysis did not yield any obvious dependence on the position of the Lorentzian components in the PSD. In Figs. 4.22 and 4.23 I show the frequency dependent lag and coherence along with the Lorentzians in the PSDs.

The evolution of the integrated lags and mean coherence is more interesting. Between E1 and E2, the coherence and lags for all observations except observation 1 were significantly above the noise level in 1–10 Hz band. The evolution of integrated lag and mean coherence in this band can be seen in Fig. 4.24. I also show the evolution of the spectral index along with coherence and lag in this figure, which clearly correlates with the integrated lag. Before the LS observations, the mean coherence is lower and the integrated lags are much higher compared to the LS observations.

Good statistics in E3 also allow me to study the band dependence of X-ray lags.

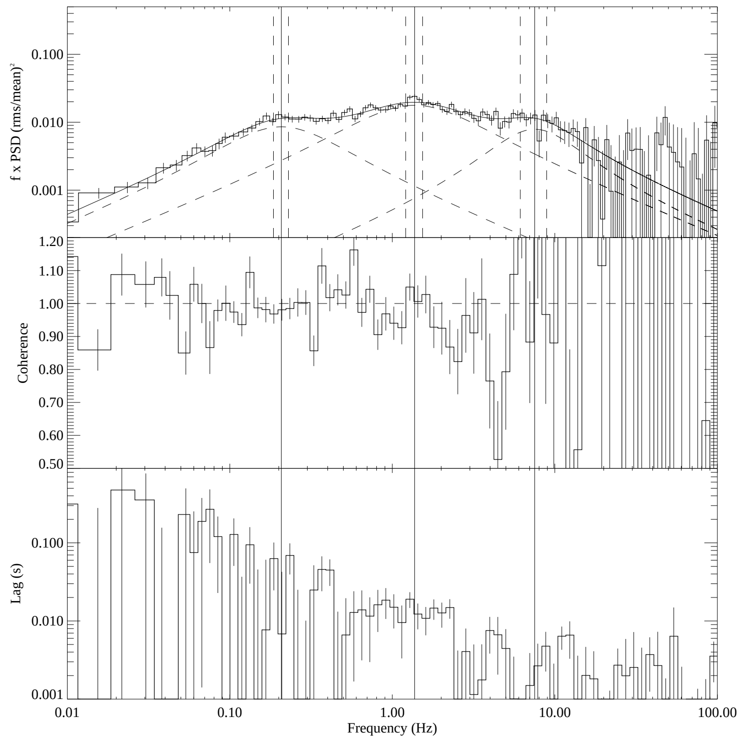

Figure 4.22: Frequency dependent coherence and lags for observation 3. The top panel is the PSD in E2. The middle panel is the coherence function and the bottom panel is the lag. The vertical solid lines are the peak frequencies and the dashed lines are the errors in peak frequencies. The horizontal dashed line in the middle panel indicates the unity coherence.

For both E2 vs. E1 and E3 vs E1, the lags and coherence were above the noise level for 0.2–2 Hz band in LS. The integrated lag and coherence values in this band for all the LS observations are given in Table 4.12. For the first three observations in the LS, the integrated lag increases with increasing energy band interval. This is consistent with the expectations in a system with thermal Comptonization.

4.5.3 Summary

GX 339−4 is a well studied and important source. The frequent radio monitoring led to an establishment of the relation between hard X-rays and radio, which perhaps has common features in all black hole systems. My analysis showed that a transition to the LS occurred from the TS. The evolution after the transition was similar to other sources, as the peak frequencies decreased, the rms amplitude increased and

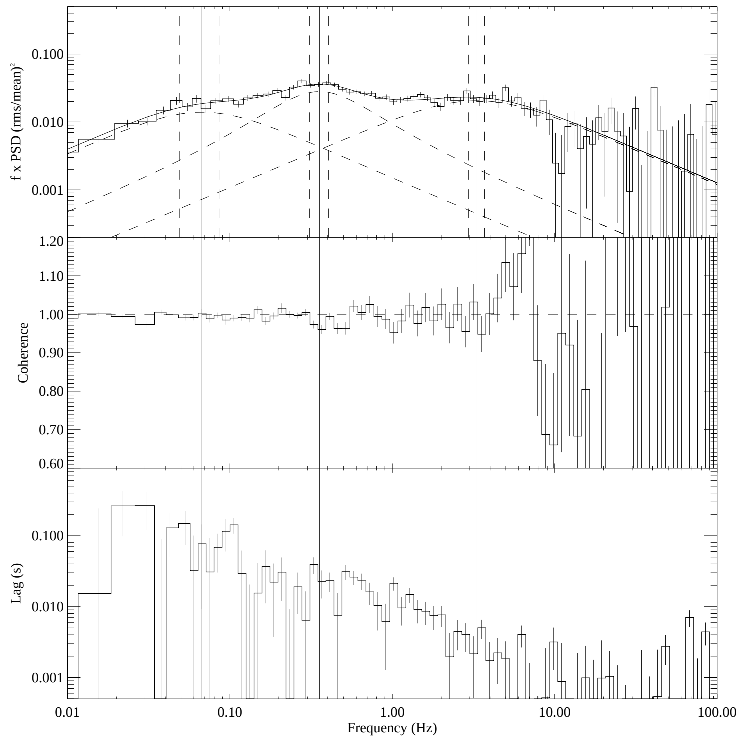

Figure 4.23: Frequency dependent coherence and lags for observation 5. The top panel is the PSD in E2. The middle panel is the coherence function and the bottom panel is the lag. The vertical solid lines are the peak frequencies and the dashed lines are the errors in peak frequencies. The horizontal dashed line in the middle panel indicates the unity coherence.

the power-law component in the X-ray spectrum hardened. Unfortunately, the coverage was sparse, and detailed evolution at the state transition was missed. The energy dependent PSD analysis showed that the TS observations have strong energy dependence such that the rms increases with energy. Neither in the TS nor in the LS the peak frequencies change substantially with energy. The frequency dependent coherence and lag measurements did not show any dependence on the position of Lorentzian components in the PSD fits. At the TS, the integrated lags are much higher and the mean coherence is much lower than that of LS observations.

Table 4.13 characterizes the physical properties of XTE J1650−500 during the state transition.

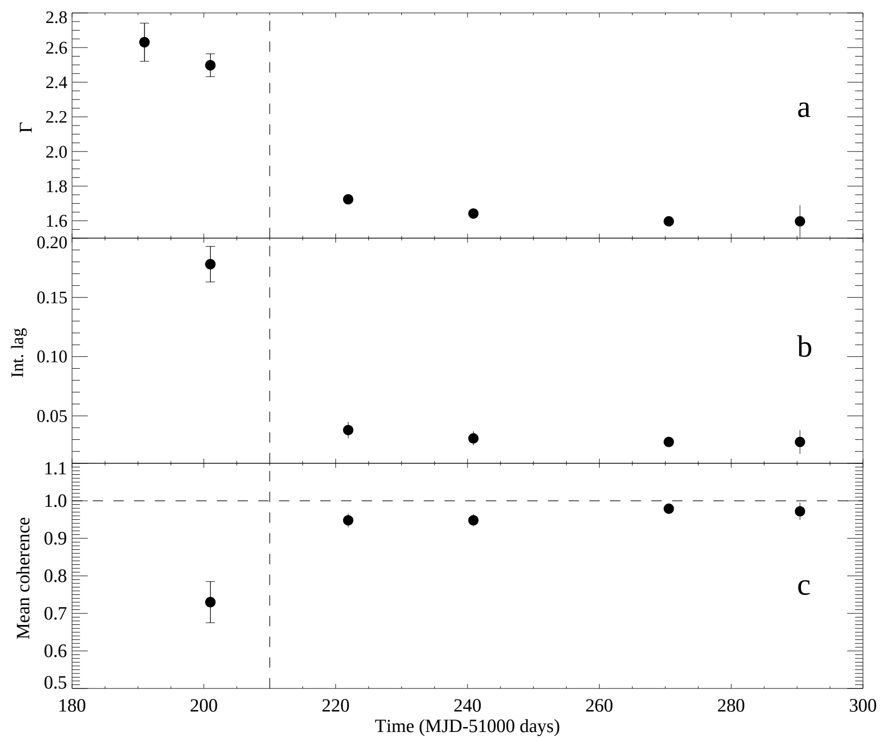

Figure 4.24: The evolution of mean coherence and integrated lag of GX 339−4. (a) Spectral index. (b) Integrated lag in 1–10 Hz band between E1 and E2. (c) Mean coherence, same frequency and energy bands as lag. The horizontal dashed line is unity coherence. The vertical dashed line separates the TS and LS observations.

Table 4.10: Temporal fit parameters of GX 339−4.

Broad Lorentzians

Obs	ν_1	rms 1 (%)	ν_2	rms 2 (%)	ν_3	rms 3 (%)	total rms (%)
1	0.015 ± 0.005	2.30 ± 0.39	1.104 ± 0.023	7.53 ± 0.10	-	-	7.88 ± 0.21
2	0.016 ± 0.001	3.71 ± 0.09	2.676 ± 0.062	10.98 ± 0.08	-	-	11.81 ± 0.12
3	0.196 ± 0.031	13.11 ± 1.53	1.288 ± 0.290	21.07 ± 4.17	8.206 ± 2.136	12.66 ± 2.56	28.51 ± 5.10
4	0.166 ± 0.008	22.89 ± 0.62	0.599 ± 0.021	15.93 ± 0.32	3.743 ± 0.131	21.33 ± 0.33	35.11 ± 0.75
5	0.125 ± 0.005	25.80 ± 0.03	0.404 ± 0.001	14.45 ± 0.03	2.946 ± 0.005	24.31 ± 0.02	38.73 ± 0.05
6	0.053 ± 0.011	28.74 ± 2.99	0.180 ± 0.017	15.28 ± 2.27	0.427 ± 0.122	16.77 ± 2.95	-
6[a]	2.491 ± 0.172	27.27 ± 1.15	-	-	-	-	45.66 ± 4.46

QPO parameters

Obs	ν_1	rms 1 (%)	FWHM 1 (Hz)	ν_2	rms 2 (%)	FWHM 2 (Hz)
2	8.158 ± 0.043	2.25 ± 0.17	0.518 ± 0.473	-	-	-
3	0.732 ± 0.016	2.87 ± 0.83	0.072 ± 0.045	1.39 ± 0.03	5.38 ± 1.30	0.333 ± 0.130
5	0.272 ± 0.005	4.84 ± 0.05	0.020 ± 0.005	0.630 ± 0.013	3.32 ± 0.03	0.040 ± 0.007

[a] Fourth Lorentzian

Table 4.11: Energy dependent temporal fit parameters of GX 339−4.

Obs/band	ν_1	rms 1 (%)	ν_2	rms 2 (%)	ν_3	rms 3 (%)	total rms (%)
1/E1	0.022^{a}	2.24 ± 0.25	1.104 ± 0.041	5.69 ± 0.17	-	-	6.12 ± 0.20
1/E2	0.022 ± 0.008	3.50 ± 0.38	1.146 ± 0.029	14.10 ± 0.42	-	-	14.53 ± 0.47
2/E1	0.003 ± 0.001	3.62 ± 0.07	2.881 ± 0.039	10.27 ± 0.04	-	-	10.89 ± 0.08
2/E2	0.016 ± 0.001	5.89 ± 0.03	2.604 ± 0.014	14.61 ± 0.04	-	-	17.12 ± 0.057
3/E1	0.207 ± 0.003	15.47 ± 0.06	1.289 ± 0.014	21.94 ± 0.09	8.504 ± 0.310	15.54 ± 0.17	31.01 ± 0.20
3/E2	0.207 ± 0.022	13.53 ± 0.65	1.372 ± 0.163	20.15 ± 1.10	7.520 ± 1.388	11.41 ± 1.04	26.82 ± 1.60
3/E3	0.246 ± 0.047	12.64 ± 1.00	1.461 ± 0.263	16.71 ± 1.32	6.936 ± 0.855	11.56 ± 1.20	23.93 ± 2.03
4/E1	0.145 ± 0.005	22.47 ± 0.28	0.577 ± 0.014	18.11 ± 0.15	3.778 ± 0.138	22.71 ± 0.24	36.73 ± 0.40
4/E2	0.162 ± 0.005	21.65 ± 0.25	0.603 ± 0.014	17.20 ± 0.13	4.074 ± 0.119	20.03 ± 0153	34.14 ± 0.31
4/E3	0.155 ± 0.013	20.87 ± 0.88	0.613 ± 0.039	15.16 ± 0.61	3.275 ± 0.464	22.22 ± 1.47	34.05 ± 1.76
5/E1	0.074 ± 0.017	21.63 ± 3.10	0.371 ± 0.034	23.49 ± 1.42	3.156 ± 0.188	23.43 ± 0.78	39.61 ± 3.02
5/E2	0.067 ± 0.018	20.00 ± 2.74	0.356 ± 0.047	23.36 ± 1.82	3.323 ± 0.370	24.76 ± 2.68	39.48 ± 4.16
5/E3	0.074 ± 0.008	20.75 ± 0.96	0.350 ± 0.021	21.53 ± 0.57	3.370 ± 0.392	25.99 ± 1.52	39.62 ± 1.82
6/E1	0.033 ± 0.014	20.13 ± 4.73	0.173 ± 0.029	29.78 ± 3.96	2.535 ± 0.236	28.28 ± 1.98	45.74 ± 5.95
6/E2	0.029 ± 0.012	17.73 ± 4.24	0.176 ± 0.020	33.15 ± 3.71	2.564 ± 0.248	25.53 ± 1.17	45.44 ± 5.09
6/E3	0.034 ± 0.013	30.32 ± 5.40	0.188 ± 0.051	41.16 ± 5.67	2.640 ± 0.977	38.26 ± 4.93	63.85 ± 9.18

a Zero centered Lorentzian, peak frequency fixed to E2 band value

Table 4.12: Energy dependence of integrated lag and mean coherence of GX 339−4.

	E2 vs E1		E3 vs E1	
Obs	Int. Lag	Mean Coherence	Int. Lag	Mean Coherence
3	0.038 ± 0.007	0.977 ± 0.010	0.087 ± 0.019	0.881 ± 0.038
4	0.031 ± 0.006	0.978 ± 0.005	0.062 ± 0.012	0.935 ± 0.015
5	0.028 ± 0.004	0.989 ± 0.031	0.062 ± 0.010	0.954 ± 0.013
6	0.028 ± 0.010	0.988 ± 0.009	0.058 ± 0.019	0.921 ± 0.039

Table 4.13: GX 339−4

Name :	GX 339−4
Mass :	-
Distance :	∼4 kpc
Gal. Coord. :	338.9, -4.3
N_H :	$0.6 \times 10^{22}\,\mathrm{cm}^{-2}$ [a]
Peak Flux[b] :	9.5
Peak Luminosity :	1.82 [c]
For the first LS observation:	
Flux :	0.9
Luminosity :	0.17
τ :	1.72
T_{in} :	-
power-law flux :	0.87

a From Nowak, Wilms & Dove (2002).
b All fluxes in this table are in 1.5-12 keV band, in units of $10^{-9}\,\mathrm{ergs\,cm^{-2}\,s^{-1}}$
c All luminosities in this table are in 1.5-12 keV band, in units of $10^{37}\,\mathrm{ergs\,s^{-1}}$

4.6 4U 1630−47

4U 1630−47 was discovered by the *Uhuru* mission (Jones et al. 1976). It lies in the general direction of the Galactic center, and is heavily absorbed in X-rays, indicating a large ($\geq$ 10 kpc) distance within the disk of our Galaxy (Cui, Chen & Zhang 2000). No optical counterpart has been discovered, and therefore the mass has not been determined dynamically. The X-ray properties are very similar to other black hole systems (Cui, Chen & Zhang 2000). Although it is a transient source, it shows frequent outbursts, with a period of ∼600 days (Kuulkers et al. 1997), however a strict regularity was ruled out by observations of several out of phase outbursts (McCollough et al. 1999). The absorption dips observed in 1996 and 1998 outburst led to a suggestion of a high (60°–75°) inclination angle (Dieters et al. 2000, and references therein).

The radio observations during the 1996 outburst did not yield a measurable radio flux. It was first detected in radio during the 1998 outburst, and the spectrum indicated an optically thin synchrotron emission throughout the outburst. The radio emission was linearly polarized (Hjellming et al. 1999).

4.6.1 1996 outburst

The 1996 outburst of 4U 1630−47 was covered with *RXTE* with 16 observations, and up to date there have been no publications on the temporal properties of this outburst. A detailed spectral study, concentrating on the iron line emission was published by Cui, Chen & Zhang (2000). The X-ray spectrum was fitted with the usual diskbb and a power-law, and the results indicate that there was never a transition to the LS since the power-law indexes are always greater than 3. To be sure, I analyzed the timing properties of five observations during the decay in 2–13 keV band. The PSDs were almost identical and fitted with a power-law of index ∼-0.9 and showed an 0.01-10 Hz rms amplitude of ∼7%. These PSD properties are consistent with HS, and due to lack of state transition I did not do any further timing analysis.

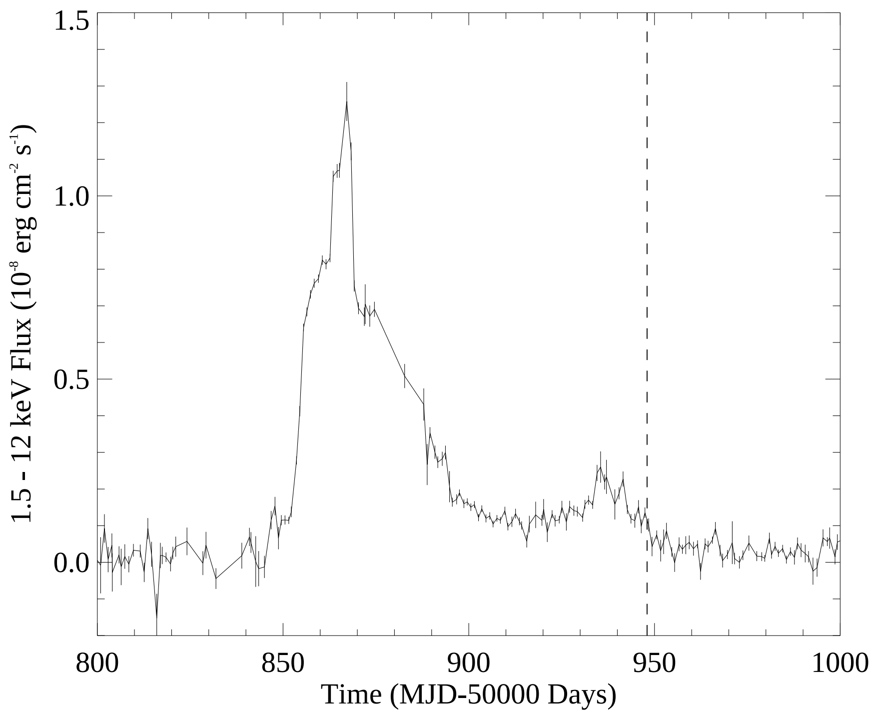

Figure 4.25: ASM light curve of 4U 1630−47 during the 1998 outburst. The dashed line indicates the time of transition to the LS.

4.6.2 1998 outburst

The 1998 outburst was first detected by BATSE on MJD 50481, and later was confirmed by the ASM on *RXTE* (Kuulkers et al. 1998). The ASM flux increased rapidly, decayed, and showed a secondary maximum as seen in Fig. 4.25. After the secondary maximum, it decayed to quiescence, and during this decay a transition to the LS occurred (Tomsick & Kaaret 2000). The spectral and temporal evolution of the 1998 outburst were analyzed extensively using *RXTE* data by Dieters et al. (2000) for the rise and the top, and Tomsick & Kaaret (2000) for the decay of the outburst. This outburst was well covered in other X-ray bands too, by *ROSAT*, *Beppo*SAX (Oosterbroek et al. 1998), by BATSE and in radio (Hjellming et al. 1999).

Observations and Analysis

Detailed temporal and spectral analysis of the outburst during the decay were done by Tomsick & Kaaret (2000). I only analyzed the coherence, lags and energy

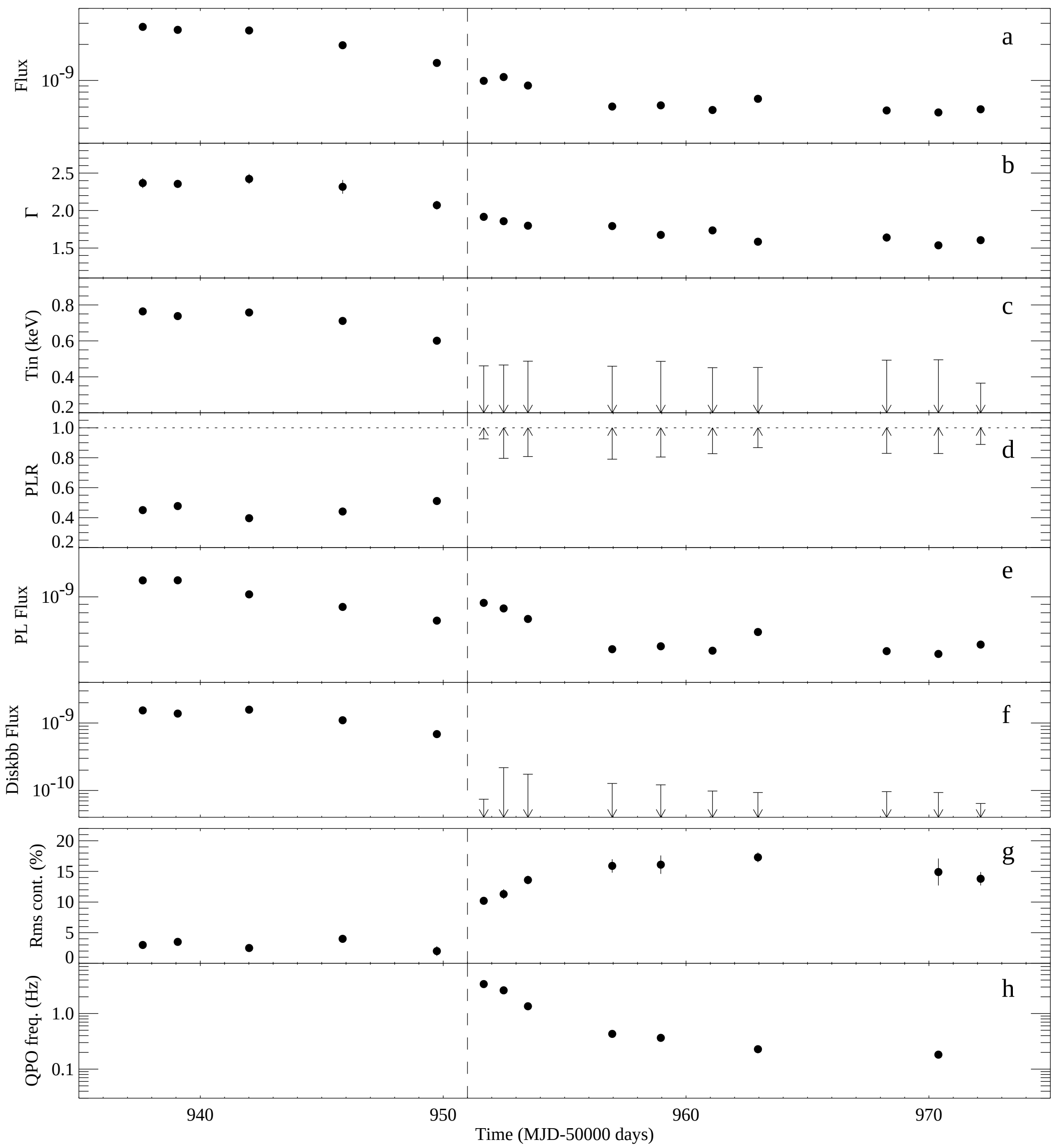

Figure 4.26: Spectral and temporal evolution of 4U 1630−47 around and after the state transition for the 1998 outburst. (a) 2.5–20 keV flux in units of ergs $\mathrm{cm}^{-2}\,\mathrm{s}^{-1}$. (b) Power-law index. (c) Inner disk temperature (d) PLR, the ratio of power-law flux to total flux in 2.5–20 keV band. (e) Power-law flux. (f) Diskbb flux. (g) Rms amplitude of the PSD continuum. (h) QPO frequency. The vertical dashed line indicates the date of state transition. All values are from Tomsick & Kaaret (2000).

dependence of the PSD which were not discussed in Tomsick & Kaaret (2000). I used the 2–5 (E1) and 5–13 keV (E2) bands for the cross-spectral and the PSD analysis. I have not done any spectral analysis, and used directly the results from Tomsick

& Kaaret (2000), Table 5, where a diskbb, power-law, a narrow emission line and a broad absorption edge were used. Unfortunately, the statistics were not good enough to do either frequency dependent or band limited cross spectral studies.

Spectral and temporal evolution

Fig. 4.26 summarizes the evolution of spectral and temporal parameters of 4U 1630−47 around and after the state transition. The flux (a) gradually decreases, as the power-law index (b) decreases (spectrum gets harder). The change in temporal properties and the diskbb component in the X-ray spectrum is much more abrupt during the state transition. Before the transition, the inner disk temperature (c) is around 0.8 keV, and after the transition the diskbb component is not required in the fit. This also reflects in the PLR (d, ratio of the power-law flux to total flux in 2.5–20 keV band) as it jumps to more than 0.8 after the state transition from values of around 0.4 before the state transition. The power-law flux (e) shows a slight increase at the transition, then declines, and the diskbb flux (f) drops sharply after the transition. The rms amplitude of the PSD (g) jumps from $\sim$3% before the transition to 10% and more after the transition. The transition is also accompanied with the appearance of a QPO at 3.4 Hz. As the rms amplitude increases the QPO frequency (h) decreases, as usual for black hole transients during the decay.

Temporal fits and energy dependence of PSD components

I fit the PSDs of all 8 observations that show significant variability in E1 and E2. All observations, except the last one are modeled with a broad Lorentzian for the continuum and a QPO (see Table 4.14). Although this model is different from what Tomsick & Kaaret (2000) used (the FT model, see section 1.5.2), the break frequency of the FT model and the peak frequency of the Lorentzian are usually close to each other and can be compared. For this reason, I have not worked on fitting of the combined band PSD, since the fit results can be found in Tomsick & Kaaret (2000). Except for observation 2, the peak frequencies do not change with energy. The rms amplitude of the Lorentzians increase with energy. Similarly, the QPO rms amplitude also increases with energy, but the QPO frequencies remain constant.

Table 4.14: Temporal fit parameters of 4U 1630−47 during the 1998 outburst

	Broad Lorentzian		QPO			
Obs/Band	ν_1 (Hz)	rms 1 (%)	ν_{QPO} (Hz)	$\mathrm{FHWM_{QPO}}$ (Hz)	$\mathrm{rms_{QPO}}$ (%)	rms total (%)
1/E1[a]	3.836 ± 0.562	11.96 ± 0.67	3.380 ± 0.588	0.148 ± 1.094	5.84 ± 0.54	13.31 ± 0.72
1/E2[b]	4.235 ± 0.337	12.70 ± 0.40	3.427 ± 0.366	0.267 ± 0.673	8.84 ± 0.26	15.47 ± 0.45
2/E1	0.655 ± 0.057	8.61 ± 0.24	2.658 ± 0.047	0.444 ± 0.113	7.25 ± 0.23	11.25 ± 0.33
2/E2	3.540 ± 0.247	16.45 ± 0.44	2.612 ± 0.260	0.188 ± 0.488	10.43 ± 0.36	19.47 ± 0.61
3/E1	3.016 ± 0.743	14.02 ± 2.52	1.312 ± 1.511	0.174 ± 1.465	6.70 ± 1.00	15.54 ± 2.82
3/E2	3.140 ± 0.028	16.33 ± 0.05	1.391 ± 0.025	0.321 ± 0.057	10.53 ± 0.04	19.43 ± 0.08
4/E1	1.187 ± 0.350	12.02 ± 1.49	0.427 ± 0.232	0.109 ± 0.601	6.64 ± 1.99	13.73 ± 2.23
4/E2	0.882 ± 0.204	17.79 ± 1.15	0.432 ± 0.155	0.067 ± 0.318	7.10 ± 1.35	19.15 ± 1.64
5/E1	0.922 ± 0.197	13.41 ± 1.04	0.372 ± 0.194	0.073 ± 0.388	4.63 ± 1.01	14.18 ± 1.41
5/E2	1.474 ± 0.156	17.78 ± 0.60	0.370 ± 0.123	0.199 ± 0.308	10.09 ± 0.62	20.44 ± 0.88
6/E1	0.887 ± 0.058	13.93 ± 0.31	0.237 ± 0.052	0.022 ± 0.117	4.91 ± 0.24	14.77 ± 0.41
6/E2	0.713 ± 0.067	18.34 ± 0.85	0.225 ± 0.081	0.063 ± 0.130	5.82 ± 1.01	19.25 ± 1.07
7/E1	0.857[c]	< 11.21	0.176 ± 0.089	0.008 ± 0.262	5.43 ± 7.80	< 12.45
7/E2	0.857 ± 0.012	18.09 ± 0.10	0.187 ± 0.009	0.043 ± 0.025	8.42 ± 0.10	19.95 ± 0.14
8/E1	-	-	-	-	-	-
8/E2	0.646 ± 0.088	17.79 ± 0.86	-	-	-	17.79 ± 0.86

a E1:2–5 keV band
b E2:5–13 keV band
c Fixed to E2 value

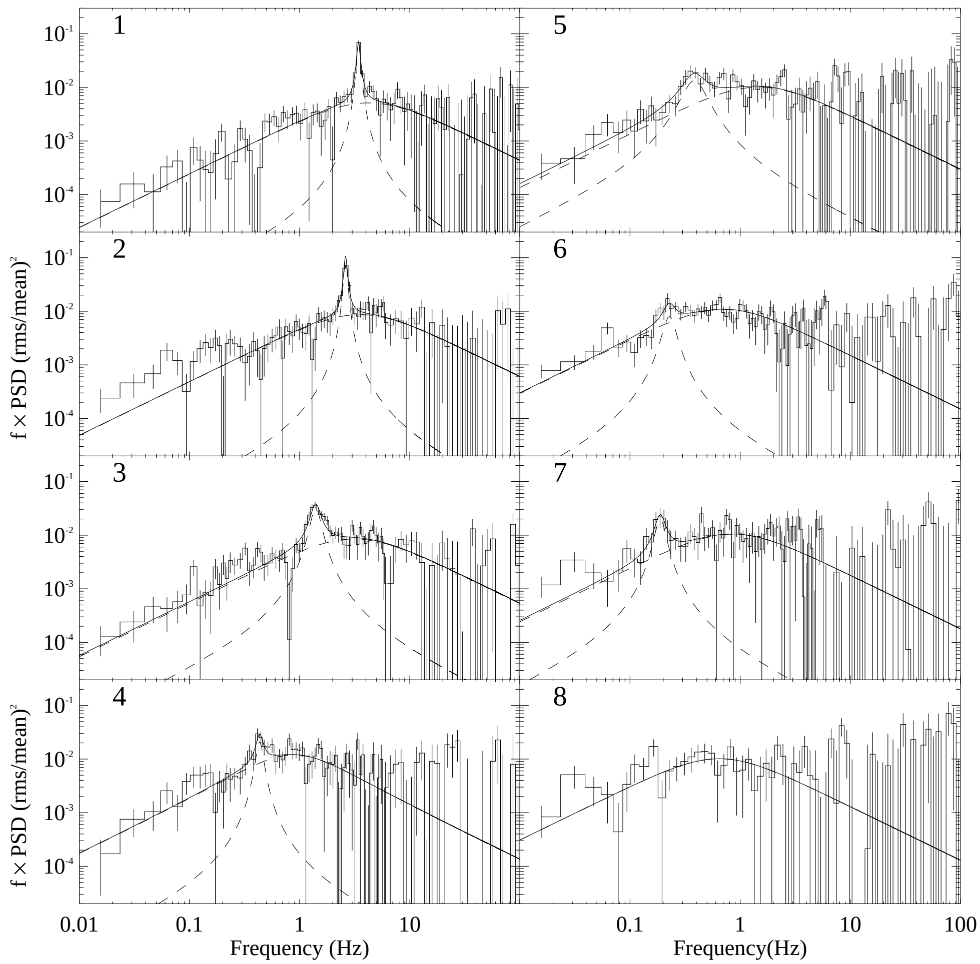

Figure 4.27: Lorentzian fits to all observations that show significant variability during the decay. The solid curve is the overall fit and the dashed curves are individual Lorentzian components. The solid vertical lines indicate peak frequencies while the dashed vertical lines show their errors.

Both the QPO frequencies and peak frequencies decrease during the decay. Fig. 4.27 shows the Lorentzian fits in E2 which show the decay of the characteristic frequencies.

Summary

4U 1630−47 is the first source that has been analyzed in detail with very good coverage during the state transition (Tomsick & Kaaret 2000). This evolution of spectral and temporal parameters can be summarized as the hardening of the power-law index, and the decreasing of inner disk temperature leading to the transition to

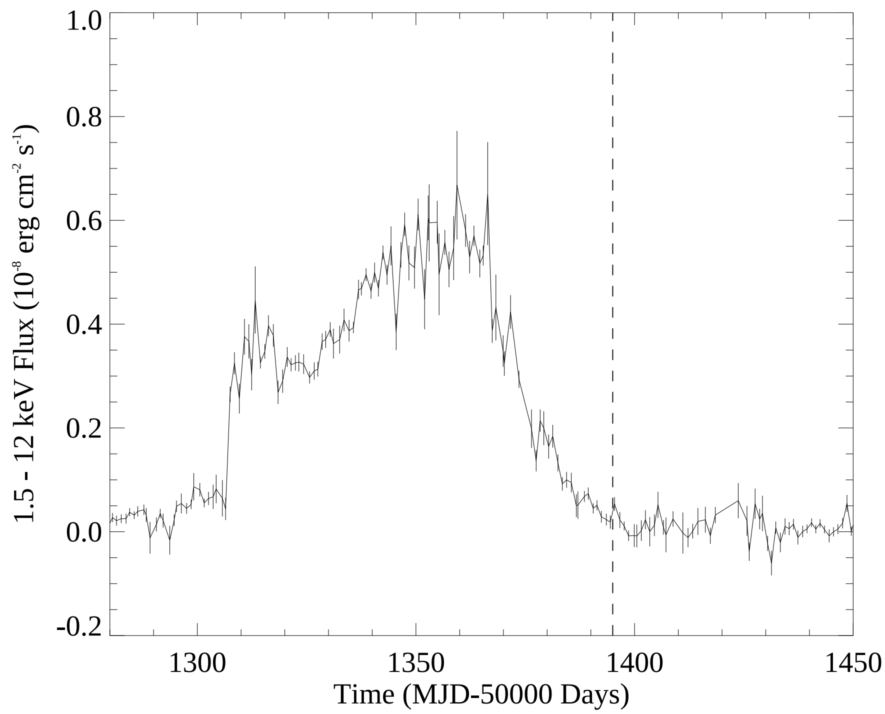

Figure 4.28: ASM light curve of 4U 1630−47 for the 1999 outburst. The dashed line indicates the time of transition to the LS.

the LS. The transition is marked by the appearance of a strong band limited noise component in the PSD and a QPO. For the following observations the QPO frequency and the characteristic frequencies of the continuum decreased. The rms amplitudes increase with energy and the peak frequencies do not show any dependence on energy. Due to poor statistics, it was not possible to do cross spectral studies.

4.6.3 1999 outburst

This out of phase outburst was detected by BATSE on May 7, 1999 (McCollough et al. 1999). The *RXTE* ASM light curve is shown in Fig. 4.28. Although many pointed observations were done with *RXTE*, no analysis has been reported from this outburst. During the 1999 outburst, 4U 1630−47 was observed with the *IXAE, Indian X-ray Astronomy Experiment* on board the *IRS P-3* satellite, and a very hard spectrum (power-law index 1.7) was measured during the peak, unlike the other outbursts (Abraham et al. 2001). During the rise, 4U 1630−47 was found to be in the LS with a QPO present (McCollough et al. 1999). My analysis, which will be discussed in detail in the following sections show that a transition to the LS happened on 1999 August 5 (MJD 51395).

Observations and analysis

Since this outburst's *RXTE* data were never analyzed before, I first located the time of the state transition by investigating the PSDs of all observations during the outburst decay. Once I found significant variability, I made detailed spectral and temporal analysis of the observations before and after the transition. For the spectral analysis, I used a model consisting of a diskbb and a power-law and a narrow iron line. Only two observations showed variability, and only in 2–15 keV band. So neither energy dependence of variability studies nor cross spectral studies were possible with this outburst.

Spectral evolution

As mentioned earlier, a spectral model consisting of a diskbb, a power-law, and a Gaussian for the iron line has been used. 4U 1630−47 is heavily absorbed, and for absorption a hydrogen column density of $N_H = 9.435 \times 10^{22}\,\mathrm{cm}^{-2}$ was used as initial value following Tomsick & Kaaret (2000). This parameter was frozen for some of the observations. The iron line width was frozen to 0 for most of the observations, otherwise the fit would find a minimum χ^2 with very large widths. The iron line parameters are not interesting for my work and are not going to be discussed further. The most important fit components are the diskbb and the power-law, and the fit results for these components are summarized in Table 4.15, and shown in Fig. 4.29. The galactic ridge emission is strong where 4U 1630−47 is located, and it is possible that it is affecting the X-ray spectrum at very low flux-level observations (8, 9, 10 in Table 4.15). Only two observations showed PSD above the noise level. The first one marks the transition to the LS (observation 6, first observation after the dashed line in Fig. 4.29.

Fig. 4.29 shows the evolution of 4U 1630−47 around the state transition during the decay. The flux (a) decreased smoothly. The hardening of the X-ray spectrum

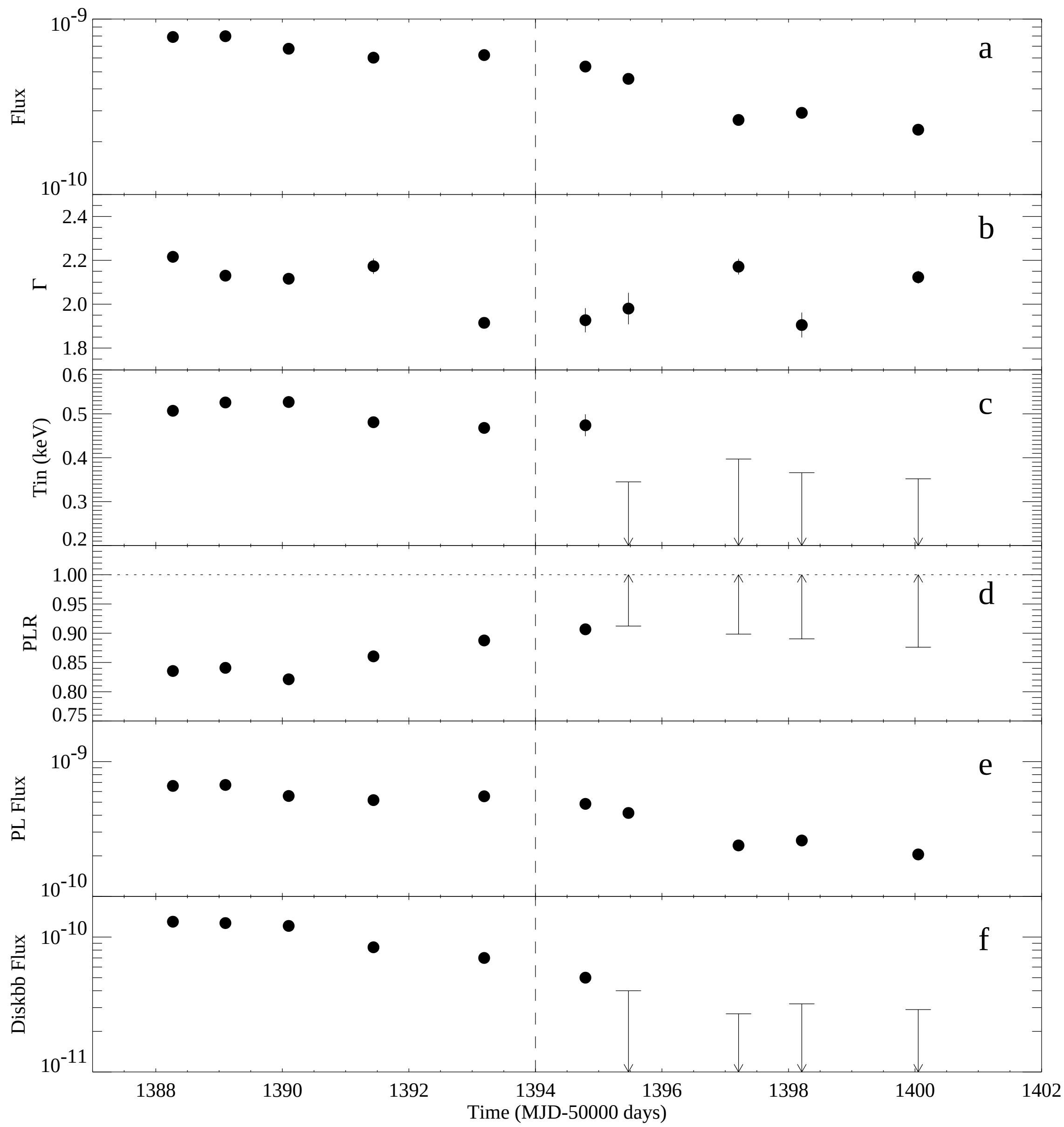

Figure 4.29: Spectral evolution of 4U 1630−47 around and after the state transition for the 1999 outburst. (a) 2.5–20 keV flux in units of $\mathrm{ergs\,cm^{-2}\,s^{-1}}$. (b) Power-law index. (c) Inner disk temperature (d) PLR, the ratio of power-law flux to total flux in 2.5–20 keV band. (e) Power-law flux. (f) Diskbb flux. The vertical dashed line indicates the date of state transition.

(decrease in the spectral index) happened one or two days before the appearance of the timing noise. The sharpest change happened in the inner disk temperature (c), where it dropped from level of 0.5 keV to level of 0.35 keV one day after the transition. The PLR (d) had its largest value around the state transition. The power-law flux

Table 4.15: Spectral fit parameters of 4U 1630−47 in the 1999 outburst.

Obs	Date[a]	Γ	T_{in} keV	power-law flux [b]	Total flux
1	1388.27	2.216 ± 0.023	0.507 ± 0.012	0.660	0.790
2	1389.10	2.130 ± 0.018	0.526 ± 0.010	0.671	0.798
3	1390.10	2.216 ± 0.022	0.527 ± 0.012	0.556	0.677
4	1391.44	2.173 ± 0.035	0.481 ± 0.010	0.518	0.602
5	1393.19	1.915 ± 0.016	0.468 ± 0.011	0.553	0.623
6[c]	1394.79	1.927 ± 0.055	0.474 ± 0.025	0.486	0.536
7	1395.47	1.980 ± 0.072	0.345 ± 0.020	0.416	0.456
8	1397.21	2.171 ± 0.036	0.397 ± 0.020	0.239	0.266
9	1398.21	1.905 ± 0.057	0.366 ± 0.014	0.260	0.292
10	1400.05	2.123 ± 0.029	0.352 ± 0.004	0.205	0.234

a MJD-50000 days
b All fluxes in this table are in 2.5–20 keV band in units of $10^{-9}\,\mathrm{ergs\,cm^{-2}\,s^{-1}}$
c Variability observed in this observation.

(e) did not show a sharp change, and the diskbb flux (f) dropped sharply after the state transition.

The temporal properties of observations 6 and 7, the only observations that showed variability, were analyzed in detail. The variability was only significant in the combined band of 3–15 keV for both cases. I modeled the PSDs with a broad Lorentzian and a QPO, however the QPOs were not statistically significant. For observation 6, the broad Lorentzian had a peak frequency of 4.090 ± 0.089 Hz and an rms amplitude of 11.77 ± 2.58 %. The QPO was at 1.820 ± 0.004 Hz, with a Q value of 7.97 and an rms amplitude of 4.21 ± 1.38 %. For observation 7, the broad Lorentzian had a peak frequency of 0.603 ± 0.517 Hz and an rms amplitude of 7.12 ± 3.08 %. The QPO was at 0.782 ± 0.083 Hz, with a Q value of 2.91 and an rms amplitude of 4.74 ± 1.52 %. The peak and QPO frequency decreased as flux decreased.

Summary

The evolution of the spectral parameters into the state transition is similar to other sources. The power-law index hardens, the hardness ratio consequently increases and the inner disk temperature decreases. The state transition is again marked by the appearance of band limited noise, and possible QPOs for two observations where

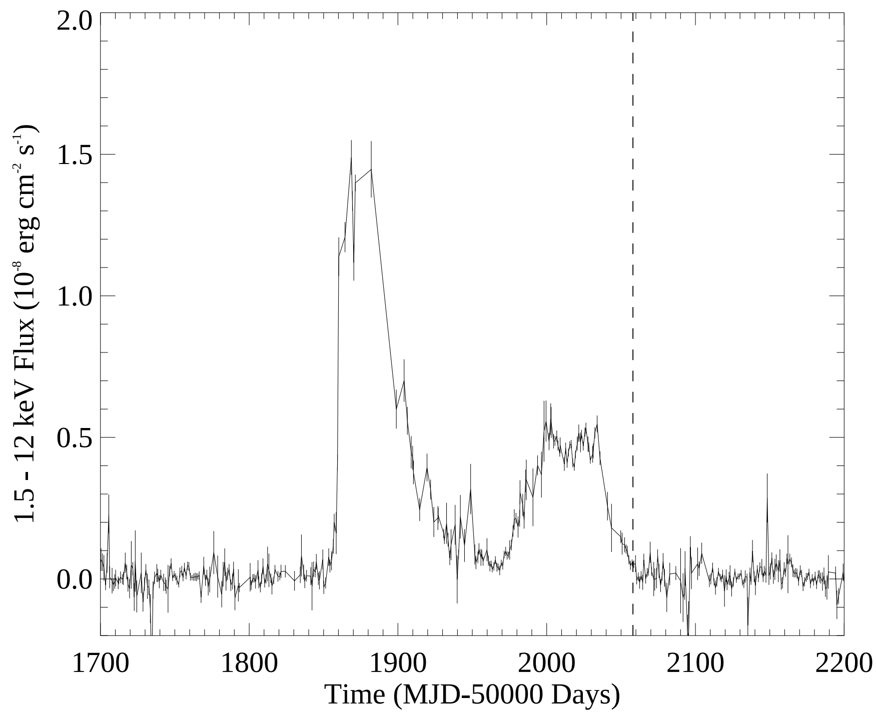

Figure 4.30: ASM light curve of 4U 1630−47 for the 2001 outburst. The dashed line indicates the time of transition to the LS.

there were enough statistics to do timing analysis. The QPO frequency and the peak frequency of the Lorentzian component decrease as the flux decrease. It was possible to do neither energy dependent PSD nor cross spectral analysis due to poor statistics.

4.6.4 2001 outburst

The *RXTE* ASM light curve of 4U 1630−47 (Fig. 4.30) showed that it was increasing rapidly on MJD 51860. We triggered our *RXTE* observations on MJD 51917, during the decay. It did not show any state transition during this decay, and re-flared for a secondary maxima. Subsequent analysis of the final decay, which is discussed in detail in the following sections show that a transition to the LS happened on May 30, 2001 (MJD 51395).

Table 4.16: Spectral fit parameters of 4U 1630−47 in the 2001 outburst.

Obs	Date[a]	Γ	T_{in} keV	power-law flux [b]	Total flux
1	2047.96	2.217 ± 0.035	0.785 ± 0.010	1.117	1.970
2	2049.75	2.232 ± 0.030	0.704 ± 0.009	0.958	1.521
3	2051.63	2.260 ± 0.026	0.674 ± 0.010	0.929	1.326
4	2053.79	2.094 ± 0.020	0.593 ± 0.009	0.867	1.118
5	2055.58	2.225 ± 0.037	0.544 ± 0.016	0.630	0.815
6	2057.96	1.969 ± 0.031	0.462 ± 0.010	0.693	0.786
7[c]	2059.38	1.579 ± 0.014	0.398 ± 0.006	0.745	0.799
8	2061.63	1.705 ± 0.026	0.436 ± 0.013	0.332	0.375
9	2063.58	1.745 ± 0.038	0.450 ± 0.027	0.263	0.297
10	2065.92	1.694 ± 0.033	0.433 ± 0.019	0.274	0.302
11	2067.88	1.545 ± 0.046	0.434 ± 0.025	0.225	0.256

a MJD-50000 days
b All fluxes in this table are in 2.5–20 keV band in units of $10^{-9}\,\mathrm{ergs\,cm^{-2}\,s^{-1}}$
c QPO and strong band limited noise observed in this observations.

Observations and analysis

Since this outburst's *RXTE* data were never analyzed before, I first located the time of state transition by investigating the PSD of all observations during the outburst decay. Once I found significant variability, I made detailed spectral and temporal analysis of the observations before and after the transition. For the spectral analysis, I used a model consisting of a diskbb, a power-law and a smeared edge (smedge), and a Gaussian for a narrow iron line when necessary. For absorption a hydrogen column density of $N_H = 9.435 \times 10^{22}\,\mathrm{cm^{-2}}$ was used and kept frozen following Tomsick & Kaaret (2000).

Spectral evolution

The most important fit components are the diskbb and power-law, and the fit results regarding these components are summarized in Table 4.16, and also used in Fig. 4.31. The galactic ridge emission is strong where 4U 1630−47 is located, and possibly affecting the X-ray spectrum at very low flux level observations (8, 9, 10 in Table 4.16).

Fig. 4.31 shows the evolution of 4U 1630−47 around the state transition during

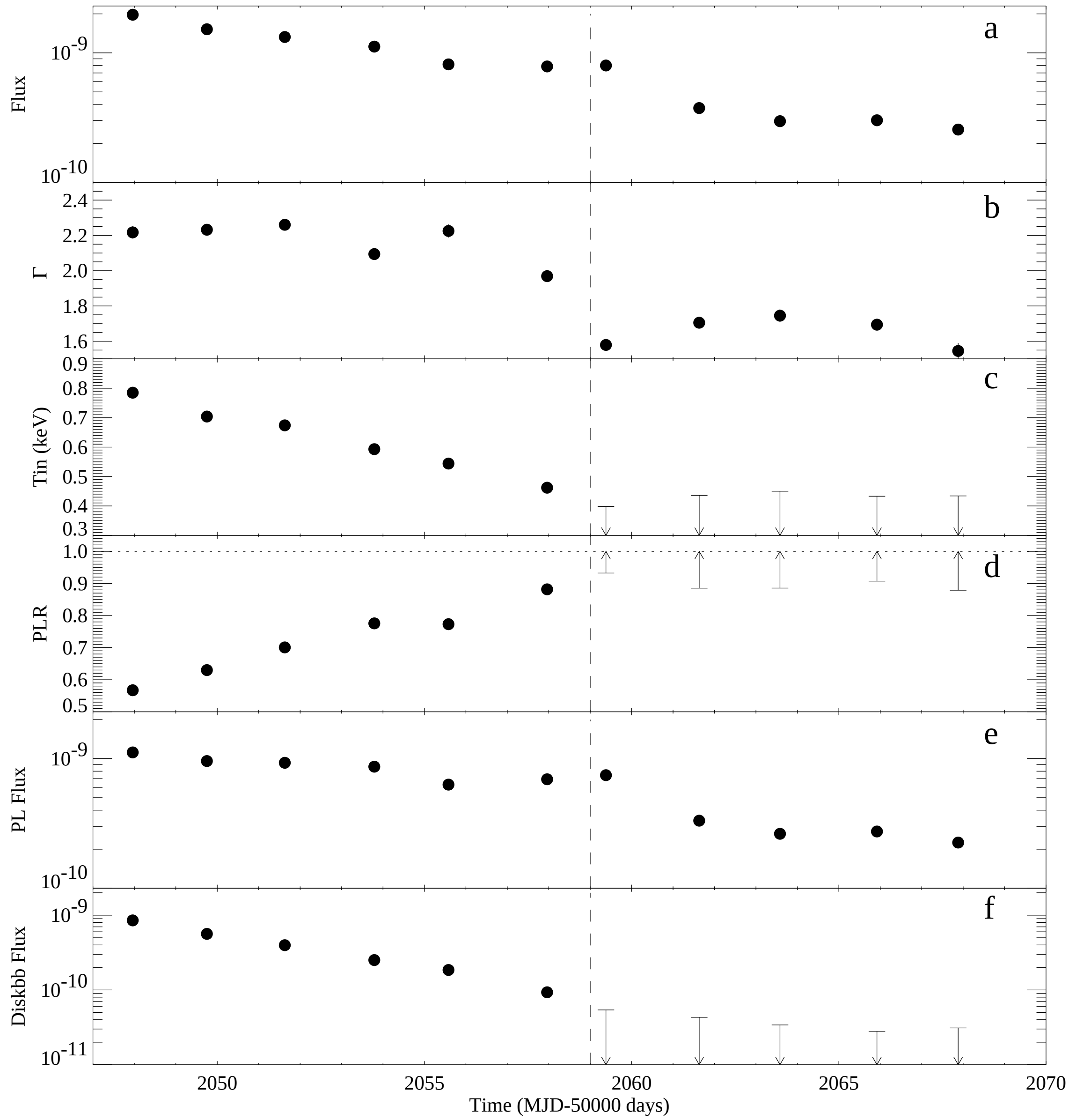

Figure 4.31: Spectral evolution of 4U 1630−47 around and after the state transition for the 2001 outburst. (a) 2.5–20 keV flux in units of $\mathrm{ergs\,cm^{-2}\,s^{-1}}$. (b) Power-law index. (c) Inner disk temperature (d) PLR, hardness ratio, the ratio of power-law flux to total flux in 2.5–20 keV band. (e) Power-law flux. (f) Diskbb flux. The vertical dashed line indicates the date of state transition.

the decay. The flux (a) decayed smoothly until the state transition, and after showed a sharp drop. The power-law index (b) started to decrease three days before the appearance of the timing noise, and showed a big jump just before the transition. The inner disk temperature (c) decreased gradually from 0.8 keV to 0.4 keV in 11 days. It was not detected after the transition. PLR (d) showed a gradual increase until the time of transition. The power-law flux (e) showed a drop after the state transition. The diskbb flux (f) showed a smooth monotonous decay until the state transition.

Temporal fits

Since the transition happened at very low flux, the statistics were not good enough to do extensive energy dependent timing analysis. Only two observations showed broad band timing noise (observations 7 and 8), and the first one had a QPO. The PSD and Lorentzian fits for these observations can be seen in Fig. 4.32.

Observation 7 requires a broad Lorentzian and a QPO to fit the PSD. The broad Lorentzian has a peak frequency at 2.52 ± 1.07 Hz and an rms amplitude of $10.26 \pm 2.61\%$. The QPO is at 1.396 ± 0.042 Hz, has an rms amplitude of $5.57 \pm 1.15\%$ and a Q value of 4.8. The energy dependent PSD analysis resulted in too large of errors in fit parameters to make any conclusions. Observation 8 PSD is fitted with one broad Lorentzian at a peak frequency of 0.297 ± 0.069 and has an rms amplitude of $9.32 \pm 0.75\%$. There was no observation of a QPO with an 90% confidence rms upper limit of 2.2% in 0.01–0.3 Hz band with a Q value of 5.

Summary

This outburst bears similarities to the 1999 outburst. The power-law index hardens, PLR increases and the inner disk temperature decreases as the source evolves to the state transition, as the 1999 outburst. The peak frequency of the broad Lorentzian decreased with decreasing flux. Again, it was possible to do neither energy dependent PSD nor cross spectral analysis due to poor statistics.

4.6.5 Overall summary for 4U 1630−47

4U 1630−47 is an important source for my analysis with its multiple outbursts and very good coverage with *RXTE*. It allows me to do comparative studies between outburst decays from the same source which is presented in Chapter 5. The overall evolution of spectral and temporal parameters are similar for all outbursts: as the

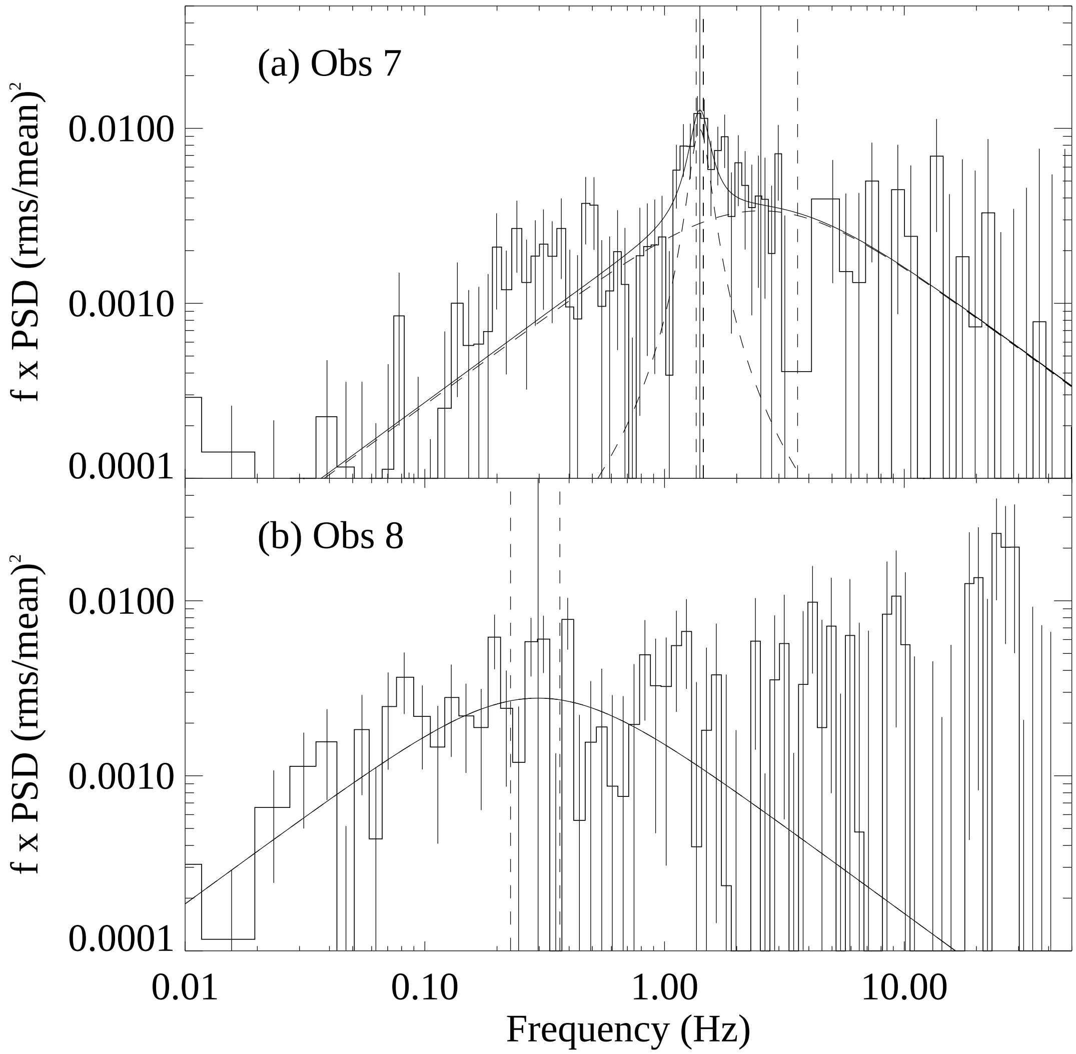

Figure 4.32: Lorentzian fits to (a) observation 7 and (b) observation 8. The solid curve is the overall fit and the dashed curves are individual Lorentzian components. The solid vertical lines indicate peak frequencies while the dashed vertical lines show their errors.

flux decreases the power-law index hardens and the inner disk temperature decreases. At the state transition there is a jump in the rms amplitude of the broad band noise component and a QPO appears. This is followed by a steady decrease in the QPO frequency and the peak frequency of the noise component.

Table 4.17 characterizes the physical properties of 4U 1630−47 during the state transitions.

Table 4.17: 4U 1630−47

Name :	4U 1630−47
Mass :	-
Distance :	$\geq$ 10 kpc
Gal. Coord. :	336.9, +0.3
N_H :	$9.44 \times 10^{22}\,\mathrm{cm}^2$ [a]
1998 Outburst	
Peak Flux[b] :	13.
Peak Luminosity :	$\geq$15.6 [c]
At the state transition:	
Flux :	2.18
Luminosity :	$\geq$2.62
Γ_{trans} :	1.92
T_{in} :	0.46 keV
Power-law flux :	1.30
1999 Outburst	
Peak Flux :	6.
Peak Luminosity :	$\geq$7.2
At the state transition:	
Flux :	1.17
Luminosity :	$\geq$1.4
Γ_{trans} :	1.93
T_{in} :	0.47 keV
Power-law flux :	0.62
2001 Outburst	
Peak Flux :	14.
Peak Luminosity :	$\geq$16.8
At the state transition:	
Flux :	1.82
Luminosity :	$\geq$2.18
Γ_{trans} :	1.58
T_{in} :	0.40 keV
Power-law flux :	0.76

a From Tomsick & Kaaret (2000).
b All fluxes in this table are in 1.5-12 keV band, in units of $10^{-9}\,\mathrm{ergs\,cm^{-2}\,s^{-1}}$
c All luminosities in this table are in 1.5-12 keV band, in units of $10^{37}\,\mathrm{ergs\,s^{-1}}$

4.7 XTE J1550−564

4.7.1 Introduction

The Soft X-ray Transient XTE J1550−564 was first detected by ASM on *RXTE* on September, 1998 (Smith 1998). A few days after the detection, it showed one of the brightest flares (∼7 Crab, $2 \times 10^{-7}\,\mathrm{ergs\,cm^{-2}\,s^{-1}}$ in 1.5 – 12 keV band) ever observed with *RXTE*. The power spectra for XTE J1550−564 showed strong aperiodic variability as well as low frequency (0.08 – 18 Hz, Cui et al. 1999; Remillard et al. 2002b) and high frequency (65 – 284 Hz, Remillard et al. 1999a; Homan et al. 2001; Kalemci et al. 2001) QPOs during some of the *RXTE* observations. The amplitudes of the low frequency QPOs can be less than 1% in the soft state and as much as 17% in the hard state. Detailed discussion of classification of these QPOs and their properties can be found in Homan et al. (2001) and Remillard et al. (2002b). The X-ray energy spectra usually show a diskbb and a power-law component along with an iron line and edge (Sobczak et al. 1999). Both the X-ray spectra and the temporal properties are similar to the other GBHs, and the mass is dynamically measured to be $10.6 \pm 1.5\ M_{\odot}$ (Orosz et al. 2001). The distance to the system is not well constrained, a preferred estimate of 5.3 – 5.9 kpc is given by (Orosz et al. 2002).

XTE J1550−564 showed another big outburst again in 2000 April (Smith et al. 2000), and two mini-outbursts in 2001 and 2002. I will summarize the properties of each outburst in detail in the following sections.

During the 1998 outburst, optical (Orosz, Bailyn & Jain 1998) and radio (Campbell-Wilson et al. 1998) counterparts were identified. A superluminal ejection was discovered in the radio establishing the source as a microquasar, (Hannikainen et al. 2000). The radio observations during the 2000 outburst revealed a compact jet in the LS. The radio flux was quenched in the VHS/IS and discrete ejection events occurred during the transition to the LS (Corbel et al. 2001).

4.7.2 1998 outburst

The 1998 outburst was first detected by ASM on *RXTE* on September 7 (MJD 51063). The ASM flux increased rapidly, then decayed to low flux levels without

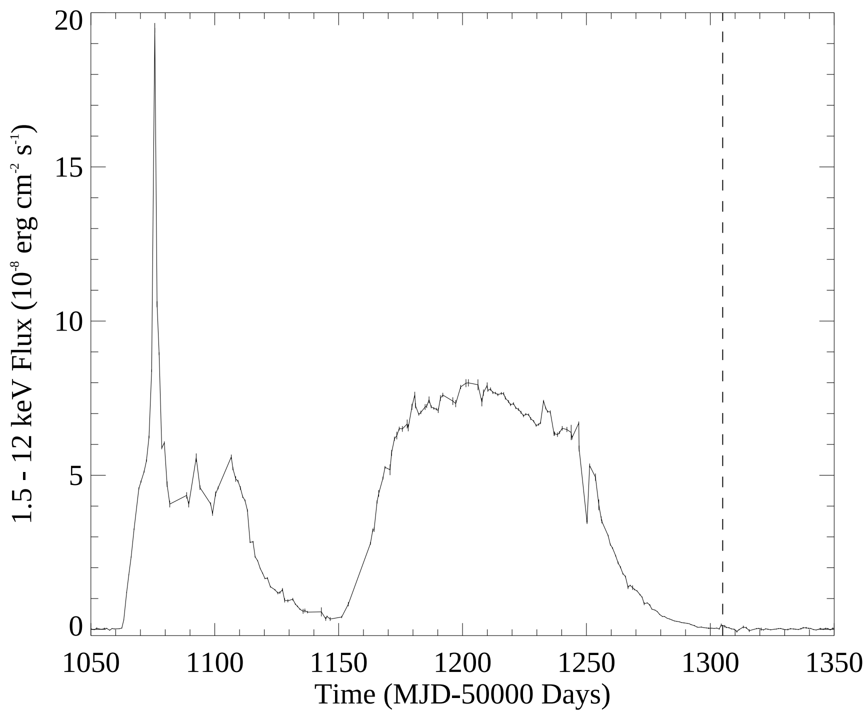

Figure 4.33: ASM light curve of 4U 1630−47 during the 1998 outburst. The dashed line indicates the time of transition to the LS.

a transition to the LS, and showed a secondary maximum as seen in Fig. 4.33. After the secondary maximum, it finally decayed to quiescence, and during this decay a transition to the LS occurred (Homan et al. 2001). The spectral properties of the whole outburst are discussed in Sobczak et al. (2000). The temporal properties of the initial rise and the first part of the outburst are discussed in detail by Cui et al. (1999) and Remillard et al. (2002b), whereas Homan et al. (2001) gives a detailed analysis of the temporal properties of the second part of the outburst. Apart from the analysis of the PSDs, extensive cross spectral temporal analysis has also been conducted (Cui, Zhang & Chen 2000; Wijnands, Homan & van der Klis 1999).

Observations and Analysis

I analyzed the observations made at the end of the decay of the 1998 outburst. Homan et al. (2001) and Sobczak et al. (2000) both pointed out the time of transition to the LS around as MJD 51060, so I started my analysis from a date a little earlier to

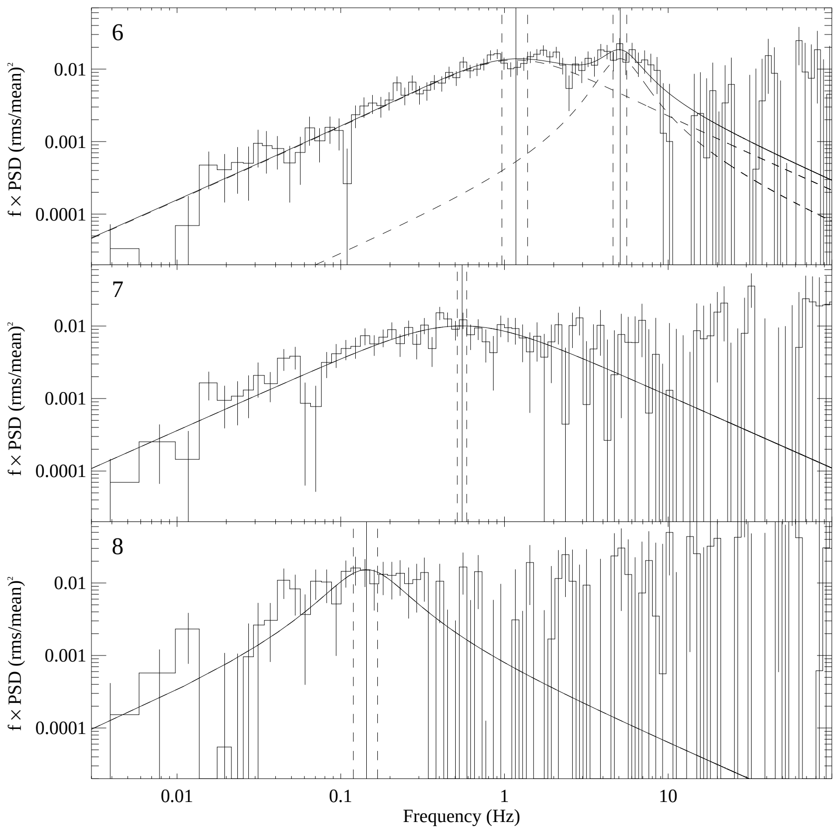

Figure 4.34: Lorentzian fits to observations 6,7,8 (observation numbers are shown in left hand corner for each panel). The solid curve is the overall fit and the dashed curves are individual Lorentzian components. The solid vertical lines indicate peak frequencies while the dashed vertical lines show their errors.

characterize the evolution. I used proposal id P40401, and analyzed 10 observations, until the source decayed into quiescence. For spectral information, I used a model consisting of a power-law, diskbb, and an iron edge to fit the X-ray spectrum following Sobczak et al. (2000). The hydrogen column density was fixed to 0.9×10^{22} cm^{-2}. The temporal analysis could only be done in two bands, 2–6 (E1) and 6–15 keV (E2), and statistically significant data could only be achieved for three observations. The same bands were used for the cross-spectral calculations. Unfortunately, the statistics were not good enough to do either frequency dependent or band averaged lag or coherence studies.

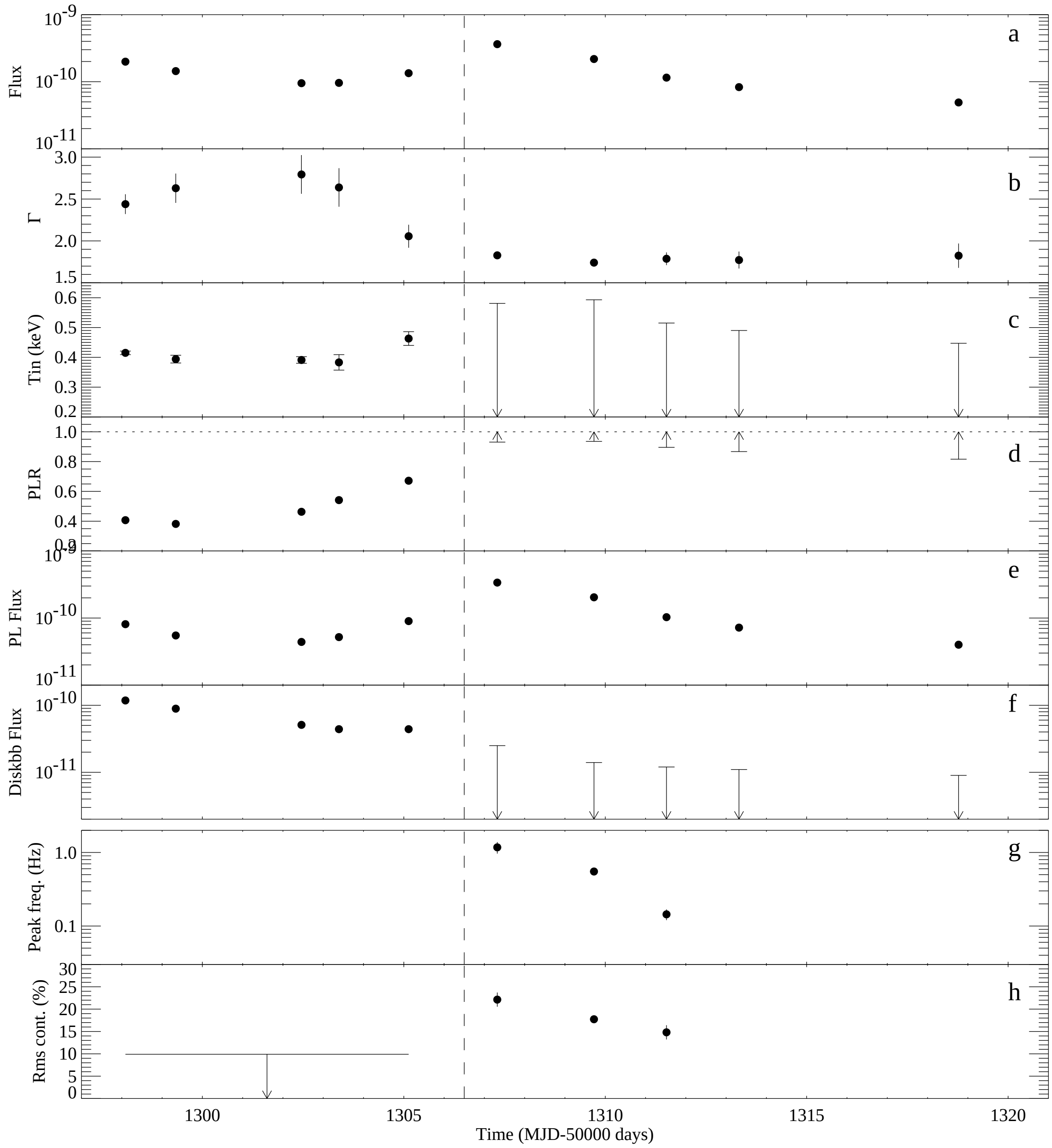

Figure 4.35: Spectral and temporal evolution of XTE J1550−564 around and after the state transition for the 1998 outburst. (a) 2.5–20 keV flux in units of ergs $\mathrm{cm}^{-2}\,\mathrm{s}^{-1}$. (b) Power-law index. (c) Inner disk temperature (d) PLR, the ratio of power-law flux to total flux in 2.5–20 keV band. (e) Power-law flux. (f) Diskbb flux. (g) Peak frequency of L_1. (h) Rms amplitude of the PSD continuum. The vertical dashed line indicates the date of state transition.

Table 4.18: Spectral fit parameters of XTE J1550−564 in the 1998 outburst.

Obs	Date[a]	Γ	T_{in} (keV)	power-law flux [b]	Total flux
1	1298.05	2.439 ± 0.118	0.415 ± 0.006	0.081	0.199
2	1299.34	2.629 ± 0.175	0.394 ± 0.013	0.055	0.144
3	1302.46	2.793 ± 0.231	0.391 ± 0.011	0.044	0.095
4	1303.39	2.638 ± 0.230	0.383 ± 0.026	0.052	0.096
5	1305.12	2.056 ± 0.137	0.463 ± 0.023	0.090	0.134
6[c]	1307.32	1.828 ± 0.029	0.581 ± 0.059	0.338	0.363
7	1309.72	1.741 ± 0.034	0.593 ± 0.068	0.204	0.218
8	1311.52	1.787 ± 0.076	0.515 ± 0.072	0.103	0.115
9	1313.32	1.772 ± 0.101	0.490 ± 0.063	0.072	0.083
10	1318.72	1.824 ± 0.145	0.447 ± 0.060	0.040	0.049

a MJD-50000 days
b All fluxes in this table are in 2.5–20 keV band in units of $10^{-9}\,\mathrm{ergs\,cm^{-2}\,s^{-1}}$
c Significant variability is observed for this observation.

Spectral and temporal evolution

The spectral fit results from my analysis are given in Table 4.18. The PSD in 2–15 keV is fitted with broad Lorentzians. The first observation with significant variability (observation 6) requires two Lorentzian components, however the remaining two observations with measurable variability require only one Lorentzian. The PSD in this band and Lorentzian fits are shown in Fig. 4.34 and fit parameters are given in Table 4.19.

Fig. 4.35 summarizes the evolution of spectral and temporal parameters of XTE J1550−564 around and after the state transition. The flux (a) first decreases and shows a temporary increase during the transition. The power-law index (b) decreases (spectrum gets harder) sharply just one observation before the transition. Before the transition, the inner disk temperature (c) is around 0.4 keV, and after the transition the diskbb component is not well constrained. This also reflects in the PLR (d), (the ratio of the power-law flux to total flux in 2.5–20 keV band) as it jumps to more than 0.8 after the state transition from values of around 0.4 before the state transition. As can be seen, the increase in overall flux is due to the increase in power-law flux (e) during the transition. The diskbb flux (f) decays smoothly to the transition, and then disappears. In (g), and also in Fig. 4.34, the decrease of the peak frequencies

Table 4.19: Temporal fit parameters of XTE J1550−564 in the 1998 outburst.

Obs	ν_1 (Hz)	Rms 1 (%)	ν_2 (Hz)	Rms 2 (%)	Total rms (%)
6	1.175 ± 0.210	19.05 ± 1.25	5.097 ± 0.489	11.26 ± 1.01	22.13 ± 1.59
7	0.551 ± 0.036	17.74 ± 0.60	-	-	17.74 ± 0.60
8	0.144 ± 0.024	14.81 ± 1.60	-	-	14.81 ± 1.60

Table 4.20: Energy dependent temporal fit values of XTE J1550−564 during the 1998 outburst.

	Lorentzian 1		Lorentzian 2		
O/B[a]	ν_1 (Hz)	rms 1 (%)	ν_2 (Hz)	rms 2 (%)	rms total (%)
6/E1[b]	0.978 ± 0.204	18.64 ± 1.30	5.316 ± 0.693	9.81 ± 1.34	21.06 ± 1.79
6/E2[c]	1.123 ± 0.336	17.05 ± 1.81	5.338 ± 1.18	14.83 ± 1.98	22.60 ± 2.66
7/E1	0.482 ± 0.162	15.15 ± 1.71	-	-	15.15 ± 1.71
7/E2	0.390 ± 0.098	18.31 ± 2.93	-	-	18.31 ± 2.93
8/E1	0.142 ± 0.033	9.56 ± 1.26	-	-	9.56 ± 1.26
8/E2	0.129 ± 0.027	16.48 ± 1.53	-	-	16.48 ± 1.53

a Observation/Band
b E1:2–5 keV band
c E2:5–13 keV band

is clearly seen. The evolution of the rms amplitude can be seen in (h). Although individual observations before the transition do not show any significant variability, the combined PSD has an 90% confidence rms upper limit of 10.9 % (Homan et al. 2001). After the transition, the rms amplitude decreases.

Energy dependence of PSD components

I fit the PSDs of the 3 observations that show significant variability in E1 and E2. The first observation required two Lorentzians in both bands, and the second and the third required only one Lorentzian. The fit results are given in Table 4.20.

The peak frequencies do not show any change as a function of energy within 1σ uncertainty. The rms amplitude seems to be increasing with energy, especially for observation 7 and 8, although a constant rms amplitude is also permitted within 2σ uncertainty.

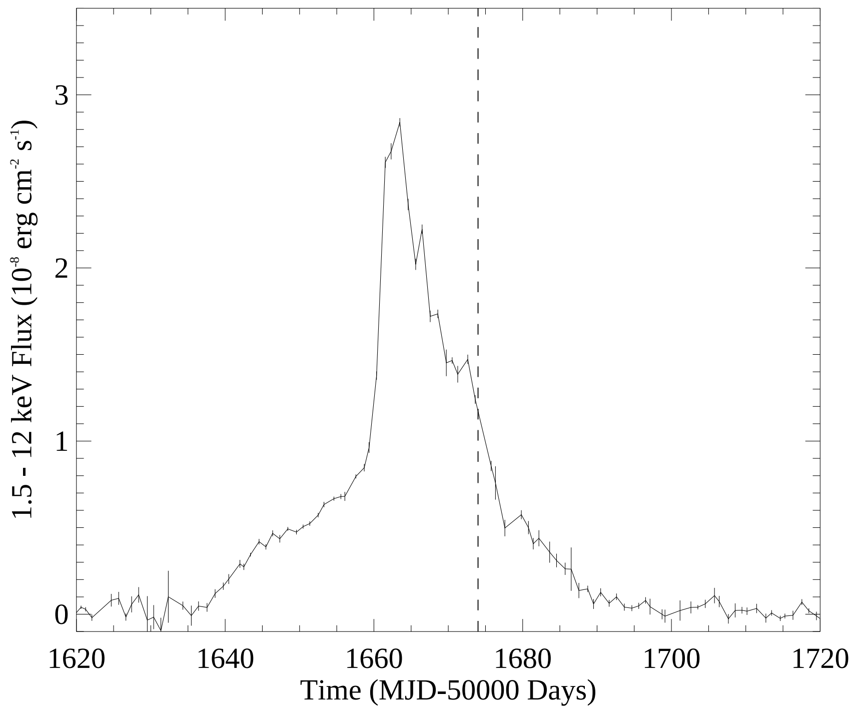

Figure 4.36: ASM light curve of XTE J1550−564 in the 2000 outburst. The dashed line indicates the time of transition to the LS.

Summary

XTE J1550−564 is a well studied source with a relatively good mass and distance determination. The evolution to the state transition showed the usual hardening of the X-ray spectrum with decreasing power-law index. The peak frequencies decreased after the transition. The low count rates only permitted to do PSD analysis in three observations, and no cross-spectral analysis could be done.

4.7.3 2000 outburst

XTE J1550−564 became active in X-rays again in 2000 April (Smith et al. 2000). The outburst reached its maximum ASM count rate at the end of 2000 April (see Fig. 4.36). The X-ray flux decayed over the next few months and a transition to the LS occurred. The spectral investigation of the whole outburst until the decay was reported by Rodriguez et al. (2002a). The decay spectral analysis was done by

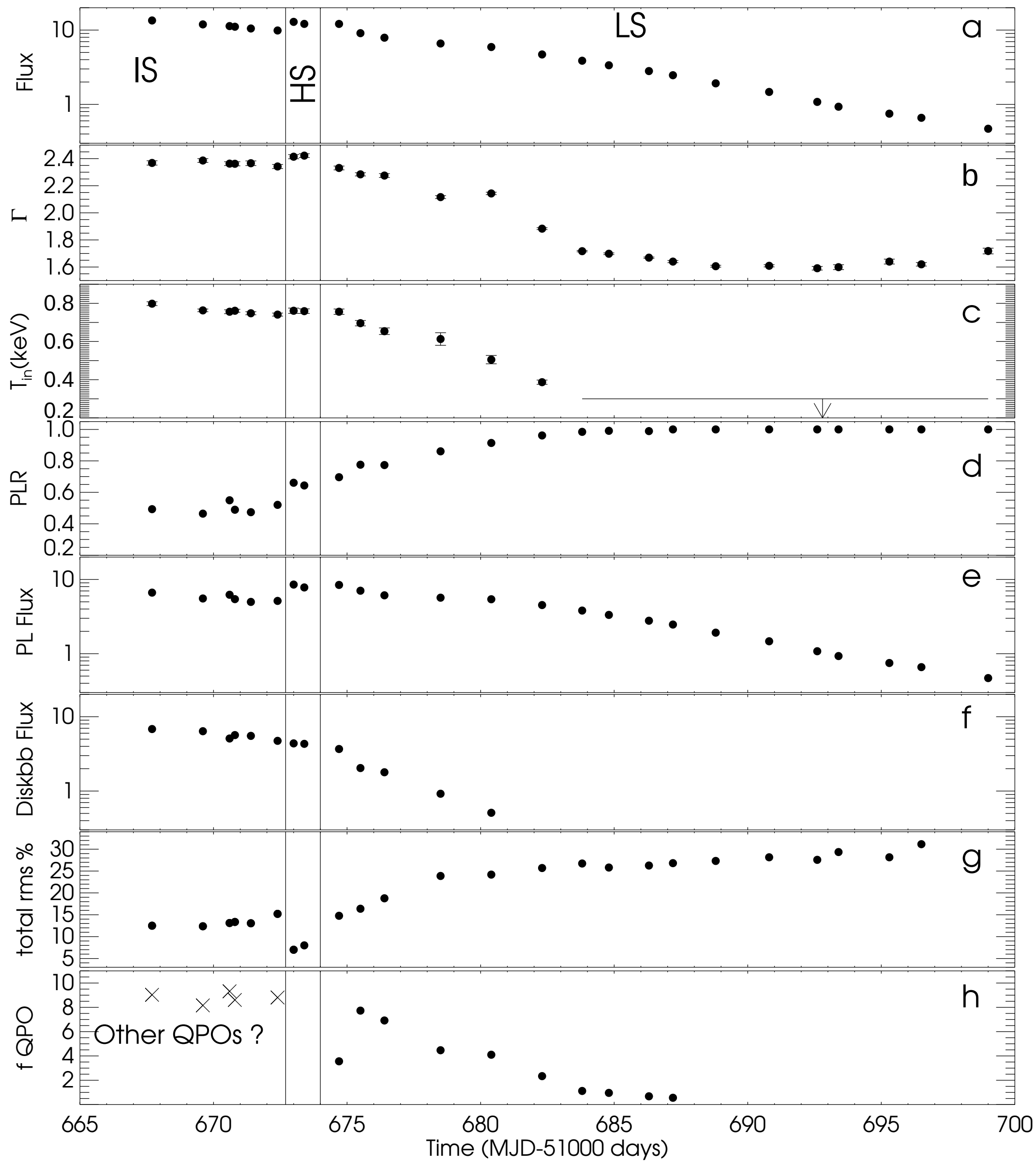

Figure 4.37: Spectral and temporal evolution of XTE J1550−564 around the state transition for the 2000 outburst. (a) 2.5–20 keV unabsorbed flux in units of ergs $\mathrm{cm}^{-2}\,\mathrm{s}^{-1}$. (b) Power-law index. (c) Inner disk temperature (d) PLR, ratio of power-law flux to total flux. (e) Power-law flux. (f) Diskbb flux. (g) Total rms amplitude. (h) QPO frequency. Temporal parameters (g,h) are from Kalemci et al. (2001).

Tomsick, Corbel & Kaaret (2001) and I worked on the temporal properties (Kalemci et al. 2001). An investigation of the temporal evolution of the whole outburst was reported by Rodriguez et al. (2002b). Radio properties were reported by Corbel et al. (2001), where emission with a negative spectral index (probably due to a discrete plasma ejection) was observed on MJD 51665. On MJD 51697, a flat spectrum indicative of a compact jet was detected in the LS.

Observations and analysis

Spectral analysis of the last part of the decay was discussed by Tomsick, Corbel & Kaaret (2001). I fit all the PCA spectra with the model discussed in this paper. This model consists of a diskbb, power-law, iron line and edge. The fit parameters can be found in Table 4.21.

For each observation, I computed the power spectra for two energy bands, 2 – 6 keV (E1), and 6 – 15 keV (E2). When there is enough flux, I also computed 15 – 67 keV band E3) PSD. Above 67 keV, the source was never significantly above the background. I also computed the 2–15 keV band power spectrum. I used 128s light curve segments and the Nyquist frequency was 256 Hz. During the analysis I detected a 65 Hz high frequency QPO in one of the observations. The discussion of the high frequency QPO was given in Kalemci et al. (2001), and it is beyond the scope of this thesis.

Spectral and temporal evolution

The important spectral fit parameters are given in Table 4.21. Their evolution, along with the evolution of the QPO frequency and the total rms amplitude are shown in Fig. 4.37. The temporal parameters for this figure are taken from Kalemci et al. (2001). As seen in this figure, the decay was quite complex. Until MJD 51673 the source was in the IS. The power-law index (b) was around 2.4 and did not show an evolution. The inner disk temperature (c) slowly decreased. PLR (d) was less than 40%. Both the power-law flux (e) and the diskbb flux (f) smoothly decreased. There was significant energy dependent variability with rms amplitude (g) less than 15%. Moreover, a narrow QPO was present with a steady frequency (h) around 8 - 9 Hz which could only be detected in E2 (see also Fig. 4.38). For the next two observations (7 and 8 in Table 4.21) there were significant changes in the temporal properties, and some changes in the spectral properties. The QPO disappeared, and the rms amplitude dropped down to ~5%, as can be seen in Fig. 4.38. Due to this

Table 4.21: Spectral fit parameters of XTE J1550−564 in the 2000 outburst.

Obs[a]	Date[b]	Γ	T_{in} keV	power-law flux [c]	Total flux
1	51667.7	2.368 ± 0.016	0.798 ± 0.010	6.640	13.47
2	51669.6	2.386 ± 0.014	0.763 ± 0.007	5.540	11.93
3	51670.6	2.363 ± 0.014	0.756 ± 0.010	6.220	11.32
4	51670.8	2.362 ± 0.015	0.761 ± 0.008	5.430	11.10
5	51671.4	2.366 ± 0.017	0.748 ± 0.008	4.980	10.51
6	51672.4	2.342 ± 0.015	0.741 ± 0.008	5.140	9.880
7	51673.0	2.414 ± 0.015	0.761 ± 0.014	8.530	12.91
8	51673.4	2.422 ± 0.014	0.759 ± 0.012	7.800	12.12
9	51674.7	2.331 ± 0.014	0.756 ± 0.014	8.430	12.11
10	51675.5	2.284 ± 0.012	0.696 ± 0.014	7.050	9.090
11	51676.4	2.275 ± 0.014	0.654 ± 0.017	6.110	7.900
12	51678.5	2.116 ± 0.011	0.613 ± 0.033	5.680	6.600
13	51680.4	2.143 ± 0.012	0.505 ± 0.022	5.410	5.920
14	51682.3	1.883 ± 0.013	0.387 ± 0.043	4.520	4.700
15	51683.8	1.717 ± 0.005	0.35[d]	3.810	3.870
16	51684.8	1.698 ± 0.006	0.35	3.330	3.360
17	51686.3	1.669 ± 0.005	0.35	2.780	2.810
18	51687.2	1.640 ± 0.008	0.35	2.470	2.470
19	51688.8	1.606 ± 0.007	0.35	1.920	1.920
20	51690.8	1.609 ± 0.008	0.35	1.470	1.470
21	51692.6	1.591 ± 0.013	0.35	1.080	1.080
22	51693.4	1.599 ± 0.018	0.35	0.930	0.930
23	51695.3	1.640 ± 0.018	0.35	0.750	0.750
24	51696.5	1.620 ± 0.013	0.35	0.660	0.660
25	51699.0	1.718 ± 0.021	0.35	0.470	0.470

a Observations 1–6 are IS, 7 and 8 are HS, 9 and 10 are TS, and 11–25 are LS.
b MJD
c All fluxes are unabsorbed, in 2.5–20 keV band in units of $10^{-9}\,\mathrm{ergs\,cm^{-2}\,s^{-1}}$
d After this observation, the inner disk temperature was fixed to 0.35

drop in the rms amplitude, I called this HS. However, they are spectrally not high state observations, since a power-law component is still present, and actually stronger (e) than those of the IS observations. On MJD 51674.7 (observation 9), a very strong QPO appeared in observation 9 (shown as TS in Fig. 4.38), and the rms amplitude jumped to ∼15%. Following, the usual evolution pattern is observed similar to the LS of other sources. As the flux decreased, the inner disk temperature decreased until it was undetectable with the PCA. The power-law index decreased, and the spectrum

Table 4.22: QPO fit parameters of XTE J1550−564 during the 2000 outburst, LS

Obs.	QPO freq. (Hz)	QPO rms (%)	FWHM (Hz)	harm. freq.[a] (Hz)	harm. RMS (%)
9	3.579 ± 0.015	7.84 ± 0.15	0.653 ± 0.037	6.58 ± 0.19	4.46 ± 0.22
10	7.687 ± 0.089	2.20 ± 0.29	1.050 ± 0.312	16.81 ± 0.18	2.73 ± 0.25
11	6.927 ± 0.020	4.98 ± 0.22	0.568 ± 0.077	14.41 ± 0.17	3.29 ± 0.44
12	4.489 ± 0.014	10.42 ± 0.22	0.75 ± 0.04	9.16 ± 0.10	4.63 ± 0.46
13	4.090 ± 0.015	10.4 ± 0.2	0.72 ± 0.04	8.75 ± 0.15	5.8 ± 0.4
14	2.337 ± 0.010	12.8 ± 0.3	0.44 ± 0.03	4.77 ± 0.04	$< 1.8\%$[b]
15	1.119 ± 0.007	11.9 ± 0.3	0.26 ± 0.02	2.35 ± 0.02	$< 2.0\%$
16	0.962 ± 0.016	10.0 ± 0.8	0.28 ± 0.05	1.83 ± 0.05	$< 4.2\%$
17	0.678 ± 0.010	10.7 ± 0.6	0.19 ± 0.03	-	-
18	0.559 ± 0.012	11.4 ± 1.0	0.21 ± 0.05	-	-
19	0.355 ± 0.005	7.1 ± 0.9	0.05 ± 0.02	-	-

a Frequency of the first harmonic
b 90% confidence upper limit

hardened. The rms amplitude increased up to 45% and the QPO frequency, along with the peak frequencies of the Lorentzian components decreased. Since observation 9 and 10 showed different PSD characteristics from rest of the LS observations, they are called "transitional state" (TS) observations.

The evolution of the QPO in the LS is interesting and different from the evolution usually observed in other GBHs. I summarized the QPO and its harmonic's properties in Table 4.22. The QPO central frequency first increased and then showed a decrease. This is the first time that a such inversion of a QPO frequency has been observed during the LS of a black hole binary system. A possible explanation is given in the context of the accretion ejection instability by Rodriguez et al. (2002b) and further discussed in section 5.2.2.

The rms amplitudes also showed an interesting behavior. In observation 9, the rms amplitude was high. Then there was a sharp drop for observations 10 and 11. It increased back to its nominal level of 10% after observation 12.

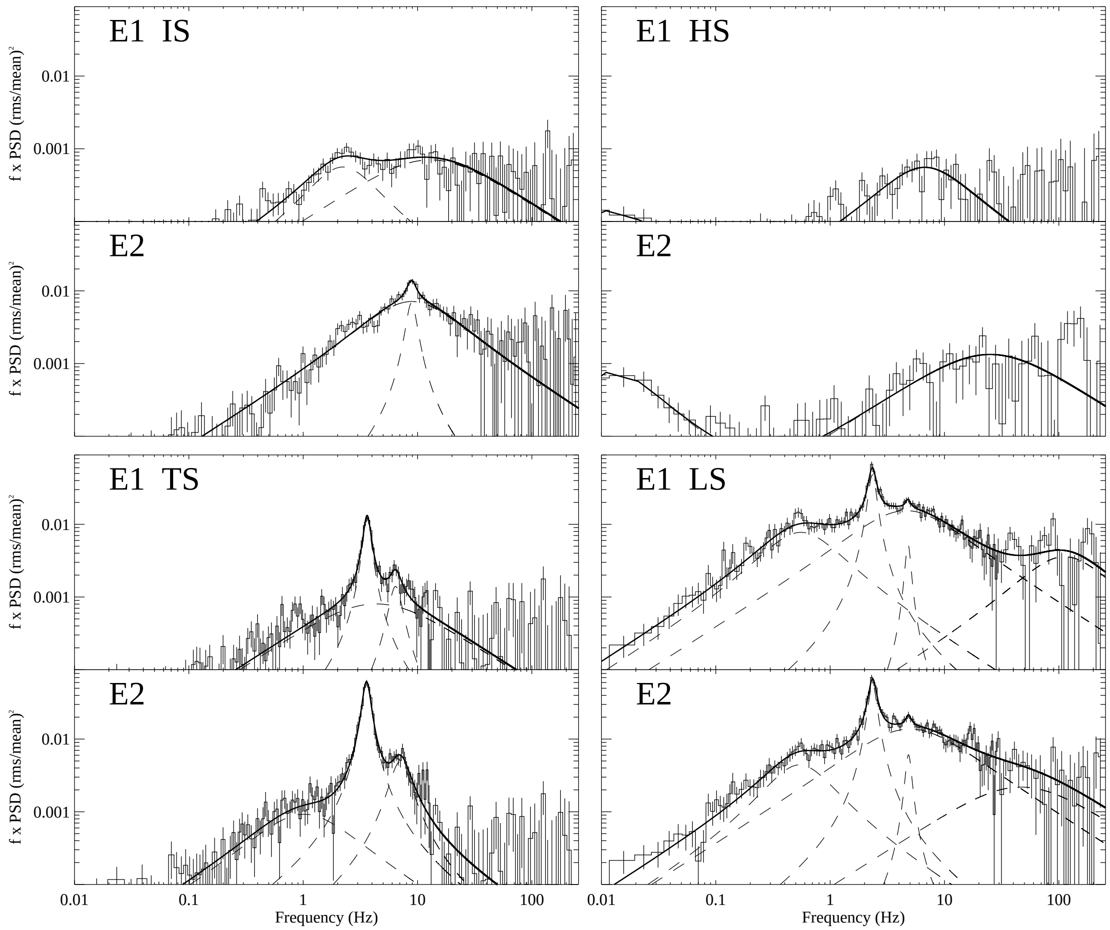

Figure 4.38: Lorentzian fits in E1 and E2 to observations in different states; observation 6 in the IS, observation 7 in the HS, observation 9 in the TS and observation 14 in the LS. The solid curve is the overall fit and the dashed curves are individual Lorentzian components.

Energy dependence of PSD components

PSDs in E1, E2 and for some observations E3 were calculated to analyze the energy dependence of the fit components. The PSDs and their Lorentzian fits in two energy bands for representative observations from different spectral states are shown in Fig. 4.38. The fit parameters are also shown in Table 4.23 for observations in the IS and HS, and in Tables 4.25, 4.26, 4.27, and 4.28 for the LS.

The energy dependence of the temporal parameters depends strongly on the state. During the IS, it is strongly energy dependent. The rms amplitude is lower in E1. For E2, not only is the rms amplitude higher, but also a narrow QPO is present which is

Table 4.23: Energy dependent temporal fit values of XTE J1550−564 during the 2000 outburst, IS and HS

O/B[a]	ν_1 (Hz)	rms 1 (%)	ν_2 (Hz)	rms 2 (%)	rms total (%)
1/E1	6.229 ± 0.261	4.31 ± 0.07	-	-	4.31 ± 0.07
1/E2	10.01 ± 1.264	11.23 ± 0.26	-	-	12.18 ± 0.47
2/E1	4.621 ± 0.318	3.91 ± 0.10	-	-	3.91 ± 0.10
2/E2	9.571 ± 0.894	11.56 ± 0.25	-	-	11.93 ± 0.33
3/E1	2.267 ± 0.298	3.00 ± 0.15	11.71 ± 1.34	4.39 ± 0.24	5.30 ± 0.28
3/E2	9.951 ± 0.601	12.46 ± 0.17	-	-	13.01 ± 0.22
4/E1	2.746 ± 0.829	3.60 ± 0.71	11.60 ± 3.64	2.61 ± 0.46	4.44 ± 0.84
4/E2	2.486 ± 0.701	3.58 ± 0.72	9.615 ± 0.932	11.73 ± 0.36	12.86 ± 0.64
5/E1	2.569 ± 0.772	3.20 ± 0.43	12.03 ± 4.825	2.84 ± 0.56	4.28 ± 0.69
5/E2	2.124 ± 0.740	3.05 ± 0.59	9.699 ± 0.653	12.42 ± 0.31	12.78 ± 0.45
6/E1	2.224 ± 0.306	3.162 ± 0.32	12.95 ± 2.903	4.65 ± 0.74	5.62 ± 0.79
6/E2	8.906 ± 0.768	12.95 ± 0.24	-	-	13.81 ± 0.36
7/E1	0.015 ± 0.006	1.26 ± 0.15	5.959 ± 1.037	3.36 ± 0.17	3.59 ± 0.21
7/E2	0.017 ± 0.002	2.00 ± 0.08	11.60 ± 1.51	5.44 ± 0.25	5.79 ± 0.26
8/E1	0.009 ± 0.002	2.11 ± 0.31	6.735 ± 1.076	3.51 ± 0.15	4.09 ± 0.29
8/E2	0.012 ± 0.002	4.15 ± 0.02	23.93 ± 0.42	6.39 ± 0.04	7.62 ± 0.04

[a] Observation/Band

Table 4.24: QPOs in the IS of XTE J1550−564 during the 2000 outburst decay.

Obs	ν (Hz)	FWHM (Hz)	rms (%)
1	9.030 ± 0.240	3.330 ± 1.180	4.71 ± 0.57
2	8.161 ± 0.136	0.876 ± 0.511	2.96 ± 0.68
3	9.336 ± 0.088	1.427 ± 0.320	3.75 ± 0.41
4	8.607 ± 0.116	1.443 ± 0.462	3.86 ± 0.67
6	8.811 ± 0.141	1.957 ± 0.575	4.79 ± 0.72

undetectable in E1. The properties of this QPOs are given in Table 4.24.

Coherence and lags

I analyzed the frequency dependent coherence and lags among the energy bands given as well as the frequency averaged values. The coherence and lag behavior is very rich and complex for this outburst, especially because of the presence of very strong QPOs. As I did for other sections, I investigated the behavior in the IS, TS and LS separately.

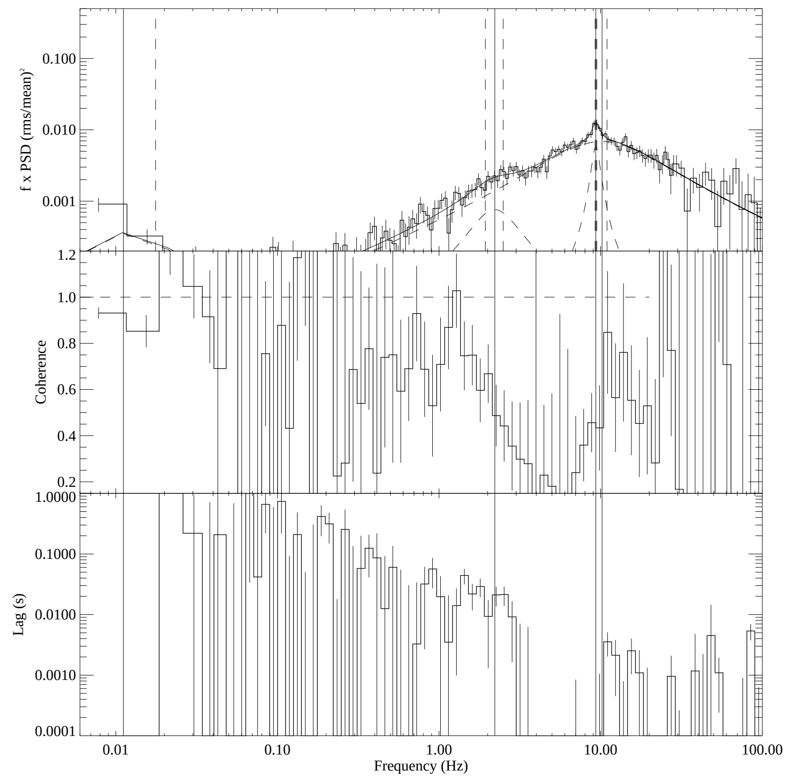

Figure 4.39: Frequency dependent coherence, lags and PSD for observation 3. The top panel is the PSD in 2–15 keV band. The middle panel is the coherence function, and the bottom panel is the time lag. The vertical solid lines are the peak frequencies and the dashed lines are the errors in peak frequencies. The horizontal dashed line in the middle panel indicates the unity coherence.

For IS observations, the statistics only let us analyze the lags and coherence between E1 and E2. The frequency dependent analysis showed that the coherence is high enough in 0.2 – 2 Hz band to analyze the mean properties. An example of frequency dependent coherence and lags is shown in Fig. 4.39. All observations show a sharp drop in coherence at 3 Hz. The mean coherence for observations 1 to 6 is $\sim 0.7 \pm 0.1$ The integrated lags have large error bars, with typical values of $\sim 0.06 \pm 0.03$.

For HS observations (7 and 8) the statistics are very poor to get a reliable coherence or lag measurement. The mean values for both quantities are consistent with zero.

The coherence and lag behavior for the LS observations is very complex, and I had difficulty finding common grounds to do comparative analysis between all of the observations. I divided the observations into four groups based on their coherence and lag properties. Observation 9 is a case itself, observations 10–13, observations 14–18 and observations 19–20. After observation 20, the statistics were not good enough to conduct this analysis. Below, I discuss some of these separate cases in detail.

Observation 9: Observation 9's PSD almost entirely consists of the very strong QPO and its harmonic. The statistics are quite poor for coherence and lags, except where the QPO is, as can be seen in Fig. 4.40. Between E1 and E2, the coherence function peaks ($\sim$0.9) at the QPO central frequency, moreover the lags are also positive at the frequency band where the QPO dominates. The integrated lag in 2.5 – 4.5 Hz band is 0.0176 ± 0.0023. Between E1 and E3, the frequency dependency is similar, such that the coherence peaks at the QPO frequency, with a mean coherence of $\sim$0.7. The integrated lag is much higher with a value of 0.0425 ± 0.0068. So the lag increases with energy for this QPO.

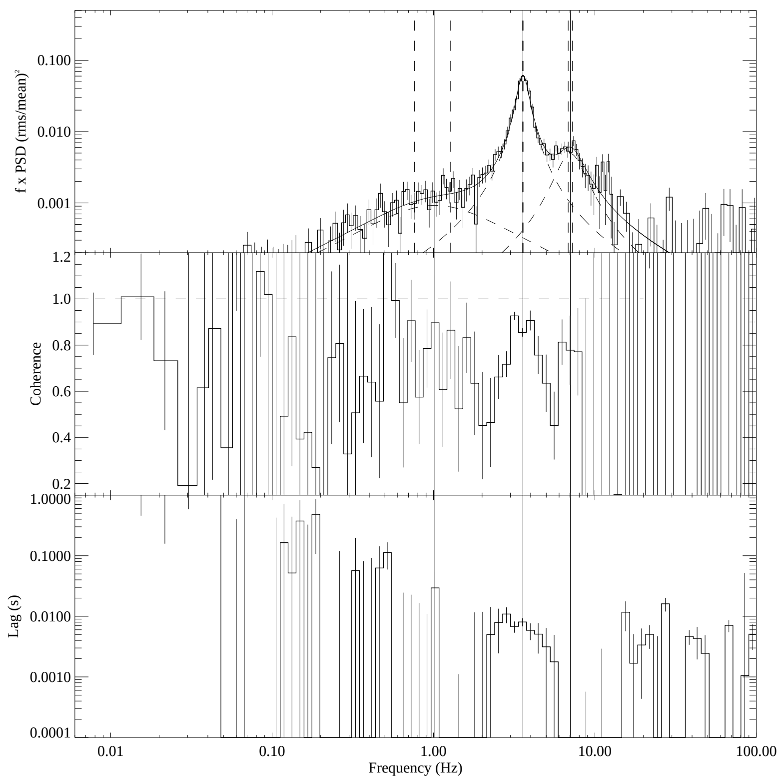

Figure 4.40: Frequency dependent coherence, lags and PSD for observation 9. The top panel is the PSD in 2–15 keV band. The middle panel is the coherence function, and the bottom panel is the time lag between E1 and E2. The vertical solid lines are the peak frequencies and the dashed lines are the errors in peak frequencies. The horizontal dashed line in the middle panel indicates the unity coherence.

Observations 10-13: The situation is different for observation 10. Between E1 and E2, the coherence function is not particularly higher at the QPO centroid frequency, in fact it is slightly lower, as seen in Fig. 4.41. For frequencies greater than 0.2 Hz, the coherence decreases as the frequency increases. It is around 0.5 between 2 Hz and 8 Hz, and then starts to increase as a function of frequency. The lags are positive between 1 Hz and 2.5 Hz, negative between 2.5 Hz and 8 Hz, and then positive again between 8 Hz and 20 Hz. The peak frequencies of the Lorentzians limit the region where the lags are negative. Between E1 and E3, the statistics are not good enough to do coherence and lag analysis. Observation 11 to 13 are not shown, because they have very similar characteristics to observation 10. The coherence shows a dip between 0.1 Hz and 10 Hz and the lag is negative near the QPO centroid.

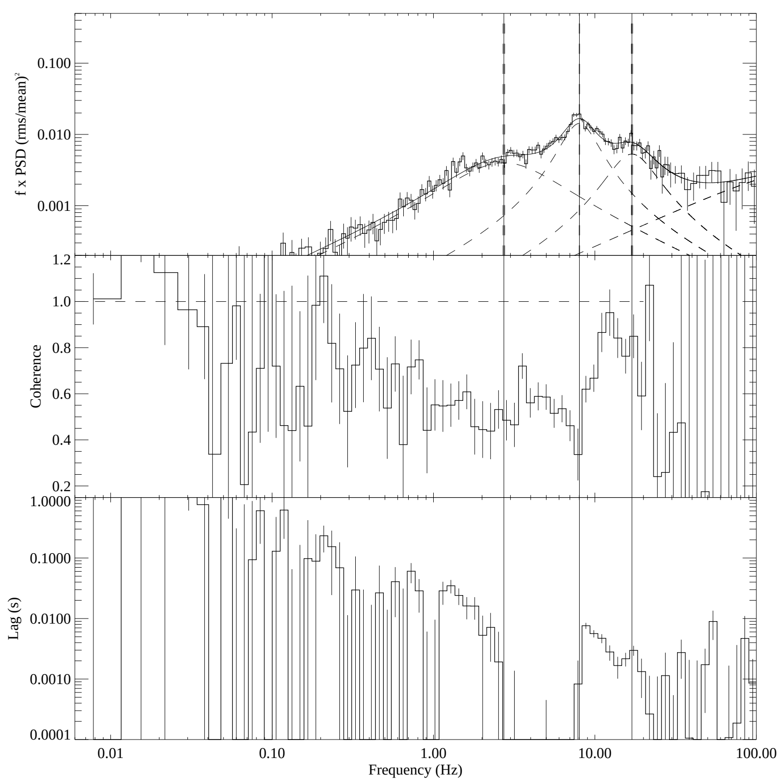

Figure 4.41: Frequency dependent coherence, lags and PSD for observation 10. The top panel is the PSD in 2–15 keV band. The middle panel is the coherence function, and the bottom panel is the time lag between E1 and E2. The vertical solid lines are the peak frequencies and the dashed lines are the errors in peak frequencies. The horizontal dashed line in the middle panel indicates the unity coherence.

Observations 14-18: Starting from observation 14, for E1 to E2, the coherence function is very high from 0.01 Hz to 10 Hz without the dip, as seen in Fig. 4.42. The lag is negative again close to the QPO centroid. For E1 to E3, the statistics are not good enough to do coherence and lag analysis. Observation 14 to 18 are not shown, because they have very similar characteristics to observation 14.

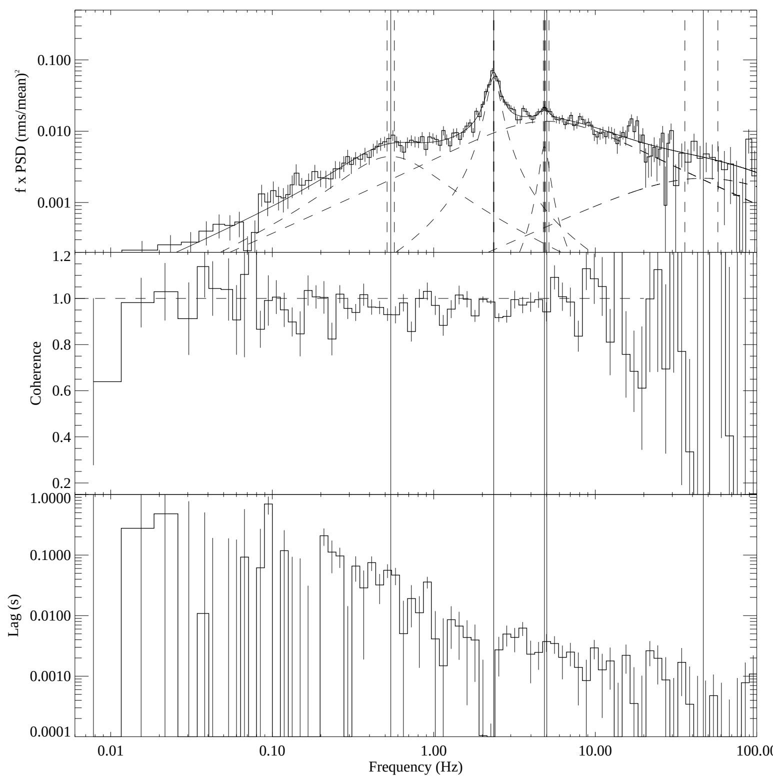

Figure 4.42: Frequency dependent coherence, lags and PSD for observation 14. The top panel is the PSD in 2–15 keV band. The middle panel is the coherence function, and the bottom panel is the time lag between E1 and E2. The vertical solid lines are the peak frequencies and the dashed lines are the errors in peak frequencies. The horizontal dashed line in the middle panel indicates the unity coherence.

For observations 19–20, the coherence is high between E1 and E2 without a dip, and statistics is not good enough to do lag studies. The shape of the coherence function does not depend on the PSD Lorentzian components.

Summary

This outburst has a very complex evolution during the outburst decay. From IS, it makes a transition to a state for which the temporal properties are similar to that of HS. However, due to the increasing hardness ratio in this state, it is unlikely that the source really is in the HS. Then it makes another transition where the temporal properties are similar to the LS observations. After this transition, as the flux decreases, the spectral index decreases, the inner disk temperature decreases, the hardness ratio and the total rms amplitude of variability increases. The QPO frequency shows an inversion, it first increases, and then decreases contrary to the evolution observed in other sources.

The PSDs in the IS are extremely energy dependent such that the rms amplitude is much higher in E2, and there is also a narrow QPO at around 9 Hz, which is not present in E1. The power spectra in the LS is very complex with several broad Lorentzian components and a QPO and its harmonic. In the LS, until observation 13, the rms amplitude increases with energy, and after that decreases or stays constant with energy.

The coherence and lag behavior is very complex. The frequency dependent lag and coherence depends on the position of the QPO, which is evident especially for observations 9–17.

This section, in part, has previously appeared in *The Astrophysical Journal* as "X-ray observations of XTE J1550−564 During the Decay of the 2000 Outburst-II. Timing", Kalemci, E., Tomsick, J. A., Rothschild, R. E., Pottschmidt, K., Kaaret, P. 2002, Volume 563, page 269.

Table 4.25: Energy dependent temporal fit values of XTE J1550−564 during the 2000 outburst, LS, I.

Obs/Band	ν_1 (Hz)	rms 1 (%)	ν_2 (Hz)	rms 2 (%)	ν_3 (Hz)	rms 3 (%)	rms total (%)
9/E1	4.344 ± 0.252	5.00 ± 0.11	-	-	-	-	7.78 ± 0.13
9/E2	1.019 ± 0.257	4.70 ± 0.36	-	-	-	-	14.77 ± 0.29
10/E1	1.449 ± 0.151	3.53 ± 0.42	5.558 ± 0.391	10.62 ± 0.37	-	-	11.54 ± 0.51
10/E2	1.794 ± 0.137	4.94 ± 0.35	9.301 ± 0.729	14.39 ± 0.36	-	-	16.38 ± 0.52
11/E1	2.016 ± 0.397	7.14 ± 1.09	7.770 ± 1.515	10.37 ± 1.21	-	-	13.34 ± 1.62
11/E2	2.425 ± 0.429	7.96 ± 0.83	10.88 ± 1.150	14.42 ± 0.68	-	-	18.77 ± 0.96
12/E1	1.431 ± 0.075	12.68 ± 0.22	10.28 ± 1.132	11.71 ± 0.33	-	-	20.32 ± 0.44
12/E2	1.148 ± 0.092	9.74 ± 0.39	8.176 ± 0.755	15.69 ± 0.55	88.95 ± 19.92	8.22 ± 0.75	23.88 ± 0.89
13/E1	0.836 ± 0.014	9.93 ± 0.47	5.228 ± 0.058	16.29 ± 0.74	-	-	21.69 ± 0.95
13/E2	1.014 ± 0.083	9.53 ± 0.28	5.935 ± 0.540	14.80 ± 0.42	44.25 ± 14.39	10.01 ± 1.33	24.19 ± 1.10
14/E1	0.511 ± 0.053	11.08 ± 0.69	4.382 ± 0.387	21.14 ± 1.32	-	-	26.59 ± 1.53
14/E2	0.558 ± 0.029	8.88 ± 0.13	6.229 ± 0.190	19.40 ± 0.19	-	-	25.70 ± 0.27
15/E1	0.333 ± 0.026	10.95 ± 0.29	2.317 ± 0.114	10.04 ± 0.41	4.023 ± 0.223	21.43 ± 0.50	29.25 ± 0.70
15/E2	0.337 ± 0.015	9.24 ± 0.11	2.464 ± 0.062	14.45 ± 0.11	9.041 ± 0.378	16.62 ± 0.20	26.73 ± 0.26
16/E1	0.457 ± 0.042	13.11 ± 0.43	2.137 ± 0.089	9.28 ± 0.25	3.711 ± 0.216	19.33 ± 0.33	27.63 ± 0.61
16/E2	0.647 ± 0.049	13.20 ± 0.37	2.217 ± 0.086	11.30 ± 0.20	10.11 ± 0.783	15.91 ± 0.35	25.91 ± 0.58

Table 4.26: Energy dependent temporal fit values of XTE J1550−564 during the 2000 outburst, LS, II.

Obs/Band	ν_1 (Hz)	rms 1 (%)	ν_2 (Hz)	rms 2 (%)	ν_3 (Hz)	rms 3 (%)	rms total (%)
17/E1	0.254 ± 0.015	10.63 ± 0.19	1.661 ± 0.056	18.11 ± 0.16	8.400 ± 0.697	14.53 ± 0.34	28.09 ± 0.43
17/E2	0.249 ± 0.026	8.11 ± 0.78	1.576 ± 0.356	17.38 ± 2.16	11.37 ± 2.278	14.96 ± 3.31	26.47 ± 3.77
18/E1	0.220 ± 0.026	9.91 ± 0.30	1.393 ± 0.068	20.17 ± 0.24	11.40 ± 1.522	14.83 ± 0.61	29.75 ± 0.67
18/E2	0.207 ± 0.056	8.89 ± 1.37	1.286 ± 0.381	17.84 ± 2.68	9.320 ± 3.265	15.21 ± 4.03	26.81 ± 4.85
19/E1	0.187 ± 0.070	13.69 ± 2.05	0.966 ± 0.179	19.13 ± 1.82	5.571 ± 1.548	17.04 ± 3.01	29.92 ± 3.96
19/E2	0.357 ± 0.048	16.64 ± 0.90	1.015 ± 0.104	11.21 ± 0.70	5.022 ± 0.697	17.63 ± 1.14	27.32 ± 1.66
20/E1	0.425 ± 0.038	22.20 ± 0.84	3.840 ± 0.493	20.26 ± 1.31	-	-	30.06 ± 1.51
20/E2	0.607 ± 0.037	23.44 ± 0.77	5.980 ± 2.852	15.58 ± 1.78	-	-	28.15 ± 1.64
21/E1	0.367 ± 0.009	24.62 ± 0.48	3.641 ± 0.057	9.96 ± 0.44	-	-	26.55 ± 0.61
21/E2	0.345 ± 0.008	24.12 ± 0.18	3.760 ± 0.290	13.35 ± 0.25	-	-	27.57 ± 0.28
22/E1	0.291 ± 0.017	21.57 ± 0.46	3.877 ± 0.736	15.68 ± 0.96	-	-	26.67 ± 0.94
22/E2	0.286 ± 0.028	23.25 ± 1.33	3.774 ± 1.088	17.91 ± 2.59	-	-	29.35 ± 2.65
23/E1	0.190 ± 0.006	21.76 ± 0.22	2.809 ± 0.145	20.38 ± 0.31	-	-	29.82 ± 0.37
23/E2	0.198 ± 0.015	22.24 ± 0.55	2.637 ± 0.378	18.05 ± 0.77	-	-	28.65 ± 0.92
24/E1	0.186 ± 0.004	23.66 ± 0.18	3.132 ± 0.167	17.64 ± 0.26	-	-	29.51 ± 0.30
24/E2	0.239 ± 0.005	24.86 ± 0.16	3.724 ± 0.169	18.75 ± 0.23	-	-	31.15 ± 0.27

Table 4.27: QPOs in the LS of XTE J1550−564 during the 2000 outburst, I.

	QPO fundamental			QPO harmonic		
Obs	ν (Hz)	FWHM (Hz)	rms (%)	ν (Hz)	FWHM (Hz)	rms (%)
9/E1	3.612 ± 0.012	0.567 ± 0.028	5.53 ± 0.09	6.361 ± 0.113	1.756 ± 0.264	2.46 ± 0.13
9/E2	3.566 ± 0.013	0.633 ± 0.035	13.06 ± 0.24	6.893 ± 0.173	2.941 ± 0.434	5.70 ± 0.32
9/E3	3.561 ± 0.037	0.923 ± 0.103	16.15 ± 0.55	-	-	-
10/E1	7.77^a	4.1^b	< 4.47	16.90 ± 0.25	3.655 ± 0.845	2.87 ± 0.30
10/E2	7.773 ± 0.057	1.541 ± 0.219	5.91 ± 0.40	16.74 ± 0.30	0.813 ± 0.416	1.70 ± 0.44
10/E3	7.728 ± 0.132	1.307 ± 0.330	8.50 ± 1.05	-	-	-
11/E1	6.958 ± 0.050	0.608 ± 0.203	2.92 ± 0.36	14.13 ± 0.17	2.013 ± 0.579	3.38 ± 0.42
11/E2	6.922 ± 0.041	0.606 ± 0.104	9.13 ± 0.20	-	-	-
11/E3	6.849 ± 0.039	0.200 ± 0.342	11.66 ± 6.72	-	-	-
12/E1	4.482 ± 0.015	0.871 ± 0.049	9.42 ± 0.19	8.996 ± 0.168	3.300 ± 0.503	5.54 ± 0.49
12/E2	4.473 ± 0.010	0.586 ± 0.034	12.61 ± 0.27	9.222 ± 0.125	0.713 ± 0.591	2.39 ± 0.68
12/E3	4.472 ± 0.033	0.700 ± 0.104	13.27 ± 0.99	-	-	-
13/E1	4.115 ± 0.023	0.710 ± 0.082	9.37 ± 0.45	8.673 ± 0.220	2.212 ± 0.838	4.74 ± 0.98
13/E2	4.093 ± 0.015	0.577 ± 0.043	12.30 ± 0.34	9.231 ± 0.248	2.549 ± 0.712	5.31 ± 0.74
13/E3	4.067 ± 0.043	0.602 ± 0.123	12.48 ± 1.02	-	-	-
14/E1	2.335 ± 0.012	0.389 ± 0.044	11.18 ± 0.48	4.875 ± 0.123	0.839 ± 0.498	3.93 ± 1.15
14/E2	2.342 ± 0.008	0.459 ± 0.020	13.19 ± 0.19	4.663 ± 0.094	1.719 ± 0.210	6.22 ± 0.29
14/E3	2.348 ± 0.021	0.457 ± 0.064	13.64 ± 0.77	-	-	-

a Fixed to the QPO frequency observed in 6–15 keV band
b Fixed to the FWHM observed in 6–15 keV band

Table 4.28: QPOs in the LS of XTE J1550−564 during the 2000 outburst, II.

	QPO fundamental			QPO harmonic		
Obs	ν (Hz)	FWHM (Hz)	rms (%)	ν (Hz)	FWHM (Hz)	rms (%)
15/E1	1.128 ± 0.006	0.257 ± 0.015	11.30 ± 0.23	2.374 ± 0.033	0.787 ± 0.075	6.92 ± 0.25
15/E2	1.122 ± 0.005	0.205 ± 0.012	10.45 ± 0.21	2.418 ± 0.052	0.854 ± 0.116	5.54 ± 0.29
15/E3	1.136 ± 0.016	0.397 ± 0.050	12.16 ± 0.61	-	-	-
16/E1	0.985 ± 0.019	0.306 ± 0.071	11.39 ± 1.23	-	-	-
16/E2	0.964 ± 0.011	0.292 ± 0.028	11.10 ± 0.36	-	-	-
16/E3	0.931 ± 0.020	0.217 ± 0.057	10.28 ± 1.06	1.817 ± 0.078	0.606 ± 0.296	9.73 ± 2.62
17/E1	0.678 ± 0.006	0.189 ± 0.017	11.97 ± 0.34	-	-	-
17/E2	0.673 ± 0.009	0.187 ± 0.038	10.66 ± 0.98	-	-	-
17/E3	0.684 ± 0.004	0.137 ± 0.011	7.56 ± 0.21	-	-	-
18/E1	0.553 ± 0.009	0.249 ± 0.025	13.10 ± 0.45	-	-	-
18/E2	0.555 ± 0.011	0.159 ± 0.053	9.73 ± 1.55	-	-	-
18/E3	0.560 ± 0.026	0.073 ± 0.049	5.54 ± 1.81	-	-	-
19/E1	0.350 ± 0.006	0.043 ± 0.015	7.24 ± 1.04	-	-	-
19/E2	0.358 ± 0.008	0.037 ± 0.012	5.77 ± 0.84	-	-	-
19/E3	0.346 ± 0.005	0.053 ± 0.013	7.82 ± 0.69	-	-	-

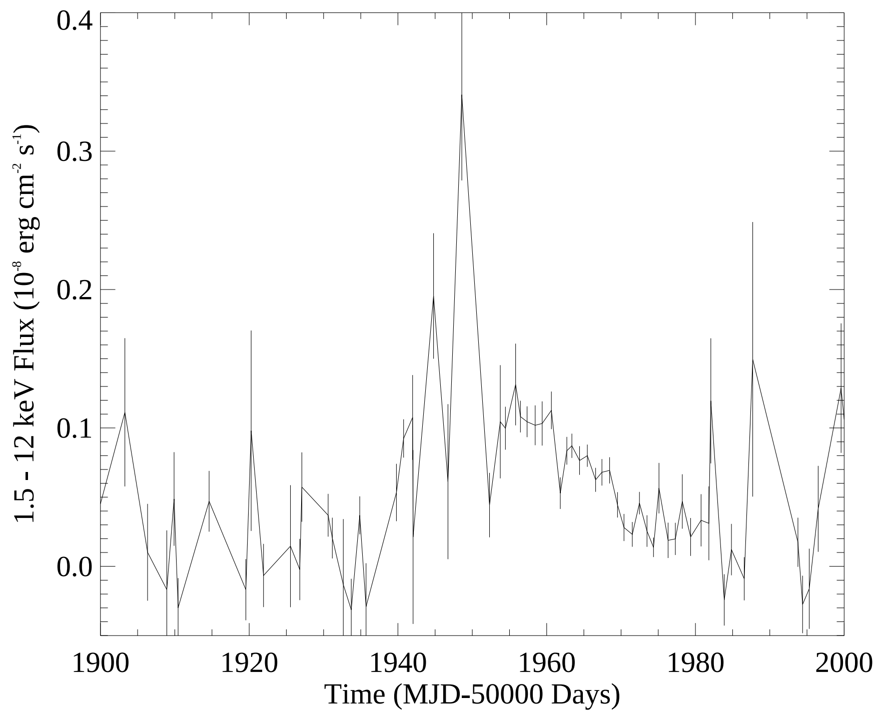

Figure 4.43: ASM light curve of XTE J1550−564 for the 2001 outburst.

4.7.4 2001 mini-outburst

The ASM on *RXTE* indicated another outburst from XTE J1550−564 (see Fig. 4.43 for the ASM light curve) between MJD 51900 and MJD 52000. Pointed observations were done with *RXTE* which showed that the source was in the LS, and optical observations showed that it was significantly brighter than the quiescence levels (Tomsick et al. 2001). This is what I call a mini-outburst, since the flux from XTE J1550−564 in this outburst is minuscule compared to 1998 and 2000 outburst peak flux levels.

Observations and analysis

Since this outburst's *RXTE* data had never been analyzed before, I tried to locate the date of state transition by investigating the PSD of all observations during the outburst decay. It turned out that XTE J1550−564 was in the LS throughout the outburst. Therefore I decided to analyze the whole outburst with evenly spaced

Table 4.29: Spectral fit parameters of XTE J1550−564 in the 2001 outburst.

Obs	Date[a]	Γ	Total flux[b]
1	1940.96	1.396 ± 0.010	1.184
2	1944.76	1.383 ± 0.013	1.432
3	1950.00	1.374 ± 0.009	1.588
4	1955.50	1.385 ± 0.011	1.586
5	1960.54	1.396 ± 0.010	1.441
6	1968.58	1.461 ± 0.013	0.797
7	1972.58	1.529 ± 0.025	0.464
8	1974.25	1.587 ± 0.013	0.348
9	1976.41	1.663 ± 0.022	0.257
10	1978.11	1.714 ± 0.019	0.207
11	1980.50	1.752 ± 0.100	0.179
12[c]	2003.38	2.196 ± 0.116	0.018

a MJD-50000 days
b PCA flux in 2.5–20 keV band in units of $10^{-9}\,\mathrm{ergs\,cm^{-2}\,s^{-1}}$
c This is to estimate the Galactic ridge contribution

pointed *RXTE* observations. Only at very low flux levels I sampled the observations with higher frequency to analyze the evolution of spectral and temporal parameters to quiescence. For the spectral analysis, I used a model consisting of a smeared iron edge, an iron line and a power-law. The hydrogen column density was kept as a free parameter unless it drifted to values higher or lower than ever reported for XTE J1550−564. In that case it was fixed to $0.9 \times 10^{22}\,\mathrm{cm^{-2}}$. I calculated PSDs with a Nyquist frequency of 128 Hz, using 256 s light curve segments in 2–6, 6–15, 15–30 (E1, E2, E3 respectively).

Spectral and temporal evolution

As mentioned earlier, a model consisting of a power-law, smedge and iron line was used for spectral analysis. The power-law index and flux in 2.5 – 20 keV band are given in Table 4.29, and are also used in Fig. 4.44.

The PSDs in 2–15 keV band were fitted with three Lorentzians. The fit results are given in Tables 4.31 and 4.32. The Lorentzian fits only during the decay are shown in Fig. 4.45.

The information in Tables 4.29, 4.31, 4.32 and in Fig. 4.44 can be summarized

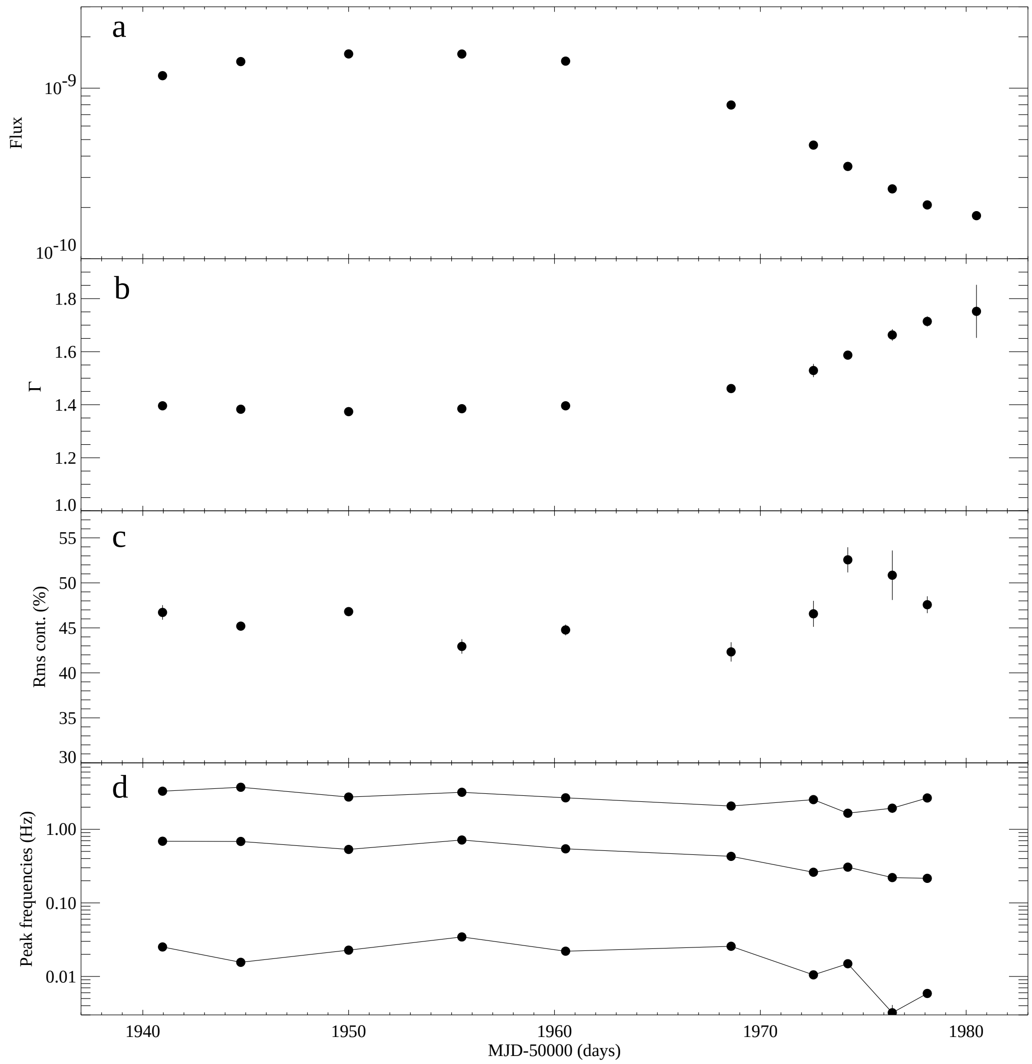

Figure 4.44: Spectral and temporal evolution of XTE J1550−564 for the 2001 outburst. (a) 2.5–20 keV flux in units of $\mathrm{ergs\,cm^{-2}\,s^{-1}}$. (b) power-law index. (c) Rms amplitude of PSD (d) Peak frequencies.

as follows. The pointed observations missed the output rise, but the decay is well covered. As the source flux decays, the spectrum softens. The softening cannot be solely due to Galactic ridge emission. The reason is as follows. Observation 36 was done at a flux level that is consistent with the dominant emission component coming from Galactic ridge emission (Tomsick & Kaaret 2001). I used this observation as a background for observation 11. When I refit the data, I obtained a power-law index consistent with the previous fitting with the modeled background. I conclude,

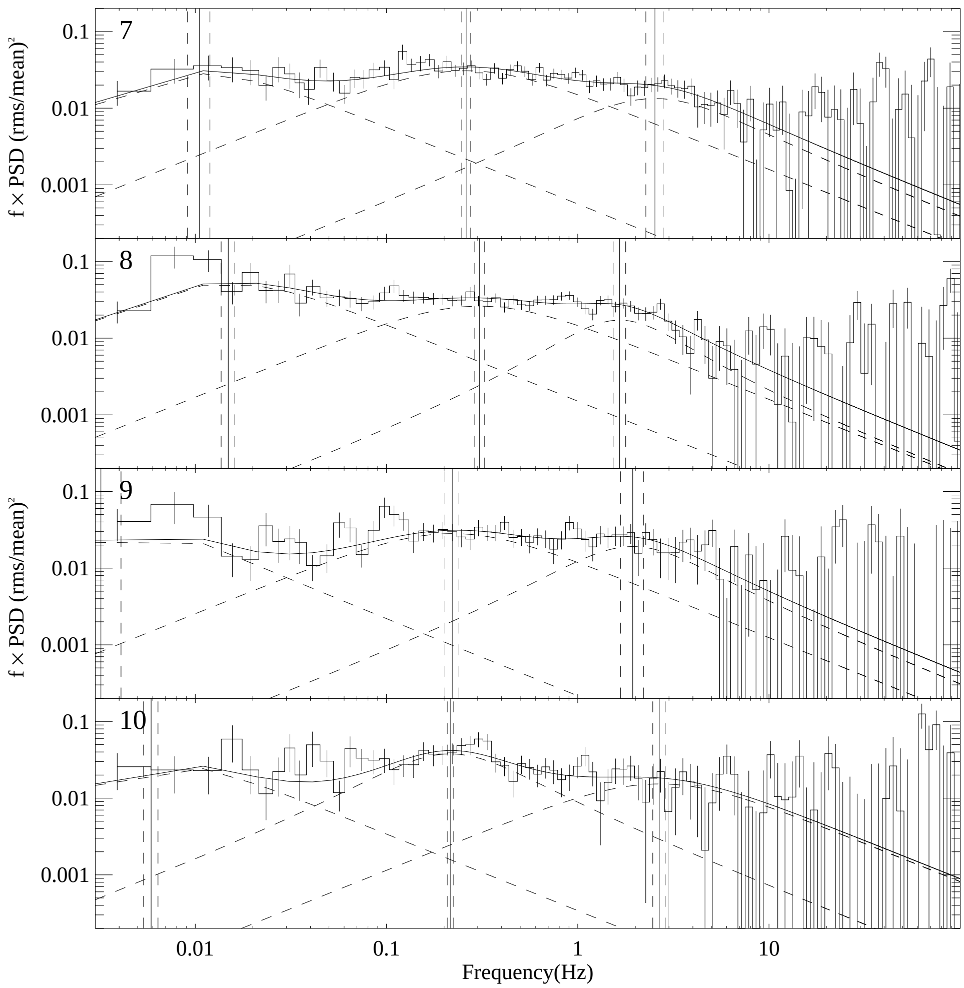

Figure 4.45: Lorentzian fits to observations 7 through 10. Observation numbers are shown at the upper left hand corner of each panel. The solid curve is the overall fit and the dashed curves are individual Lorentzian components. The solid vertical lines indicate peak frequencies while the dashed vertical lines show their errors.

therefore that the Galactic ridge emission is not affecting the power-law indices I obtained using the standard background model.

The rms amplitude does not show any evolution until the beginning of the decay, and then it rises for observation 8 before it decreases to its nominal level. The statistics were not good enough for the last observation to place a third Lorentzian and perhaps the rms amplitude reported is a lower limit. The rms amplitudes of individual Lorentzians do not follow a pattern. The peak frequencies for all Lorentzians are consistently lower during the decay than during the peak. However, only ν_2 shows a

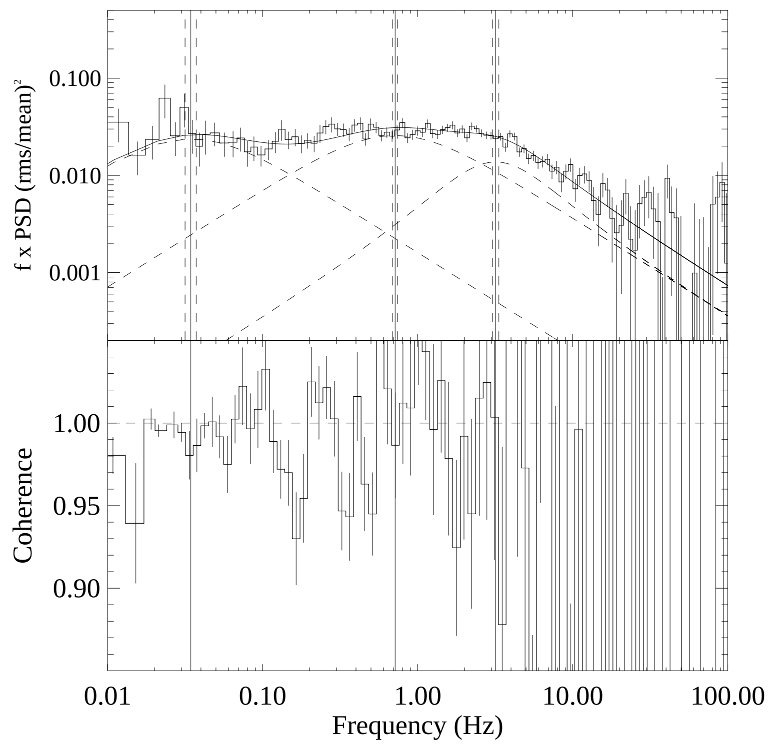

Figure 4.46: The PSD and frequency dependent coherence for observation 4. The top panel is the PSD in 2–15 keV band. The bottom panel is the coherence function. The vertical solid lines are the peak frequencies and the dashed lines are the errors in peak frequencies. The horizontal dashed line in the bottom panel indicates the unity coherence.

regular decrease as the source decays into quiescence, as can be seen in Fig. 4.44.

Energy dependence of the PSD components

The peak frequencies and the rms amplitudes in E1, E2 and E3 are given in Table 4.30. The peak frequencies are the same within 2σ error. Up to observation 6, the rms amplitudes also do not show a dependence on energy within 2σ error. E3 of observations 7,8, and probably 9 has much stronger rms amplitude than the E1 and E2.

Coherence and lags

I analyzed the frequency dependent and mean coherence for different energy bands. The lag spectrum was very noisy, and the mean values were consistent with zero.

The mean coherence values in 0.01 – 2 Hz band between E1 and E2 were very high (>0.98). I also analyzed frequency dependent coherence and studied the dependence of its shape on the Lorentzian components. Some of the observations seem to have lower coherence values where L_1 and L_2 intersect. I show an example in Fig. 4.46. To quantify this effect and to test if this is present for all observations, I determined a 0.1 Hz wide band where L_1 and L_2 intersect for all observations, and compared the mean coherence in this band to that of the 0.01 – 2 Hz band. The results are given in Table 4.33. For observations 1 and 4, within 2σ, in the restricted band where the Lorentzians intersect the coherence is lower compared to the whole band.

Summary

This is the first of the two hard mini-outbursts. The spectrum was hard throughout the outburst. The spectrum softens and the spectral index increases as flux decreases at the end of the decay. The peak frequencies also decrease at the end of the decay. The peak frequencies of the Lorentzians do not depend on energy. The rms amplitude of the PSD of the E3 band is significantly higher than those of E1 and E2 band PSDs for observations 6, 7, 8. The lag spectra were noisy, and the means are consistent with zero. The coherence is very high. They seem to be lower at the frequency bands where Lorentzian components intersect.

Table 4.30: Temporal fit parameters of XTE J1550−564 in the 2001 outburst.

Obs	ν_1 (Hz)	rms 1 (%)	ν_2 (Hz)	rms 2 (%)	ν_3 (Hz)	rms 3 (%)	rms total (%)
1	0.025 ± 0.001	32.22 ± 0.84	0.688 ± 0.017	31.18 ± 0.25	3.296 ± 0.183	13.08 ± 0.20	46.71 ± 0.81
2	0.015 ± 0.001	28.42 ± 0.51	0.683 ± 0.010	32.77 ± 0.17	3.728 ± 0.157	12.66 ± 0.13	45.19 ± 0.48
3	0.022 ± 0.001	30.65 ± 0.52	0.532 ± 0.008	29.22 ± 0.17	2.746 ± 0.054	19.92 ± 0.10	46.80 ± 0.49
4	0.034 ± 0.002	27.18 ± 0.83	0.715 ± 0.024	28.33 ± 0.30	3.186 ± 0.152	17.37 ± 0.20	42.93 ± 0.81
5	0.022 ± 0.001	29.66 ± 0.62	0.542 ± 0.013	26.43 ± 0.21	2.679 ± 0.073	20.61 ± 0.14	44.76 ± 0.60
6	0.025 ± 0.003	25.37 ± 1.07	0.428 ± 0.023	27.00 ± 0.45	2.070 ± 0.126	20.46 ± 0.30	42.32 ± 1.07
7	0.010 ± 0.001	29.45 ± 1.46	0.260 ± 0.013	31.01 ± 0.50	2.532 ± 0.261	18.38 ± 0.46	46.56 ± 1.44
8	0.014 ± 0.001	40.07 ± 1.30	0.305 ± 0.018	28.63 ± 0.51	1.655 ± 0.125	18.33 ± 0.36	52.55 ± 1.40
9	0.003 ± 0.001	35.68 ± 2.85	0.220 ± 0.018	29.74 ± 0.78	1.938 ± 0.266	20.66 ± 0.68	50.84 ± 2.75
10	0.005 ± 0.001	30.24 ± 0.90	0.215 ± 0.007	29.44 ± 0.24	2.666 ± 0.198	21.93 ± 0.46	47.56 ± 0.93

Table 4.31: Energy dependent temporal fit parameters of XTE J1550−564 during the 2001 outburst, I.

Obs/Band	ν_1 (Hz)	rms 1 (%)	ν_2 (Hz)	rms 2 (%)	ν_3 (Hz)	rms 3 (%)	rms total (%)
1/E1	0.019 ± 0.002	33.06 ± 0.96	0.566 ± 0.021	30.47 ± 0.34	2.699 ± 0.216	14.63 ± 0.30	47.28 ± 0.99
1/E2	0.024 ± 0.003	31.98 ± 0.87	0.667 ± 0.020	31.66 ± 0.29	3.635 ± 0.260	13.95 ± 0.26	47.12 ± 0.87
1/E3	0.012 ± 0.002	36.88 ± 3.14	0.336 ± 0.040	31.95 ± 1.69	2.161 ± 0.339	22.93 ± 1.22	53.92 ± 3.67
2/E1	0.015 ± 0.003	28.96 ± 1.38	0.524 ± 0.041	28.48 ± 0.72	1.611 ± 0.234	19.14 ± 0.68	44.91 ± 1.63
2/E2	0.016 ± 0.001	26.57 ± 0.50	0.500 ± 0.012	29.91 ± 0.23	2.529 ± 0.105	20.39 ± 0.18	44.91 ± 0.53
2/E3	0.018 ± 0.007	32.41 ± 3.73	0.407 ± 0.127	32.00 ± 7.01	3.175 ± 1.150	17.75 ± 3.60	48.88 ± 8.42
3/E1	0.021 ± 0.001	31.49 ± 0.57	0.541 ± 0.011	29.44 ± 0.20	2.747 ± 0.083	19.31 ± 0.14	47.24 ± 0.56
3/E2	0.022 ± 0.001	30.32 ± 0.19	0.576 ± 0.013	30.34 ± 0.26	2.984 ± 0.031	18.01 ± 0.24	46.52 ± 0.38
3/E3	0.020 ± 0.001	31.29 ± 0.61	0.485 ± 0.015	29.64 ± 0.29	2.618 ± 0.137	21.14 ± 0.27	48.01 ± 0.70
4/E1	0.027 ± 0.006	24.77 ± 1.83	0.305 ± 0.081	22.95 ± 3.51	1.925 ± 0.239	26.29 ± 2.37	42.80 ± 4.42
4/E2	0.026 ± 0.008	25.54 ± 3.44	0.328 ± 0.104	22.45 ± 3.65	2.173 ± 0.270	26.74 ± 2.44	43.26 ± 5.45
4/E3	0.023 ± 0.002	28.06 ± 0.98	0.485 ± 0.037	27.94 ± 0.64	2.774 ± 0.339	21.73 ± 0.65	45.17 ± 1.31
5/E1	0.020 ± 0.002	30.44 ± 1.69	0.433 ± 0.031	25.73 ± 0.81	2.424 ± 0.170	22.42 ± 0.62	45.73 ± 1.89
5/E2	0.019 ± 0.003	27.92 ± 2.00	0.327 ± 0.053	21.98 ± 2.58	1.970 ± 0.136	26.82 ± 1.46	44.52 ± 3.42
5/E3	0.021 ± 0.001	30.53 ± 0.71	0.519 ± 0.026	27.49 ± 0.40	2.351 ± 0.215	19.84 ± 0.43	45.63 ± 0.91

Table 4.32: Energy dependent temporal fit parameters of XTE J1550−564 during the 2001 outburst, II.

Obs/Band	ν_1 (Hz)	rms 1 (%)	ν_2 (Hz)	rms 2 (%)	ν_3 (Hz)	rms 3 (%)	rms total (%)
6/E1	0.027 ± 0.001	26.89 ± 0.40	0.569 ± 0.012	28.24 ± 0.17	3.067 ± 0.170	14.22 ± 0.18	41.51 ± 0.44
6/E2	0.024 ± 0.003	25.33 ± 1.14	0.479 ± 0.026	29.07 ± 0.49	2.191 ± 0.174	18.85 ± 0.37	42.92 ± 1.17
6/E3	0.022 ± 0.003	30.47 ± 1.53	0.461 ± 0.047	33.32 ± 0.99	3.145 ± 0.532	22.58 ± 1.05	50.48 ± 2.05
7/E1	0.010 ± 0.001	29.73 ± 1.39	0.268 ± 0.021	28.24 ± 0.66	2.077 ± 0.457	17.35 ± 1.09	44.53 ± 1.78
7/E2	0.010 ± 0.002	26.95 ± 1.97	0.181 ± 0.020	32.43 ± 1.85	2.454 ± 0.457	24.20 ± 2.22	48.62 ± 3.44
7/E3	0.008 ± 0.001	39.28 ± 1.85	0.273 ± 0.027	51.99 ± 1.70	-	-	65.17 ± 2.48
8/E1	0.012 ± 0.001	36.95 ± 1.46	0.242 ± 0.019	28.54 ± 0.67	1.927 ± 0.312	17.69 ± 0.69	49.93 ± 1.71
8/E2	0.016 ± 0.001	41.72 ± 1.35	0.378 ± 0.028	29.62 ± 0.62	1.807 ± 0.186	17.85 ± 0.52	54.19 ± 1.55
8/E3	0.012 ± 0.001	63.39 ± 2.62	0.481 ± 0.073	49.03 ± 2.36	-	-	80.14 ± 3.51
9/E1	0.003 ± 0.001	32.83 ± 2.66	0.288 ± 0.027	30.97 ± 0.89	-	-	45.14 ± 2.56
9/E2	0.004 ± 0.001	37.34 ± 0.99	0.363 ± 0.013	33.23 ± 0.34	-	-	49.99 ± 0.97
9/E3	0.004	< 55.97	0.3	< 72.80	-	-	< 91.83
10/E1	0.006 ± 0.001	25.95 ± 0.79	0.248 ± 0.010	25.71 ± 0.25	2.030 ± 0.207	17.87 ± 0.46	40.67 ± 0.87
10/E2	0.007 ± 0.003	32.75 ± 7.37	0.202 ± 0.044	32.91 ± 2.50	2.037 ± 2.254	17.06 ± 6.52	49.47 ± 9.01
10/E3	-	-	-	-	-	-	-

Table 4.33: Mean coherence of XTE J1550−564 in the 2001 outburst.

Obs	Res. Band[a]	0.01–2 Hz
1	0.973 ± 0.007	0.988 ± 0.002
2	0.986 ± 0.013	0.994 ± 0.003
3	0.989 ± 0.002	0.993 ± 0.001
4	0.973 ± 0.009	0.993 ± 0.002
5	0.987 ± 0.005	0.988 ± 0.002
6	0.981 ± 0.011	0.989 ± 0.004
7[b]	-	0.983 ± 0.007
8	-	0.982 ± 0.005
9 - 12[c]	-	-

a Mean coherence in 0.06-1.6 Hz band or 0.1-0.2 Hz band depending on the point of intersection.
b Statistics were not good enough to obtain meaningful mean coherence in the restricted band for observations 7 through 12.
c Statistics were not good enough to obtain meaningful mean coherence in the whole band.

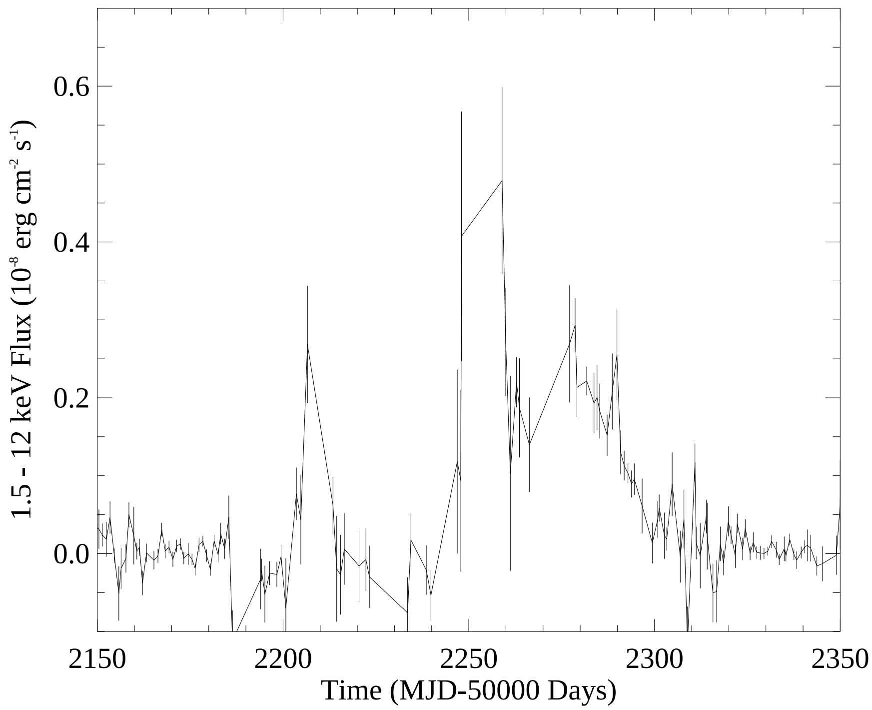

Figure 4.47: ASM light curve of XTE J1550−564 for the 2002 outburst.

4.7.5 2002 mini-outburst

In 2002, the ASM on *RXTE* detected another outburst from XTE J1550−564 (see Fig. 4.47 for the ASM light curve) between MJD 52200 and MJD 52300 (Swank, Smith & Markwardt 2002). Pointed public observations were done with *RXTE* and spectral and temporal analysis of this source was reported by (Belloni et al. 2002). This is also a mini-outburst, since the flux from XTE J1550−564 in this outburst is minuscule compared to 1998 and 2000 outburst peak flux levels, just like the 2001 outburst. Corbel, Fender & Tzioumis (2002) reported a flat radio spectrum during this outburst.

Observations and Analysis

A detailed spectral and temporal analysis of this outburst was reported by Belloni et al. (2002). I used the spectral and temporal parameters given in this paper. In addition, I conducted spectral analysis for low flux observations that are not reported in Belloni et al. (2002), and I also worked on energy dependent PSD, coherence and lags. I used 2–6 keV, 6–15 keV and 15–30 keV bands for this analysis (E1, E2, E3 respectively).

Spectral and temporal evolution

Belloni et al. (2002) used a cut-off power-law and extinction, where the column density is fixed to $0.85\times10^{22}\mathrm{cm}^{-2}$. The cut-off energies are higher than 150 keV before the decay, indicating high coronal temperatures. During the decay, although not well constrained, they are of the order of 100 keV (Belloni et al. 2002). Temporal analysis was done in 2–15 keV band and the PSDs were fitted with two broad Lorentzians. The fit parameters are given in Table 2 of Belloni et al. (2002). By using these values I created Fig. 4.48 which describes the evolution of spectral and temporal parameters of XTE J1550−564 during the 2002 outburst.

The evolution of spectral and temporal parameters can be summarized as follows. The rise was missed, as in the 2001 outburst. As the flux decayed, the peak frequencies also decreased. The rms amplitude stayed constant. The power-law index showed a softening at low fluxes, again similar to the 2001 outburst.

Energy dependence of PSD components

I investigated the energy dependence of the Lorentzian fits for all observations. Following Belloni et al. (2002), I used two broad Lorentzians to model the PSDs. The fit results are given in Tables 4.34 and 4.35.

I noticed that for most of the observations, the ν_2 of E2 peaks at a higher frequency than that of E1. To make this more clear, I plot the ratio of ν_2 of E2 and ν_2 of E1, and the same ratio for ν_1 in Fig. 4.49. Although it is clear that higher energy PSD Lorentzian peaks at a higher frequency for L_2, no such effect is present for L_1. I quantified this shift by calculating the reduced χ^2 for both cases. For L_2, the deviation of the ratio from the expected value of 1 resulted in a reduced χ^2 of 6.546 for 9 degrees of freedom. 8 of the 10 observations are higher than 1, and the two are only slightly less than 1. In fact the low points' contribution to the reduced χ^2 is only 0.003, therefore all the deviation is due to points higher than 1. For L_1, the reduced χ^2 is

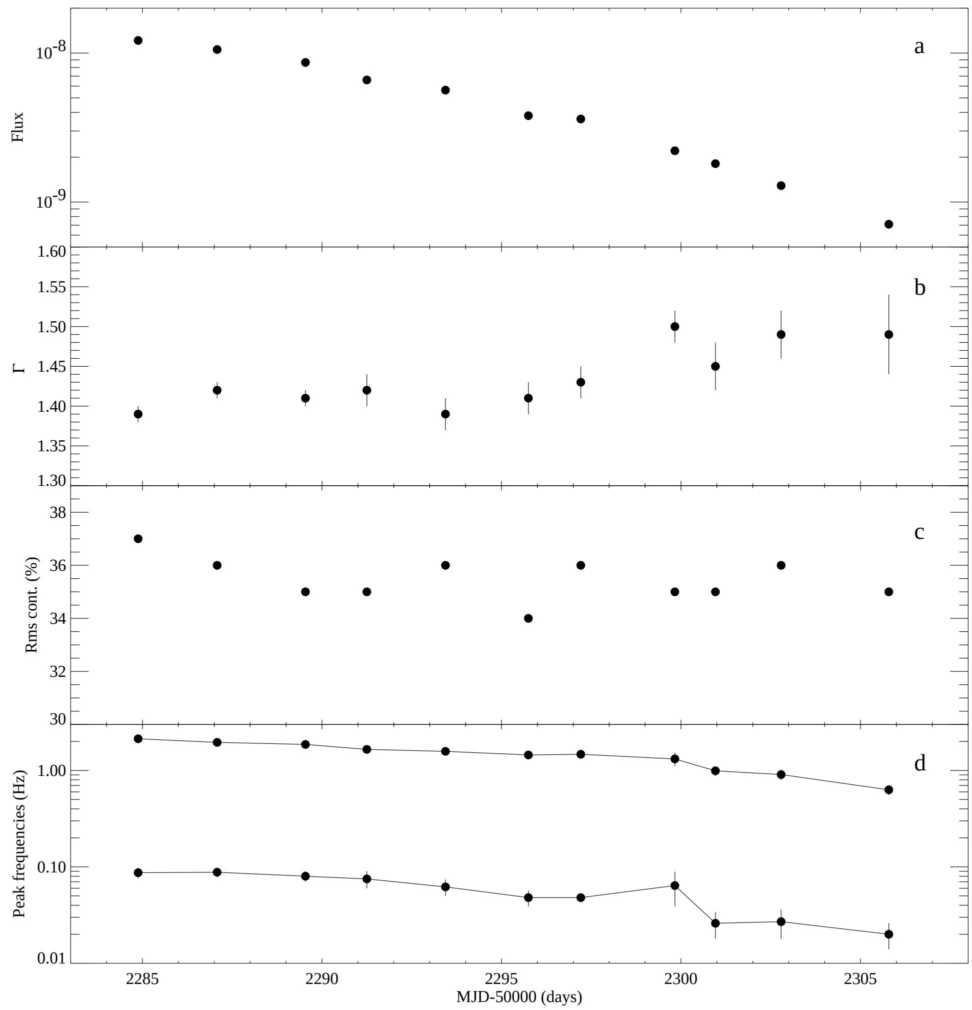

Figure 4.48: Spectral and temporal evolution of XTE J1550−564 for the 2002 outburst. (a) 3–150 keV flux in units of ergs $\mathrm{cm}^{-2}\,\mathrm{s}^{-1}$. (b) power-law index. (c) Rms amplitude of PSD in 0.002 - 10 Hz band. (d) Peak frequencies. All values are from Table 2 of Belloni et al. (2002).

0.798, thus statistically, the peak frequency does not change with energy. However, again, 8 of the 10 points are higher than 1. I also checked the peak frequencies for E3 vs E1. Although the reduced χ^2 for the ratio for L_2 was unacceptably higher than unity, there are points both above and below unity, and the above and below points contribute similarly to the total χ^2.

The rms amplitudes as a function of energy do not change until observation 5, for both individual Lorentzian components and the total. After observation 5 the rms amplitude increases with energy for the total amplitude. This is also generally true

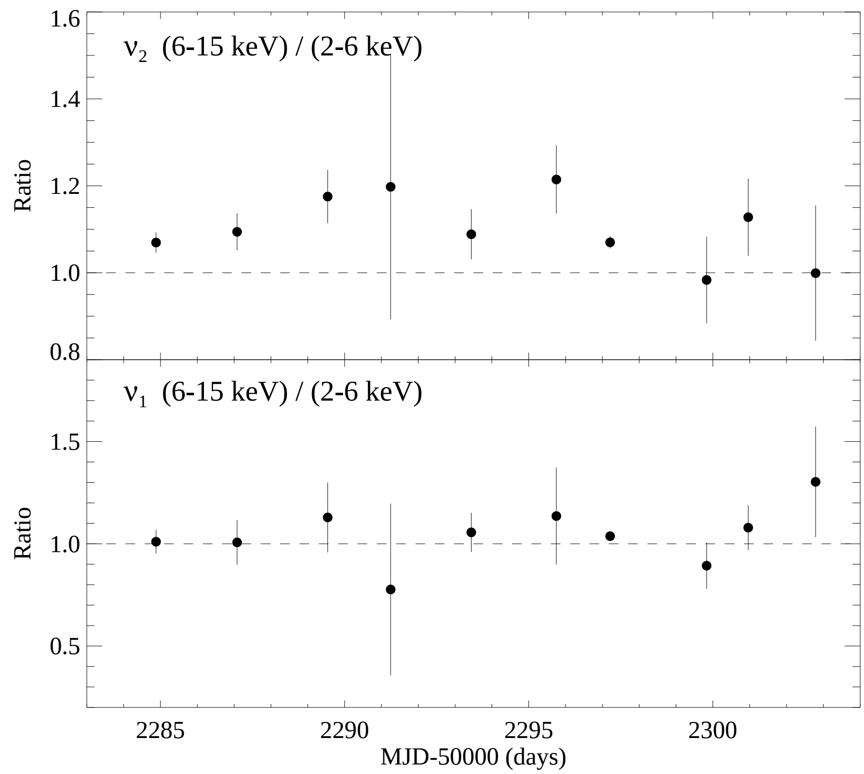

Figure 4.49: Upper panel: Ratio of 6–15 keV ν_2 and 2–6 keV ν_2. Lower panel: Ratio of 6–15 keV ν_1 and 2–6 keV ν_1.

for individual Lorentzians.

Coherence and Lags

Coherence and lag behavior of this outburst can be summarized as follows. The coherence between E2 and E1, and also E3 and E1 is very high (>0.98, see Table 4.36). As flux decreases, it shows a decrease, but this is probably due to low count rates and lack of statistics. Also in general, the coherence between E3 and E1 is lower than between E1 and E2. I also investigated the frequency dependent coherence and compared it to the Lorentzian fits. An example is shown in Fig. 4.50. For almost all cases, I found that the coherence increases as a function of frequency up to the peak frequency of the first Lorentzian, and then stays more or less constant very close to unity up to the frequency that the errors start to dominate. They do not show a dip at the intersection of the two Lorentzians. The lags are above the noise level only for the

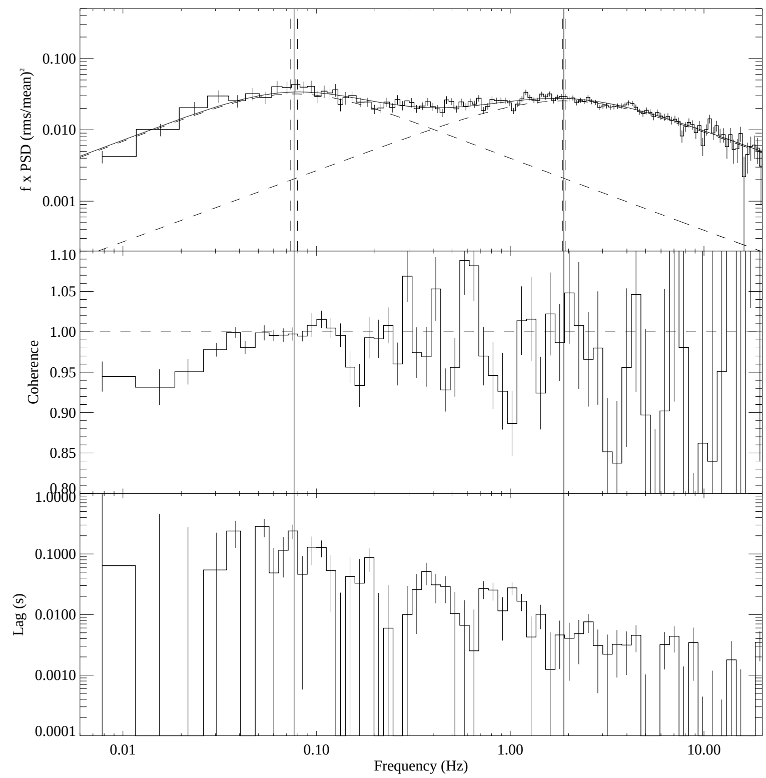

Figure 4.50: Frequency dependent coherence and lags. The top panel is the PSD in 2–6 keV band. The middle panel is the coherence function and the bottom panel is the lag. Coherence and lag are for between E3 and E1. The vertical solid lines are the peak frequencies and the dashed lines are the errors in peak frequencies. The horizontal dashed line in the middle panel indicates the unity coherence.

first three observations. The frequency dependent lags do not show any dependence on the PSD components. The integrated lags for the first three observations, which are shown in Table 4.36 show that they increase with energy.

Summary

This is the second hard mini-outburst of XTE J1550−564. It was hard throughout the outburst and spectral fits indicated very high coronal temperatures. The peak frequencies decreased during the decay as the source got fainter. At the end of the decay, a softening of the power-law index was again observed. The rms amplitudes did not show a particular evolution. The most interesting result from this outburst is the presence of a peak frequency shift with energy, similar to the ones observed in

Cyg X-1 and XTE J1650$-$500. The coherence was very high. The integrated lags increased with energy for the first three observations with good statistics.

Table 4.34: Energy dependent temporal fit values of XTE J1550−564 during the 2002 outburst, I.

Obs/Band	Date [a]	ν_1 (Hz)	rms 1 (%)	ν_2 (Hz)	rms 2 (%)	rms total (%)
1/E1	2284.88	0.078 ± 0.003	30.27 ± 0.34	2.060 ± 0.032	29.44 ± 0.15	42.22 ± 0.35
1/E2		0.079 ± 0.001	27.96 ± 0.12	2.203 ± 0.013	28.33 ± 0.05	39.81 ± 0.12
1/E3		0.074 ± 0.003	28.08 ± 0.34	2.133 ± 0.060	29.31 ± 0.26	40.60 ± 0.42
2/E1	2287.08	0.076 ± 0.003	30.37 ± 0.36	1.890 ± 0.030	28.26 ± 0.15	41.48 ± 0.37
2/E2		0.077 ± 0.005	29.05 ± 0.73	2.068 ± 0.046	28.70 ± 0.36	40.84 ± 0.77
2/E3		0.074 ± 0.003	29.44 ± 0.38	2.224 ± 0.065	29.13 ± 0.27	41.42 ± 0.46
3/E1	2289.54	0.071 ± 0.005	27.70 ± 0.66	1.696 ± 0.044	28.64 ± 0.43	39.85 ± 0.77
3/E2		0.081 ± 0.005	27.19 ± 0.82	1.993 ± 0.051	27.97 ± 0.39	39.01 ± 0.85
3/E3		0.073 ± 0.009	27.98 ± 1.21	1.844 ± 0.102	29.90 ± 2.12	40.95 ± 2.37
4/E1	2291.25	0.075 ± 0.022	24.93 ± 2.18	1.360 ± 0.199	26.34 ± 2.09	36.27 ± 3.01
4/E2		0.058 ± 0.014	23.36 ± 1.40	1.629 ± 0.175	30.49 ± 1.60	38.41 ± 2.12
4/E3		0.111 ± 0.020	23.45 ± 1.02	2.203 ± 0.478	28.86 ± 1.91	37.19 ± 2.13
5/E1	2293.44	0.057 ± 0.002	29.82 ± 0.50	1.543 ± 0.042	27.76 ± 0.24	40.74 ± 0.53
5/E2		0.060 ± 0.002	29.88 ± 0.50	1.680 ± 0.042	28.25 ± 0.22	41.12 ± 0.52
5/E3		0.063 ± 0.003	33.28 ± 0.60	1.782 ± 0.101	30.32 ± 0.53	45.02 ± 0.80

[a] MJD-50000

Table 4.35: Energy dependent temporal fit values of XTE J1550−564 during the 2002 outburst, II.

Obs/Band	Date [a]	ν_1 (Hz)	rms 1 (%)	ν_2 (Hz)	rms 2 (%)	rms total (%)
6/E1	2295.75	0.045 ± 0.001	24.56 ± 0.22	1.354 ± 0.019	27.33 ± 0.11	36.74 ± 0.23
6/E2		0.051 ± 0.009	27.81 ± 1.18	1.645 ± 0.083	27.61 ± 0.60	39.19 ± 1.26
6/E3		0.045 ± 0.003	29.15 ± 0.88	1.169 ± 0.082	32.26 ± 0.70	43.49 ± 1.11
7/E1	2297.21	0.041 ± 0.000	28.55 ± 0.17	1.340 ± 0.013	27.20 ± 0.08	39.44 ± 0.17
7/E2		0.043 ± 0.000	29.39 ± 0.05	1.434 ± 0.004	28.06 ± 0.02	40.63 ± 0.05
7/E3		0.039 ± 0.001	31.85 ± 0.20	1.247 ± 0.023	32.05 ± 0.17	45.19 ± 0.26
8/E1	2299.83	0.063 ± 0.004	27.81 ± 0.60	1.268 ± 0.070	25.38 ± 0.41	37.65 ± 0.72
8/E2		0.056 ± 0.003	29.27 ± 0.65	1.247 ± 0.056	28.12 ± 0.38	40.59 ± 0.73
8/E3		0.035 ± 0.003	30.92 ± 0.73	0.883 ± 0.081	36.94 ± 1.08	48.17 ± 1.30
9/E1	2300.96	0.022 ± 0.001	29.29 ± 0.87	0.883 ± 0.051	26.94 ± 0.46	39.80 ± 0.95
9/E2		0.024 ± 0.000	30.25 ± 0.32	0.996 ± 0.020	28.32 ± 0.16	41.44 ± 0.34
9/E3		0.026 ± 0.001	37.59 ± 0.42	1.159 ± 0.054	37.14 ± 0.54	52.84 ± 0.68
10/E1	2302.79	0.026 ± 0.003	28.34 ± 1.86	0.788 ± 0.073	26.21 ± 1.33	38.60 ± 2.27
10/E2		0.034 ± 0.002	28.99 ± 0.76	0.787 ± 0.048	28.03 ± 0.49	40.32 ± 0.89
10/E3		0.030 ± 0.001	40.25 ± 0.53	1.720 ± 0.146	35.75 ± 0.95	53.83 ± 1.02

[a] MJD-50000

Table 4.36: Mean coherence and integrated lag of XTE J1550−564 during the 2002 outburst.

Obs	Coh. E2/E1	Coh. E3/E1	Lag E2/E1	Lag E3/E1
1	0.995 ± 0.002	0.981 ± 0.002	0.017 ± 0.003	0.031 ± 0.004
2	0.995 ± 0.002	0.988 ± 0.002	0.014 ± 0.002	0.028 ± 0.004
3	0.995 ± 0.002	0.981 ± 0.002	0.012 ± 0.003	0.024 ± 0.004
4	0.987 ± 0.008	0.990 ± 0.019	-	-
5	0.990 ± 0.002	0.972 ± 0.005	-	-
6	0.990 ± 0.003	0.966 ± 0.008	-	-
7	0.989 ± 0.002	0.979 ± 0.005	-	-
8	0.989 ± 0.004	0.980 ± 0.011	-	-
9	0.979 ± 0.006	0.966 ± 0.014	-	-
10	0.983 ± 0.006	0.952 ± 0.019	-	-

4.7.6 Overall summary for XTE J1550−564

This is another very important source for my analysis because of several reasons. There is a mass and distance estimate. It showed multiple outbursts to do comparative analysis. It also showed some peculiar behavior which has not been seen in any other source.

The 1998 and 2000 outburst decays showed transitions to the LS. Although the evolution of the 1998 decay showed similar characteristics to that of the evolution of other sources such as spectral hardening, decrease of peak frequencies, etc., the evolution of the 2000 outburst was much more complex which went through a peculiar state before transiting into the LS. It also showed an increase in the QPO frequency before decreasing in the beginning of the transition which has not been observed for any other source.

Table 4.37 characterizes the physical properties of 4U 1630−47 during the state transitions.

The 2001 and 2002 outbursts have peak flux levels minuscule compared to the 1998 and 2000 outburst peak levels, and moreover both were spectrally hard throughout the outbursts, and did not show any transition. The most notable observations were the softening of the spectral index at the end of the 2001 decay, and the frequency shift with energy of a Lorentzian PSD component in the 2002 outburst.

Table 4.37: XTE J1550−564

Name :	XTE J1550−564
Mass :	10.6 ± 1.5 $M_\odot$
Distance :	5.6 ± 0.3 kpc
Gal. Coord. :	325.9, -1.8
N_H :	$0.94 \times 10^{22}\,\mathrm{cm}^{-2}$ [a]
1998 Outburst	
Peak Flux[b] :	200, 70[c]
Peak Luminosity[d] :	75.3, 26.3
At the state transition:	
Flux :	0.38
Luminosity :	0.14
Γ_{trans} :	1.83
T_{in} :	0.58
power-law flux :	0.33
2000 Outburst	
Peak Flux :	29.
Peak Luminosity :	10.91
At the state transition:	
Flux :	13.75
Luminosity :	5.17
Γ_{trans} :	2.33
T_{in} :	0.76 keV
power-law flux :	8.35

a From Tomsick, Corbel & Kaaret (2001).
b All fluxes in this table are in 1.5-12 keV band, in units of $10^{-9}\,\mathrm{ergs\,cm^{-2}\,s^{-1}}$
c Flux of the first peak and the plateu level respectively.
d All luminosities in this table are in 1.5-12 keV band, in units of $10^{37}\,\mathrm{ergs\,s^{-1}}$

4.8 GRS J1737−31

GRS J1737−31 was discovered during an outburst with the *SIGMA* detector aboard the *GRANAT* satellite on March 14, 1997 (Sunyaev et al. 1997). A re-analysis of PCA scans in this region showed that the source was detected by this instrument as early as February 17 (Cui et al. 1997b). The outburst peaked about two weeks later (Marshall & Smith 1997). Fig. 4.51 shows the ASM light curve during the outburst.

The *RXTE* and the *GRANAT* analysis revealed that the spectrum was hard throughout the outburst without any state transition (Cui et al. 1997b; Trudolyubov et al. 1999). The inferred Hydrogen column density suggested a source location close to the Galactic center (Cui et al. 1997c). The X-ray spectrum does not show a soft component and can be characterized by a power-law with a hard index of ∼1.6 up to 300 keV from the combined PCA and *SIGMA* data. Even for the *ASCA* data, a soft component was not needed (Ueda et al. 1997).

The timing analysis was conducted by Cui et al. (1997b) using the PCA data from three pointed observations. No high frequency QPOs were detected and the PSD was the typical flat top shape. The rms amplitude was found to be ∼30%.

4.8.1 Observations and analysis

I analyzed the data from 3 pointed *RXTE* observations during the outburst (proposal id P20409). The energy spectral information is summarized in Table 4.38 where all the data are taken from Cui et al. (1997b). For the timing analysis, I used three energy bands, approximately corresponding to 2–5 keV (E1), 5–13 keV (E2) and 13–26 keV band (E3). I also analyzed the spectral data from the pointed observations close to the source, to establish a correct background flux since the source is close to the Galactic center. The correction in the background flux affects the rms amplitude of PSDs as described in Kalemci et al. (2001) and in Section 3.2.2. Note that, the uncertainty in the background can be as high as 20%, which dominates the errors both in the X-ray spectrum and in the rms amplitudes of the PSD components (Cui et al. 1997b).

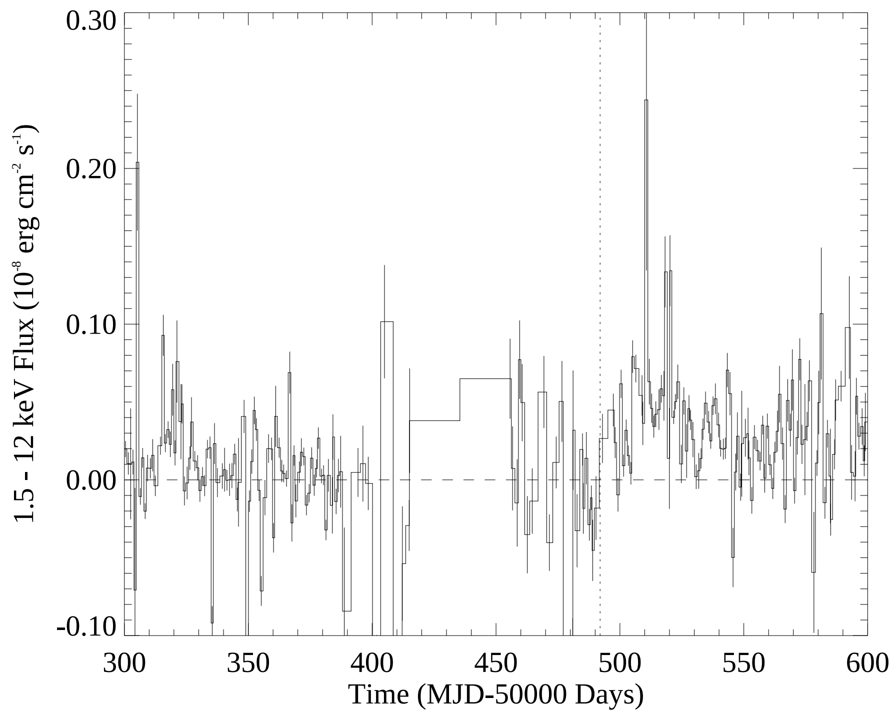

Figure 4.51: ASM light curve of GRS J1737−31. The dotted line shows roughly when the outburst started.

Table 4.38: Spectral fit parameters

Observation	Date[a]	τ[b]	E_c (keV)	Flux[c]
1.......	528.6	1.69 ± 0.07	6.61 ± 0.01	2.30 ± 0.30
2.......	535.5	1.68 ± 0.09	6.62 ± 0.02	1.80 ± 0.30
3.......	540.6	1.76 ± 0.10	6.70 ± 0.10	1.30 ± 0.20

a MJD-50000 days
b All values are from Cui et al. (1997b)
c Observed 2-200 keV flux, in units of $10^{-9}\,\mathrm{cm}^{-2}\,\mathrm{s}^{-1}$.

4.8.2 Temporal fit results

I fit the PSDs in three energy bands with two Lorentzians. The PSDs and their corresponding fits are shown in Figs. 4.52, 4.53, 4.54. The fit parameters can be found in Table 4.39.

The total rms amplitude increases with energy. When I look at individual components, the rms amplitude of the low frequency Lorentzian increases with energy for all three observations. The rms amplitude of the high frequency Lorentzian increases with energy for observations 1, increases or stays constant for observation 2 and shows a turnover for observation 3.

The peak frequencies show an interesting behavior. The low frequency Lorentzian peak frequency does not have an energy dependence, and remains constant within 1σ error. The peak frequency of the second Lorentzian on the other hand increases with energy. This behavior had been also observed in XTE J1550−564 during its hard outburst.

Coherence and lags

I analyzed the coherence and lags for all three observations, between three energy bands. They all show the same characteristics without an evolution. I show the coherence function as a function of frequency in Fig. 4.55 along with the corresponding PSD. The other observations are very similar. There is unity coherence up to ~ 0.1 Hz, and then noise dominates. Between all energy bands and for all three observations, the mean coherence in 0.003 – 0.1 Hz range is consistent with being unity within 1σ error bars. There is no dependence on the shape of the PSD.

The frequency dependent lags are not above the noise level. The mean lag in 0.003 Hz – 0.1 Hz range is consistent with zero with large error bars.

4.8.3 Summary

The spectrum of GRS J1737−31 was hard throughout the outburst, and it did not show a state transition. The physical parameters of this system are not well known. The energy dependent PSD analysis shows that the peak frequencies change with energy. The frequency dependent coherence does not show any dependence on PSD components and the lag spectrum is not above the noise level.

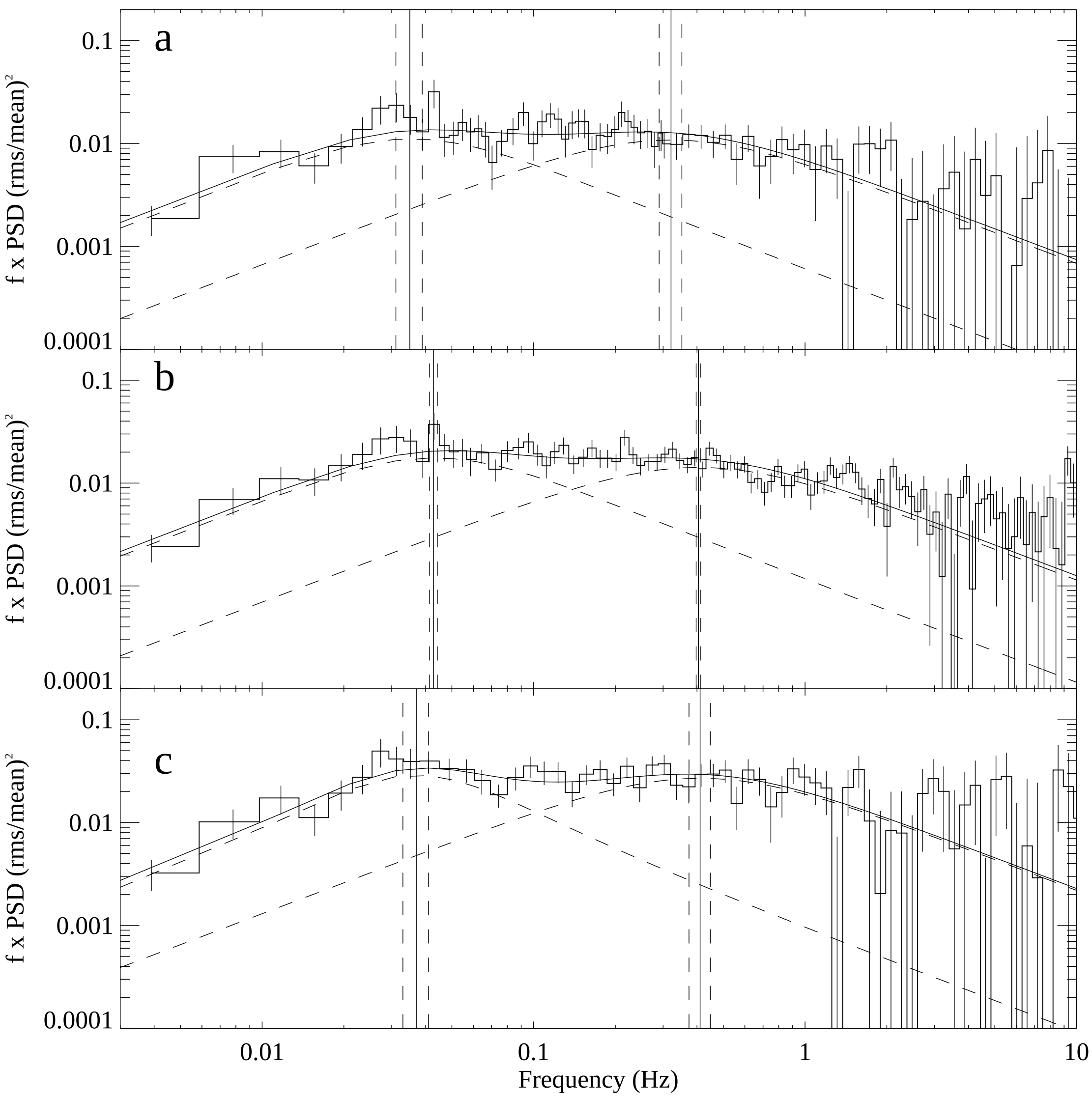

Figure 4.52: Fits to power spectra in (a) E1, (b) E2, and (c) E3 for observation 1. The dashed curves are individual Lorentzian components, the solid curve is the overall fit, the solid vertical lines are peak frequencies of Lorentzians, the dashed vertical lines are their errors.

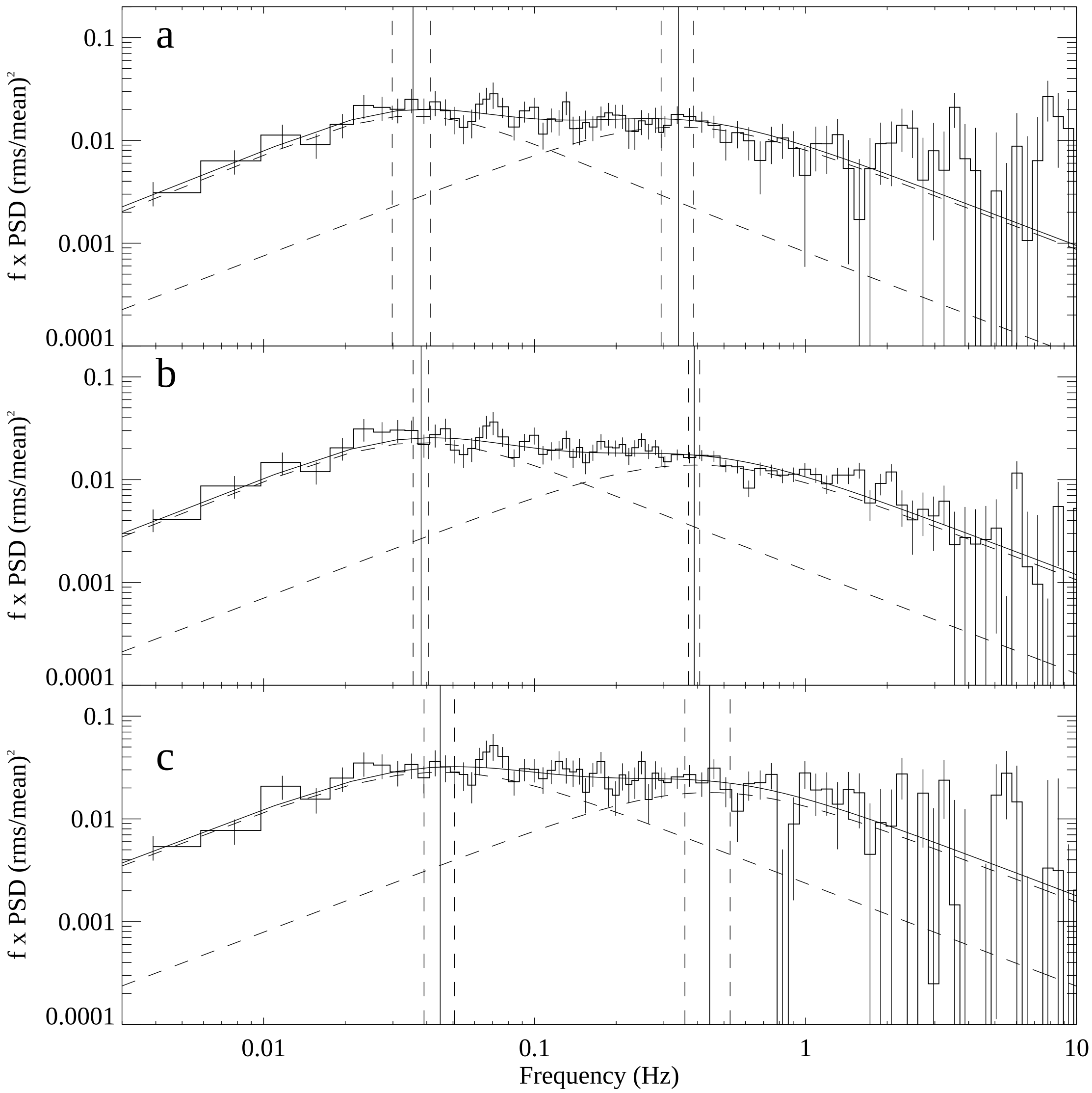

Figure 4.53: Fits to power spectra in (a) E1, (b) E2, and (c) E3 for observation 2. The dashed curves are individual Lorentzian components, the solid curve is the overall fit, the solid vertical lines are peak frequencies of Lorentzians, the dashed vertical lines are their errors.

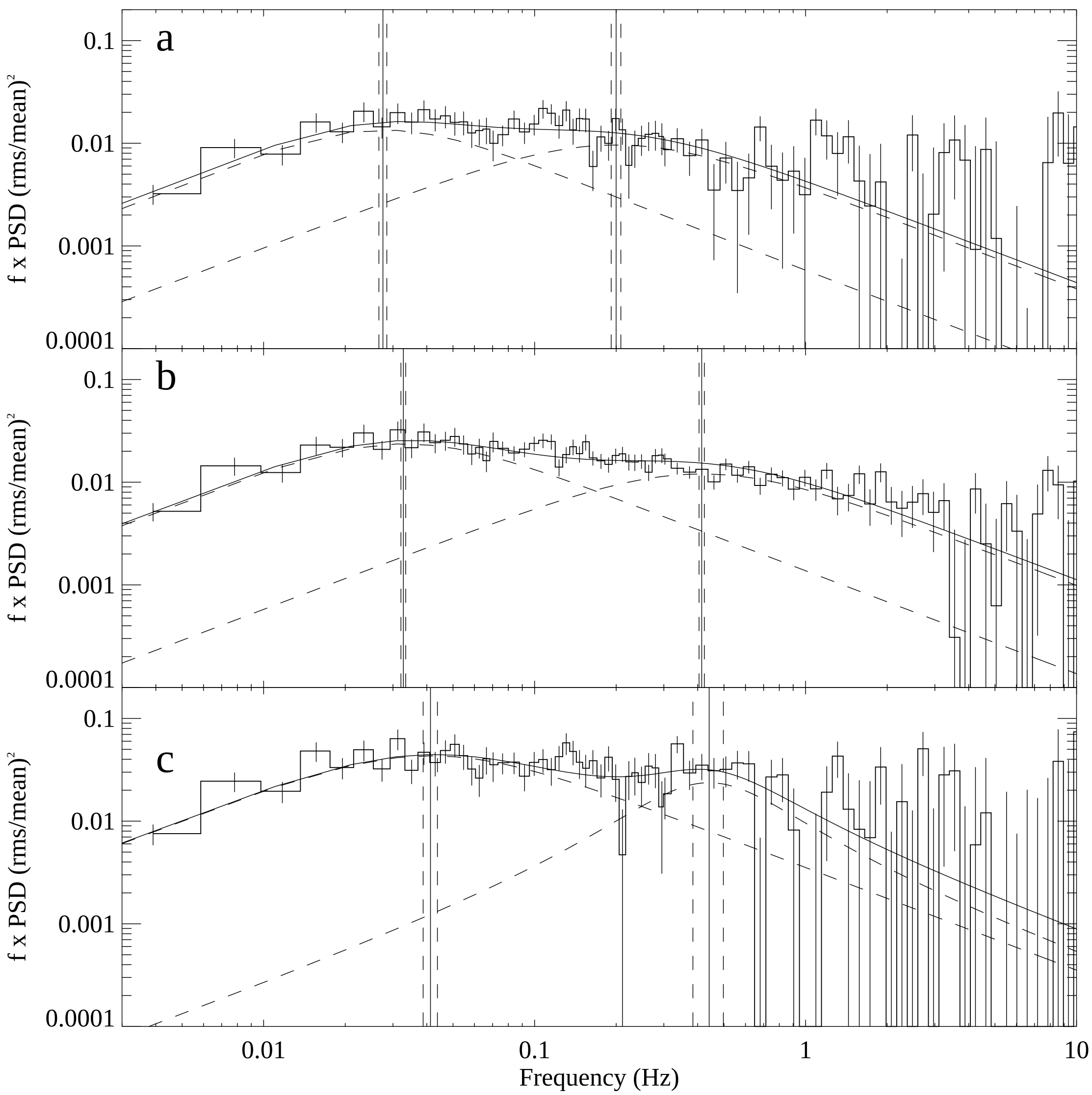

Figure 4.54: Fits to power spectra in (a) E1, (b) E2, and (c) E3 for observation 3. The dashed curves are individual Lorentzian components, the solid curve is the overall fit, the solid vertical lines are peak frequencies of Lorentzians, the dashed vertical lines are their errors.

Table 4.39: Energy dependent temporal fit parameters

Obs/Band	ν_1 (Hz)	rms 1 (%)	ν_2 (Hz)	rms 2 (%)	rms total (%)
1/E1	0.034 ± 0.003	17.79 ± 0.64	0.320 ± 0.030	18.27 ± 0.51	25.50 ± 0.95
1/E2	0.042 ± 0.001	22.37 ± 0.19	0.404 ± 0.007	21.08 ± 0.11	30.74 ± 0.21
1/E3	0.036 ± 0.003	25.71 ± 0.64	0.410 ± 0.036	28.85 ± 0.76	38.64 ± 0.99
2/E1	0.035 ± 0.005	21.52 ± 1.36	0.339 ± 0.046	20.26 ± 1.33	29.56 ± 1.90
2/E2	0.038 ± 0.002	25.37 ± 0.45	0.388 ± 0.018	20.81 ± 0.30	32.81 ± 0.54
2/E3	0.044 ± 0.005	29.49 ± 1.84	0.442 ± 0.084	23.66 ± 2.19	37.81 ± 2.79
3/E1	0.027 ± 0.001	19.62 ± 0.17	0.199 ± 0.008	17.26 ± 0.18	26.20 ± 0.28
3/E2	0.032 ± 0.001	26.62 ± 0.16	0.413 ± 0.009	19.40 ± 0.11	32.94 ± 0.24
3/E3	0.041 ± 0.002	36.80 ± 0.75	0.440 ± 0.056	20.65 ± 0.70	42.20 ± 1.00

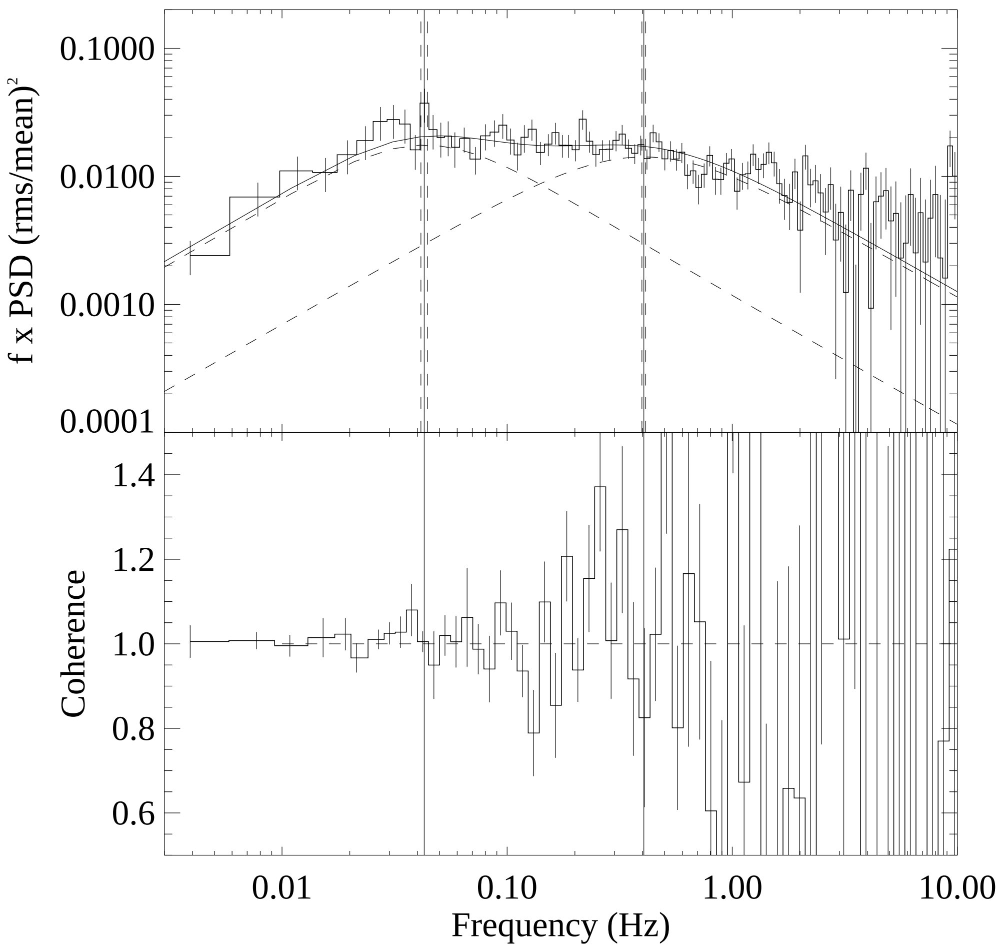

Figure 4.55: Frequency dependent coherence and lags. The top panel is the PSD in 5–13 keV band. The middle panel is the coherence function. The vertical solid lines are the peak frequencies and the dashed lines are the errors in peak frequencies. The horizontal dashed line in the middle panel indicates the unity coherence. The horizontal dashed line indicated unity coherence.

4.9 GS 1354−644

GS 1354−644 was discovered by the ASM on board the *Ginga* satellite on February 13, 1987 during an outburst (Makino 1987), however the source might have been detected earlier and given other names (Revnivtsev et al. 2000, and references therein). The X-ray data were well fitted with a soft diskbb component at ~0.7 keV and a hard power-law index of 2.1. It was also observed in the optical during this outburst (Kitamoto et al. 1990). There are two other transient sources in the error circle of the position of GS 1354−644, Cen X-2 and MX 1353−64. Cen X-2 is a much brighter source, and if all these sources are the same, then GS 1354−644 shows four different spectral states (Brocksopp et al. 2001).

GS 1354−644 observed in outburst again (see fig. 4.56 for the *RXTE* ASM light curve) in 1997 November (Remillard, Marshall & Takeshima 1997). The optical and infrared counterparts were also detected during this outburst (Castro-Tirado et al. 1997; Soria, Bessell & Wood 1997). The optical line emission indicated an accretion disk (Buxton et al. 1998). The source was also detected in radio by Fender et al. (1997b). No indication of an orbital period was detected in any wavelength (Brocksopp et al. 2001). A detailed X-ray spectral and temporal analysis were carried by Revnivtsev et al. (2000), and they showed that the source was in the LS throughout the outburst with no state transition. Further analysis of the PCA observations yielded the presence of a very low frequency QPO with frequency increasing from 13.6 mHz to 46 mHz as the outburst progressed (Brocksopp et al. 2001). Radio observations yielded no extended emission of a jet, and the radio flux does not correlate with the X-ray flux. The radio spectral index indicates an optically thin emission, probably related to relativistic ejections. The index becomes positive at the end of the outburst and might be a result of a self absorbed jet (Brocksopp et al. 2001).

4.9.1 Observations and analysis

I did not conduct any spectral analysis for this source and used values from Revnivtsev et al. (2000). I used three energy bands for the timing analysis, 2–5 keV, 5–13 keV, 13–27 keV band, E1, E2 and E3 respectively. The frequency band for the timing analysis is 0.004 Hz to 256 Hz. I investigated the energy dependence of

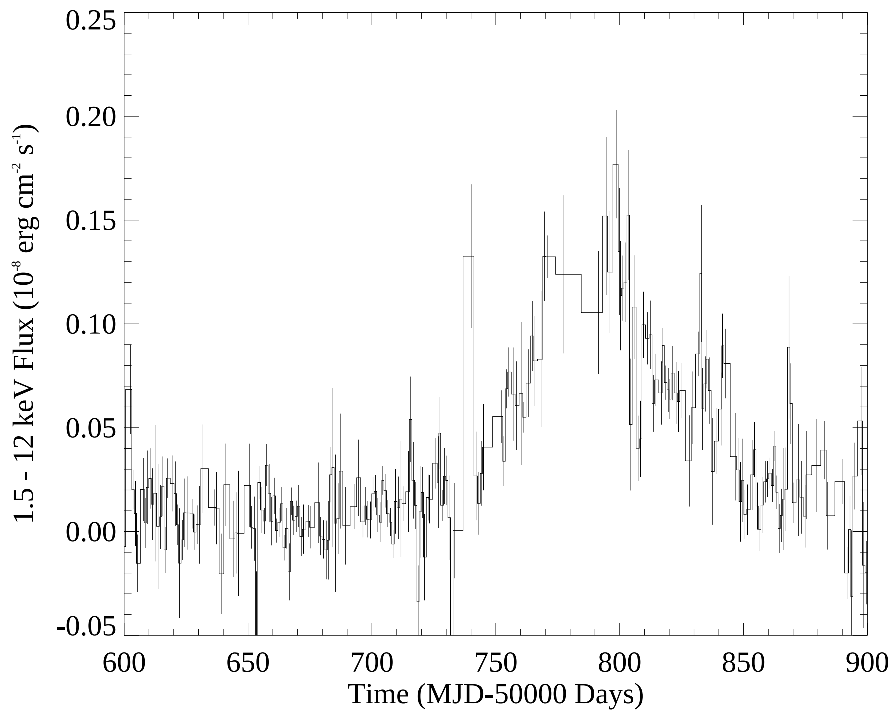

Figure 4.56: The *RXTE* ASM light curve of GS 1354−644.

the PSD components as well as lag and coherence behavior.

4.9.2 Results

Revnivtsev et al. (2000) used various models (cut-off power-law + reflection, broken power-law with cut-off and various Comptonization models) to fit the X-ray spectrum of GS 1354−644, and summarized their results in Table 3. All observations have two common features, they are hard (index of ∼1.5 for a cut-off power-law + reflection model), and they all need a reflection component from a cold accretion disk, a power-law itself is not an acceptable fit. The fits do not require a soft component.

I analyzed the temporal information from the PSDs in different energy bands mentioned in the previous section. Although some observations show limited variability in 27–60 keV band, the noise dominates the power spectrum above 1 Hz, and therefore this band is not used in my analysis. In general, the dependence of peak frequency and rms amplitude on energy is very weak for all observations, as can be seen in Tables 4.40 and 4.41. Following Brocksopp et al. (2001) I separated the observations into four classes, rise 1 (observation 1), rise 2 (observations 2 and 3), top (observations 3 and 4), and decay (observations 5 to 9). In Brocksopp et al. (2001), rise class includes observation one, however, I realized that the PSD of observation 1 is closer in properties to the decay observations than the other rise observations which led me to classify it differently.

Except observation 1, the peak frequencies do not depend on energy within 1σ uncertainty. Because of this weak energy dependence, I only show PSDs from two representative observations in 3 energy bands in Figs. 4.57 and 4.58. The rms amplitudes do not show a strong dependence on energy either. For the observations classified as rise 2, E3 rms amplitude is slightly lower than the rms amplitude of the other bands. Except that, the rms amplitude does not change with energy within 1σ error for all observations for all energy bands.

Coherence and lags

I analyzed the coherence and lags for all observations, between three energy bands mentioned earlier. The frequency dependent analysis do not show any obvious relation of the coherence and lags to the Lorentzian components in the PSD. Fig. 4.59 is a representative case that shows the frequency dependent lags and coherence along with the PSD and the Lorentzian fit. Although coherence seems to be lower at frequencies where Lorentzian components meet in this figure, inspection of the remaining observations did not show such effect.

As I did with the other sources I also analyzed the evolution and energy dependence of integrated lags and coherence. For all observations, 0.02–2 Hz frequency band coherence was above the noise therefore I chose this band for my analysis. Table 4.42 is a result of this effort and points out two important results. First, the lags are positive and increase with energy. Second, the mean coherences are high, above 0.9 throughout the outburst. Observation 1 seems to behave differently, although the coherence is high, the lags are significantly lower, in fact, the integrated lag is consistent with zero. As can be seen in Table 4.40, this observation is peculiar also in terms of peak frequency behavior.

4.9.3 Summary

This is another source for which the whole outburst is in the LS. The energy spectrum does not contain a soft component, moreover a reflection component from the cold accretion disk is required. The energy dependent PSD analysis do not show anything that is particularly interesting, the fit parameters do not change with energy for most of the observations within 1σ error. The frequency dependent coherence does not depend on the position of Lorentzians in the PSD. The mean coherence is very high, generally above 0.98, and the integrated lags increase with energy.

Table 4.40: Temporal fit parameters, I.

O/B[a]	ν_1 (Hz)	rms 1 (%)	ν_2 (Hz)	rms 2 (%)	ν_3 (Hz)	rms 3 (%)	rms total (%)
	Rise 1						
1/E1	0.089 ± 0.002	37.51 ± 0.33	-	-	1.803 ± 0.040	27.11 ± 0.16	46.29 ± 0.36
1/E2	0.116 ± 0.006	37.52 ± 0.74	-	-	2.264 ± 0.098	25.59 ± 0.30	45.41 ± 0.78
1/E3	0.082 ± 0.005	37.84 ± 1.02	-	-	1.419 ± 0.129	25.18 ± 0.67	45.45 ± 1.21
	Rise 2						
2/E1	0.025 ± 0.001	27.39 ± 0.39	0.405 ± 0.015	20.18 ± 0.24	2.338 ± 0.059	22.44 ± 0.15	40.76 ± 0.47
2/E2	0.027 ± 0.002	26.32 ± 0.83	0.378 ± 0.030	18.97 ± 0.63	2.534 ± 0.075	23.47 ± 0.34	40.05 ± 1.04
2/E3	0.028 ± 0.001	23.65 ± 0.37	0.322 ± 0.016	18.20 ± 0.28	2.494 ± 0.083	22.11 ± 0.22	37.15 ± 0.50
3/E1	0.025 ± 0.003	27.37 ± 1.36	0.461 ± 0.070	17.94 ± 2.09	2.334 ± 0.156	23.08 ± 1.21	40.05 ± 2.58
3/E2	0.029 ± 0.001	27.36 ± 0.99	0.411 ± 0.039	13.71 ± 0.46	2.361 ± 0.056	24.89 ± 0.31	39.45 ± 1.04
3/E3	0.027 ± 0.002	24.41 ± 0.94	0.435 ± 0.043	17.85 ± 0.74	2.764 ± 0.183	20.61 ± 0.55	36.60 ± 1.30
	Top						
4/E1	0.053 ± 0.008	26.92 ± 1.79	0.736 ± 0.565	16.10 ± 1.85	2.790 ± 0.857	20.22 ± 1.23	37.33 ± 2.29
4/E2	0.060 ± 0.005	26.95 ± 1.27	0.808 ± 0.19	14.89 ± 2.15	3.415 ± 0.318	20.71 ± 1.49	37.11 ± 2.64
4/E3	0.054 ± 0.006	23.68 ± 0.96	0.548 ± 0.109	16.65 ± 2.30	3.375 ± 0.324	21.68 ± 1.77	36.17 ± 2.77
5/E1	0.064 ± 0.006	27.53 ± 1.056	0.934 ± 0.452	16.39 ± 5.057	3.305 ± 0.638	18.91 ± 3.405	37.20 ± 4.93
5/E2	0.065 ± 0.007	26.58 ± 0.95	0.885 ± 0.458	15.78 ± 1.76	3.270 ± 0.746	21.27 ± 1.90	37.52 ± 1.84
5/E3	0.070 ± 0.006	25.74 ± 0.70	0.678 ± 0.103	7.237 ± 1.74	2.569 ± 0.267	23.04 ± 2.09	35.29 ± 2.27

a Observation/Band

Table 4.41: Temporal fit parameters, II

	Decay						
O/B[a]	ν_1 (Hz)	rms 1 (%)	ν_2 (Hz)	rms 2 (%)	ν_3 (Hz)	rms 3 (%)	rms total (%)
6/E1	0.084 ± 0.007	27.75 ± 0.77	-	-	2.008 ± 0.088	24.95 ± 1.42	37.32 ± 1.53
6/E2	0.088 ± 0.004	27.43 ± 0.49	-	-	2.357 ± 0.058	26.24 ± 0.34	37.96 ± 0.59
6/E3	0.090 ± 0.003	26.00 ± 0.26	-	-	2.322 ± 0.082	24.69 ± 0.28	35.86 ± 0.38
7/E1	0.086 ± 0.003	28.20 ± 0.24	-	-	2.043 ± 0.052	25.51 ± 0.20	38.02 ± 0.31
7/E2	0.086 ± 0.001	27.70 ± 0.09	-	-	2.161 ± 0.015	26.07 ± 0.05	38.04 ± 0.10
7/E3	0.084 ± 0.001	26.58 ± 0.10	-	-	2.183 ± 0.030	27.00 ± 0.11	37.89 ± 0.15
8/E1	0.092 ± 0.000	27.67 ± 0.03	-	-	2.215 ± 0.008	24.66 ± 0.03	37.06 ± 0.04
8/E2	0.095 ± 0.001	26.98 ± 0.09	-	-	2.434 ± 0.020	25.42 ± 0.06	37.07 ± 0.11
8/E3	0.099 ± 0.009	27.11 ± 0.82	-	-	2.525 ± 0.223	24.91 ± 2.78	36.82 ± 2.51
9/E1	0.082 ± 0.003	30.45 ± 0.86	-	-	2.158 ± 0.164	23.23 ± 0.80	38.30 ± 1.17
9/E2	0.085 ± 0.006	27.75 ± 1.00	-	-	2.269 ± 0.104	25.59 ± 1.41	37.75 ± 1.68
9/E3	0.103 ± 0.010	28.89 ± 1.70	-	-	2.360 ± 0.411	24.48 ± 3.16	37.87 ± 3.36

[a] Observation/Band

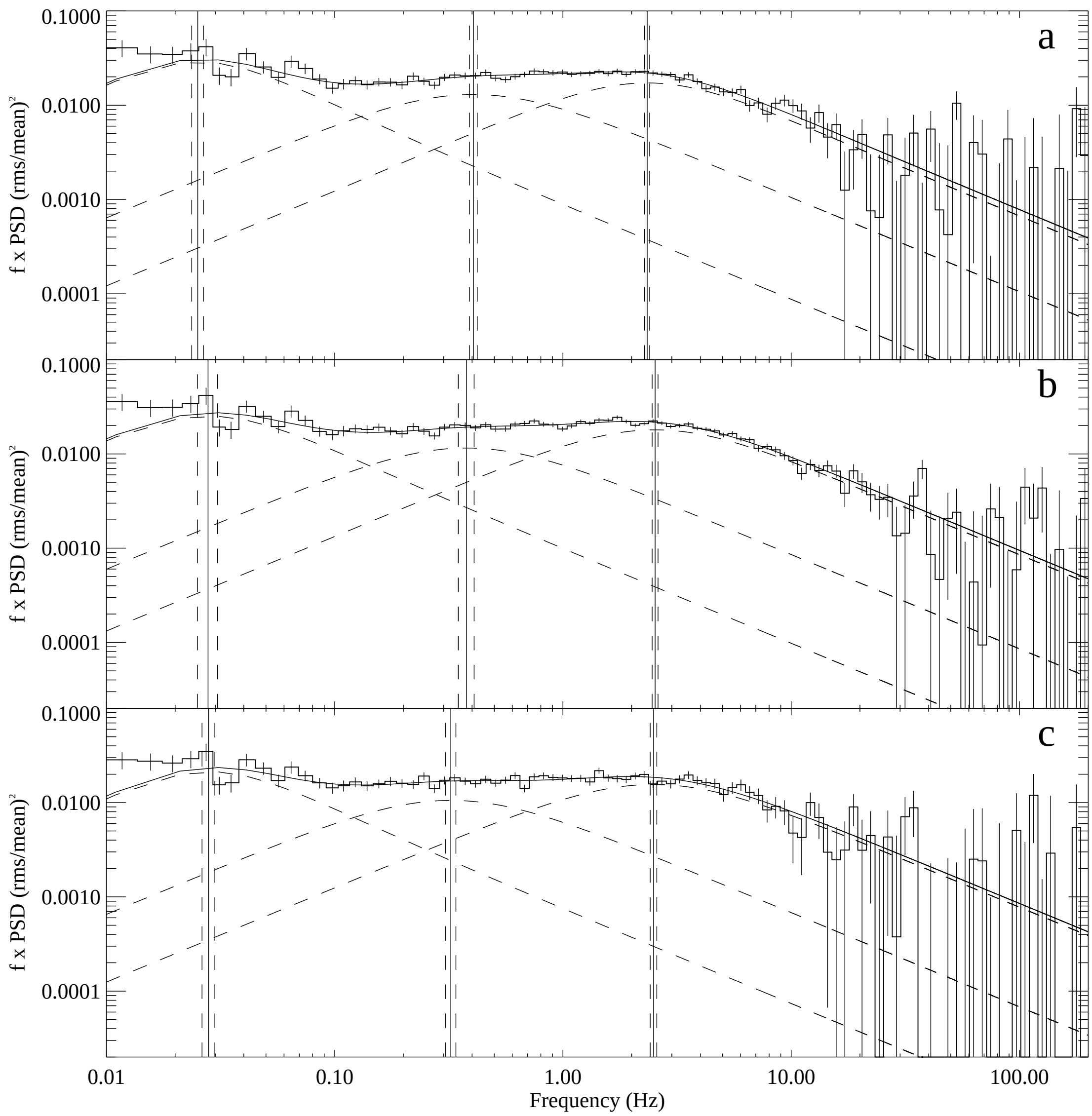

Figure 4.57: Fits to power spectra in (a) E1, (b) E2, and (c) E3 for observation 2 during rise. The dashed curves are individual Lorentzian components, the solid curve is the overall fit, the solid vertical lines are peak frequencies of Lorentzians, the dashed vertical lines are their errors.

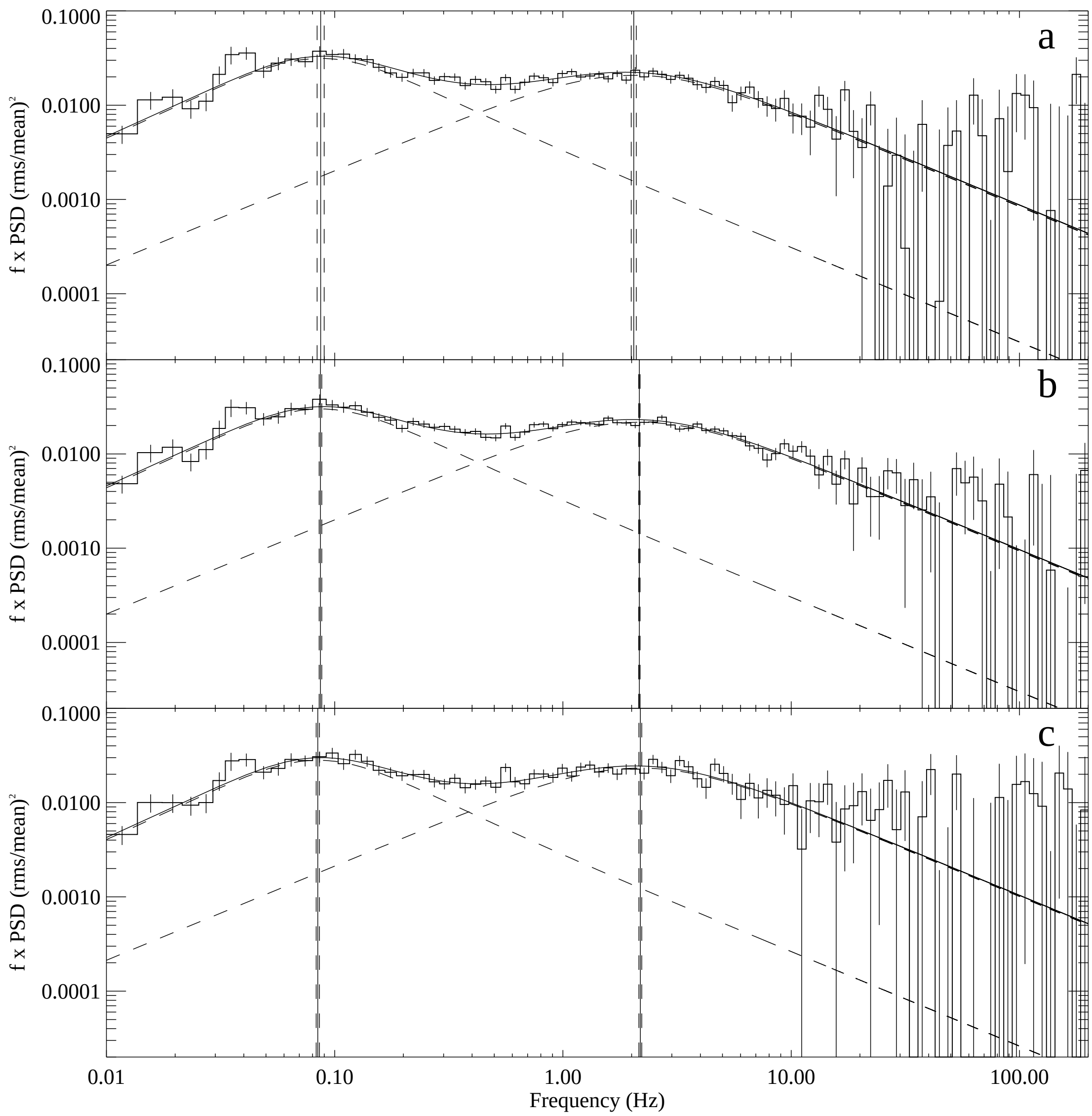

Figure 4.58: Fits to power spectra in (a) E1, (b) E2, and (c) E3 for observation 7 during decay. The dashed curves are individual Lorentzian components, the solid curve is the overall fit, the solid vertical lines are peak frequencies of Lorentzians, the dashed vertical lines are their errors.

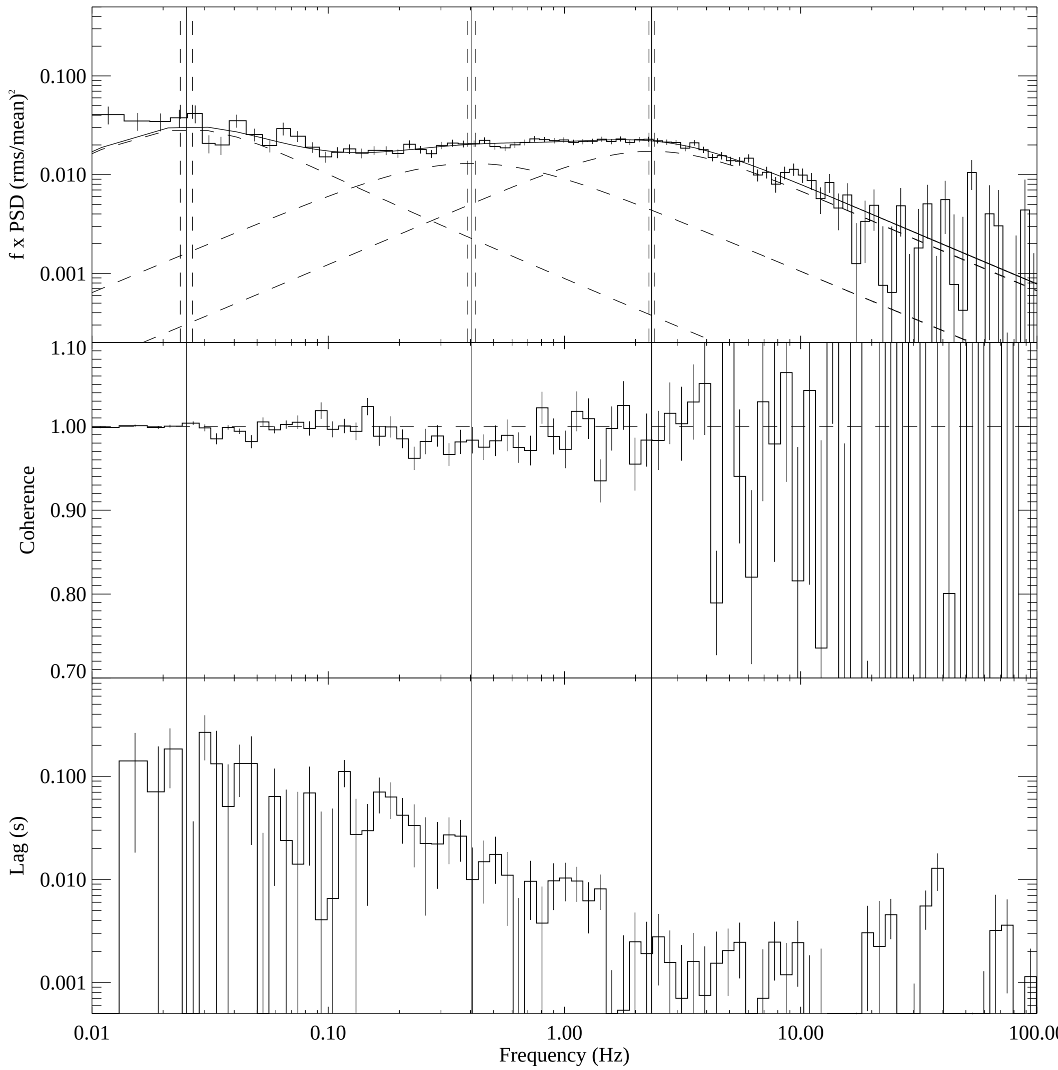

Figure 4.59: Frequency dependent coherence and lags. The top panel is the PSD in 2–5 keV band. The middle panel is the coherence function. The bottom panel is the lag spectrum. The cross spectrum is calculated between E1 and E2. The vertical solid lines are the peak frequencies and the dashed lines are the errors in peak frequencies. The horizontal dashed line in the middle panel indicates the unity coherence.

Table 4.42: Energy dependence of integrated lag and coherence in GS 1354−644.

	E2 vs E1		E3 vs E1	
Obs	Int. Lag$\times 10^3$	Mean Coherence	Int. Lag$\times 10^3$	Mean Coherence
1	2.34 ± 5.73	0.991 ± 0.007	8.03 ± 9.18	0.971 ± 0.013
2	27.03 ± 3.08	0.980 ± 0.004	49.77 ± 4.22	0.953 ± 0.007
3	25.96 ± 2.94	0.989 ± 0.004	44.81 ± 4.20	0.986 ± 0.007
4	25.72 ± 2.98	0.985 ± 0.004	39.24 ± 4.40	0.945 ± 0.008
5	28.79 ± 3.27	0.991 ± 0.005	57.75 ± 4.82	0.976 ± 0.009
6	26.75 ± 3.91	0.975 ± 0.006	67.76 ± 5.66	0.981 ± 0.012
7	27.66 ± 4.20	0.982 ± 0.007	47.47 ± 6.19	0.953 ± 0.013
8	34.03 ± 4.78	0.982 ± 0.008	53.81 ± 7.30	0.952 ± 0.017
9	24.70 ± 6.21	0.968 ± 0.012	44.51 ± 9.47	0.914 ± 0.023

4.10 XTE J1118+480

XTE J1118+480 was discovered with the ASM on *RXTE* on March 29, 2000, and retrospective ASM data analysis indicated that there was a modest previous outburst between Jan 2 - 29 (Remillard et al. 2000). The ASM light curve of the outburst is shown in Fig. 4.60. No X-ray pulsations were detected, and the preliminary (and the subsequent) X-ray spectral analysis showed a hard power-law extending up to 120 keV (Remillard et al. 2000; Wilson & McCollough 2000). Based on these observations and also detection of a broad band noise and a low frequency QPO (Revnivtsev, Sunyaev & Borozdin 2000; Wood et al. 2000), the source was classified as black hole.

XTE J1118+480 has high Galactic latitude (62.3°) placing the source in the Galactic halo (Wagner et al. 2001). Correspondingly, the interstellar extinction is very little which led to a very extensive multi-wavelength campaign. The complete and simultaneous spectral coverage of the source led to the testing of the ADAF model by Esin et al. (2001). The X-ray variability is characterized by repeated flaring on time scales of a few seconds (Wood et al. 2000). The PSD shows a variable frequency LFQPO near 0.1 Hz (Revnivtsev, Sunyaev & Borozdin 2000). Outstandingly, the QPO has been seen also in the EUV and optical (Haswell et al. 2000). The optical observations during the quiescence yielded a mass function of 6.1 ± 0.3 $M_{\odot}$ (McClintock et al. 2001), confirming the black hole nature of the object. Uemura et al. (2002) claimed that the analysis of a super hump observed in optical along with the known mass ratio yielded a black hole mass greater than 9.5 $M_{\odot}$.

The radio counterpart was discovered shortly after the X-ray discovery (Pooley & Waldram 2000). The radio spectrum of the system is persistently inverted, which points out a compact radio jet (Fender et al. 2001, and references therein). Recently, the multi-wavelength observations of XTE J1118+480 were used to challenge the canonical views of the black hole systems. Markoff, Falcke & Fender (2000) claimed that the whole spectrum is a result of synchrotron emission from a very powerful jet, instead of the canonical accretion disk - Compton corona interpretation.

In X-rays, detailed timing and some spectral analysis with the *USA* instrument and with the *RXTE* were presented by Wood et al. (2000). They observed a QPO with a fractional rms amplitude of ∼5% and a FWHM of ∼0.01 Hz. The QPO

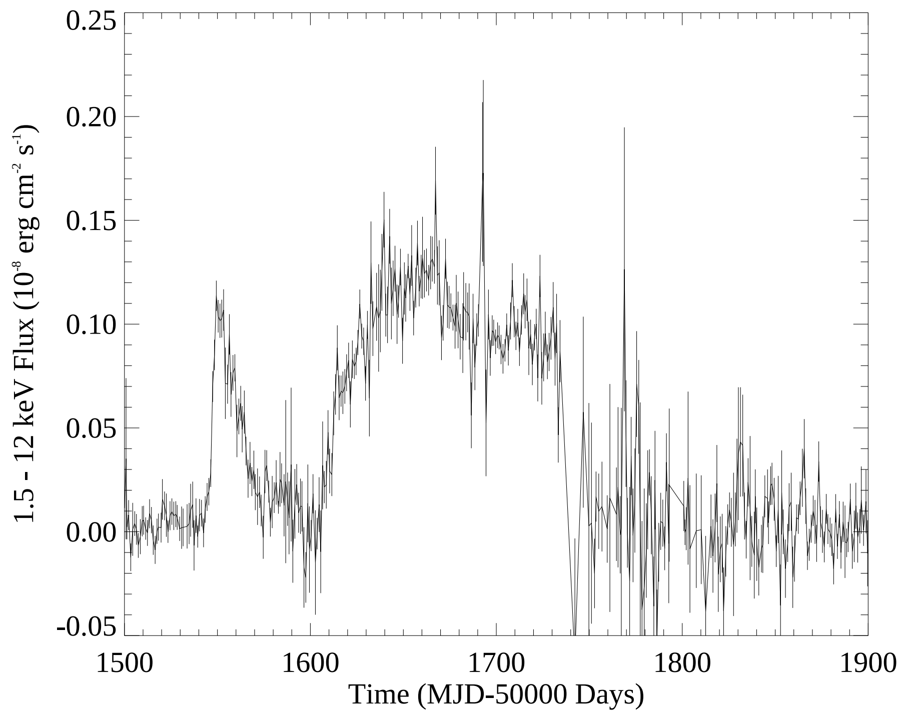

Figure 4.60: The *RXTE* ASM light curve of XTE J1118+480.

frequency monotonically moved up, although during the same period the ASM flux already started to decrease. They established that the outburst was hard throughout the outburst. The discussion of the decay part of the outburst in X-rays has never been reported to the best of my knowledge.

4.10.1 Observations and analysis

I analyzed the data from 11 observations at the end of the decay as the source was going into quiescence (proposal ids P50407, P50133). Earlier observations were discussed in detail by Wood et al. (2000). For spectral analysis, I used a spectral model with only a power-law following Wood et al. (2000), which was an excellent fit for all of the observations. Due to high latitude, no absorption was needed in the model. The timing analysis was done in three energy bands when possible. Unfortunately, the two observation sets I used for this analysis have different data modes which resulted in slightly different energy bands. For all observations except 3 and 6, my bands are roughly 2–6 keV (E1), 6–15 keV (E2) and 15–30 keV (E3). For observations 3 and 6 they are 2–7.5 keV, 7.5–15 keV and 15–30 keV. I studied the evolution of spectral and temporal properties during the decay, energy dependence of PSD fits, and lags and coherence among the given energy bands.

4.10.2 Results

Spectral and temporal evolution

The source was in the LS throughout the outburst before my observations (Wood et al. 2000), and my spectral and temporal analysis showed that it remained in the LS during the decay. Until the very low flux levels, the spectral fits with a power-law indicated an index of ~1.75 as seen Table 4.43, consistent with the analysis of the previous observations by Wood et al. (2000).

For temporal analysis, I first obtained PSDs in the 2–15 keV and and fit them with Lorentzians. The fit results are shown in Table 4.43. I plot the evolution of spectral and temporal properties in Fig. 4.61. The first seven observations are during the peak of the outburst, and for these observations there is no change in temporal and spectral properties. As the source decayed in flux, an evolution is observed. The power-law index softened, the rms amplitude decreased and the peak frequency of the first Lorentzian decreased. (For the last two observations that show variability, due to poor statistics, the peak frequency of the second Lorentzian is not well determined, as well as its total rms amplitude.)

To show the Lorentzian fits and to make the peak frequency decaying of the Lorentzians more clear, I also plot the PSD of last four observations that show variability (observations 7–10) in Fig. 4.62.

Energy dependence of PSD components

As I did for other sources, I also analyzed the energy dependence of the PSD fit parameters. The fit results are given in Table 4.44. There seems to be no strong dependence of any parameters to energy. Most of the parameters are consistent with each other within 2σ error.

Table 4.43: Spectral and temporal fit parameters of XTE J1118+480.

Obs	Date[a]	Γ	Total flux[b]	ν_1 (Hz)	ν_2 (Hz)	Total rms (%)
1	1710.79	1.742 ± 0.006	1.240	0.084 ± 0.006	1.617 ± 0.146	32.71 ± 0.92
2	1715.42	1.757 ± 0.005	1.286	0.122 ± 0.006	2.739 ± 0.185	32.61 ± 0.58
3	1719.88	1.741 ± 0.005	1.213	0.104 ± 0.001	1.910 ± 0.032	33.61 ± 0.32
4	1723.17	1.720 ± 0.005	1.297	0.122 ± 0.006	2.204 ± 0.133	31.38 ± 0.50
5	1729.79	1.759 ± 0.005	1.105	0.112 ± 0.004	2.273 ± 0.119	31.91 ± 0.42
6	1733.83	1.744 ± 0.003	0.931	0.122 ± 0.004	1.970 ± 0.105	30.81 ± 0.34
7	1738.67	1.741 ± 0.006	1.049	0.133 ± 0.008	3.581 ± 0.400	30.69 ± 0.63
8	1747.79	1.850 ± 0.008	0.394	0.094 ± 0.006	1.582 ± 0.200	29.93 ± 0.77
9	1750.83	1.883 ± 0.011	0.227	0.058 ± 0.002	0.994 ± 0.282	29.84 ± 0.40
10	1755.04	1.901 ± 0.017	0.095	0.032 ± 0.003	1.431 ± 0.318	32.03 ± 1.48
11	1759.88	2.090 ± 0.068	0.025	-	-	-
12	1760.29	2.058 ± 0.076	0.020	-	-	-

a MJD-50000 days
b 3–25 keV PCA flux in units of $10^{-9}\, ergs\, cm^{-2}\, s^{-1}$

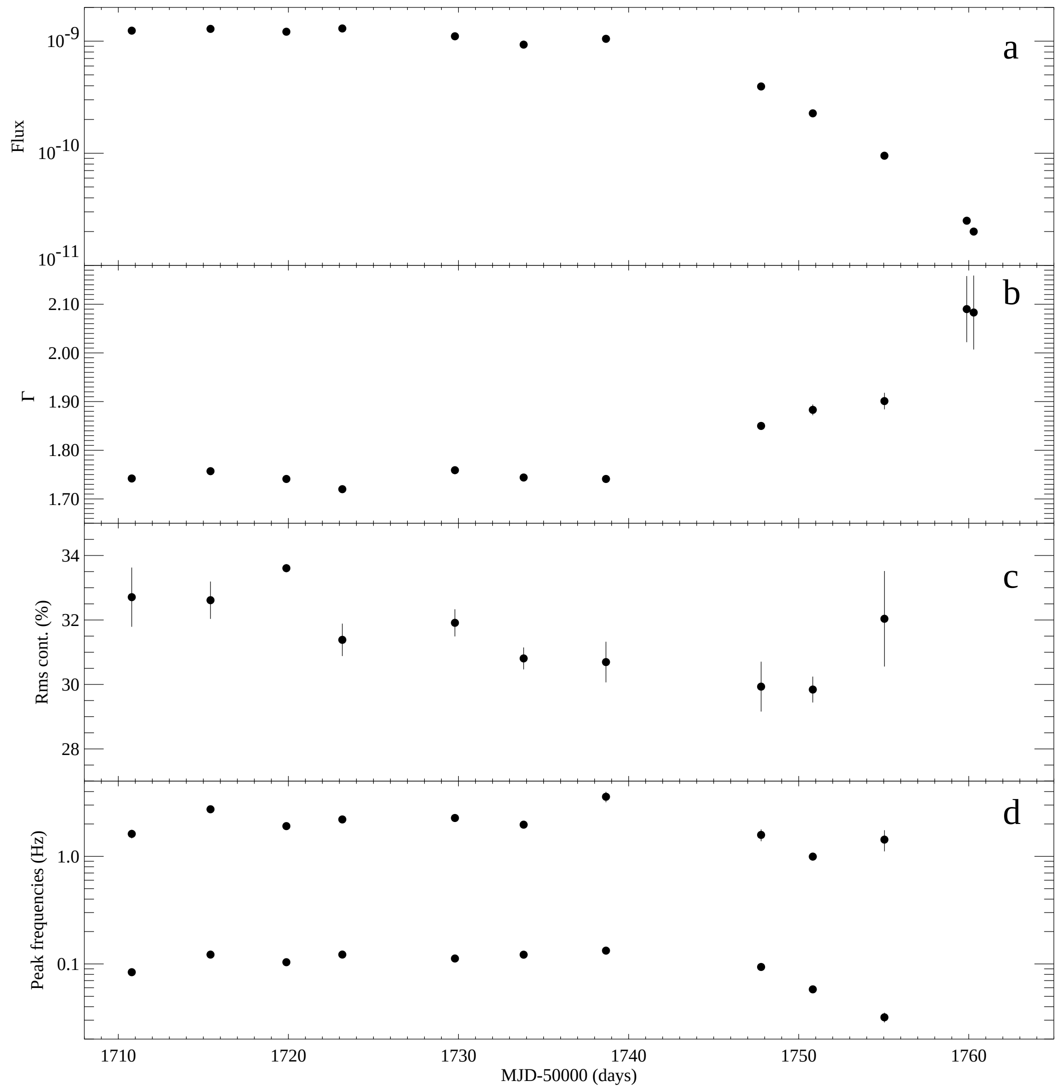

Figure 4.61: Spectral and temporal evolution of XTE J1118+480. (a) Flux in 3–25 keV band in units of $10^{-9}\,\mathrm{ergs\,cm^{-2}\,s^{-1}}$. (b) power-law index. (c) Total rms amplitude in 1–15 keV band.(d) Peak frequencies of Lorentzians

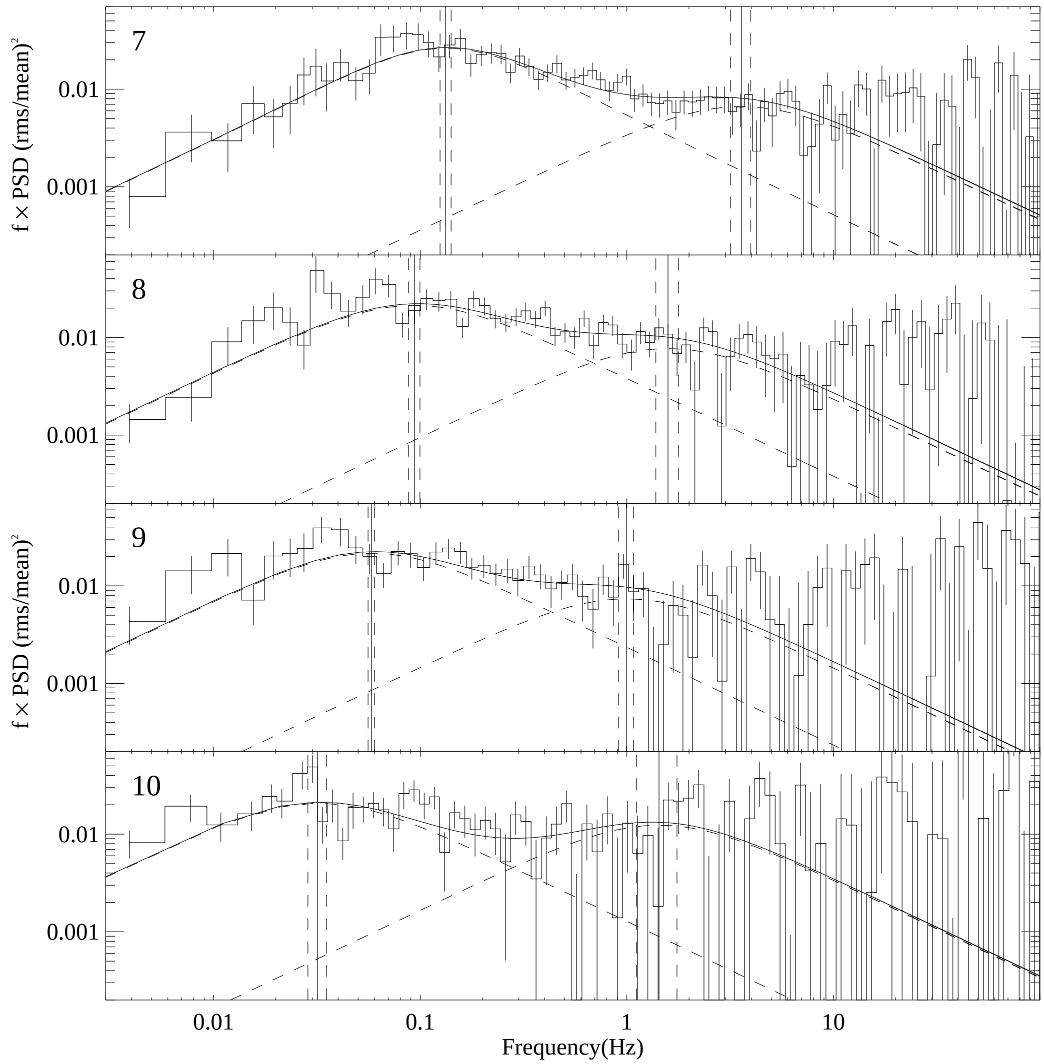

Figure 4.62: Lorentzian fits to PSD of XTE J1118+480. The observation number is shown on the left hand corner in each panel. The solid line is the overall fit and the dashed lines are the individual Lorentzian components. The vertical solid line is the peak frequency and the dashed vertical lines are the errors in peak frequencies.

Table 4.44: Energy dependent temporal fit parameters for XTE J1118+480.

Obs/band	ν_1	rms 1 (%)	ν_2	rms 2 (%)	total rms (%)
1/E1	0.077 ± 0.002	26.49 ± 0.32	1.287 ± 0.073	17.48 ± 0.25	31.73 ± 0.41
1/E2	0.081 ± 0.002	29.22 ± 0.35	1.341 ± 0.075	18.36 ± 0.27	34.51 ± 0.44
2/E1	0.122 ± 0.006	26.36 ± 0.54	2.609 ± 0.253	16.56 ± 0.48	31.13 ± 0.72
2/E2	0.093 ± 0.009	29.01 ± 0.23	1.706 ± 0.006	18.44 ± 0.17	34.37 ± 0.28
3/E1	0.112 ± 0.001	29.01 ± 0.11	2.220 ± 0.055	15.23 ± 0.10	32.77 ± 0.14
3/E2	0.100 ± 0.003	30.28 ± 0.34	1.791 ± 0.129	17.84 ± 0.38	35.15 ± 0.48
4/E1	0.098 ± 0.005	25.49 ± 0.50	1.545 ± 0.124	17.22 ± 0.40	30.76 ± 0.63
4/E2	0.115 ± 0.007	26.20 ± 0.46	1.204 ± 0.104	17.21 ± 0.43	31.35 ± 0.62
5/E1	0.106 ± 0.004	26.47 ± 0.40	1.743 ± 0.138	15.81 ± 0.36	30.83 ± 0.53
5/E2	0.106 ± 0.003	29.10 ± 0.41	2.444 ± 0.196	16.16 ± 0.39	33.29 ± 0.55
6/E1	0.116 ± 0.004	26.59 ± 0.29	1.576 ± 0.111	14.47 ± 0.29	30.27 ± 0.39
6/E2	0.117 ± 0.005	27.28 ± 0.32	1.472 ± 0.136	16.20 ± 0.43	31.73 ± 0.50
7/E1	0.112 ± 0.003	24.17 ± 0.19	1.175 ± 0.072	15.51 ± 0.24	28.72 ± 0.29
7/E2	0.120 ± 0.009	27.77 ± 0.52	2.349 ± 0.384	14.81 ± 0.75	31.48 ± 0.81
8/E1	0.071 ± 0.006	25.62 ± 0.56	0.567 ± 0.095	15.46 ± 0.57	29.93 ± 0.77
8/E2	0.081 ± 0.007	25.67 ± 0.60	0.907 ± 0.150	17.82 ± 0.85	31.26 ± 0.98
9/E1	0.058 ± 0.002	25.38 ± 0.31	1.475 ± 0.174	15.36 ± 0.55	29.67 ± 0.55
9/E2	0.034 ± 0.007	22.16 ± 2.61	0.204 ± 0.093	20.79 ± 7.06	30.39 ± 6.89
10/E1	0.029 ± 0.001	25.91 ± 0.34	-	-	25.91 ± 0.34
10/E2	0.030 ± 0.001	27.80 ± 0.43	-	-	27.80 ± 0.43

Coherence and lags

I also analyzed the lag and coherence behavior of XTE J1118+480 for all observations. The crude first results are, very high coherence between E1 and E2 and no measurable lags. The frequency dependent analysis did not yield any obvious dependence on the position of the Lorentzian components in the PSD. In more detail, all observations have coherence function above the noise level up to 0.2 Hz, and for the first 4 observations up to 2 Hz. In 0.02–0.2 Hz band the mean coherence is above 0.99 until observation 7. After observation 7, it is still high, but due to less count rates and statistics, the errors get bigger. Nevertheless, within 1σ the mean coherences after observation 7 are consistent with the ones observed before observation 6. The mean coherence between E1 and E3 are slightly lower than that of between E1 and E2 ($\sim$0.97 compared to 0.99). For all energy bands and frequency bands the lags are below the noise level, and the mean values are consistent with 0.

4.10.3 Summary

The importance of this source is due to its high latitude and therefore very small extinction which makes it possible to conduct extensive multi-wavelength campaigns. It is also in the list of the hard outburst systems which did not show a state transition. Although it did not show a transition, the spectral and temporal properties evolved at the end of the decay; as flux decreased, the power-law index softened and the peak frequencies decayed. The softening of the index might be a natural result of an ADAF system and it will be discussed later in Chapter 5. The temporal fit parameters did not show any dependence on energy. The lags between bands were not measurable and were consistent with zero and the mean coherence for all observations were very high, above 99%.

4.11 XTE J1859+226

XTE J1859+226 was discovered by the ASM on *RXTE* on October 9, 1999 (Wood et al. 1999). The outburst light curve is approximately a FRED, as seen in Fig. 4.63. The outburst started hard, and softened close to the peak. The decline phase showed a plateau ∼60 days after the maximum where the spectrum hardened slightly. QPOs were detected in 0.5 – 10 Hz range and also in 150 – 200 Hz range (Markwardt, Focke & Swank 2001). Narrow high frequency QPOs were marginally detected at 187 and 150 Hz (Cui et al. 2000). The centroid frequency of these QPOs might be variable, with a maximum at 250 Hz. LFQPOs were also detected throughout the outburst in the range 0.5 – 10 Hz, often with triplet peaks with the middle peak being the strongest, similar to some XTE J1550−564 observations.(Markwardt, Focke & Swank 2001). The *RXTE* energy spectrum can be described by a multicolor disk-blackbody and a power-law with reflection (Markwardt 2001).

The radio counterpart was discovered on October 11, 1999 with the *Ryle Telescope* and *VLA* (Pooley & Hjellming 1999). A day later, the optical counterpart was discovered (Garnavich, Stanek & Berlind 1999). The *VLA* observations on December 1, 1999 appear to be resolved (Brocksopp et al. 2002) and therefore XTE J1859+226 might be a microquasar. Five flares (relativistic ejections) have been observed in radio. These ejection events are well correlated with the hard X-rays. Most of the time, the radio spectral index is either optically thin or consistent with zero, and it is possible that both components are present (Brocksopp et al. 2002). During the radio outbursts, the low and high frequency QPOs disappeared.

The source has been observed in X-rays with *RXTE* as it passed into quiescence. There was low level of activity in X-rays in the summer of 2000 (Tomsick & Heindl 2000). A potential modulation at 9.15 h was discovered in optical (Garnavich & Quinn 2000). More recently, a mass function of $7.4 M_\odot$ has been determined confirming the black hole nature of the source (Filippenko & Chornock 2001). The source is at Galactic latitude $+8.5°$. Optical extinction measurements suggest a minimum distance of 1-3 kpc. The PCA and HEXTE fits to to energy spectrum gives a neutral hydrogen column density of N_H=$1.1 \times 10^{22}\,\mathrm{cm}^{-2}$ (Markwardt 2001).

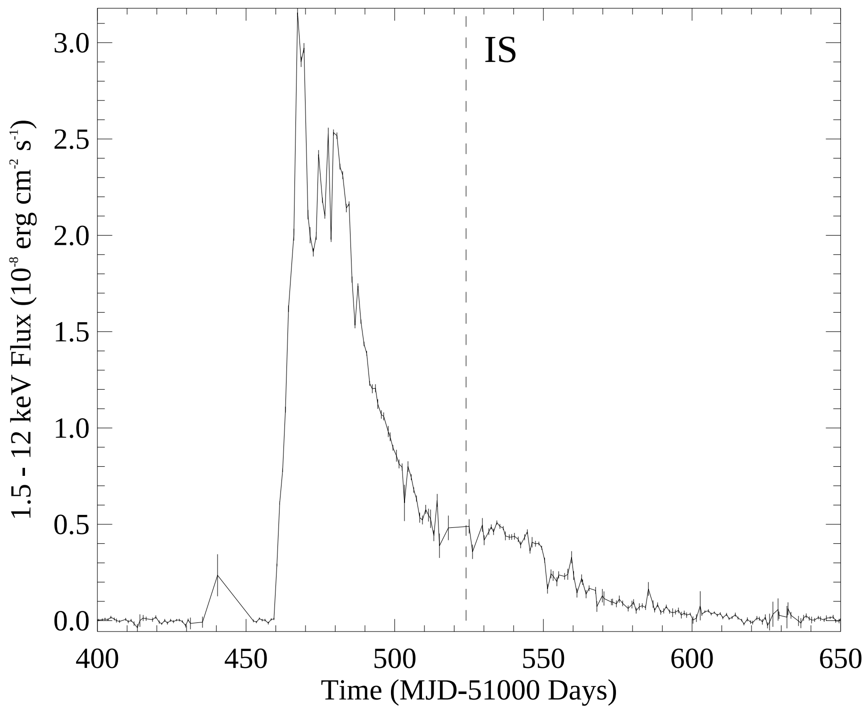

Figure 4.63: The *RXTE* ASM light curve of XTE J1859+226. The dashed line shows the approximate date for the transition to the intermediate state.

4.11.1 Observations and analysis

I analyzed the archival *RXTE* data of XTE J1859+226 during outburst decay. I started my analysis at the date which corresponds to 15 cts/s in ASM based on our successful triggering criteria of *RXTE* observations to catch the state transition for bright X-ray transients. This date corresponds to 11 November 1999, MJD 51510. I performed spectral and temporal analysis of all observations after this date until the source decayed into quiescence, which added up to 48 observations. The data set includes observations from proposal ids P40124, P40122, P40440 and P50401. For all observations, I extracted light curves in 2 - 6 keV (E1), 6 - 15 keV (E2) and 15 - 30 keV band (E3). Up to 15 keV, I used binned data modes, and above 15 keV I used the event mode.

A state transition was found on MJD 51524, which turned out to be a transition from HS to IS rather than to the LS as will be discussed in the next section.

Table 4.45: Spectral fit results in XTE J1859+226.

Obs	Time[a]	T_{in}	τ	Tot. Flux[b]	Ratio 1[c]	Ratio 2[d]
1	523.94	0.630 ± 0.002	2.371 ± 0.012	2.278	0.583	0.706
2	524.94	0.635 ± 0.002	2.361 ± 0.011	2.371	0.625	0.636
3	525.35	0.632 ± 0.002	2.336 ± 0.016	2.188	0.562	0.727
4	527.00	0.624 ± 0.003	2.374 ± 0.009	2.554	0.695	0.596
5	527.74	0.627 ± 0.005	2.380 ± 0.015	2.566	0.690	0.601
6	530.13	0.622 ± 0.002	2.505 ± 0.013	2.437	0.602	0.655
7	537.13	0.661 ± 0.002	2.349 ± 0.019	2.372	0.468	0.779
8	547.77	0.607 ± 0.002	2.301 ± 0.011	1.923	0.639	0.673

[a] MJD-51000 days
[b] Unabsorbed PCA flux in 3 – 25 keV band in units of $10^{-9}\,\mathrm{ergs\,cm^{-2}\,s^{-1}}$.
[c] Ratio of the power-law flux to the total flux in 3 – 25 keV band.
[d] Ratio of the diskbb flux to the total flux in E1.

4.11.2 Spectral and temporal fits

Spectral fit results

The spectral fits were performed on the PCA data in 3 - 25 keV band with a model consisting of a multicolor disk-blackbody, a power-law, a smeared edge and absorption. Some observations also required a weak iron line with no significant effect on the diskbb and power-law fit parameters. The column density of Hydrogen was fixed to N_H=1.1 $\times$ $10^{22}\,\mathrm{cm}^{-2}$ as reported by Markwardt (2001). The results of temporal fits are summarized in Table. 4.45 and in Fig. 4.64. In the table, only the observations which show significant variability ($\geq$15% in E2) are shown. In Fig. 4.64, these observations are shown with filled circles. Strong variability is observed after MJD 51523, which marks a possible state transition. The power-law index and the inner disk temperature do not show a sharp change, on the other hand the power-law flux almost doubles compared to observations that do not show variability (see Fig. 4.64). There is a threshold power-law flux $\sim 1.0 \times 10^{-9}\mathrm{ergs\,cm^{-2}\,s^{-1}}$ above which there is significant variability and below which no variability. With the steep $\sim$2.4 power-law index and the rms amplitudes of 15% in E2, this fits the definition of a transition into the IS from HS.

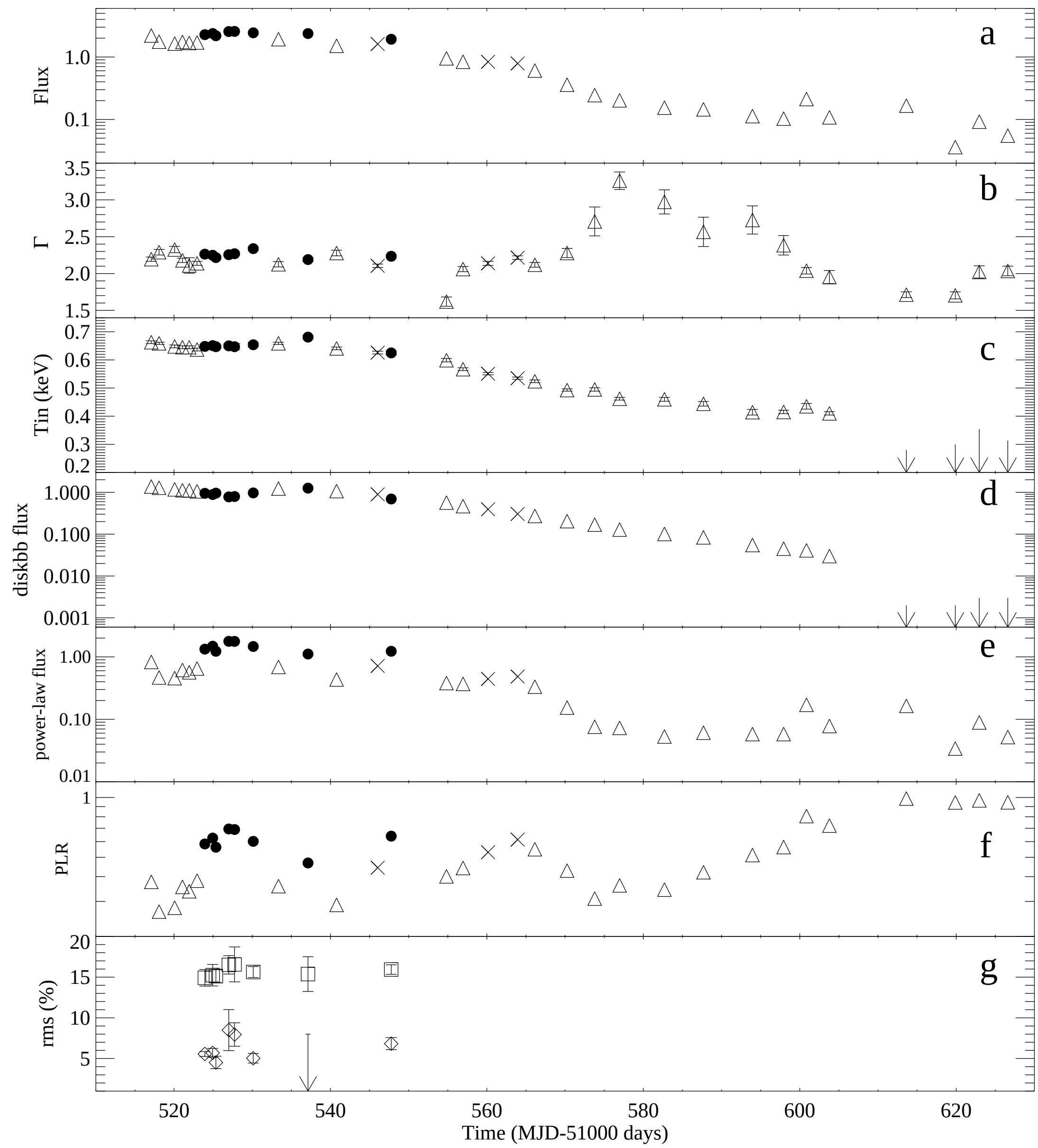

Figure 4.64: Results of the spectral and temporal fits from XTE J1859+226: (a) 3–25 keV flux (all fluxes in this figure are in 3–25 keV band, unabsorbed, in units of $10^{-9}\mathrm{ergs\,cm^{-2}\,s^{-1}}$). (b) Power-law index. (c) Inner disk temperature. (d) Diskbb flux. (e) power-law flux. (f) PLR, ratio of the power-law flux to the total flux. Different plotting symbols represent the level of variability. Filled circles represent strong variability (more than 15% rms amplitude in 6–15 keV), crosses show little variability (less than 10% rms amplitude) and open tringles show no variability. (g) Rms amplitude of variability in different bands for those with strong variability. Diamonds represent E1 values, squares represent E2 values.

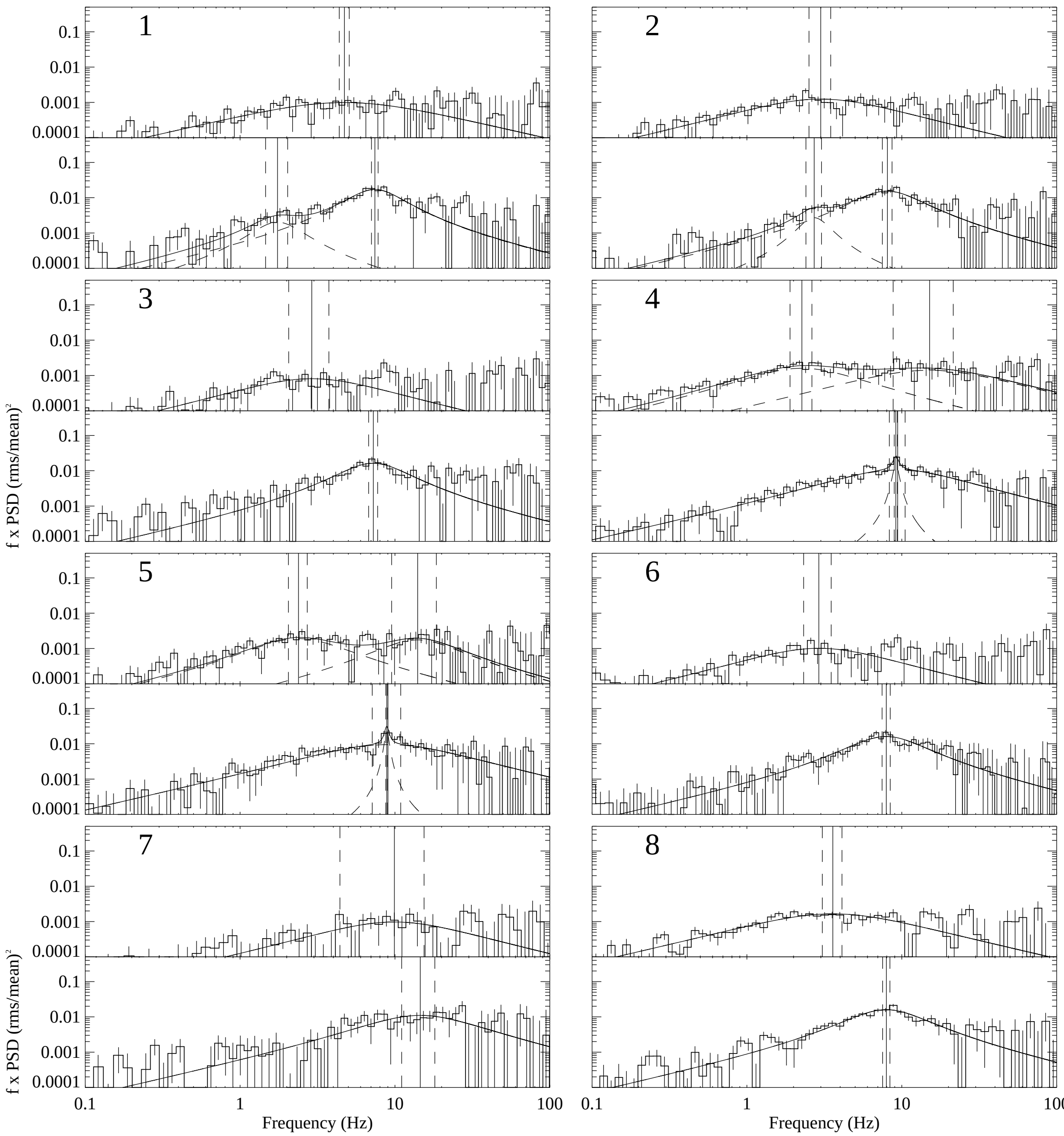

Figure 4.65: Lorentzian fits to all observations that show significant variability. The upper panels are E1 and the lower panels are E2 PSDs. The dashed Lorentzians show individual components and the solid curve is the overall fit. The solid vertical lines are the peak frequencies of the Lorentzians whereas the dashed vertical lines indicate their errors. The numbering of the observations is the same as in Table 4.45.

Temporal fits

I extracted light curves in E1 and E2 and calculated the PSDs for those bands. (I also calculated the PSDs for higher energy bands which showed no variability.) In

Table 4.46: QPOs in IS of XTE J1859+226.

Obs	Time (MJD days)	Freq. (Hz)	FWHM (Hz)	rms (%)
4	51527.00	9.15 ± 0.09	0.86 ± 0.20	5.28 ± 0.60
5	51527.74	8.96 ± 0.22	1.27 ± 0.56	5.46 ± 1.14

Fig. 4.65, I show all the fits to the observations which has strong variability. In this figure, the upper panels are E1, and lower panels are E2. The narrow QPOs are rarely present and their properties are summarized in Table 4.46. There are some cases in which the PSD is only slightly above the noise level which are shown by crosses in Fig. 4.64. The strength of variability is hard to constrain for these cases, and the upper limits for the rms amplitudes are less than 10%. The PSDs are strongly energy dependent, which is characteristic of IS observations. For the cases where both energy band PSDs are fitted with one Lorentzian, the higher energy PSD peaks at a higher frequency. This behavior is similar to what we observe for XTE J1650−500 during the transition. Again, similar to this observation, the rms amplitude of E2 is much stronger than the rms amplitude of E1. The rms amplitudes in E1 and E2 are also shown in Fig. 4.64 (g).

The two observations which have the strongest power-law flux also show QPOs in addition to the broad Lorentzians. The properties of the QPOs are shown in Table. 4.46.

Coherence and lags

I calculated the mean coherence and integrated lag in 1 – 10 Hz band between E1 and E2. The results are shown in Fig. 4.66.

The coherence values are low, and this could easily be explained by the strong diskbb emission in E1 compared to E2 (see Table. 4.45). The cross-spectrum due to this strong disk emission is too noisy to do any frequency dependent studies. When measurable, the lags are positive and of the order of 100 ms. Neither the integrated lag nor the mean coherence evolve significantly with time or show different behavior as observed in the state transitions of XTE J1650−500 and GX 339−4.

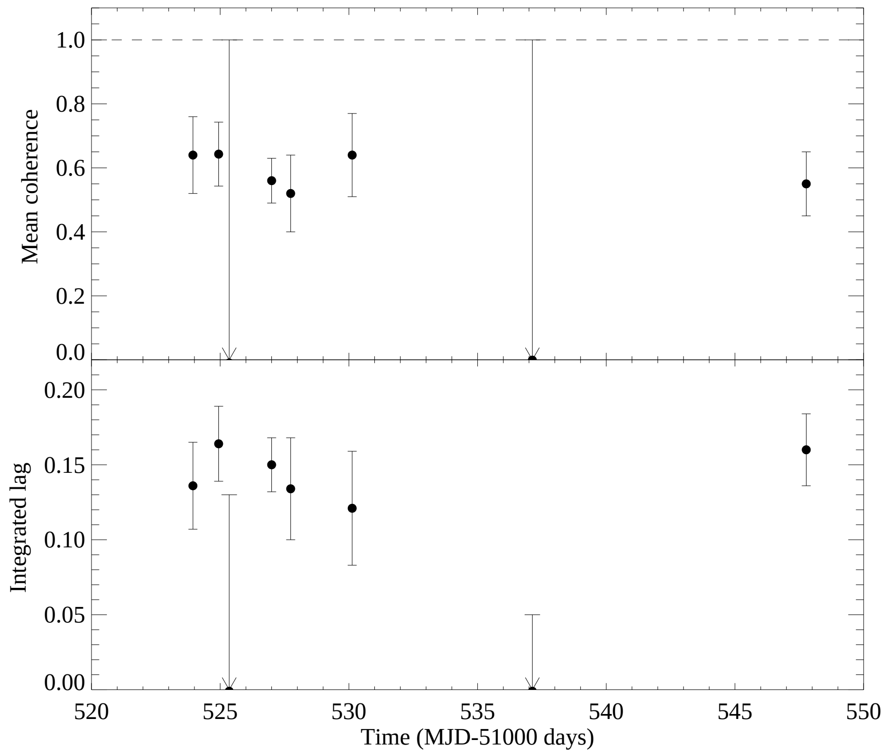

Figure 4.66: Integrated lags (upper panel) and mean coherence (lower panel) in 1 – 10 Hz of XTE J1859+226. The dashed line indicates perfect coherence. The upper limits are for 90% confidence limits.

Decay to quiescence

I analyzed all the available data to the lowest flux levels detectable by PCA during the decay hoping to catch another transition, this time to the LS. There were some interesting changes in the spectral properties during the decay, however we could not detect a transition to the LS in terms of appearance of strong band limited noise in the PSD. Fig. 4.64 shows the evolution of spectral parameters into quiescence. Until MJD 51555, the flux (a) did not vary (except little jumps during the observations with significant variability), and then decayed smoothly. The spectral index (b) stayed around 2.3 until MJD 51565, and then steepened to around 3. During this steeping (e) the power-law flux was also low. The diskbb component on the other hand had constant T_{in} (c) until MJD 51555, and then showed a very regular monotonic decay. This decay probably indicates retreating of the inner disk radius. Coincident with this decay was the decay of the diskbb flux (d). Around MJD 51600, the power-law index hardened again, and then remained around 2.1 until the source decayed into quiescence. I checked whether this hardening is accompanied by temporal changes as an indication of transition to the LS, however due to very low count rates, my results are inconclusive about a transition to the LS in terms of temporal properties. Miller et al. (2000) reported a spectrum with just a power-law emission with index of 1.54 for a later observation on MJD 51733. Although the X-ray spectrum is consistent with the LS, again, the flux was too low to do any temporal analysis for this observation. Note that, after MJD 51560, the PLR is also close to unity, which is only observed in the LS for other sources.

4.11.3 Summary

I have not detected the state transition to the LS in terms of temporal properties, but there was a state transition from the HS to the IS on MJD 51524. This transition is not sharp in terms of spectral properties, however, depending on the power-law flux, the temporal properties change significantly (see Fig. 4.64). Whenever the power-law flux in 3–25 keV band was greater than $10^{-9}\,\mathrm{ergs\,cm^{-2}\,s^{-1}}$, the observations show significant variability. The PSD is strongly energy dependent, with rms amplitude increasing with energy, as seen in Fig. 4.65. The coherence and lags did not show any particular evolution (Fig. 4.66). There was only one radio observation coincident with the observations that I analyzed on MJD 51526 which showed an optically thin spectrum, similar to the previous radio observations of this source (Brocksopp et al. 2002).

Chapter 5

Discussion

"Jessep : You want answers?
Kasse : I want the truth!
Jessep : You can't handle the truth! "

- From "A few good men"

5.1 Introduction

In the Results chapter, I presented data from the analysis of eleven sources in sixteen outburst decays. Table 5.1 shows the complete list of the sources and the outbursts. Of these eleven sources, seven of them made a transition to the LS during the outburst decay, and one of them (XTE J1859+226) made a transition to the IS. For five outbursts, the source was in the LS throughout the outburst without a state transition. These are called the "hard outbursts".

In this thesis work I defined the state transition in terms of the appearance of strong variability, and not through any spectral changes. Before going any further in the discussion, I want to restate the definition of states. The properties of each state are discussed in detail in section 1.4. I mostly followed those definitions when denoting an observation to be in a particular state. Naturally, most of my observations are in the LS. When defining states, I also take into account the PSD shape and

Table 5.1: List of sources and states.

Outbursts with State Transition		
Source / Year[a]	State, #[b]	Comments[c]
XTE J1650−500 / 2001	HS, 4	HS : T02
	TS, 2	TS : Obs. 1 and 2 in Table 4.1
	LS, 5	LS : Obs. 3–7 in Table 4.1
GRO J1655−40 / 1996	HS, 2	HS : M98
	LS, 3	LS : Obs. 1 and 2 in Table 4.3
XTE J1748−288 / 1998	HS, 3	HS : R00
	LS, 8	LS : Obs. 1–6 in Table 4.5
XTE J1755−324 / 1997	HS, 2	HS : Obs. 1 and 2 in Table 4.7
	LS, 2	LS : Obs. 3 and 4 in Table 4.7
GX 339−4 / 1998	TS, 2	TS : Obs. 1 and 2 in Table 4.9
	LS, 4	LS : Obs. 3–7 in Table 4.9
4U 1630−47 / 1998	HS, 5	HS : T00
	LS, 10	LS : Obs. 1–18 in Table 4.14
4U 1630−47 / 1999	HS, 5	HS : Obs. 1–5 in Table 4.15
	LS, 10	LS : Obs. 6–10 in Table 4.15
4U 1630−47 / 2001	HS, 6	HS : Obs. 1–6 in Table 4.16
	LS, 5	LS : Obs. 7–11 in Table 4.16
XTE J1550−564 / 1998	HS, 5	HS : Obs. 1–5 in Table 4.18
	LS, 5	LS : Obs. 6–10 in Table 4.18
XTE J1550−564 / 2000	IS, 6	IS : Obs. 1–6 in Table 4.21
	HS, 2	HS like : Obs. 7–8 in Table 4.21
	TS, 2	TS : Obs. 9–10 in Table 4.21
	LS, 15	LS : Obs. 11–25 in Table 4.21
XTE J1859+226 / 1999	HS, 27	HS : Fig. 4.64
	IS, 8	IS : Obs. 1–8 in Table 4.45
Hard Outbursts		
XTE J1550−564 / 2001	LS, 12	in Table 4.29
XTE J1550−564 / 2002	LS, 10	B02
GRS J1737−31	LS, 3	in Table 4.38
GS 1354−644	LS, 9	R00b
XTE J1118+480	LS, 12	in Table 4.43

a Year in which the outburst was first detected.
b Number of observations in each state.
c T02 : Tomsick et al. (2002a), M98 : Méndez, Belloni & van der Klis (1998), R00 : Revnivtsev, Trudolyubov & Borozdin (2000), T00 : Tomsick & Kaaret (2000), B02 : Belloni et al. (2002), R00b : Revnivtsev et al. (2000).

its resemblance to other observations in the same source. For example, I called all XTE J1859+226 observations and the first six observations of the 2000 outburst of XTE J1550−564 as IS, since they show characteristics of IS, and are also similar to each other. Observations just before and after the state transition for some sources have PSD shapes which are very different than the LS and/or the IS PSD shapes. To amplify this difference, these observations are called transitional state (TS) observations. These are observations 1 and 2 of XTE J1650−500 and GX 339−4, and observations 9 and 10 of the 2000 outburst of XTE J1550−564. Observations 7 and 8 of the 2000 outburst of XTE J1550−564 show temporal characteristics different than both the IS observations and the LS observations, and are called HS-like in section 4.7.3. They are grouped with the IS observations in spectral correlations, since their spectral properties are close to that of the IS. Table 5.1 lists the spectral states for all outbursts and number of observations in each state.

My general objectives in this work are to understand the accretion structure (i.e., geometry, temperature and density profile of accretion components) and the nature of variability of GBH transients. Although the discussion of individual outbursts in the Results chapter provides some insight to achieve this goal, the amount and depth of information enrich tremendously when the results from individual observations are combined. This chapter consists of five main sections. In section 5.2 I discuss the evolution of spectral and temporal parameters before and after the state transition. Section 5.3 reports correlations among spectral and temporal parameters for all sources and their interpretation. In section 5.4, the energy dependence of temporal fit parameters is discussed. Cross-spectral temporal properties (lag and coherence) are discussed in section 5.5. These sections are more aimed towards explaining the nature of variability. Finally, the results related to the accretion structure of GBHs are discussed in section 5.6.

5.2 Evolution of spectral and temporal parameters during and after the state transition

I analyzed the evolution of spectral and temporal parameters during and after the state transition for seven sources and eleven outbursts. Here, I combine this information from individual outbursts, and discuss them in two sections. In the first section, I discuss the physical evolution of these systems that leads to state transition. I also discuss the physical parameter that drives the appearance of variability. In the second section, I concentrate on the evolution of spectral and temporal properties after the transition.

5.2.1 Physical conditions that lead to state transitions

It is generally accepted that the state transitions involve large changes in the accretion structure of GBHs (Esin, McClintock & Narayan 1997; Pottschmidt et al. 2002). The transition to the LS not only results in sharp changes in the X-ray spectrum, but also creates a physical environment that shows broad band variability and QPOs. The changes in the spectral parameters close to the state transition might provide important clues to understand and quantify the physical environment of the GBH. For this analysis, I investigated the evolution of the spectral index (Γ), the inner disk temperature (T_{in}), the power-law flux, the disk-blackbody (diskbb) flux and the power-law ratio (PLR, ratio of the power-law flux to the total flux in 3–25 keV band). Thanks to our group's monitoring program of GBHs with *RXTE* during outburst decays, I obtained very good coverage for 5 sources, in 7 different outbursts (1998, 1999 and 2001 outbursts of 4U 1630$-$47, 1998 and 2000 outbursts of XTE J1550$-$564, and the 2001 outburst of XTE J1650$-$500 with almost daily monitoring). GRO J1655$-$40, GX 339$-$4, and XTE J1755$-$324 are excluded since they have very poor coverage ($\geq$10 days between observations) of the transition, and it is not possible to track the spectral changes. XTE J1748$-$288 which has a better coverage ($\sim$5 days between observations) are included in this discussion. The hard outbursts, of course, are also excluded.

I compare the spectral fit parameters of the individual sources just before and after

Table 5.2: Evolution to the state transition.

	Evolution[a]					Discontinuity[b]				
Source	Γ	T_{in}	Flux$_\Gamma$	Flux$_{\mathrm{dbb}}$	PLR	$\Delta\Gamma$	ΔT_{in}	ΔFlux$_\Gamma$	ΔFlux$_{\mathrm{dbb}}$	ΔPLR
XTE J1650−500	$\searrow$	$\rightarrow$	$\nearrow$	$\rightarrow$	$\nearrow$	$\bullet$	$\bullet$	$\surd$	$\bullet$	$\surd$
XTE J1748−288[c]	$\searrow$	$\rightarrow$	$\nearrow$	$\rightarrow$	$\nearrow$	?	?	?	?	?
4U 1630−47, 1998	$\searrow$	$\searrow$	$\rightarrow$	$\searrow$	$\nearrow$	$\bullet$	?	$\surd$	$\surd$	$\surd$
4U 1630−47, 1999	$\searrow$	$\rightarrow$	$\rightarrow$	$\searrow$	$\nearrow$	$\bullet$	$\bullet$	$\bullet$	$\bullet$	$\bullet$
4U 1630−47, 2001	$\searrow$	$\searrow$	$\rightarrow$	$\searrow$	$\nearrow$	?	?	$\bullet$	?	?
XTE J1550−564, 1998	$\searrow$	$\nearrow$	$\nearrow$	$\searrow$	$\nearrow$	$\bullet$	?	$\surd$	?	$\bullet$
XTE J1550−564, 2000[d]	$\rightarrow$	$\rightarrow$	$\nearrow$	$\searrow$	$\nearrow$	$\surd$	$\bullet$	$\surd$	$\bullet$	$\surd$
XTE J1859+226[e]	NA	NA	NA	NA	NA	$\bullet$	$\bullet$	$\surd$	$\bullet$	$\surd$

a Evolution to the state transition. $\searrow$ Decrease. $\nearrow$ Increase. $\rightarrow$ Constant

b Comparison of the parameters of observations just before and after the state transition. $\surd$ Large change (see text) in parameter. $\bullet$ No large change in parameter. ? Not constrained due to either being below detection limit or sparse coverage.

c Sparse coverage.

d Transition from the IS to the HS like.

e The transition is not to the LS, therefore the evolution parameters are denoted NA, not applicable. The discontinuity parameters in this case compares the observations without variability and with variability.

the transition (observations just before and after the dashed lines in Figs. 4.2, 4.13, 4.18, 4.26, 4.29, 4.31, 4.35, 4.37). The evolution of these parameters for each source is summarized in Table 5.2, part "Evolution". For all outbursts except the 2000 outburst of XTE J1550−564, a change in Γ is the pre-cursor of the state transition. It starts to decrease 3-5 days before the transition, and continues to decrease until the transition. Except for the 1998 outburst of XTE J1550−564, T_{in} either decreases or stays constant before the transition. The power-law flux either increases or stays constant, and the diskbb-flux decreases for majority of the outbursts, or stays constant. The cumulative effect of the power-law and diskbb-flux evolution is the increasing PLR for all outbursts before the transition. These results point out that the emission from the corona relative to the emission from the disk strengthens before the transition.

One important problem is the relation between the appearance of the broad band noise and QPOs with the spectral changes summarized above. To understand which physical parameter drives the appearance of variability, two observations are compared: the one that shows variability (first observation after the dashed line in the figures mentioned above), and the last without variability (the one just before the dashed line). This comparison is summarized in Table 5.2, part "Discontinuity". A check-mark indicates that either the slope of the parameter as a function of time changes sign or the percentage change in the value of the parameter compared to the previous observation is at least three times that of the previous observation. Two parameters show a discontinuity for the majority of the outbursts: the power-law flux and the PLR. PLR is not an independent parameter, and in this case its increase is driven by the increase in the power-law flux. For the 1999 outburst of 4U 1630−47, there is no sharp change in any of the spectral parameters between those two observations, yet one observation shows no variability and the next one shows strong variability. Note that the power-law index showed a drop for an earlier observation for this source. The situation is more complicated for the 2000 outburst of XTE J1550−564, as seen in Fig. 4.37. There is a large increase in the power-law flux and PLR when the system makes a transition from the IS to HS-like, but this change corresponded to a decrease in the rms amplitude! When it made a transition to the LS with strong variability, no parameters showed a large change, as in the 1999 outburst of 4U 1630−47. Below, I discuss three possible reasons for the appearance of variability based on these observations.

Suppose, almost all of the variability we observe is due to the photons coming from the corona and the disk photons are providing mostly Poisson noise. This is not a far-fetched assumption. Indeed, very little or no variability is observed during the HS when the diskbb dominates and strong variability is observed when the power-law component dominates in the LS. The anti-correlation between the diskbb flux and the rms amplitude observed both in XTE J1650−500 (Fig. 4.2) and the 2000 outburst of XTE J1550−564 (Fig. 4.37) is also consistent with this argument. It is conceivable that the Poisson noise-dominated diskbb flux reduces the rms amplitudes to unobservable levels. Then the PLR would be a good indicator of when the variability will be observed since higher the PLR, lower the diskbb flux compared to the total flux. For all of our sources, if the PLR<0.45 no variability has been observed. However, the value of PLR cannot be the sole determinant of when the variability will be observed. For most of the sources the PLR has to be greater than 0.8 for the variability to appear, although it can be as low as 0.45 for the IS of XTE J1859+226. To test the argument that the diskbb flux might reduce the rms amplitudes to unobservable levels, I conducted very simple simulations. I added various levels of Poisson noise to the E1 band light curve of GRO J1655−40 and compared the resultant PSD with the original PSD. I chose this observation since it has a complex structure, and no diskbb flux, so all the emission is coming from the corona. The results are shown in Fig. 5.1. Although this figure clearly shows that the rms amplitude of the PSD depends on the PLR, it also shows that even for a PLR of 0.3, the variability is clearly observed. There is no large change in the PSD shape. I calculated the total rms amplitude for various levels of Poisson noise additions (corresponding to various levels of PLR). The results are shown in Fig. 5.2. The rms amplitude varies linearly with PLR. Moreover, lack of diskbb emission **does not** guarantee broad band variability even if a corona exists. There is strong emission in E2 of most of the sources before the transition and spectral analysis shows that only a few percent of the emission in this band is from diskbb. Nonetheless, although completely corona dominated, these observations do not show variability. Note that, these simple simulations do not take into account the effects of strong diskbb emission on the corona. The two emission components are not independent of each other, because Compton cooling of the corona by the

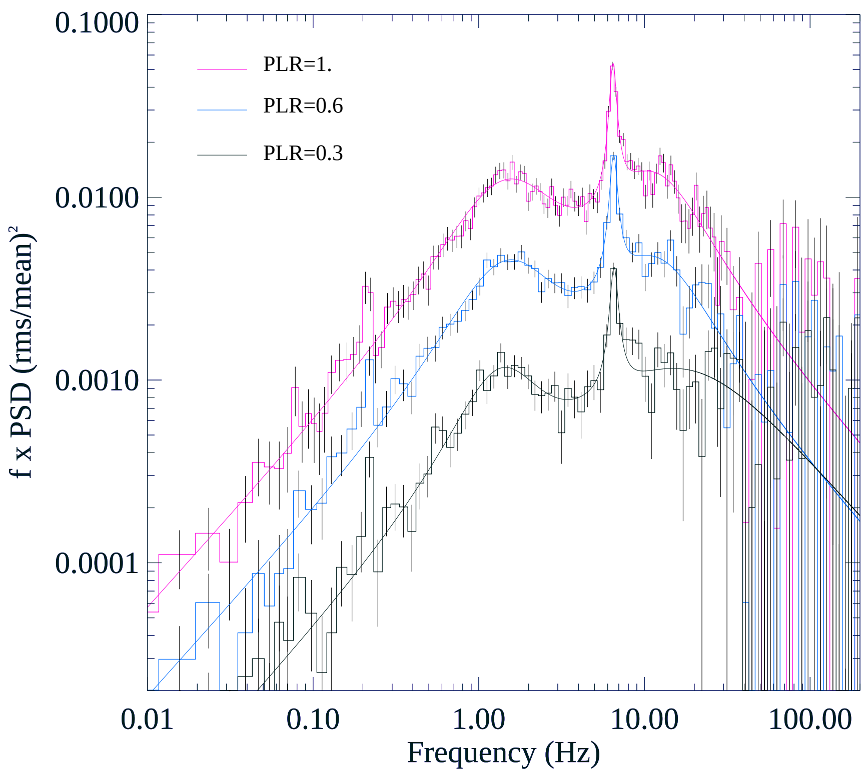

Figure 5.1: PSD of observation 1 of GRO J1655−40 in E1 band is shown in red. The blue and green data are the PSDs when pure Poisson noise is added to the original light curve. The blue PSD corresponds to a PLR of 0.6 and the red corresponds to a PLR of 0.3.

diskbb emission can affect the temperature and density structure of the corona. In this sense, although it is absolutely correct that the diskbb emission decreases the rms amplitude, the linear relation might not be accurate. The amount of diskbb radiation cannot be ruled out as an important parameter in determining when the variability will be observed.

The fact that the emission from the hard component only is not enough to create broad band variability suggests a model in which an interplay between the disk and corona is required for the observed variability. Perhaps, under special circumstances the variability is created in the disk with small amplitudes, and amplified strongly in the corona. The state transition then corresponds to a change in the physical conditions of the corona such that the amplification is enabled. Two possibilities discussed below is based on this assumption.

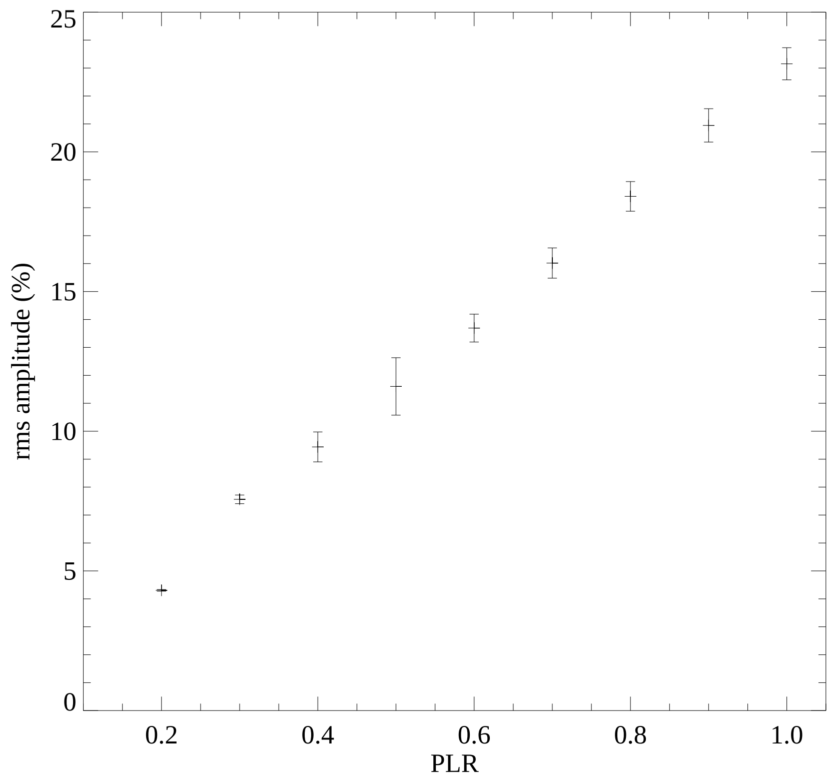

Figure 5.2: The rms amplitude as a function of PLR for different levels of Poisson noise in the PSD shown in Fig. 5.1. The original PSD with PLR of 1 has an rms amplitude of ∼23%. The relation is linear.

In the first case, the variability strongly depends on the geometry of the system and the state transition changes the geometry from the one that does not favor strong variability to the one that favors it. For example, an outflow of material (optically thin outflow during the transitions and compact/optically thick jets during the LS) might be needed to create the observed variability (see for example Nobili 2002). The radio emission is usually quenched during the VHS of GBHs (Corbel et al. 2001), however there is significant variability in this state which weakens this argument. Other alternatives are passage from a sphere+disk geometry with overlap of two components to no overlap of them (or vice versa), and from a sphere+disk system to ADAF where the source of input photons might be different.

Another possibility is passage from bulk motion Comptonization to thermal Comptonization. It is claimed that both play a role in creating the observed power-law spectrum, and it is possible that before the transition, the bulk motion Comptonization is the dominant effect (since it is more associated with steeper Γ), whereas once thermal Comptonization becomes dominant, variability arises. The transition may be so violent (involving outflows and large changes in geometry) that for 3-5 days the timing signatures may be suppressed. This can explain the sudden appearance of variability although there is no large change in the power-law flux one observation earlier for some sources.

A discussion of transition fluxes

It is extremely important to get an idea of when the transition happens during the decay for effective monitoring of the sources with *RXTE*. Often the sources are not monitored frequently enough (i.e., once a day) with pointed observations, but the ASM measures the flux in 3 energy bands very frequently (see section 2.1.3), which gives the observers a chance to detect transitions without re-pointing the satellite. The transition is often detected by a sudden increase in the hardness ratio 2 (HR2, the ratio of 5–12 keV flux to 1.5–3 keV flux). As shown in the Results chapter and as will be discussed further in this chapter, a few days just before and after the transition may manifest the most interesting behavior, but pointed observations may not be performed due to scheduling problems. A relationship between the peak flux and the transition flux (1.5 – 12 keV flux for the observation that shows variability) had been realized earlier (Tomsick, private communication). I plot this relation for all of the outbursts that show a state transition in Fig. 5.3. Except the 1998 outburst of XTE J1550−564, which showed one of the strongest flares in the *RXTE* history, the transition flux increases with the peak flux. The Spearman's rank order correlation coefficient (r_S) for this data set (excluding the 1998 outburst of XTE J1550−564) is 0.900, pointing out a correlation. On the other hand, the linear correlation coefficient (r) is 0.515, indicating a relation which is not strictly linear.

Some outbursts have the usual FRED shape (such as XTE J1748−288 in Fig. 4.12), and some have a very complicated shape (such as 4U 1630−47 in 2001 shown in Fig. 4.30). For the complicated ones, I also plotted the plateau ASM flux just before they start to decay along with the peak flux. The plateau points show a better linear correlation than that of the peak points with r of 0.706. These correlations are not very strong, but give a good perspective of when the transition might happen,

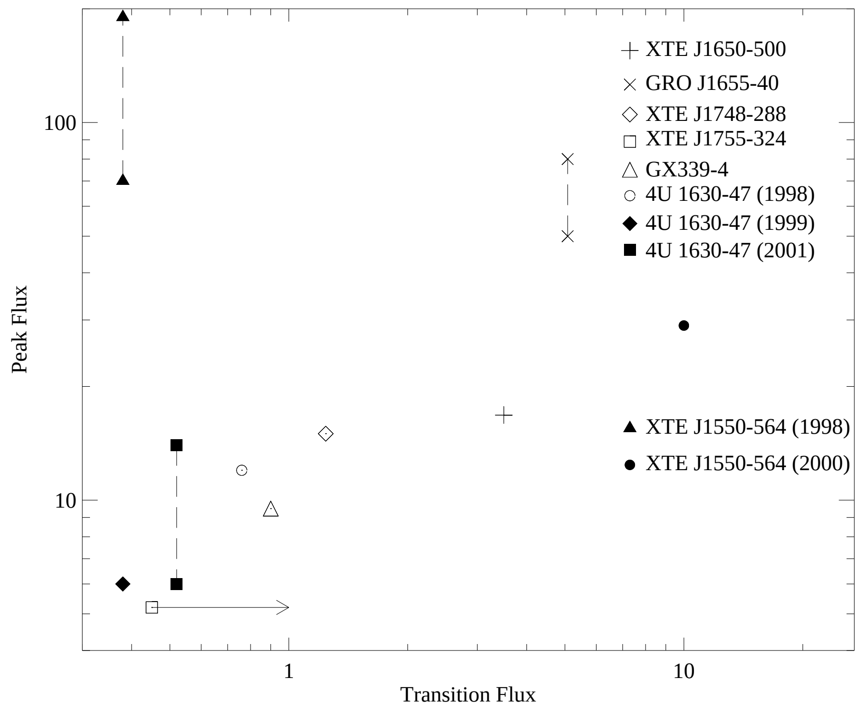

Figure 5.3: Peak flux versus transition flux in 1.5 – 12 keV band. Fluxes are in units of $10^{-9}\,\mathrm{ergs\,cm^{-2}\,s^{-1}}$. For the points connected with dashed lines, both peak fluxes and plateau fluxes are shown.

and when to start frequent monitoring observations. Indeed, our trigger criteria to start *RXTE* monitoring observations of GBHs during outburst decay depends on the peak ASM flux, for a peak flux greater than $20\times\,10^{-9}\,\mathrm{ergs\,cm^{-2}\,s^{-1}}$, the trigger is at $4\times\,10^{-9}\,\mathrm{ergs\,cm^{-2}\,s^{-1}}$, whereas for smaller peak fluxes it is $2\times\,10^{-9}\,\mathrm{ergs\,cm^{-2}\,s^{-1}}$.

5.2.2 Evolution of spectral and temporal parameters after the transition

Spectral and temporal evolution after the state transition are easier to interpret since all the sources show a similar evolution. The evolution of these parameters are summarized in Table 5.3. Except for XTE J1748−288, Γ decreases or stays constant after the transition. Note that the X-ray spectrum of XTE J1748−288 is heavily affected by the Galactic ridge emission, and the intrinsic Γ may not be increasing for this source. The power-law flux decreases for all outbursts except XTE J1650−500,

Table 5.3: Evolution after the state transition.

	Spectral[a]					Temporal[b]	
Source	Γ	T_{in}	Flux_{Γ}	$\mathrm{Flux}_{\mathrm{dbb}}$	PLR	ν_c[c]	rms[d]
XTE J1650−500	$\searrow$	$\searrow$	$\nearrow\rightarrow$	$\searrow$	$\nearrow\rightarrow$	$\searrow\rightarrow$	$\nearrow\rightarrow$
GRO J1655−40	?	$\searrow$	$\searrow$	?	$\rightarrow$	$\searrow$	$\rightarrow$
XTE J1748−288	$\nearrow$	?	$\searrow$	?	$\rightarrow$	$\searrow$	$\searrow$
GX 339−4	$\searrow$?	?	?	?	$\rightarrow$	$\searrow$	$\nearrow$
4U 1630−47, 1998	$\searrow$	?	$\searrow$	?	$\rightarrow$	$\searrow$	$\nearrow\rightarrow$
4U 1630−47, 1999	$\searrow$	$\searrow$?	$\searrow$	?	$\rightarrow$	NA	NA
4U 1630−47, 2001	$\rightarrow$?	?	$\searrow$	?	$\rightarrow$	NA	NA
XTE J1550−564, 1998	$\rightarrow$	?	$\searrow$	?	$\rightarrow$	$\searrow$	$\searrow$
XTE J1550−564, 2000	$\searrow\rightarrow$	$\searrow$	$\searrow$	$\searrow$	$\nearrow\rightarrow$	$\searrow$	$\nearrow\rightarrow$

a Evolution of spectral parameters. $\searrow$ Decrease. $\nearrow$ Increase. $\rightarrow$ Constant. $\nearrow\rightarrow$ Increase, then level off. $\searrow\rightarrow$ Decrease, then level off. ? Lower limit, or irregular.

b Evolution of temporal properties.

c Characteristic frequencies.

d Total rms amplitude of variability.

where it first increases and then stays constant. The diskbb-flux and T_{in} decrease monotonically for the cases when they are measurable, and for the remaining they already decreased to undetectable levels right after the transition. For all outbursts, the diskbb component is unobservable within a week of the state transition. For XTE J1650−500 and the 2000 outburst of XTE J1550−564, the PLR first increase and then stay constant. For all other outbursts, the PLR is very close to unity and does not vary.

For all observations except the 2000 outburst of XTE J1550−564, the peak frequencies of Lorentzians as well as the QPO frequencies decrease after the transition. The behavior of the rms amplitudes are more complicated. The 1998 outburst of XTE J1550−564 and XTE J1748−288 show a decreasing trend. The rms amplitudes for XTE J1650−500, the 2000 outburst of XTE J1550−564 and the 1998 outburst of 4U 1630−47 increase and level off. For GRO J1655−40, the rms amplitudes are consistent with being constant. For GX 339−4 on the other hand, the rms amplitude increases.

The evolution of the inner disk temperature, the diskbb flux, the power-law index and the characteristic frequencies of the variability are consistent with the idea of the inner disk retreat discussed in section 1.4.5. In the basic formulation of Makishima et al. (1986), the optically thick disk has a temperature profile that decreases with increasing radius. Therefore, if the inner disk evaporates as part of the transition, it is expected that both T_{in} and diskbb flux decrease. The relation between the covering factor and spectral index was discussed earlier in section 1.6.1, which indicates a larger inner radius for smaller Γ. It is intuitively expected that the characteristic frequencies decrease as the inner disk radius increases. The dynamical timescale (the fastest timescale) in the accretion disk is shorter close to the BH, and it is expected that higher frequency variability is created close to the BH. As the inner disk radius retreats (or inner disk evaporates) the dynamical timescale (at the inner edge) increases, and therefore the characteristic frequencies in the PSD decrease. The exact relation between the characteristic frequencies and the dynamical timescales is not clear yet. The overall evolution of both spectral and temporal properties therefore indicates that the inner edge of the accretion disk retreats as the system progresses in the LS, in accordance with the model of Esin, McClintock & Narayan (1997) as

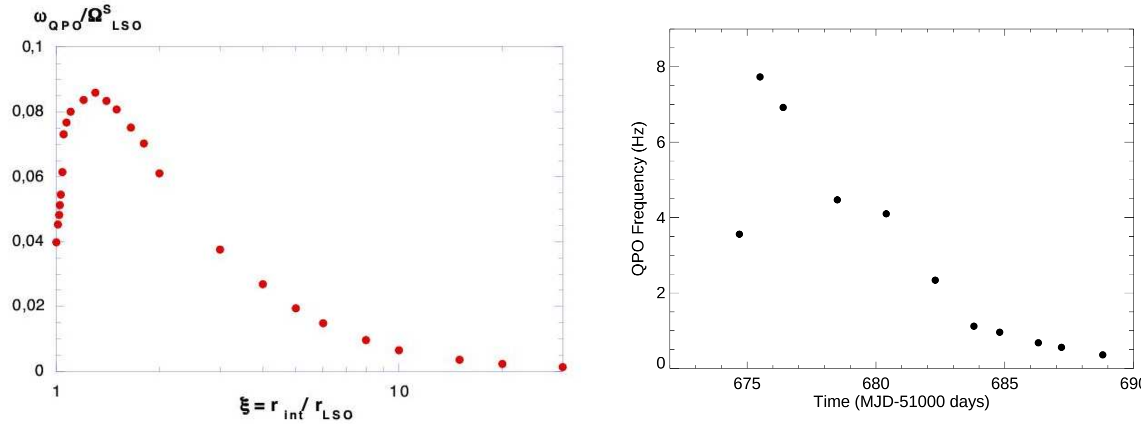

Figure 5.4: Left panel: The frequency of the QPO (normalized to the orbital frequency at the ISCO) against radius in units of the ISCO radius. At large radii, the frequency varies as $r_{int}^{-3/2}$ whereas at lower radii, the relativistic effects modify the relation near the inner disk edge. From Varnière, Rodriguez & Tagger (2002). Right panel: The QPO frequency as a function of time during the outburst decay of the 2000 outburst of XTE J1550−564. It shows a similar behavior predicted by the AEI if the time tracks the inner accretion disk. The errors are smaller than the symbols used in the plot.

discussed in section 1.4.5.

The exceptional case of the 2000 outburst of XTE J1550−564 is worth additional discussion. Just after the transition, the QPO is at 3.6 Hz. Next day, the QPO frequency was observed to be 7.7 Hz, and for the following days, it showed a monotonic decrease. This is the only case for which such behavior has been observed, and seems to contradict the idea that the inner disk retreats after the state transition. However, it is possible that the relation between the QPO frequency and the inner disk radius is not monotonic. In fact, this behavior is exactly what the Accretion Ejection Instability (AEI) model predicts for the evolution of the QPO frequency as a function of radius if initially the inner disk radius is very close to the marginally stable orbit (ISCO radius, see section 1.1.1). The AEI is a spiral instability driven by magnetic stresses that are present in accretion disks threaded by a moderate amplitude (near equipartition) magnetic field. This model predicts creation of a Rossby vortex at the co-rotation radius by a spiral wave. The orbital frequency of the vortex can be detected as a QPO (Tagger & Pellat 1999). The numerical calculations of the QPO frequency as a function of inner disk radius showed that there is an inversion in this relation such that the QPO frequency first increases as a function of radius, and then decreases as $R_{in}^{-3/2}$ (Varnière, Rodriguez & Tagger 2002). The result of this numerical calculation is seen in Fig. 5.4, left panel. In this figure, I also show the evolution of the QPO in the 2000 outburst of XTE J1550−564 (Fig. 5.4, right panel). Note that the similarity in these figures only makes sense if the inner disk radius retreats monotonically in time after the state transition, as the evolution of T_{in} and Γ indicates. The more detailed analysis of this behavior and its implications are presented in Rodriguez et al. (2002a).

The interpretation of the behavior of the rms amplitudes is more complex. I showed the relation between the PLR and the rms amplitudes earlier (see Figs. 5.1 and 5.2). The "Poissonic" nature of the disk component causes a decrease in the rms amplitudes at lower energies due to the diskbb energy spectrum peaking at those energies. This might explain the increase and leveling of the rms amplitudes in XTE J1650−500 and the 2000 outburst of XTE J1550−564. Although the rms amplitudes seem to be decreasing after the transition for the 1998 outburst of XTE J1550−564, it might be a result of not constraining the high frequency part of the PSD. The first observation requires two Lorentzians to fit, and results in a high PSD amplitude, whereas for the remaining observations, the second Lorentzian, although statistically not required, cannot be excluded. The fits are better for XTE J1748−288 and it also shows a decreasing behavior. As discussed in section 5.4.1, the interpretation of the rms amplitudes of XTE J1748−288 is complicated due to the high absorption column density. The Galactic ridge emission may also be affecting the rms amplitudes at low flux levels by supplying additional Poissonic emission. The rms amplitude of GX 339−4 increases after the transition although there is no diskbb flux in the 3-25 keV band.

5.3 Correlations among spectral and temporal fit parameters

It is well known in GBHs that the spectral and temporal properties are coupled to each other and show interesting correlations as discussed in detail in section 1.6. These correlations can be divided into three sections, correlations among spectral parameters, correlations among temporal parameters and correlations between spectral and temporal parameters. In this section, I discuss each of these cases and combine all the individual observations to develop a unified description of the underlying physics.

5.3.1 Correlations among spectral fit parameters

Choice of parameters and analysis technique

The spectral parameters that can be used for this study are Γ, T_{in}, total flux (in 3–25 keV band), power-law flux, diskbb flux, and PLR. Unfortunately the distances and binary inclinations of most of my sources are not known, which makes it difficult to calculate luminosities for use as a parameter. Since fluxes depend on the distance and inclination, they can not be used when all the sources are combined. So, for the correlations involving all sources, Γ, T_{in} and PLR are used. I used different symbols for each source, and different symbols for different states in a source (i.e. I used three symbols for the 2000 outburst of XTE J1550−564 one for the IS, one for the TS and one for the LS).

Spectral index vs. inner disk temperature

I start with the two main parameters of the spectral fits, Γ and T_{in} and plot them in Fig. 5.5. I differentiated between different spectral states. This figure shows that most of the systems are found to be in the LS when T_{in} is less than 0.6 keV and Γ is less than 2.2. As can be seen, for most of the LS, T_{in} values are upper limits and it is hard to interpret their contribution to this analysis. Therefore I removed them from the plot and investigate the other states in more detail, which is done in Fig. 5.6. The majority of the sources (sources with $T_{in} > 0.55$) show a correlation (with r=0.772) between the inner disk temperature and the spectral index. The simplest explanation comes from the standard picture of these systems where a cold accretion disk illuminates a hot electron corona. As discussed in detail and shown by Monte Carlo simulations (Dove, Wilms & Begelman 1997; Dove et al. 1997) these systems are thermally stable within a certain range of inner disk temperature and spectral index parameters. This range is determined by the geometry (or more precisely the covering factor). As the inner disk temperature increases, the cooling due to the soft photons increases

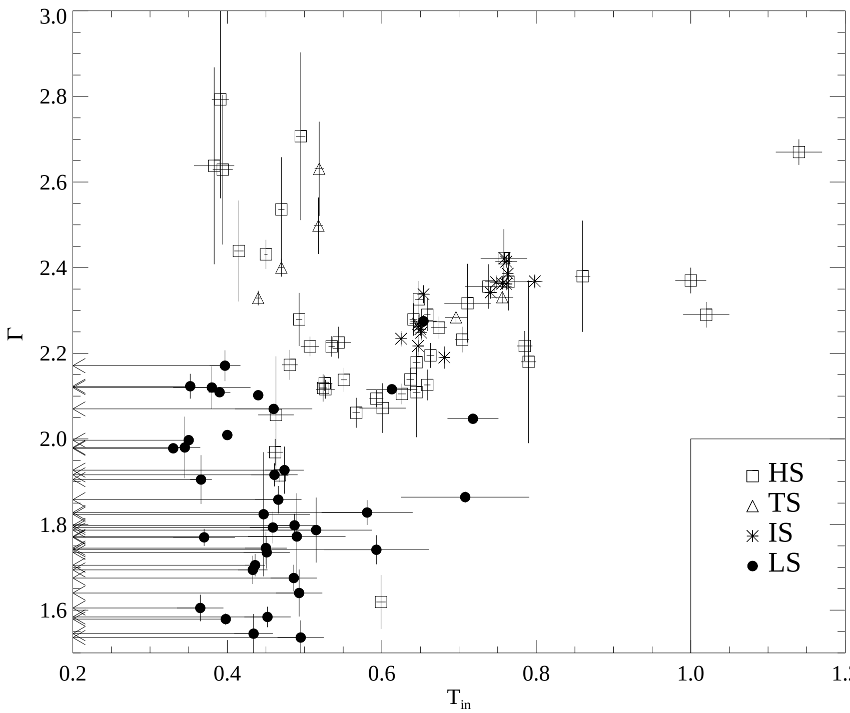

Figure 5.5: Spectral index versus inner disk temperature for all observation for all states. The squares are for the HS, the triangles are for the TS, the stars are for the IS and the circles are for the LS. Majority of the LS observations for T_{in} are upper limits.

and therefore the spectral index increases and the X-ray spectrum softens. The exceptions in this figure for the correlation are XTE J1650−500, the transitional state observations of GX 339−4, the HS of the 1998 outburst of XTE J1550−564, and some of the XTE J1859+226 observations. Although these observations do not obey the correlation, they occupy an area in this plot where it is theoretically possible to coexist, since the system can have a low inner disk temperature and low corona temperature/density, but cannot have a high inner disk temperature and a hard X-ray spectrum (which would be the bottom right of Fig. 5.6). They might also represent the cases for which the bulk motion Comptonization is the dominant mechanism for creating the power-law part of the spectrum, and therefore they are not affected by cooling.

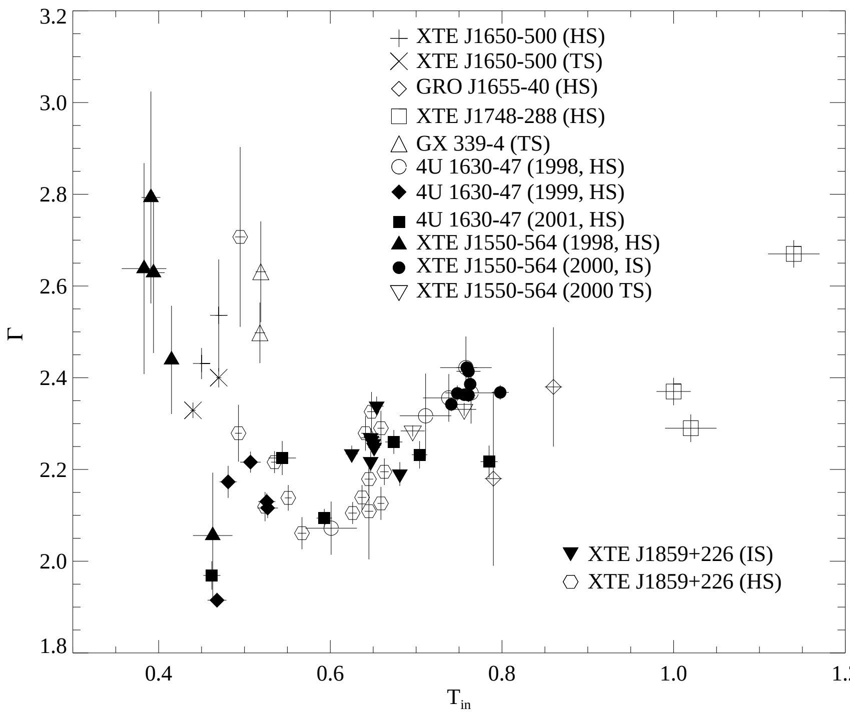

Figure 5.6: Spectral index versus inner disk temperature for all observation for all states except the LS observations.

Spectral index and inner disk temperature vs. power-law ratio

As mentioned earlier, since PLR is a ratio, it permits source by source comparisons unlike the diskbb or power-law flux. And again, since the majority of the diskbb detections in the LS are upper limits, the resulting PLR values are lower limits. This makes it difficult to interpret the relation between PLR and spectral index in the LS. I therefore do not show the LS data for clarity. In Fig. 5.7 I plot the spectral index as a function of PLR for the HS, IS and TS data.

Fig. 5.7 shows that there is no correlation between these parameters. Even for individual sources and outbursts, this is the case. I also checked whether the PLR depends on the diskbb parameter T_{in} as shown in Fig. 5.8. Again, the PLR does not show any global correlation to T_{in} involving all observations. On the other hand, if analyzed case by case basis, 1999 and 2001 HS of 4U 1630−47, XTE J1748−288 in HS, XTE J1859+226 in HS but not in IS, and XTE J1550−564 in TS show a correlation. However, if a linear fit is applied for the individual sources that show

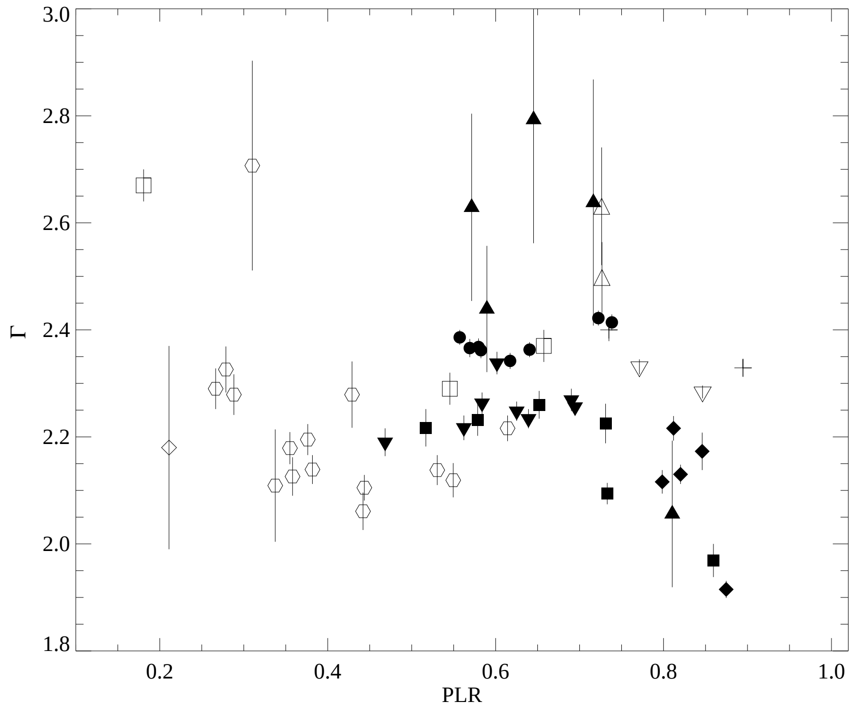

Figure 5.7: Spectral index versus PLR for all observation for all states except the LS observations. Same labels are used in Fig. 5.6.

a correlation, the slopes and the amplitudes of the lines are different causing the random appearance of the whole plot.

5.3.2 Correlations among temporal fit parameters

The analysis of correlations among temporal fit parameters is motivated by several studies that showed that these correlations exist, span decades of frequency range and are valid for several types of X-ray sources. These correlations are between the characteristic frequencies of the PSD fits (such as the QPO frequency, the break frequency, Lorentzian peak frequencies) and are summarized in section 1.6.2. In addition to the correlations between the peak frequencies, Pottschmidt et al. (2002) demonstrated the correlations between mean lag and peak frequencies.

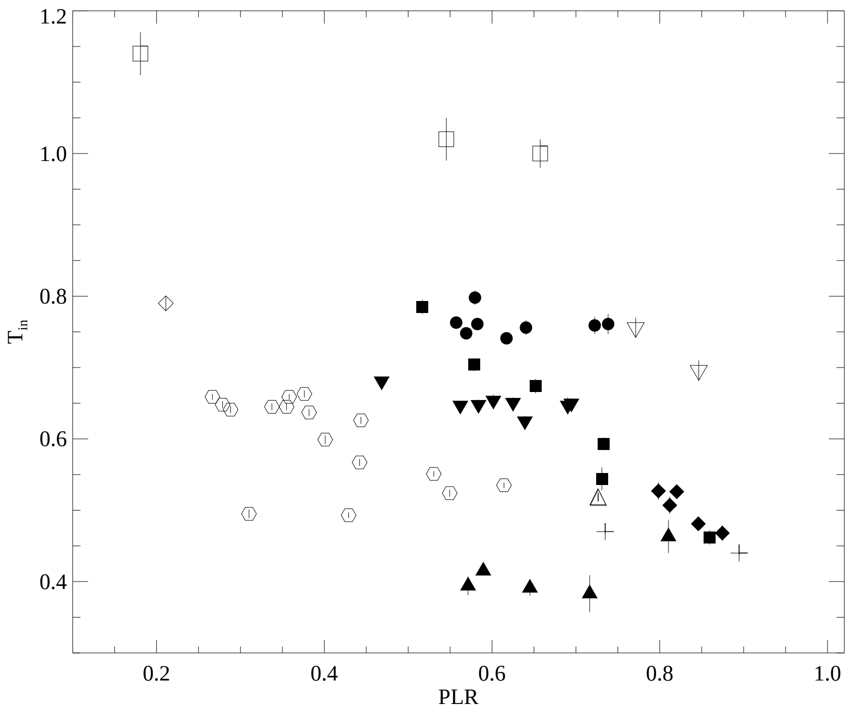

Figure 5.8: Inner disk temperature versus PLR for all observation for all states except the LS observations. Same labels are used as in Fig. 5.6.

Choice of parameters and analysis technique

I have performed two types of temporal analysis, fitting the PSDs with Lorentzians, and calculating the cross-spectral parameters, time lag and coherence. The PSD fit parameters I used for this analysis are the peak frequencies of the broad Lorentzian components, and the central frequency of the QPOs. I also used mean coherence and integrated lag from cross-spectral analysis. As in the previous section, I used different symbols for each source, for each outburst, and for each state. For some cases, the hard outburst data are shown with one symbol. Where appropriate, I showed the correlations from earlier works to compare to my data. During the state transitions and for some IS observations I showed that the PSD is strongly energy dependent. So it is not obvious which energy band to use for the correlations. Therefore I only used the LS observations for this study.

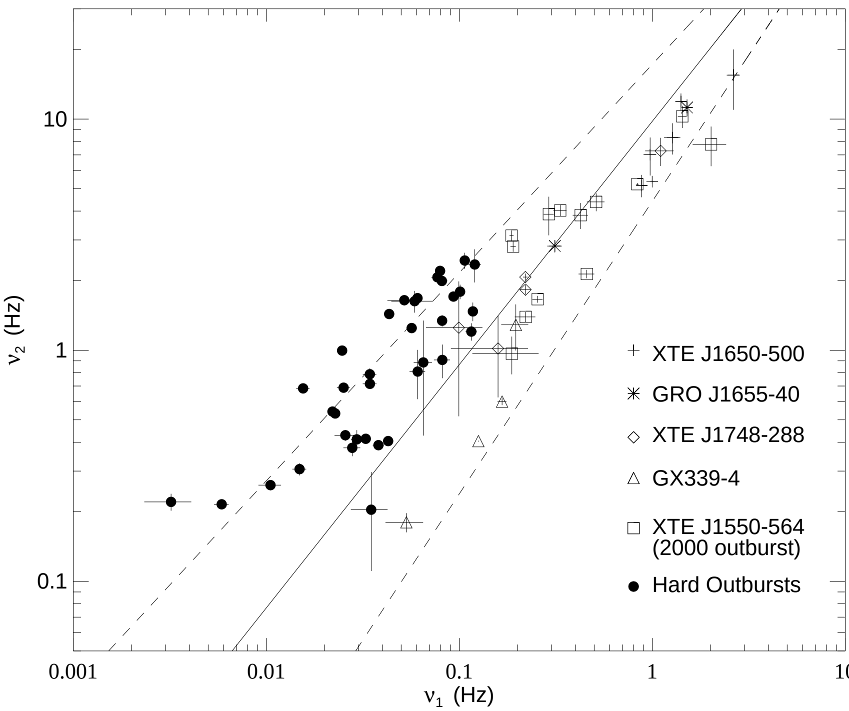

Figure 5.9: Correlation between ν_1 and ν_2 for all LS observations. The solid line is the fit to the correlation reported by Psaltis, Belloni & van der Klis (1999), and the dashed lines are 1σ errors to this fit. Note that all the hard outburst data is above the the Psaltis fit.

Correlations among peak frequencies

The first case that I discuss is the relation between ν_1 and ν_2 (defined in section 3.7.2) which is shown in Fig. 5.9. I also plot the fit from the correlation reported in Psaltis, Belloni & van der Klis (1999) over, along with its errors. First of all, the peak frequencies show a correlation (with r=0.945) which is consistent with the Psaltis correlation. It is rather surprising because the Psaltis correlation is between the QPO and a broad Lorentzian frequency, whereas this figure does not include QPO central frequencies. Note that, the $\nu_1 - \nu_2$ correlation for Cyg X-1 also obeys the Psaltis correlation (Pottschmidt et al. 2002).

Next, I produced the relation between ν_1 and ν_3, which is shown in Fig. 5.10. Only a few sources have a third broad peak in their PSDs, and they are often not very well constrained. As it can be seen in this figure, there is no obvious correlation for different sources.

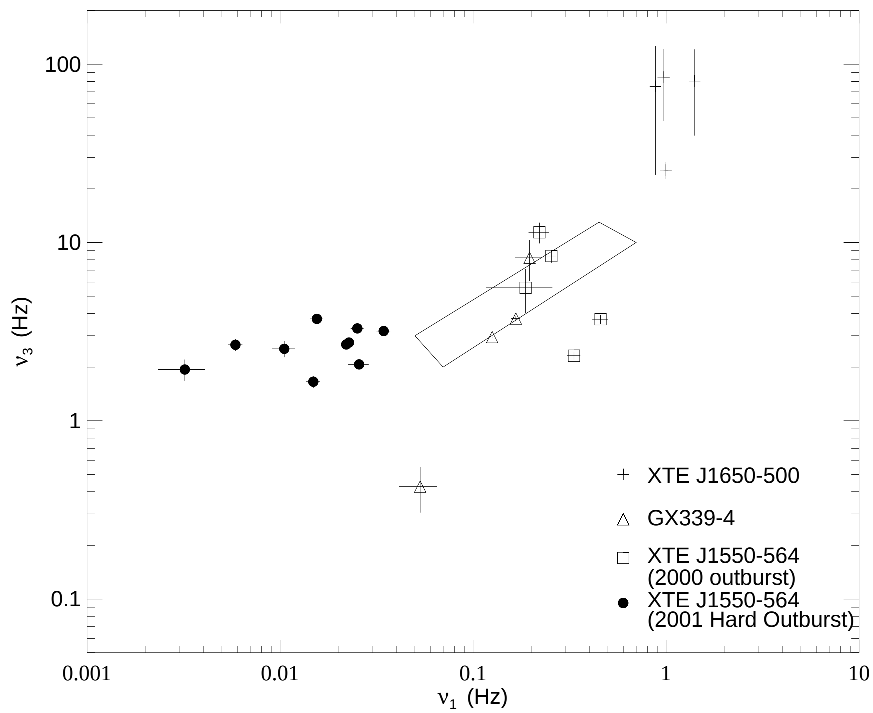

Figure 5.10: Relation between ν_1 and ν_3 for all LS observations.

Correlations between the peak frequencies and the QPO frequencies

I investigated the relation between the QPO frequency and ν_1 and the result is shown in Fig. 5.11, a. The dashed lines limit the area of the correlation reported in Wijnands & van der Klis (1999). There are two branches. The first branch includes XTE J1650−500, XTE J1550−564, GX 339−4 and GRO J1655−40, and shows a tight correlation with r=0.969, and is consistent with the Wijnands correlation. The second branch consists of data points from the 1998, 1999 and 2001 outburst of 4U 1630−47, and does not obey the Wijnands correlation, but are correlated. This was pointed out for the 1998 outburst of 4U 1630−47 earlier (Tomsick & Kaaret 2000). Note that, the Wijnands correlation is between the central QPO frequency and the break frequency when a broken power-law fit is applied to the PSD, whereas ν_1 is obtained through applying a Lorentzian fit. According to Belloni, Psaltis & van der Klis (2002) there could be a difference as high as 15% between ν_1 and the break frequency.

I also checked the relation between the QPO frequency and ν_2, although it is

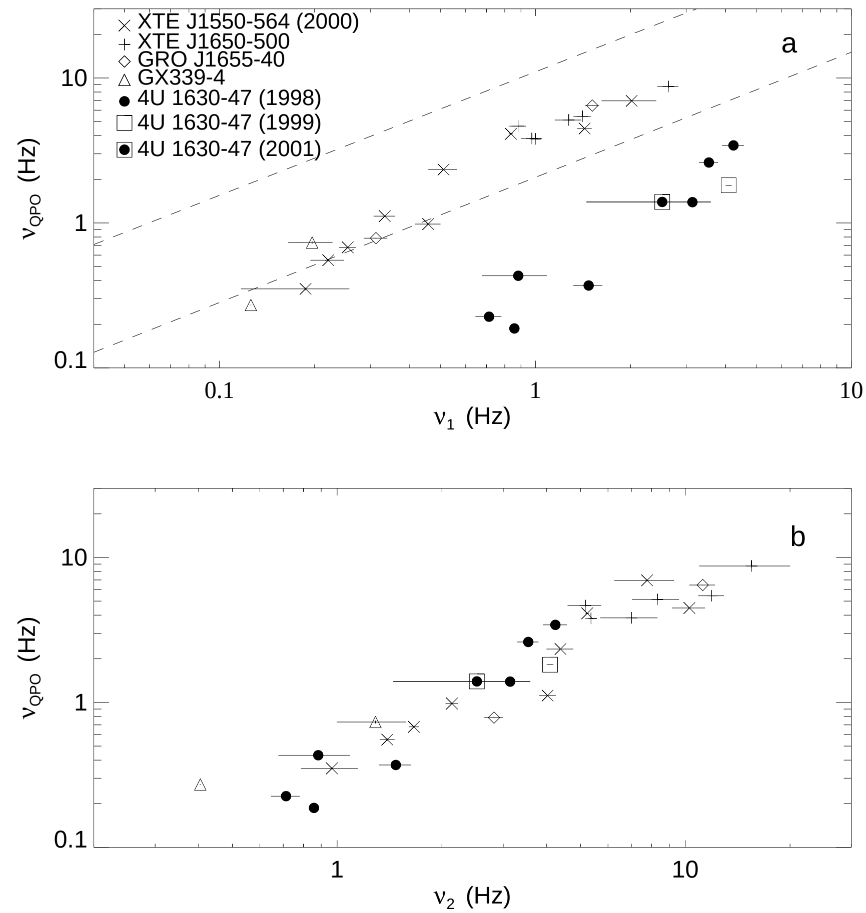

Figure 5.11: (a) Correlation between ν_1 and and the QPO frequency for all LS observations. The dashed lines limit the area that the correlation reported by Wijnands & van der Klis (1999) exist. (b) Correlation between ν_2 and and the QPO frequency for all LS observations. Since 4U 1630−47 has only one Lorentzian fit, its data points are shown in both panels.

redundant (ν_1 correlates with both the QPO frequency and ν_2, therefore ν_2 and the QPO frequency correlates). I replotted the 4U 1630−47 points assuming that the only Lorentzian is L_2. Fig. 5.11, b shows that the 4U 1630−47 observations are consistent with the correlation of the other sources. The resultant distribution has a r of 0.932. This indicates that the sole Lorentzian component in 4U 1630−47 fits may correspond to L_2, but not L_1. This may indicate that the physical process which creates L_1 is not effective, or the modulations creating L_1 are damped in 4U 1630−47.

Interpretation of the frequency correlations

I studied the correlations between the PSD peak frequencies and extended the correlations found earlier with unpublished new observations. The fact that these correlations exist among Z, atoll and BHCs suggests that similar mechanisms are responsible for creating the QPOs and the noise components, and the variability depends weakly, if at all, on the magnetic field and the presence of a hard surface. These correlations place tight constraints on the models of variability, since a successful model should be able to explain the presence of the same type of variability in sources which possess significantly different mass accretion rates, with peak frequencies that span two orders of magnitude (Psaltis, Belloni & van der Klis 1999).

The case that broad band variability and the QPO phenomenon have the same physical origin is further strengthened by the observation of a broad band noise component turning into a QPO which is seen for the atoll source 4U 1728−34 (Di Salvo et al. 2001). This relation between the QPO and the broad band noise suggests that both components are generated at the same region in the accretion flow, and can be well explained with the Psaltis & Norman (2000) model as discussed in detail in section 1.5.4.

Belloni - Hasinger correlation

The Belloni - Hasinger correlation is between the flat top power level and the break frequency in PSDs of black hole systems. It was first reported for Cyg X-1 for which Belloni & Hasinger (1990) showed that the flat top power level is proportional to $1/\nu_b$. This is seen in other BHCs and NS systems also (Belloni, Psaltis & van der Klis 2002, and references therein).

In Fig. 5.12, I plot this correlation for all of the observations in the LS. The Lorentzians I used are not forced to be zero centered, however, for most of the fits, L_1 ended up with a centroid frequency consistent with zero and a low Q. To be sure not to mix peaked Lorentzians, I only plotted the cases where the Q values are less than 0.3. In the Lorentzian modeling, flat top level corresponds the power of zero-centered Lorentzian at the minimum PSD frequency. There exists a correlation encompassing all sources. It is discussed in Belloni, Psaltis & van der Klis (2002)

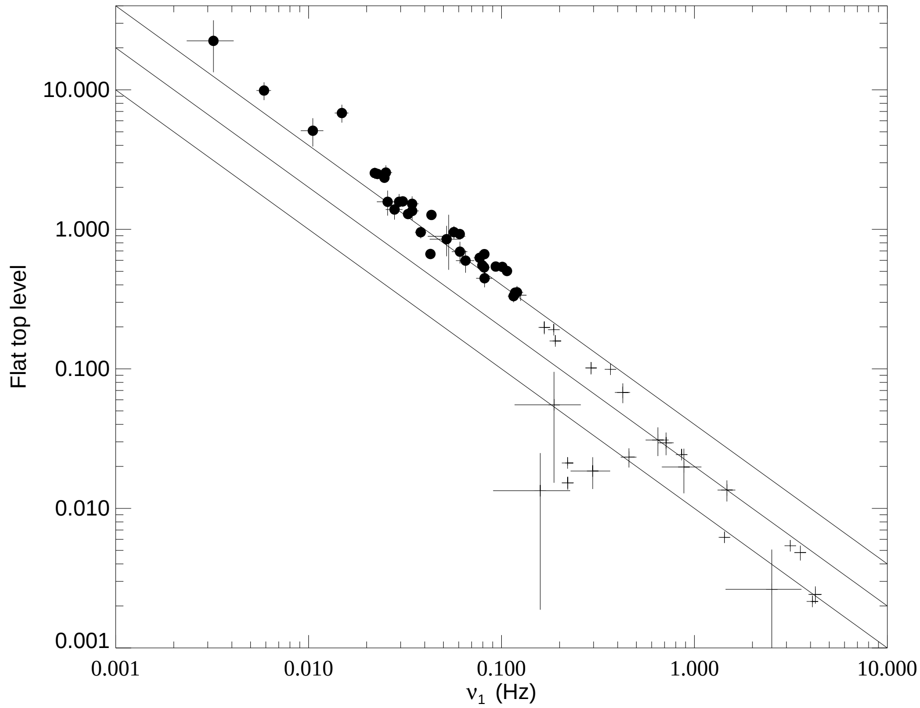

Figure 5.12: The Belloni - Hasinger correlation (between flat top power level and the break frequency) for all LS observations. The circles are for the hard outburst observations and the remaining for outbursts that show a state transition. The lines represent the predicted correlation when the rms amplitude is kept constant. In the Lorentzian modeling, flat top level corresponds the power of zero-centered Lorentzian at the minimum PSD frequency.

that the Lorentzian modeling can explain this correlation if the rms amplitude of L_1 is constant. In this case, for a zero-centered Lorentzian, the flat top power level is proportional to $1/\Delta$ and therefore $1/\nu_1$, as it can be deduced from equation 3.34 and equation 3.35. The lines in Fig. 5.12 represent the predicted correlation for constant rms amplitude. The data points, although correlated, generally do not follow those lines. On the other hand, as again discussed in Belloni, Psaltis & van der Klis (2002), this is not a global correlation, such that the rms amplitude is constant for each source, but it can be different between sources. To test this, I separated the sources and plot them in Fig. 5.13 with the expected correlations. In this figure, XTE J1550−564, and 4U 1630−47 are shown separately for clarity since they have many data points. Upper left panel shows the remaining hard outbursts, and the lower left panel has the remaining sources that show a state transition. The majority of the sources agree

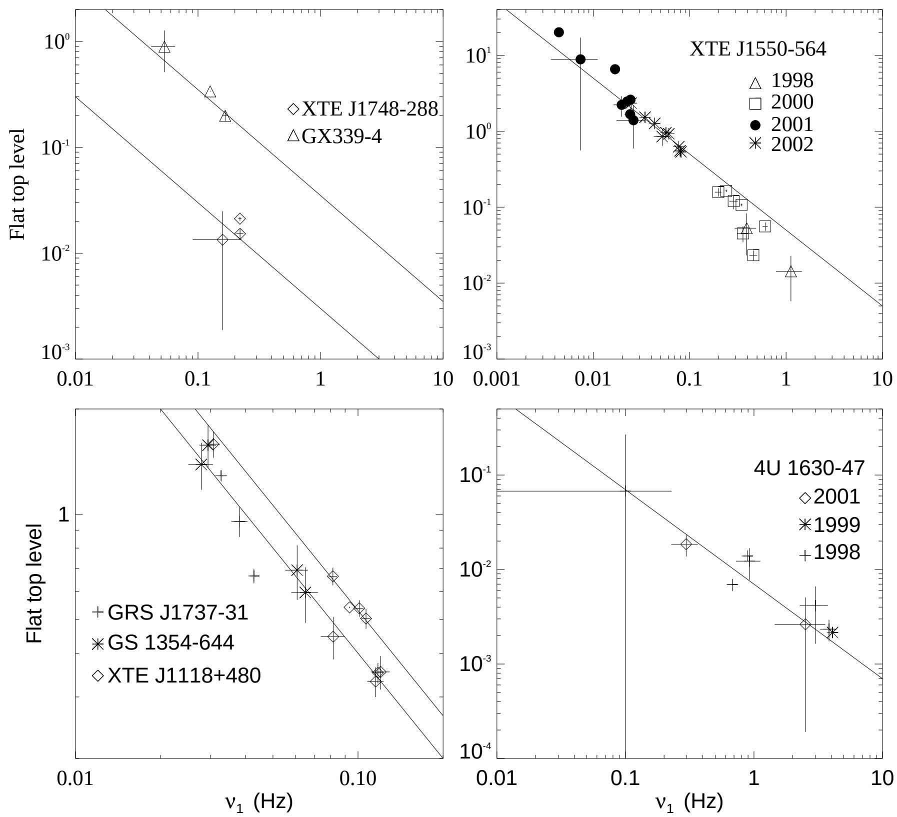

Figure 5.13: The Belloni - Hasinger correlation (between flat top power level and the break frequency) for individual sources. The lines represent the predicted correlation when the rms amplitude is kept constant.

with the prediction.

Just after their state transitions, the overall rms amplitude as well as rms amplitude of L_1 increase for XTE J1550−564, XTE J1650−500, GX 339−4 and 4U 1630−47 before they level off at some value. Curiously, for almost all of those cases, L_1 is a peaked component with $Q > 0.5$ and therefore not included in the plot. Therefore, majority of the sources with zero-centered L_1 obey the Belloni - Hasinger correlation. Within the context of Lorentzian modeling, this means that for majority of the sources, the rms amplitudes do not vary in LS, as indicated earlier in section 5.2.2.

Relation between the integrated lag and the mean coherence

I investigated the relation between the two cross-spectral temporal parameters, the integrated lag and the mean coherence in 1–10 Hz band for sources where both of

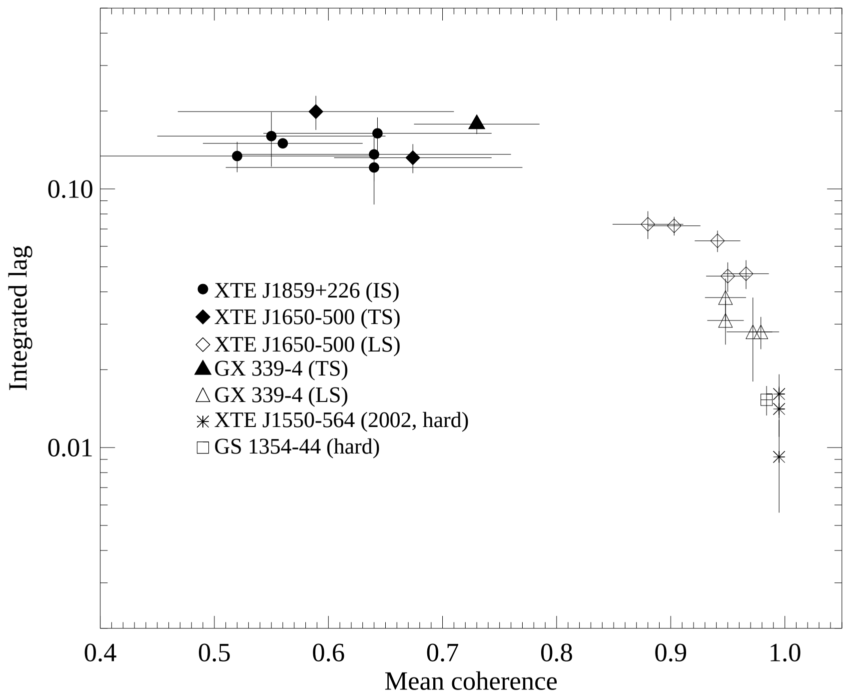

Figure 5.14: The relation between the integrated lag and the mean coherence.

these were measurable. I also investigated the relation between the cross-spectral and spectral parameters which will be discussed in the next section. The relation between the temporal fit parameters and the cross-spectral parameters is also analyzed, but not shown here to avoid redundancy. They will be mentioned in appropriate sections.

Fig. 5.14 shows the relation between the integrated lag and the mean coherence. First of all, the data are clustered into two groups. The first cluster of points includes XTE J1859+226 which was in the IS during the outburst decay, and also the transition states of XTE J1650−500 and GX 339−4, which show high values of integrated lags and low coherence values. The second cluster has the LS observations and a couple of hard outburst points. The hard outbursts have the highest coherence and lowest lags, and in fact, all the remaining hard outburst data have integrated lags consistent with being zero.

Pottschmidt et al. (2000) showed that during the state transitions of Cyg X-1, the mean lags increase substantially and the mean coherences decrease. Moreover, in between transitions, the mean lags have the same value both in the LS and the

HS. This, along with the simultaneous observations of plasma ejections with the state transitions led to the idea that the reason for the increased lag during the transitions is additional Compton scatterings of soft seed photons in a very large plasma outflow (Pottschmidt et al. 2000, 2002; Nowak, Wilms & Dove 2002). Highly variable nature of the outflow could explain the reduced coherence. Various other sources also show optically thin plasma ejections that indicate large outflows during state transitions (Fender et al. 1999a; Corbel et al. 2000; Corbel et al. 2001). For XTE J1859+226 on the other hand, although plasma ejections were reported during the beginning of the outburst, there is no report of such ejections during the decay (Brocksopp et al. 2002). Yet, the TS observations of XTE J1650−500 and GX 339−4, and IS points of XTE J1859+226 occupy the same spot in Fig. 5.14. Moreover, the plasma ejection of GX 339-4 was not observed during the TS observation, but it was simultaneous with the next observation, when the source was already in the LS in terms of temporal properties (Nowak, Wilms & Dove 2002). These observations may indicate reasons for the reduced mean coherence and larger integrated lag for our sources other than the additional scattering in the large outflow idea.

One possibility that can reduce the coherence is Compton scattering in a variable corona where variability timescale less than the observation time (Vaughan & Nowak 1997). In the TS and the IS the inner edge of the accretion disk is close to the BH and there is strong diskbb flux. This results in a strong feedback between the corona and the disk, and the consequent heating and the cooling of the corona may be changing the Compton y parameter with a timescale less than the observation time. Note that Compton scattering in a static, optically thin medium does not reduce the coherence for Fourier periods less than the diffusion time. Obviously, when the lags due to scatterings are comparable to Fourier periods, the Fourier components acquire random phases and lose coherence. High coherence and very small (if not zero) lags for the hard outbursts are consistent with the idea that the hard emission from these systems are due to simple thermal Comptonization in a static corona.

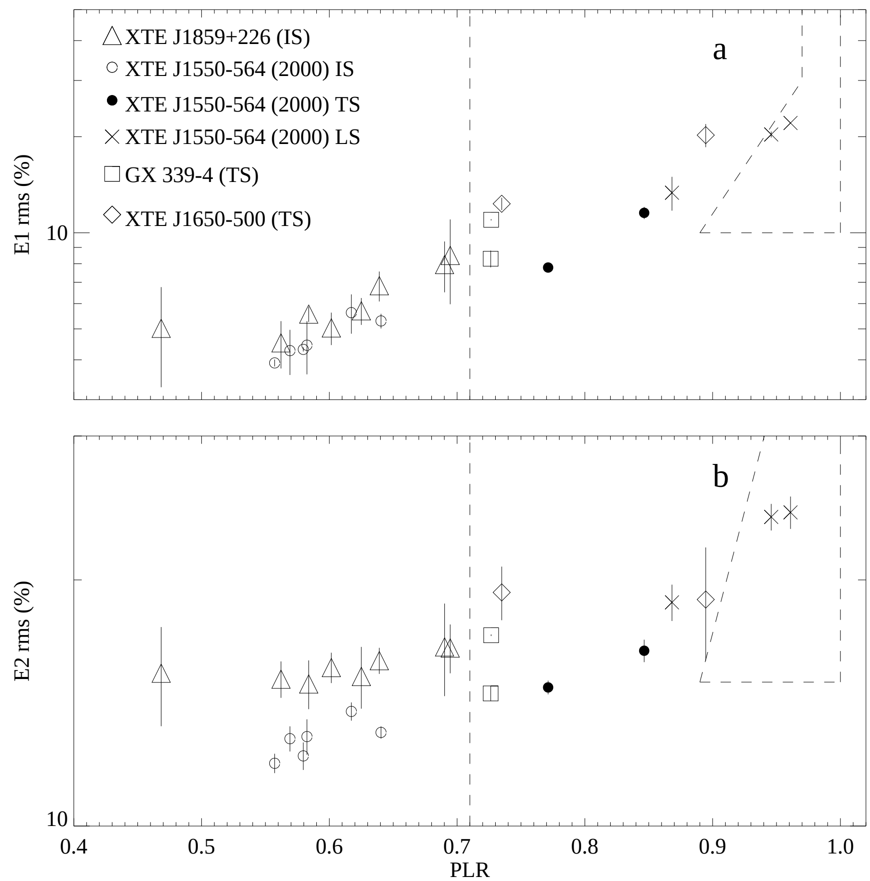

Figure 5.15: The correlation between the PLR and the rms amplitudes. The upper panel (a) is the total rms amplitude of E1 (2 – 6 keV for most of the sources), and the lower panel (b) is the total rms amplitude of E2 (6 – 15 keV for most sources). The vertical dashed lines separate the IS and other states. Most of the LS observations that have upper limit PLRs are not shown, however, the regions they occupy are shown with dashed lines on the upper right hand corners of each panel. The two XTE J1550−564 points inside this region for both cases are not upper limits, the spectra have enough statistics to have a good measurement of the diskbb component. All hard outbursts have a PLR of 1 and are not shown.

5.3.3 Correlations between spectral and temporal fit parameters

PLR and rms amplitudes

I observed that the rms amplitude increases as the PLR increases for some of these sources. The plot of this relation is shown in Fig. 5.15 for all sources to see if this correlation is global. First of all, PLR has to be greater than 0.45 in order to observe any variability at all during outburst decays as discussed in section 5.2.1. Second, transition to the LS happens if the PLR is greater then ∼0.7. E1 rms amplitude and PLR show a global correlation with r of 0.928 (Fig. 5.15, a). Moreover, the IS points of XTE J1550−564 and XTE J1859+226 occupy the same region in the plot. Fig. 5.15, b, shows the relation between the rms amplitude of E2 and PLR, for which the correlation with r=0.817 is not as strong as the E1 case. The IS points of XTE J1550−564 and XTE J1859+226 in Fig. 5.15 (lower) are separated. The reason for this separation can be attributed to the level of diskbb flux. As shown in section 5.2.1, the "intrinsic" rms amplitude from the corona will be reduced by the contribution from the disk. The T_{in} of XTE J1550−564 is high during the IS (see Table 4.21), and there is considerable (between 5% and 10%) diskbb flux in E2. On the other hand, there is no diskbb flux in E2 of XTE J1859+226, and the rms amplitude is almost constant.

Correlations between the spectral index and the rms amplitudes

I found the most impressive global correlations between the spectral index Γ and various temporal fit parameters which I discuss in detail below. I start with the correlation between Γ and the rms amplitudes of E1 and E2, which are shown in Fig. 5.16. The upper panel (a) shows Γ and the rms amplitude of E1. As can be seen, there is a global correlation (above the dashed line, with r of −0.879) involving all sources in all states except the IS, and observations of 4U 1630−47 and XTE J1748−288 in the LS. This figure shows that, as the spectral index decreases, the rms amplitude of variability increases. To best of my knowledge, there is no direct report of this global correlation in the literature, although for individual cases, this relation can be clearly observed (i.e. for Cyg X-1 see Pottschmidt et al. (2002), for 4U 1630−47 see Tomsick & Kaaret (2000), for XTE J1550−564 and XTE J1650−500 see Kalemci et al. (2001, 2002), respectively).

Here, I discuss possible reasons why the observations below the dashed line in Fig. 5.16, a, constitute a separate cluster other than the remaining sources. The common physical property of 4U 1630−47 and XTE J1748−288 is that they are heavily absorbed. Predehl & Schmitt (1995) found that there is a strong correlation between the dust and hydrogen column densities. Therefore, these two sources are behind

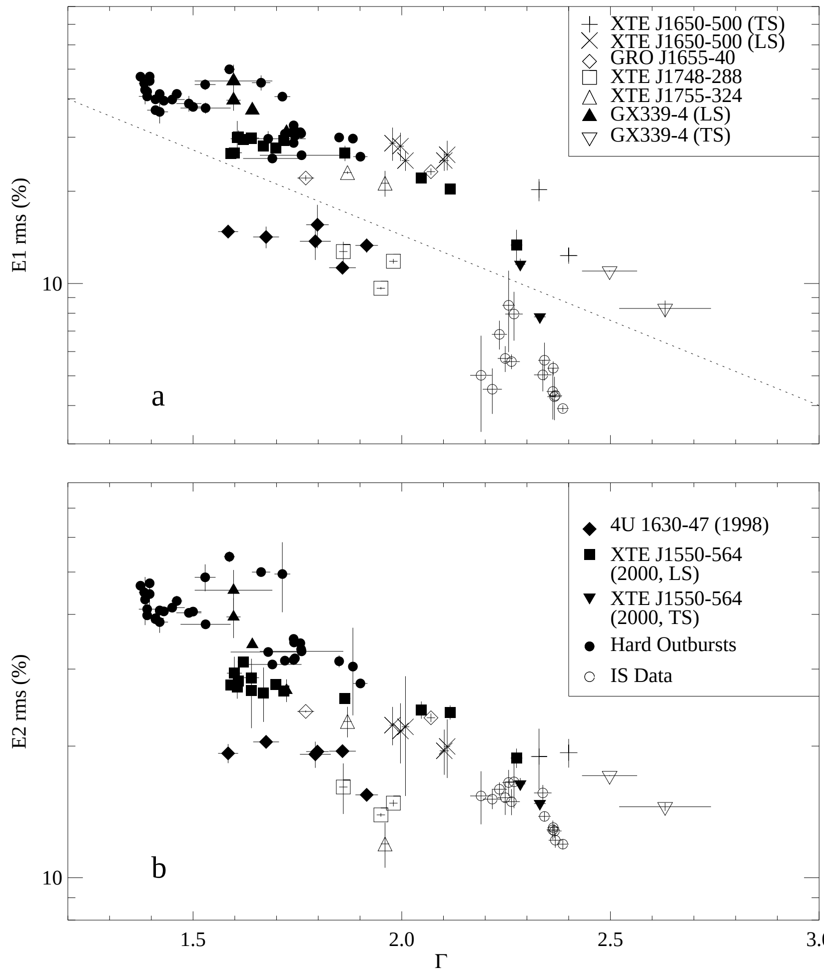

Figure 5.16: The correlation between Γ and the rms amplitudes. The upper panel is for the total rms amplitude of E1 and the lower panel is the total rms amplitude of E2. Same labels are used in both panels, and the list of labels are divided into both panels for clarity. The hard outbursts and the IS observations are shown with one symbol, and they will be discussed in detail in Fig. 5.17. The dashed line is to guide the eye to the correlation above it that exists for all observations except the IS, 4U 1630−47 and XTE J1748−288 observations.

copious amount of cosmic dust which scatters X-rays. This scattering is strongly biased into forward direction (small angle scattering, Predehl 1998), and the average scattering angle is larger for lower energy photons. Moreover, the scattering cross section goes with $1/E^2$ where E is the energy of the X-ray photon. Therefore, even though intrinsically higher and lower energy band PSD have similar rms amplitudes, the observed rms amplitude of lower energy bands may be observed lower than the

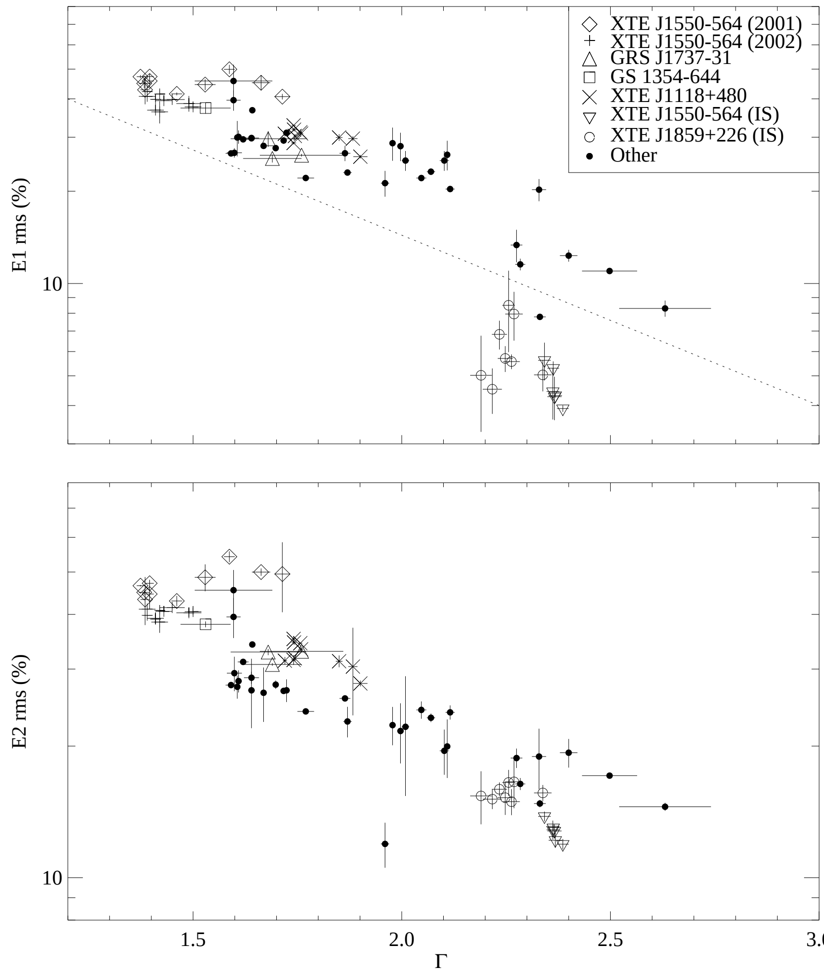

Figure 5.17: The correlation between Γ and the rms amplitudes for the hard outbursts and the IS observations. The upper panel is for the total rms amplitude of E1 and the lower panel is the total rms amplitude of E2. Same labels are used in both panels. The hard outbursts and the IS observations are shown with different symbols, and the remaining is shown with small filled circles denoted as "Other". 4U 1630−47 and XTE J1748−288 are not shown for clarity.

intrinsic values since the less energetic photons are more likely to do additional scatterings. The scattering angle is larger for lower energy photons, they will have longer path lengths and corresponding lags may cause loss of coherence and a decrease in the rms amplitude. Unfortunately, the coherence function is not well constrained for neither of the sources to test this argument directly. The high frequency variability would lose coherence more easily than the low frequency variability, and the small angle scattering should result in a larger rms drop at higher frequencies. Yet, for both XTE J1748−288 and GRS J1737−31, the drop in rms amplitude is mostly due to the lower frequency Lorentzian (see Tables 4.5, 4.39). Note that, absorption alone does not result in a decrease in the rms amplitude of variability, because it reduces both the modulated and unmodulated photons by an equal amount.

For the IS observations, the amount of the diskbb flux is an important factor in determining the rms amplitude. Since it is very strong in E1 in the IS, the observed rms amplitudes may be lower than the intrinsic amount of variability coming from the corona. This could account for the IS points being below the line. In Fig. 5.17, I show the IS observations from XTE J1550−564 and XTE J1859+226 with different symbols. As you can see, both disagree with the correlation in E1 (a), but are well correlated (with r of -0.831 for all sources) for E2 (b). Note that all the XTE J1859+226 points are clustered tightly in the lower panel, consistent with the overall correlation, whereas some of XTE J1550−564 points still have lower rms amplitudes. This may be due to the leakage of diskbb flux in E2 as discussed in the PLR correlations.

In Fig. 5.17 where I show the hard outburst and IS observations with different labels, there is another interesting behavior. The 2001 outburst of XTE J1550−564 and XTE J1118+480 have two clusters of points. For both of them, there are four that have the same rms amplitude as the remaining XTE J1550−564 observations but higher spectral index. Those are observations taken at the very low levels of flux at the end of the outbursts before decaying to quiescence. The softening of the spectrum at the end of a decay is also observed for the 2000 outburst of XTE J1550−564 (Tomsick, Corbel & Kaaret 2001). This kind of softening is predicted if an ADAF is present. As the mass accretion rate drops, the predicted spectrum gradually softens since the optical depth of the ADAF region decreases causing the Compton y parameter to decrease, and consequently Γ to increase (Esin, McClintock & Narayan 1997). The softening itself, and its timescale may be used to test ADAF models (Tomsick, Corbel & Kaaret 2001).

Correlation between the spectral index and the QPO frequency

The QPO frequencies as a function of the spectral index as shown in Fig. 5.18, are very tightly correlated with r of 0.941 for 6 sources in several states and outbursts. The only observations that are away from the main cluster of points are

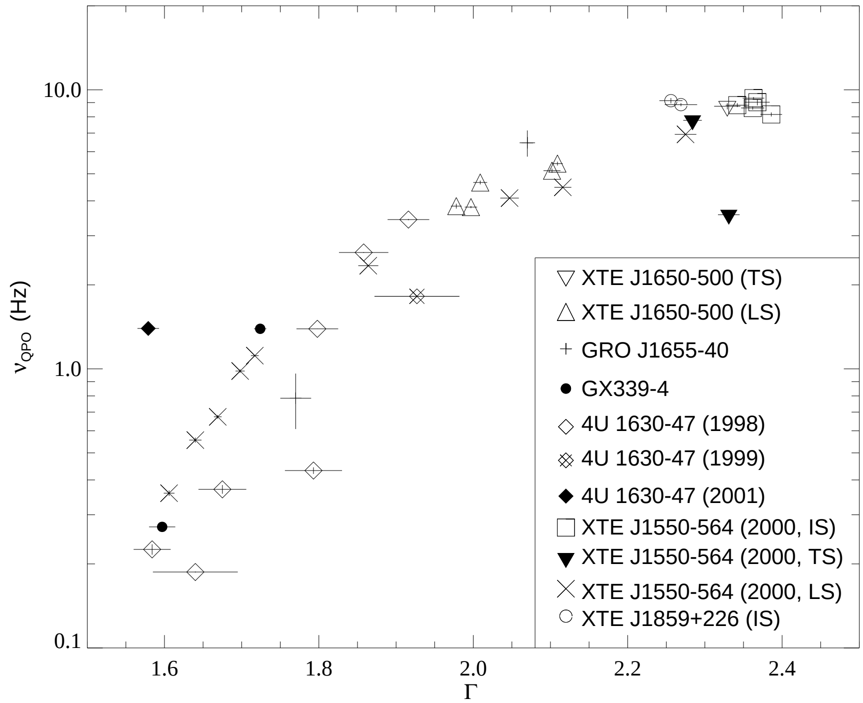

Figure 5.18: The correlation between Γ and the QPO frequency

the observation 9 of XTE J1550−564 (which is extraordinary in many respects, as discussed in section 4.7.3, and may be an evidence of the AEI model as discussed in sections 1.5.3 and 5.2.2) and the 2001 outburst of 4U 1630−47. The correlation is valid for XTE J1550−564 and XTE J1859+226 in the IS, all TS observations (except observation 9 of XTE J1550−564) and all LS observations that show a QPO except the 2001 4U 1630−47 observation.

This correlation (with fewer sources and data points) was first reported by di Matteo & Psaltis (1999), but the discussion was limited to the implications of the limited QPO frequency band on the limited change in the inner disk radius during transitions. Revnivtsev, Gilfanov & Churazov (2001) found a tight correlation between the QPO frequency and Γ in GX 339−4. As this work was being prepared, a comprehensive discussion of this correlation was reported by Vignarca et al. (2002).

The QPO frequency-Γ correlation obtains more meaning when combined with the correlation between the reflection fraction and Γ. This correlation is discussed in some detail in section 1.6.1 and shown to be valid for both GBHs and AGNs. There is strong feedback between the accretion disk and corona where they overlap. The reflection fraction and cooling is higher when the accretion disk is close to the BH. Combining these two correlations, one gets an anti-correlation between the QPO frequency and the inner disk radius. Since both the QPO frequency - Γ, and Γ - reflection fraction are tight correlations, the QPO frequency and the inner disk radius should also be a tight correlation. The challenge is to determine the correct QPO model and find its relation between the inner disk radius. After that we do not need a QPO observation in the LS to determine where the inner radius is, and can find it through the spectral index.

This correlation supports all low frequency QPO models that link the QPOs to the inner accretion disk, and does not support global oscillations of the disk, or trapped oscillations at certain fixed frequencies determined by the mass and spin of the BH (see section 1.5.3 and references therein for the discussion of some of these QPO models).

The QPOs for XTE J1550−564 in the 2000 outburst require more discussion. The QPOs observed in E2 in the IS obey the correlation indicating the same origin for the QPOs in the LS. If the inner accretion disk is closer to the BH during the IS, they should not have a higher frequency than the first TS observation (observation 9) QPO frequency if the AEI model is correct. Either the IS points obey the correlation merely by chance, or the AEI model is incorrect unless the inner disk radius moved inward before the transition. On the other hand, observation 9 discredits all other models linking the QPO frequency directly to the inner disk radius unless it is an anomaly.

Correlation between the spectral index and the peak frequencies

The QPO frequency correlates with both of the peak frequencies, as shown in section 5.3.2, therefore, at first, it seems redundant to investigate the correlation between the peak frequencies and Γ. However, there is no QPO in the hard outbursts, but the peak frequencies instead of the QPO frequencies can be used to calculate the inner disk radius if the correlation is tight. Fig. 5.19 shows ν_1 vs. Γ for the hard outbursts. As expected, the LS observations that show a state transition have a strong correlation with Γ. On the other hand, the correlation including all sources is not

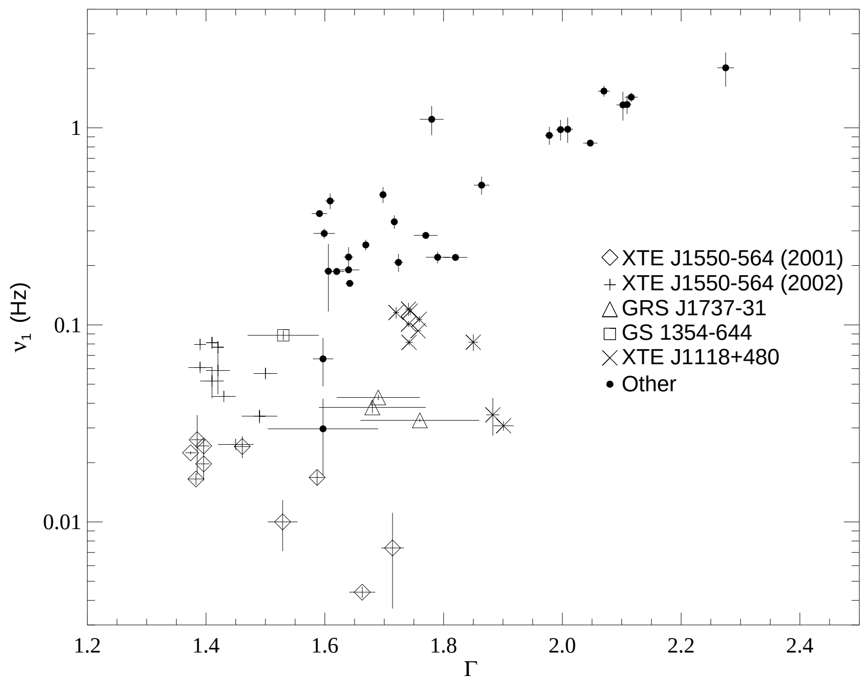

Figure 5.19: The correlation between Γ and ν_1. Hard outbursts are shown with different symbols, and the LS observations from sources that show a state transition are shown with small filled circles.

as tight with r=0.782 as compared to the QPO frequency correlation with r=0.941. Softening of the spectrum at the end of the decay for some of the sources that was discussed earlier may be a part of the reason that the correlation is not strong (the 2001 XTE J1550−564 and XTE J1118+480 observations that have higher Γ). Excluding those points increases the correlation coefficient r to 0.840. The observations of GRS J1737−31 are still away from this correlation. I have no explanation why those do not obey this correlation. Note that Cyg X-1 also shows a correlation between these parameters (Pottschmidt et al. 2002).

Relation between the inner disk temperature and the QPO frequency

QPO frequency and the inner disk temperature shows a tight correlation for XTE J1550−564 during the rise of the 1998 outburst (Sobczak et al. 2000; Remillard et al. 2002b). On the other hand, no similar correlation was observed for GRO J1655−40 (Sobczak et al. 2000). Since Γ and T_{in} were shown to be weakly

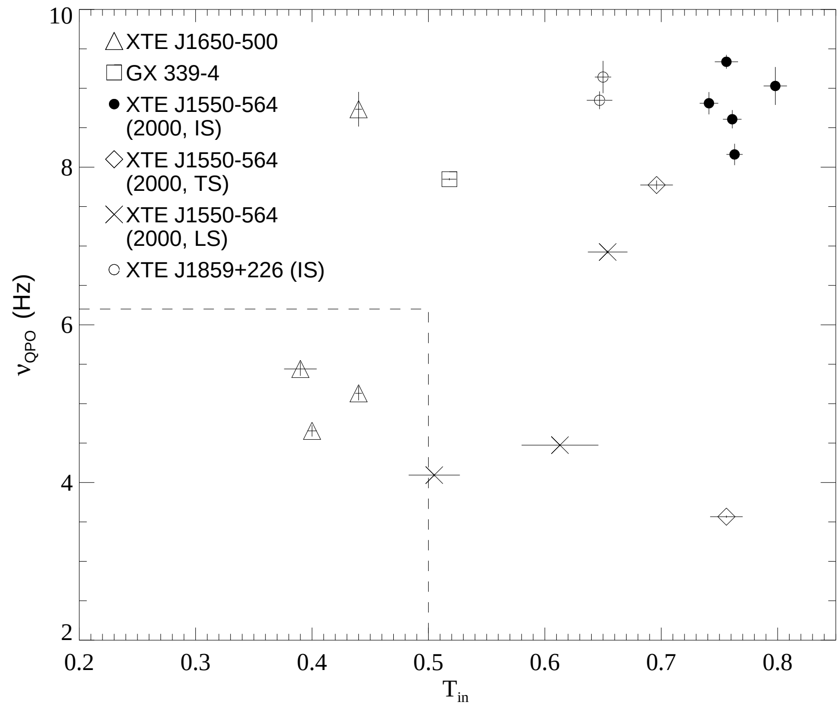

Figure 5.20: The correlation between T_{in} and the QPO frequency. The upper limit points are not shown for clarity, but the region they occupy is shown with dashed lines.

correlated (section 5.3.1), I expected a correlation between the QPO frequency and T_{in}. However, Fig. 5.20 shows that there is no global correlation between these parameters. If only the 2000 outburst of XTE J1550−564 is considered, except the extraordinary observation 9, the remaining observations show a correlation with r of 0.941. The correlation between the QPO frequency and T_{in}, along with the correlation of QPO frequency and disk flux were shown as evidence that the QPOs are originated in the accretion disk since their properties are tightly correlated with the disk parameters (Remillard et al. 2002b). My data, although not rejecting this hypothesis, does not strengthen it either.

Correlation between the spectral index and the integrated lag

Perhaps one of the most interesting correlations I found is the correlation between the spectral index and the integrated lag, as shown in Fig. 5.21. Those two parameters are very well correlated with r of 0.917 for five different sources in four

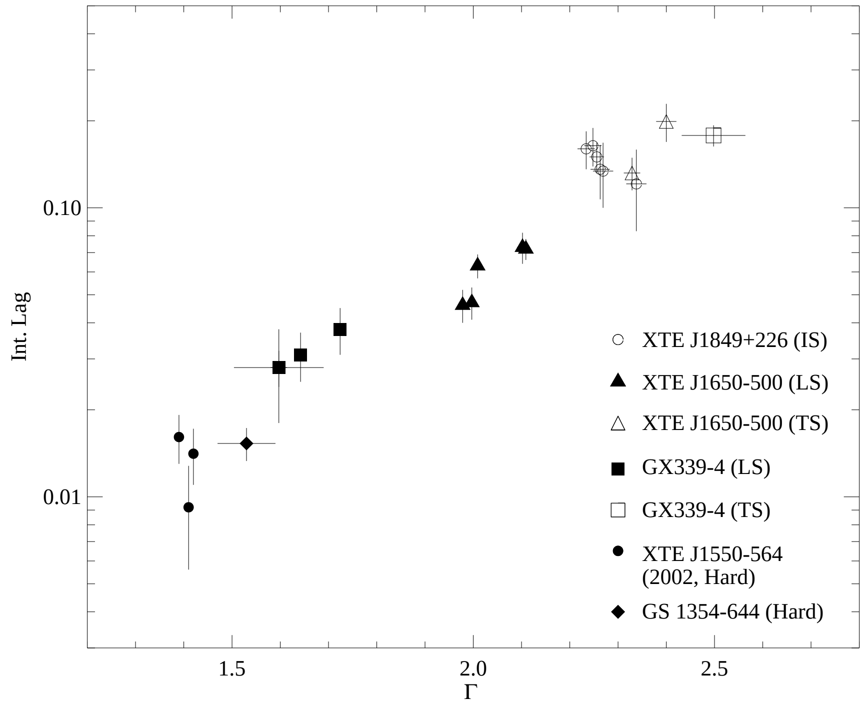

Figure 5.21: The correlation between the spectral index and the integrated lag.

different states (IS, TS, LS, hard). A correlation between the mean lags and Γ was pointed out by Pottschmidt et al. (2002) for Cyg X-1 and by Nowak, Wilms & Dove (2002) for GX 339−4. Both interpreted this relation in terms of a geometrical effect involving an accretion disk truncating at a radius, and a jet or outflow inside this radius. The simulations by Coppi (2000) suggest that larger the vertical extent of this outflow (and therefore larger the lags), the softer the spectrum. As discussed earlier in section 5.3.2, this model has problems explaining Fig. 5.21. It requires a larger outflow in the TS than observation 1 of GX 339−4, whereas radio measurements point out the opposite (Nowak, Wilms & Dove 2002). Similarly, a large outflow that is expected to be present in XTE J1859+226 in this picture did not appear in radio observations (Brocksopp et al. 2002). Although optically thin outflows are observed during state transitions, and they may contribute to the larger lags observed in Cyg X-1 during these transitions, I believe there is a simpler explanation for the correlation in Fig. 5.21. It is again based on the simple thermal Comptonization idea. The lags are related to the average number of scatterings to reach E1 and E2. When the temperature of the corona is very high as indicated by the lower spectral index, the number of scatterings to get to E1 becomes nearly equal to the number of scatterings to get to E2, resulting in small lag. Indeed, for the majority of the hard outburst observations, the lags are consistent with being zero. More scatterings are required to get to E2 than to get to E1 for a lower temperature corona, which increase the lag and may explain Fig. 5.21.

5.4 Energy dependence of power spectra

Another important aim of this work is to investigate the energy dependence of the PSD. This is done in two subsections, the energy dependence of the rms amplitudes, and the energy dependence of the peak frequencies. The reason for this study is explained in section 1.5.2.

5.4.1 Energy dependence of rms amplitudes

I begin with the IS and TS, where the rms amplitudes always increase with energy. This may be due to the strong disk component in the E1 band providing copious Poissonic noise decreasing the rms amplitude by increasing the mean count rate. Whenever the PLR is $\lesssim$0.9, the rms amplitude of variability increases with energy. This also explains the increasing rms amplitude with energy of the first five observations of the LS of the 2000 outburst of XTE J1550−564, for which the PLR$<$0.9. The older papers often quote that the rms amplitude of QPOs increase with energy. This is mostly because the QPOs were first detected when the sources are in the VHS of GBHs which have very strong disk emission.[1] This result clearly shows that the origin of variability can neither be global oscillations of the whole disk, nor a process affecting a large portion of the optically thick disk. The variability may be originated at a localized region and amplified by the corona as discussed in the Compton microscope model in section 1.5.3, or some normal mode oscillation (which

1 The kHz QPOs in NS systems also show an increasing amplitude with energy. For these, the reason for this behavior is probably different because it is believed that the coronae has much higher optical depth than that of GBHs. Lee & Miller (1998) report a comprehensive analysis of Comptonization in these systems and show that the small oscillations of the electron density of the corona result in the observed behavior for the kHz QPOs in NSs.

is not creating a modulation in the disk flux) can affect the properties of the corona creating the variability as discussed in the Psaltis-Norman model in section 1.5.4.

A more complicated case is the dependence of rms amplitudes on energy of the LS observations where the disk component is negligible. For 4U 1630−47, XTE J1748−288, and GRS J1737−31, and the last two observations of the 1998 outburst of XTE J1550−564, the rms amplitudes increase with energy. For XTE J1118−480, GS 1354−644, XTE J1755−324, the second observation of GRO J1655−40, the first observation of the 1998 outburst, final six observations of the 2000 outburst, all observations of the 2001 outburst, and the first four observations of the 2002 outburst of XTE J1550−564, the rms amplitude is consistent with being constant as a function of energy. Therefore, the majority of the sources and observations do not show an energy dependence for their total rms amplitudes. There are also exceptional cases. For XTE J1650−500, the rms amplitude decreases with energy. The second observation of GRO J1655−40, all observations of GX 339−4, and the last four observations of the 2002 outburst of XTE J1550−564 show complex behavior in terms of the energy dependence of the rms amplitudes.

4U 1630−47, XTE J1748−288, and GRS J1737−31, which all show increasing rms amplitude with energy, have much higher absorption column densities than the other sources ($6 - 9.5 \times 10^{22}\mathrm{cm}^{-2}$ compared to less than $1 \times 10^{22}\mathrm{cm}^{-2}$ for the remaining sources). This relation was first realized by Lin et al. (2000), where it was shown that 1E1740.7−2942, a persistent GBH with very high column density ($8 \times 10^{22}\mathrm{cm}^{-2}$) also shows an increasing rms amplitude with energy. As discussed earlier in section 5.3.3, a high absorption column density indicates a high dust column density and a scattering halo. Due to the energy dependence of the cross section and the scattering angle, the lower energy photons are more likely to lose coherence, and therefore the lower energy band may have a lower rms amplitude than that of the the higher energy band.

GX 339−4 shows a more complex behavior. The first observation's rms amplitude decreases with energy. For the second and the third observations, the rms amplitude is constant with energy. For the last observation, E1 and E2 rms amplitudes do not show much change, however, the rms amplitude of E3 is much larger than the E1 and E2 rms amplitudes. Similar behavior is observed in the low flux observations of both the 2001 and the 2002 outbursts of XTE J1550−564. E1 and E2 rms amplitudes are similar whereas E3 shows a huge jump. These different behaviors for different sources are possibly indicators of different geometries and temperature/density gradients. An example of how a temperature gradient causes an rms amplitude dependence on energy is discussed in section 1.5.3 as the Compton microscope model of (Lehr, Wagoner & Wilms 1999).

5.4.2 Energy dependence of peak frequencies and the overall PSD shape

The energy dependence of peak frequencies and the overall PSD shape is discussed in the following two subsections: the dependence in the IS and TS, and the dependence in the LS. It was shown by Belloni et al. (1997) with the *Ginga* data that the peak frequencies of GBHs can be energy dependent in the VHS and during the transition to the LS. I observed and reported the same behavior (higher energy band PSD peaking at higher frequency) during the transition of XTE J1650−500 with the *RXTE* data (Kalemci et al. 2002). In this thesis work, I checked whether other sources also show this effect.

IS and TS observations

During the transition to the LS, the peak frequency of XTE J1650−500 in observation 1 is higher in E2 than E1 (Kalemci et al. 2002). For GX 339−4, in observation 2, L_1 is peaking at a higher frequency in E2 than that of E1 (see Table 4.11). However, for the TS observations of GX 339−4, it is not clear whether a zero-centered Lorentzian or a power-law is a better representation of the lower frequency parts of the noisy PSD. During the IS of the 2000 outburst of XTE J1550−564, for the first two observations, L_1 peaks at a higher frequency for E2 (see Table 4.23). Moreover, a narrow QPO is observed in five of the six IS observations of the 2000 outburst of XTE J1550−564 only in E2 band but not in E1. In observations 7 and 8, the L_2 peak frequency is much higher in E2 than that of E1. However, these observations are barely above the noise level and the values of the peak frequencies are uncertain. In observations 9 and 10, the PSD shape is energy dependent. Observation 9 consists almost entirely of the QPO and its harmonic, and the additional broad Lorentzian peaks at lower frequency in the E2 band (see Tables 4.25, 4.26, 4.22 and Fig. 4.38). In observation 10, in E1, the harmonic is as strong as the fundamental, whereas in E2, although the fundamental QPO is very strong, the harmonic is absent. The IS of XTE J1859+226 show very similar characteristics to the IS of the 2000 outburst of XTE J1550−564. When the PSD is characterized by one Lorentzian, the E2 band PSD peaks at higher frequencies, and also, the two narrow QPOs are only observed in the E2 band (see Fig. 4.65). These results show that the IS and TS observations of GBHs are extremely energy dependent, and not only do the rms amplitudes differ, the overall shape and QPO properties differ also. These changes cannot be explained by just the presence of strong diskbb emission, and point out a complex geometry and strong interaction with the disk and the corona.

LS observations

The majority of the LS observations do not show a peak frequency or PSD shape dependency on energy within 2σ. Here, I will discuss a few exceptional cases. Observation 2 of 4U 1630−47 shows a higher peak frequency in the E2 band, but, the E1 observation is too noisy to claim there is an energy dependence. Observations 15 and 16 of the 2000 outburst of XTE J1550−564 show an energy dependence of PSD peaks for L_3, however, again, the higher frequency Lorentzians, although required for good fits, are not well constrained. Observation 10 of the 2002 outburst of XTE J1550−564 shows a similar behavior in E3, where the PSD is noisy. Therefore, except for the 2002 outburst of XTE J1550−564, the peak frequencies do not depend on the energy in the LS at the 2σ level when measurable. As discussed in section 4.7.5 and shown in Fig. 4.49, and Tables 4.34, and 4.35, the dependence seen in the 2002 outburst of XTE J1550−564 is statistically significant. Similarly in Cyg X-1, the highest frequency Lorentzians (denoted by ν_3 in Pottschmidt et al. 2002) peak at a higher frequency in the highest energy band. The implications of these observations will be discussed in section 5.6.

5.5 Discussion of cross-spectral parameters

5.5.1 Frequency dependent coherence and lags

For seven sources and ten outbursts, I was able to conduct frequency dependent cross-spectral analysis. For most of the hard outbursts, the lags are not statistically significant, and only coherence studies were done. The main driving argument for this study is the claim that the coherence and lag spectrum depend on the position of Lorentzian components in the PSD such that the frequency band where they overlap shows a lower coherence and lag (see section 1.5.5, and Nowak, Wilms & Dove 1999). This could be another strong argument that the PSDs are composed of individual Lorentzian components. Except for the 2001 outburst of XTE J1550−564, my analysis was limited to visual inspection to see if any obvious kinks or dips are present where the Lorentzian components meet. For GRO J1655−40 in one observation, and for six observations in the 2001 outburst of XTE J1550−564, there was a dip in the coherence and lag where two Lorentzians overlap in the PSD. I tried to quantify this dip in coherence in the 2001 outburst of XTE J1550−564, as seen Table 4.33. The change during the dip is less than 2σ. Moreover, almost all other hard state outburst data do not show any dip at all at the frequencies where the Lorentzians meet. As a summary, the data in general do not support Nowak's argument about the dependence of coherence and lag to the Lorentzian components in the PSD.

5.5.2 Integrated lag and mean coherence

For GX 339−4 and XTE J1650−500, the integrated lag is much larger and the mean coherence is much lower during the transition than in the LS, which is similar to what has been observed for the transitions in Cyg X-1. However, when the data from all sources are put together, as done in section 5.3.3, it is seen that the transitional states are not different than the IS. Therefore, the correlation between the integrated lag and Γ can easily be interpreted in the classical context of thermal Comptonization. I also found that the time lag increases with energy in GX 339−4, the 2002 outburst of XTE J1550−564, and for GS 1354−44 which is also consistent with thermal Comptonization. But thermal Comptonization fails to explain the frequency dependence and maximum value of lags unless the corona is nonphysically large (Cui 2000). This led several people to devise complicated models especially to explain the PSD and frequency dependent lags of Cyg X-1. Most of these models invoke a temperature or density gradient in a corona to explain the frequency dependent lags (Kotov, Churazov & Gilfanov 2001). In most of the hard outbursts the lags are very small and the coherence is close to unity, indicating a static, uniform corona.

5.6 Geometry and temperature/density profile of the accretion system

In this section, I will discuss some of the proposed accretion structures and their temperature/density profiles and interpret them with my observations.

There are two basic competing models for the accretion geometry: the slab model where the corona is created by the magnetic flares above and below the accretion disk, and the inner accretion flow model where the inner disk truncates at some radius and turns into a hot inner flow, the corona. There are several variations of these models to explain the spectral and temporal properties of these systems. It is accepted that the sandwich slab model that covers the whole accretion disk cannot sustain its high temperature due to strong cooling from the Compton processes and cannot explain the spectrum in the LS. However, there are several ways to get around this, such as the corona being patchy and well above the accretion disk so that the cooling times are much larger. Moreover, the creation of such a corona with magnetic flares and reconnection events, with reasonable parameters, can explain both the creation of broad band variability and its lag characteristics (Poutanen & Fabian 1999). There has been a lot of effort expended on understanding the observed spectral correlations (for example the reflection fraction and the spectral index) with this geometry, and also discussions whether the variability is due to the flares of the hard component, or flares in the disk modified by the hard component (Malzac, Beloborodov & Poutanen 2001). Unfortunately, the majority of these models try to explain the temporal properties of Cyg X-1 in the LS. With proper selection of parameters, they can get similar PSD and lag spectrum for this source. However, they often lack an explanation for the evolution of the characteristic frequencies of the PSD as it decays in the LS. They also have great difficulty explaining the Lorentzian structure of the PSDs unless they have very fine tuning of their flare parameters (see for example Zycki 2002). The evolution of these models to include the changes in the PSD characteristic frequencies remains to be seen.

The geometry with an inner accretion flow, on the other hand, very naturally accounts for the evolution of the PSD. The inner accretion disk evaporates and is replaced by the corona as the source progresses in the LS, and therefore the characteristic frequencies decrease, and the spectrum hardens. In this geometry, getting the broad band variability and the correct frequency dependent lag spectrum is challenging (Zycki 2002). Recently, a modification in these models has been proposed by several authors such that the inner accretion flow is actually the base of an outflow or a jet which has been ubiquitously observed in the LS of GBHs (Fender 2001; Nowak, Wilms & Dove 2002). These are often called hybrid models. For example, the presence of a large, optically thin outflow explains the reduced coherence and increased lags observed during the Cyg X-1 state transitions very well (Pottschmidt et al. 2002, and section 5.3.2).

XTE J1650−500 behaves remarkably similar to Cyg X-1 during the state transition. The coherence is reduced and the lags are much higher. In addition, there is a shift in the peak frequency as a function of energy such that E2 L_1 peaks at a higher frequency than E1 L_1. If indeed there were an optically thin outflow during the transition, the observational properties mentioned above can be explained by invoking a temperature gradient in the outflow as illustrated in Fig. 5.22. In this picture, the inner disk is close to the BH during the transition, and the outflow has a temperature/density gradient such that the Compton y parameter is higher close to the BH, as depicted by the color gradient in the figure. In this geometry, the emission from the inner part of the accretion disk, which creates the higher frequency variability, interacts predominantly with the higher y region whereas the outer part of the disk interacts with the lower y region. This could explain the high energy PSD peaking at higher frequencies (Kalemci et al. 2002). This picture also explains the lower coherence and higher lags due to the additional scatterings in the large variable

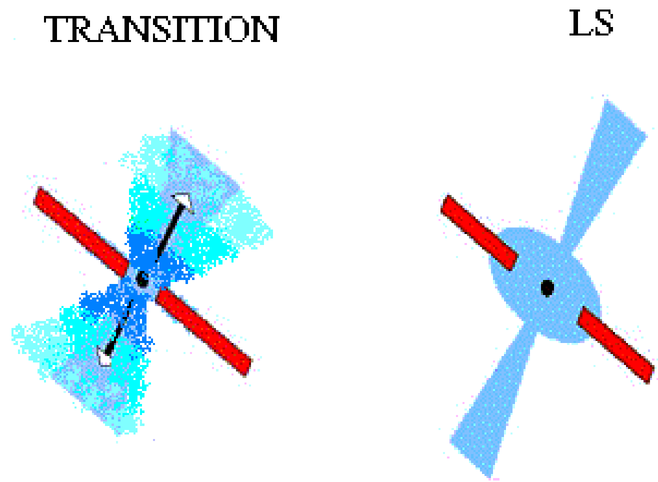

Figure 5.22: Hybrid model for the state transition of XTE J1650−500. During the transition, the disk is close to the BH. There is a temperature/density gradient in the disk such that darker color indicates higher Compton y parameter. In the LS, the accretion disk is away from the BH, the jet is compact and has little effect on timing.

outflow and consistent with the radio observations. After the transition is over, the outflow remains in the form of a compact jet, and the inner disk is at a larger distance. Note that this evolution is also consistent with the Γ - reflection fraction correlation: reflection fraction is very high during the transition, and a high Γ is observed, and it is much lower in the LS, where a lower Γ is observed. However, no large outflow is required to explain the larger lags and reduced coherence during the transitions for the sources discussed in this work (see section 5.3.3).

The 2002 outburst of XTE J1550−564 and Cyg X-1 also show a slight peak frequency dependence on energy. This dependence can be explained by a temperature/density gradient in the corona, and the level of this gradient determines how much the peak frequencies move. Interestingly, the 2002 outburst of XTE J1550−564 also showed X-ray lags unlike most of the hard outbursts. This supports the models relating X-ray lags to temperature/density gradients in the corona, for example the "lags due to accretion" model by Kotov, Churazov & Gilfanov (2001) which is discussed in some detail in section 1.5.5. For the majority of the sources, the peak frequency does not change with energy, indicating a uniform y corona which is shown to have problems explaining the frequency dependence of X-ray lags. Currently, a model that explains all the temporal properties of GBHs does not exist, but I believe this study will be a good testing ground for these models beyond Cyg X-1.

Chapter 6

Conclusions and Outlook

"Annnneeeeeeee, bittiiiiii..."

- Deli, cover of last episode

6.1 Conclusions

An important goal of black hole binary research is to understand the accretion structure (geometry, temperature and density profile of accretion components), and nature of variability of these systems. This work addresses these goals by analyzing the X-ray temporal and spectral properties of a relatively large subset of GBHs during outburst decay. Transitions to the LS are often observed during outburst decays, and they provide additional information about the vicinity of the BHs via the appearance of broad band variability, QPOs, and evolution of spectral and temporal properties before and after the transitions. This thesis work uses temporal analysis with Fourier techniques (PSD, coherence and lag), and interprets the results mostly within the context of the modern GBH accretion models. The analysis of the energy spectrum was also conducted, and used together with the temporal analysis.

For this study, a total of eleven *RXTE* sources in sixteen outbursts are analyzed.

This is the first comprehensive and comparative study of GBHs with this many sources with the same instrument. Thanks to our monitoring program, the coverage close to the transition is significantly improved, and for the first time allowed us to determine the physical changes that drives the transitions in detail.

The first problem I attacked is the evolution of spectral parameters before the state transition and appearance of broad band variability at the state transition. A change in the spectral index Γ is shown to be the pre-cursor of the transition showing a decrease 3-5 days before. I also show that the PLR increases close to the transition for all sources. Very frequent monitoring observations ($\sim$once a day) allowed me to determine the power-law flux (and consequently the PLR) as the physical parameter that drives the appearance of broad band variability. The power-law flux shows a large increase consistently for all transitions except the 1999 outburst of 4U 1630$-$47.

I investigated the evolution after the state transition. The T_{in} and diskbb flux decreased after the transition, and they were unobservable with PCA within a week of the transition for all outbursts. The characteristic frequencies of all except one observation of the 2000 outburst of XTE J1550$-$564 decreased after the state transition. These spectral and temporal changes are consistent with the idea that the inner accretion disk retreats after the state transition. In the exceptional case, the QPO frequency in observation 9 of the 2000 outburst of XTE J1550$-$564 first increased and then decreased after the transition. This behavior is consistent with the prediction of the AEI QPO model if the inner accretion disk is close to the marginally stable orbit during this observation.

For some sources, at very low flux level, I observed that the Γ increases slightly just before the source flux is below the detection limit. Although incomplete spectral modeling of the Galactic ridge emission might be the cause for some of these sources, for the 2001 outburst of XTE J1550$-$564 and XTE J1118+480, the ridge emission is negligible. The spectral softening for these sources can be explained within the context of the ADAF model. As the mass accretion rate drops, the optical depth of the ADAF region decreases causing the Compton y parameter to decrease, and consequently Γ to increase (Esin, McClintock & Narayan 1997).

I investigated the correlations between the spectral and temporal fit parameters. The majority of the sources show a correlation between T_{in} and Γ, which can be explained by the interaction between the optically thick accretion disk and the Compton corona. When the inner disk temperature is higher, there is more flux to cool the Compton corona, which results in a higher Γ.

The peak frequencies (ν_1 and ν_2) of the Lorentzians show a correlation, which is consistent with a previously reported correlation valid for several types of X-ray binaries (Z, atoll, GBH, and even white dwarf systems, Psaltis, Belloni & van der Klis 1999; Mauche 2002). The QPO frequency and ν_1 are also correlated, and except for the 4U 1630−47 observations, the correlation is consistent with the one reported by Wijnands & van der Klis (1999). This correlation also includes both neutron star and the black hole systems. My results with unpublished new observations extend the correlations found earlier. The fact that these correlations exist among Z, atoll, BHCs, and even white dwarf systems suggests that similar mechanisms are responsible for creating the QPOs and the noise components, and the variability depends weakly, if at all, on the magnetic field and the presence of a hard surface. It also place strong constraints on models explaining the X-ray variability from these systems.

The majority of the sources with zero-centered L_1 obey the Belloni - Hasinger correlation. Within the context of Lorentzian modeling, this means that for majority of the sources, the rms amplitude does not vary in the LS.

The relation between the cross-spectral parameters, the integrated lag and the mean coherence, is also investigated. This relation showed that the IS and TS have larger integrated lag and smaller coherence, whereas the LS observations have smaller lags and higher coherence. In fact, the integrated lag is zero for most of the hard outbursts. This result can be explained within the context of Compton scattering. In the LS, Γ is low,the temperature of the corona is high, and approximately same number of scatterings is enough to knock a seed photon to either the lower energy band or the higher energy band. This would result in high coherence and no or little lags. For a lower temperature corona, the average number of scatterings to jump to the lower energy band and higher energy band may be different, resulting in higher lags and reduced coherence. This can also explain the tight correlation observed between Γ and integrated lag.

The PLR and the rms amplitude show a tight, global correlation. The rms amplitude is lower for lower PLR. This can be understood if the optically thick accretion disk provides mostly "Poissonic" emission. This would not change the shape of the PSD, however by increasing the DC level of the light curve, it would reduce the intrinsic rms amplitude coming from the corona component. This correlation also shows that the variability is observed only when the PLR ≥ 0.45, and the transition to the LS happens only when the PLR exceeds 0.7.

For most of the sources, the rms amplitude of variability strongly anti-correlates with Γ. The sources that do not obey this relation are the IS observations and two other sources with very high absorption column densities. These exceptions show a smaller rms amplitude at lower energies than the other sources with the same Γ. The IS cases can be explained via the strong diskbb contribution. For the high column density sources, I interpreted the reduced rms amplitude via the small angle scatterings of X-ray photons with the ISM dust around these sources. Both the scattering cross section and the average scattering angle are larger for less energetic photons, which would cause a greater loss of coherence and rms amplitude at low energies than at high. This idea is supported by the correlation between Γ and the rms amplitude in E2 which is valid for all sources.

The QPO frequencies and Γ also show a tight, global correlation. I explained this correlation with the help of another correlation between Γ and the reflection fraction. Combination of these correlations indicate that there is a tight relation between the inner disk radius and the QPO frequency. This correlation, therefore, supports all low frequency QPO models that link the QPOs to the inner accretion disk, and does not support global oscillations of the disk, or trapped oscillations at certain fixed frequencies determined by the mass and spin of the BH

In IS and TS, the rms amplitude increases with energy, which is again interpreted via the "Poissonic" nature of the diskbb emission, which is strong in these states and more effective in lower energy bands. For the majority of the LS observations, the rms amplitudes do not change with energy. In IS and TS, not only the rms amplitudes, but also the PSD shapes depend on energy. In the 2000 outburst of XTE J1550−564 and in XTE J1859+226, narrow QPOs in IS are observed at higher, but not in lower energies. For XTE J1859+226, during the transition of XTE J1650−500, and for the 2002 outburst of XTE J1550−564, L_1 peaks at a higher frequency at higher energies than at low energies. These cases cannot be explained just by the presence of the diskbb component, and they suggest a temperature/density gradient in the corona. On the other hand, most of the hard outbursts do not require such gradient.

My results support an accretion disk structure with an optically thick accretion disk truncating at some radius and turning into an hot inner accretion flow (i.e. ADAF). The hybrid model (where the hot electron corona is the base of an optically thin outflow or a jet) is also a possibility. An optically thin, large outflow with a temperature/density gradient can explain the behavior of coherence and lag, and also the peak frequency shift during the transition of XTE J1650−500. However, the radio signature expected for such an outflow is not detected for the TS of GX 339−4, and for the IS of XTE J1859+226, although they show similar cross-spectral and PSD characteristics with XTE J1650−500 during the transition.

Currently, a model that explains all the temporal and spectral properties of GBHs does not exist, and the efforts are mainly concentrated on explaining the most studied and oldest GBH, Cyg X-1. I worked on a large data set from many similar, and this provides a new testing ground for models devised to understand GBHs.

6.2 Future work

There are two paths to follow to extend the understanding of GBHs by studying their temporal and spectral evolution during outbursts. The first one is the observational path, continuing to monitor transient systems during outburst decay with *RXTE* and extending the correlations to higher significance. We have an ongoing monitoring program for this purpose, and we continue to propose every *RXTE* cycle. This monitoring program not only extends the current studies, but also provides unobserved new results. The high frequency QPO in the LS (Kalemci et al. 2001), the frequency inversion of the QPO observed in the 2000 outburst of XTE J1550−564 (Rodriguez et al. 2002a), and the flares and oscillations observed at low flux levels of XTE J1650−500 (Tomsick et al. 2002a) are such new phenomena that have not been observed before. In addition to the regular, short ($\sim$2 ks) regular monitoring observations, we also have a longer (30 ks) but less frequent observing program to trace the evolution of temporal parameters after the state transition with very high statistics. This will allow us to explore the cross-spectral parameters and their relation to the PSD in great detail. Moreover, the HEXTE spectrum with higher statistics will help us to determine whether there is a high-energy cut-off which would indicate a thermal Comptonization process. Lack of a cut-off might support models alternative to thermal Comptonization (i.e., Markoff, Falcke & Fender 2001), or hybrid models. The radio monitoring of these sources is also extremely important and may allow us to make a better connection between the timing properties and the outflows. Our group will continue to conduct short monitoring observations, and long observations during the state transition and in addition monitor the sources in radio to explore the connection.

As discussed in section 1.4, the sources often start the outburst in the LS, and make a transition to the HS (or VHS), which is the reverse of the behavior during the decay. The comparison of the outburst rises and decays may provide additional information. For example, hysteresis has been seen in the transition luminosities for several sources (Nowak 2002), and other parameters might also show this effect. I will investigate the hysteresis effect by analyzing the *RXTE* archival data from sources observed during outburst rise and comparing them to the decay results found here.

The second path is conducting Monte Carlo simulations of accretion disk - Compton corona systems with various geometries. I have been working on such a modeling effort with a code that calculates the energy spectra and the time lags for a system where the photons are created with a diskbb distribution in the disk and undergo repeated Compton scatterings until escape from the corona or absorption in the disk. Temporal studies can also be done with these simulations. A Comptonizing corona can be described by a linear transformation function between the seed photon light curve and the final output light curve, provided that the properties of the corona are static during the observations. We can calculate this transfer function with the simulations for different geometries. Then we can feed a soft light curve from a lower energy band to the simulation, and compare the resulting temporal properties in higher energy bands in the *RXTE* data. As a summary, the future work concentrates on a combination of observational and computational efforts that are pointed towards understanding the accretion geometry and its relation to outflows, and also obtaining the physical parameters of the accretion components as well as exploring the origin of variability.

Appendix A

ATELs and IAU Circulars

A.1 ATEL 103

4U 1543−47

E. Kalemci, J. A. Tomsick, R. E. Rothschild (CASS/UCSD), S. Corbel (CEA Saclay), P. Kaaret (CfA), J. McClintock (Harvard), report: "An analysis of Rossi X-ray Timing Explorer pointed observations of the black hole transient 4U 1543-475 (see ATEL# 98 and IAUC# 7920) indicates that the source is currently in transition, possibly to the low hard state. The X-ray spectra of two observations taken on July 23 and July 24 show a multicolor disk component with ~0.4 keV inner disk temperature and a power law with a photon index of ~2.65. The 2-15 keV band power spectrum has an rms amplitude of ~20%, with a QPO at ~9 Hz and its harmonic at ~18 Hz. The rms amplitude of the QPO is ~6%. The QPO frequency did not move between observations. Further evolution of the temporal and spectral parameters of the source was seen for observations taken on July 25 and July 26. The power law index hardened to ~2.1, and the disk temperature decreased. This was accompanied by an increase in the overall rms amplitude of variability to ~30%, and a decrease in QPO frequency to 5.6 Hz. RXTE All-Sky Monitor hardness ratios indicate that the transition began on July 21 or July 22. We will continue to monitor the source with RXTE, and we encourage observations in the optical and radio bands."

A.2 IAU Circular 7837

XTE J1650−500

J. A. Tomsick and E. Kalemci, University of California at San Diego; S. Corbel, Universite Paris 7 and Laboratoire du Commissariat a l'Energie Atomique, Saclay; and P. Kaaret, Harvard-Smithsonian Center for Astrophysics, report on a series of 30 RXTE observations of the blackhole-candidate X-ray transient XTE J1650−500 (cf. IAUC 7707, 7708, 7710, 7715) taken between 2001 Dec. 27 and 2002 Feb. 24: "During this time, the 3- to 20-keV light curve exhibits a large amplitude oscillation with a 13.5- to 14.0-day period about a mean flux of $6.6 \times 10^{-11}\,\mathrm{erg\,cm^{-2}\,s^{-1}}$. The level of modulation is extremely high and roughly sinusoidal with a peak-to-peak flux variation that is close to, or possibly greater than, an order of magnitude. In addition to the four oscillation cycles we observe, the oscillation may have been present at a significantly lower level earlier in the outburst, based on the All-Sky Monitor 1.5- to 12-keV light curve. The 14-day period may be orbital, but we believe a disk precession origin (as seen in Her X-1) is more likely. Observations are encouraged to determine if the 14-day oscillation is seen at other wavelengths and to look for possible orbital or superhump signatures."

A.3 IAU Circular 7912

GX339−4

D. M. Smith, University of California, Berkeley, on behalf of a collaboration (including T. Belloni, W. A. Heindl, E. Kalemci, R. Remillard, M. Nowak, J. H. Swank, and S. Corbel), reports that the blackhole candidate GX 339-4, in outburst since Mar. 26, entered the rare Very High State (VHS) of X-ray emission around May 6. The energy spectrum is dominated by a disk blackbody but has a strong power-law tail. The power spectrum of the fast variability switches among at least three states: band-limited noise with a broad quasiperiodic oscillation (QPO) near 9 Hz, red noise with a narrower QPO near 6 Hz, and a quiet state with almost no variability. RXTE/PCA observations are taking place at least twice weekly. The RXTE ASM shows that the count rate has started to decline from its peak. Monitoring in all other wavebands is strongly encouraged; the VHS was last observed in 1988 (Miyamoto et al. 1991, Ap.J. 383, 784).

Appendix B

Useful information

B.1 Acronyms and abbreviations

ADAF: Advection dominated accretion flow

AEI: Accretion ejection instability

***ASCA*:** *Advanced Satellite for Cosmology and Astrophysics*

ASM: All Sky Monitor

BATSE: Burst And Transient Source Experiment

***Beppo*SAX:** *Beppo Satellite per Astronomia X*

***BBXRT*:** *Broad Band X-ray Telescope*

BMC: Bulk motion Comptonization

CASS: Center for Astrophysics and Space Sciences

***CGRO*:** *Compton Gamma-Ray Observatory*

DOF: Degrees of freedom

EA: Event Analyzer

EDS: Experiment Data System

ESA: European Space Agency

***EXOSAT*:** *European X-ray Observatory Satellite*

FOV: Field of view

FRED: Fast rise, exponential decay

FWHM: Full width at half maximum

GOF: Guest Observer Facility

GSFC: Goddard Space Flight Center
***HEAO*:** *High Energy Astrophysical Observatory*
HEASARC: High Energy Astrophysics Science Archive Research Center
HEXTE: High Energy X-ray Timing Experiment
HMXB: High-mass X-ray binary
HS: High-soft state
IAAT: Institute for Astronomy and Astrophysics
IDL: Interactive Data Language
***INTEGRAL*:** *International Gamma-Ray Astrophysics Laboratory*
IS: Intermediate state
ISCO: Innermost stable circular orbit
LAC: Large Area Counter
LMXB: Low-mass X-ray binary
LS: Low-hard state
MC: Multi-color disk blackbody
MHD: Magnetohydrodynamic
MIT: Massachusetts Institute of Technology
MJD: Modified Julian Day, MJD is Julian Day JD−2400000.5
MRI: Magneto-rotational instability
NASA: National Aeronautics and Space Administration
PCA: Proportional Counter Array
PCU: Proportional Counter Unit
PHA: Pulse height analyzer
PSA: Pulse shape analyzer
PSD: Power spectral density
PSPC: Position-Sensitive Proportional Counter
QPO: Quasi-Periodic Oscillation
***ROSAT*:** *Röntgen Satellite*
***RXTE*:** *Rossi X-ray Timing Explorer*
SAA: South Atlantic Anomaly
SAS: *Small Astronomy Satellite*
SNR: Signal to noise ratio

SSC:	Scanning Shadow Camera
TS:	Transitional state
UCSD:	University of California, San Diego
ULD:	Upper level discriminator
UTC:	Universal time oordinated
VHS:	Very high state
VLE:	Very large event
***XMM*:**	*X-ray Multi-Mirror Mission*
XRB:	X-ray Binary
XTE:	*X-ray Timing Explorer* (see *RXTE*)
XULD:	Extra upper level discriminator

B.2 Constants and conversions

Fine Structure Constant:	$\alpha = 7.3 \times 10^{-3}$
Speed of Light:	$c = 3.00 \times 10^{10}\,\mathrm{cm\,s^{-1}}$
Charge of an Electron:	$e = 4.80 \times 10^{-10}\,\mathrm{G\,cm^2}$
Gravitational Constant:	$G = 6.67 \times 10^{-8}\,\mathrm{gm^{-1}\,cm^3\,s^{-2}}$
Planck's Constant:	$\hbar = 1.05 \times 10^{-27}\,\mathrm{ergs\,s}$
	$= 6.58 \times 10^{-19}\,\mathrm{keV\,s}$
	$\hbar c = 1.973 \times 10^{-8}\,\mathrm{keV\,cm}$
Boltzman's Constant:	$k = 1.38 \times 10^{-16}\,\mathrm{ergs\,K^{-1}}$
	$= 8.61 \times 10^{-8}\,\mathrm{keV\,K^{-1}}$
Electron Mass:	$m_{\mathrm{e}} = 9.11 \times 10^{-28}\,\mathrm{gm}$
	$= 511\,\mathrm{keV\,c^{-2}}$
Solar Mass:	$M_{\odot} = 1.99 \times 10^{33}\,\mathrm{gm}$
Solar Radius:	$R_{\odot} = 6.69 \times 10^{10}\,\mathrm{cm}$
Solar Luminosity	$L_{\odot} = 3.90 \times 10^{33}\,\mathrm{ergs\,s^{-1}}$
Earth Mass:	$M_{\oplus} = 5.68 \times 10^{27}\,\mathrm{gm}$
Earth Radius:	$R_{\oplus} = 6.37 \times 10^{8}\,\mathrm{cm}$

$$
\begin{aligned}
1\,\mathrm{keV} &= 1.602 \times 10^{-9}\,\mathrm{ergs} \\
1\,\mathrm{kpc} &= 3.09 \times 10^{21}\,\mathrm{cm} \\
1\,\mathrm{M_{\odot}\,yr^{-1}} &= 6.31 \times 10^{25}\,\mathrm{gm\,s^{-1}}
\end{aligned}
$$

Bibliography

Abraham, L., Agrawal, V., Sreekumar, P., & Seetha, S., 2001, Bulletin of the Astronomical Society of India, 29, 365

Abramowicz, M. A., Björnsson, G., & Igumenshchev, I. V., 2000, PASJ, 52, 295

Agol, E., Krolik, J., Turner, N. J., & Stone, J. M., 2001, ApJ, 558, 543

Arnaud, K. A., 1996, in ASP Conf. Ser. 101: Astronomical Data Analysis Software and Systems V, Vol. 5, 17

Augusteijn, T., Coe, M., & Groot, P., 2001, IAU Circular, 7710

Böttcher, M., & Liang, E. P., 1998, ApJ, 506, 281

Böttcher, M., & Liang, E. P., 1999, ApJ, 511, L37

Balbus, S. A., & Hawley, J. F., 1991, ApJ, 376, 214

Balucinska-Church, M., & McCammon, D., 1992, ApJ, 400, 699

Bao, G., & Ostgaard, E., 1995, ApJ, 443, 54

Belloni, T., 2001, in X-ray Emission from Accretion onto Black Holes

Belloni, T., Colombo, A. P., Homan, J., Campana, S., & van der Klis, M., 2002, A&A, 390, 199

Belloni, T., & Hasinger, G., 1990, A&A, 227, L33

Belloni, T., Méndez, M., van der Klis, M., Lewin, W. H. G., & Dieters, S., 1999, ApJ, 519, L159

Belloni, T., Mendez, M., van der Klis, M., Hasinger, G., Lewin, W. H. G., & van

Paradijs, J., 1996, ApJ, 472, L107

Belloni, T., Psaltis, D., & van der Klis, M., 2002, ApJ, 572, 392

Belloni, T., van der Klis, M., Lewin, W. H. G., van Paradijs, J., Dotani, T., Mitsuda, K., & Miyamoto, S., 1997, A&A, 322, 857

Beloborodov, A. M., 1999, ApJ, 510, L123

Beloborodov, A. M., 2000, in High Energy Processes in Accreting Black Holes, ASP Conf. Ser. 161: High Energy Processes in Accreting Black Hole, eds. Poutanen, J. and Svensson, R., (1999)

Bendat, J. S., & Piersol, A. G., 1986, Random Data: Analysis and Measurement Procedures, (New York: John Wiley & Sons)

Berger, M., & van der Klis, M., 1998, A&A, 340, 143

Bisnovatyi-Kogan, G. S., & Blinnikov, S. I., 1977, A&A, 59, 111

Blandford, R. D., & Begelman, M. C., 1999, MNRAS, 303, L1

Blandford, R. D., & Konigl, A., 1979, ApJ, 232, 34

Borozdin, K., Revnivtsev, M., Trudolyubov, S., Shrader, C., & Titarchuk, L., 1999, ApJ, 517, 367

Brocksopp, C., Fender, R. P., McCollough, M., Pooley, G. G., Rupen, M. P., Hjellming, R. M., de la Force, C. J., Spencer, R. E., Muxlow, T. W. B., Garrington, S. T., & Trushkin, S., et al., 2002, MNRAS, 331, 765

Brocksopp, C., Jonker, P. G., Fender, R. P., Groot, P. J., van der Klis, M., & Tingay, S. J., 2001, MNRAS, 323, 517

Buxton, M., Vennes, S., Ferrario, L., & Wickramasinghe, D. T., 1998, IAU Circular, 6815

Callanan, P. J., Charles, P. A., Honey, W. B., & Thorstensen, J. R., 1992, MNRAS, 259, 395

Campbell-Wilson, D., McIntyre, V., Hunstead, R., Green, A., Wilson, R. B., & Wilson, C. A., 1998, IAU Circular, 7010

Cannizzo, J. K., Wheeler, J. C., & Ghosh, P., 1985, in ASSL Vol. 113: Cataclysmic Variables and Low-Mass X-ray Binaries, 307

Castro-Tirado, A. J., Ilovaisky, S., Pedersen, H., Gonzalez, J.-F., Pizarro, M., Miranda, J., & Boehnhardt, H., 1997, IAU Circular, 6775

Castro-Tirado, A. J., Kilmartin, P., Gilmore, A., Petterson, O., Bond, I., Yock, P., & Sanchez-Fernandez, C., 2001, IAU Circular, 7707

Caunt, S. E., & Tagger, M., 2001, A&A, 367, 1095

Chakrabarti, S. K., 2000, in Il Nouvo Cimento (In press); Proceedings of 3rd ICRA workshop (July 12-21, 1999)

Coppi, P. S., 2000, in High Energy Processes in Accreting Black Holes, ASP Conf. Ser. 161: High Energy Processes in Accreting Black Hole, eds. Poutanen, J. and Svensson, R., (1999)

Corbel, S., Fender, R., & Tzioumis, A., 2002, IAU Circular, 7795

Corbel, S., Fender, R. P., Tzioumis, A. K., Nowak, M., McIntyre, V., Durouchoux, P., & Sood, R., 2000, A&A, 359, 251

Corbel, S., Kaaret, P., Jain, R. K., Bailyn, C. D., Fender, R., Tomsick, J. A., Kalemci, E., McIntyre, V., Campbell-Wilson, D., Miller, J., & McCollough, M. L., et al., 2001, ApJ, 554, 43

Cui, W., 2000, in High Energy Processes in Accreting Black Holes, ASP Conf. Ser. 161: High Energy Processes in Accreting Black Hole, eds. Poutanen, J. and Svensson, R., (1999)

Cui, W., Chen, W., & Zhang, S. N., 2000, ApJ, 529, 952

Cui, W., Heindl, W. A., Rothschild, R. E., Zhang, S. N., Jahoda, K., & Focke, W., 1997a, ApJ, 474, 57

Cui, W., Heindl, W. A., Swank, J. H., Smith, D. M., Morgan, E. H., Remillard, R., & Marshall, F. E., 1997b, apj, 487, L73

Cui, W., Morgan, E. H., Heindl, W. A., Swank, J. H., & Smith, D. M., 1997c, iauc, 6604

Cui, W., Shrader, C. R., Haswell, C. A., & Hynes, R. I., 2000, ApJ, 535, L123

Cui, W., Zhang, S. N., & Chen, W., 2000, ApJ, 531, L45

Cui, W., Zhang, S. N., Chen, W., & Morgan, E. H., 1999, ApJ, 512, L43

Cui, W., Zhang, S. N., Focke, W., & Swank, J. H., 1997d, ApJ, 484, 383

di Matteo, T., & Psaltis, D., 1999, ApJ, 526, L101

Di Salvo, T., Méndez, M., van der Klis, M., Ford, E., & Robba, N. R., 2001, ApJ, 546, 1107

Dieters, S. W., Belloni, T., Kuulkers, E., Woods, P., Cui, W., Zhang, S. N., Chen, W., van der Klis, M., van Paradijs, J., Swank, J., Lewin, W. H. G., & Kouveliotou, C., et al., 2000, ApJ, 538, 307

Done, C., & Nayakshin, S., 2001, ApJ, 546, 419

Dove, J. B., Wilms, J., & Begelman, M. C., 1997, ApJ, 487, 747

Dove, J. B., Wilms, J., Maisack, M., & Begelman, M. C., 1997, ApJ, 487, 759

Dove, J. B., Wilms, J., Nowak, M. A., Vaughan, B. A., & Begelman, M. C., 1998, MNRAS, 298, 729

Doxsey, R., Bradt, H., Johnston, M., Griffiths, R., Leach, R., Schwartz, D., Schwarz, J., & Grindlay, J., 1979, ApJ, 228, L67

Ebisawa, K., 2000, in High Energy Processes in Accreting Black Holes, ASP Conf. Ser. 161: High Energy Processes in Accreting Black Hole, eds. Poutanen, J. and Svensson, R., (1999)

Ebisawa, K., Mitsuda, K., & Inoue, H., 1989, PASJ, 41, 519

Ebisawa, K., Ogawa, M., Aoki, T., Dotani, T., Takizawa, M., Tanaka, Y., Yoshida, K., Miyamoto, S., Iga, S., Hayashida, K., Kitamoto, S., & Terada, K., et al., 1994, PASJ, 46, 375

Esin, A. A., McClintock, J. E., Drake, J. J., Garcia, M. R., Haswell, C. A., Hynes, R. I., & Muno, M. P., 2001, ApJ, 555, 483

Esin, A. A., McClintock, J. E., & Narayan, R., 1997, ApJ, 489, 865

Fabian, A. C., & Barcons, X., 1992, ARA&A, 30, 429

Falcke, H., Beckert, T., Markoff, S., Koerding, E., Bower, G. C., & Fender, R., 2001, in Lighthouses of the Universe, ed. R. Sunyaev, M. Gilfanov, E. Churazov, (Heidelberg: Springer)

Fender, R., Corbel, S. ., Tzioumis, T., McIntyre, V., Campbell-Wilson, D., Nowak, M., Sood, R., Hunstead, R., Harmon, A., Durouchoux, P., & Heindl, W., et al., 1999a, ApJ, 519, L165

Fender, R. P., 2001, MNRAS, 322, 31

Fender, R. P., Garrington, S. T., McKay, D. J., Muxlow, T. W. B., Pooley, G. G., Spencer, R. E., Stirling, A. M., & Waltman, E. B., 1999b, MNRAS, 304, 865

Fender, R. P., Hjellming, R. M., Tilanus, R. P. J., Pooley, G. G., Deane, J. R., Ogley, R. N., & Spencer, R. E., 2001, MNRAS, 322, L23

Fender, R. P., Spencer, R. E., Newell, S. J., & Tzioumis, A. K., 1997a, MNRAS, 286, L29

Fender, R. P., Tingay, S. J., Higdon, J., Wark, R., & Wieringa, M., 1997b, IAU Circular, 6779

Filippenko, A. V., & Chornock, R., 2001, IAU Circular, 7644

Fox, D., & Lewin, W., 1998, IAU Circular, 6964

Frank, J., King, A., & Raine, D., 1992, Accretion Power in Astrophysics, (Cambridge: Cambridge University Press)

Fryer, C. L., & Kalogera, V., 2001, ApJ, 554, 548

Galeev, A. A., Rosner, R., & Vaiana, G. S., 1979, ApJ, 229, 318

Garnavich, P., & Quinn, J., 2000, IAU Circular, 7388

Garnavich, P. M., Stanek, K. Z., & Berlind, P., 1999, IAU Circular, 7276

Gierliński, M., Maciołek-Niedźwiecki, A., & Ebisawa, K., 2001, MNRAS, 325, 1253

Gierliński, M., Zdziarski, A. A., Poutanen, J., Coppi, P. S., Ebisawa, K., & Johnson, W. N., 1999, MNRAS, 309, 496

Gierlinski, M., Zdziarski, A. A., Done, C., Johnson, W. N., Ebisawa, K., Ueda, Y., Haardt, F., & Phlips, B. F., 1997, MNRAS, 288, 958

Grebenev, S. A., Sunyaev, R. A., Pavlinsky, M. N., & Dekhanov, I. A., 1991, Pis ma Astronomicheskii Zhurnal, 17, 985

Groot, P., Tingay, S., Udalski, A., & Miller, J., 2001, IAU Circular, 7708

Grove, J. E., Johnson, W. N., Kroeger, R. A., McNaron-Brown, K., Skibo, J. G., & Phlips, B. F., 1998, ApJ, 500, 899

Hameury, J., King, A. R., & Lasota, J., 1990, ApJ, 353, 585

Hannikainen, D., Campbell-Wilson, D., Hunstead, R., McIntyre, V., Lovell, J., Reynolds, J., Tzioumis, T., & Wu, K., 2000, in 'Proceedings of the Third Microquasar Workshop: Granada Workshop on galactic relativistic jet sources', Eds: A. J. Castro-Tirado, J. Greiner and J. M. Paredes, Astrophysics and Space Science, in press, astro-ph/0011051

Hannikainen, D. C., Hunstead, R. W., Campbell-Wilson, D., & Sood, R. K., 1998, A&A, 337, 460

Haswell, C. A., Skillman, D., Patterson, J., Hynes, R. I., & Cui, W., 2000, IAU Circular, 7427

Hawley, J. F., & Balbus, S. A., 1991, ApJ, 376, 223

Hawley, J. F., Balbus, S. A., & Stone, J. M., 2001, ApJ, 554, L49

Hawley, J. F., & Krolik, J. H., 2001, ApJ, 548, 348

Heitler, W., 1954, Quantum theory of radiation, (Oxford: International Series of Monographs on Physics)

Herrero, A., Kudritzki, R. P., Gabler, R., Vilchez, J. M., & Gabler, A., 1995, A&A, 297, 556

Hjellming, R. M., & Rupen, M. P., 1995, Nature, 375, 464

Hjellming, R. M., Rupen, M. P., Ghigo, F., Waltman, E. B., Mioduszewski, A. J., Fender, R. P., Stappers, B. W., Wieringa, M., Wark, R., & Green, D. W. E., et al., 1998a, IAU Circular, 6937

Hjellming, R. M., Rupen, M. P., Mioduszewski, A. J., Kuulkers, E., McCollough, M., Harmon, B. A., Buxton, M., Sood, R., Tzioumis, A., Rayner, D., Dieters, S., & Durouchoux, P., et al., 1999, ApJ, 514, 383

Hjellming, R. M., Rupen, M. P., Mioduszewski, A. J., Smith, D. A., Harmon, B. A., Waltman, E. B., Ghigo, F. D., & Pooley, G. G., 1998b, American Astronomical Society Meeting, 30, 1405

Homan, J., Wijnands, R., van der Klis, M., Belloni, T., van Paradijs, J., Klein-Wolt, M., Fender, R., & Méndez, M., 2001, ApJS, 132, 377

Hua, X., Kazanas, D., & Cui, W., 1999, ApJ, 512, 793

Hua, X., & Titarchuk, L., 1995, ApJ, 449, 188

Ichimaru, S., 1977, ApJ, 214, 840

Jahoda, K., Swank, J. H., Giles, A. B., Stark, M. J., Strohmayer, T., Zhang, W., & Morgan, E. H., 1996, SPIE, 2808, 59

Janiuk, A., Czerny, B., & Życki, P. T., 2000, MNRAS, 318, 180

Jernigan, J. G., Klein, R. I., & Arons, J., 2000, ApJ, 530, 875

Jones, C., Forman, W., Tananbaum, H., & Turner, M. J. L., 1976, ApJ, 210, L9

Kalemci, E., Tomsick, J. A., & Rothschild, R. E., 2000, AAS/High Energy Astrophysics Division, 32, 3105

Kalemci, E., Tomsick, J. A., Rothschild, R. E., Pottschmidt, K., & Kaaret, P., 2001, ApJ, 563, 239

Kalemci, E., Tomsick, J. A., Rothschild, R. E., Pottschmidt, K., Wijnands, R., Miller, J. M., & Kaaret, P., 2002, ApJ, in press, astro-ph/0205470

Kato, S., 1990, PASJ, 42, 99

Kazanas, D., & Hua, X., 1999, ApJ, 519, 750

Kazanas, D., Hua, X., & Titarchuk, L., 1997, ApJ, 480, 735

Kerr, R. P., 1963, Phys. Rev. Lett., 11, 237

Kitamoto, S., Tsunemi, H., Pedersen, H., Ilovaisky, S. A., & van der Klis, M., 1990, ApJ, 361, 590

Knoll, G. F., 1979, Radiation Detection and Measurement, (New York: John Wiley & Sons)

Kong, A. K. H., Charles, P. A., Kuulkers, E., & Kitamoto, S., 2002a, MNRAS, 329, 588

Kong, A. K. H., McClintock, J. E., Garcia, M. R., Murray, S. S., & Barret, D., 2002b, ApJ, 570, 277

Kotov, O., Churazov, E., & Gilfanov, M., 2001, MNRAS, 327, 799

Kuulkers, E., Dieters, S., McCollough, M., Wieringa, M., Buxton, M., & Remillard, R., 1998, IAU Circular, 6822

Kuulkers, E., Parmar, A. N., Kitamoto, S., Cominsky, L. R., & Sood, R. K., 1997, MNRAS, 291, 81

Leahy, D. A., Darbro, W., Elsner, R. F., Weisskopf, M. C., Kahn, S., Sutherland, P. G., & Grindlay, J. E., 1983, ApJ, 266, 160

Lee, H. C., & Miller, G. S., 1998, Mon. Not. R. Astron. Soc., 299, 479

Lehr, D. E., Wagoner, R. V., & Wilms, J., 1999, ApJ Letters, submitted

Levine, A. M., Bradt, H., Cui, W., Jernigan, J. G., Morgan, E. H., Remillard, R., Shirey, R. E., & Smith, D. A., 1996, ApJ, 469, L33

Li, H., Colgate, S. A., Wendroff, B., & Liska, R., 2001, ApJ, 551, 874

Liang, E. P. T., & Price, R. H., 1977, ApJ, 218, 247

Lin, D., Smith, I. A., Böttcher, M., & Liang, E. P., 2000, ApJ, 531, 963

Lin, D. N. C., & Taam, R. E., 1984, in High Energy Transients in Astrophysics, 83

Lochner, J. C., Swank, J. H., & Szymkowiak, A. E., 1991, ApJ, 376, 295

Makino, F., 1987, IAU Circular, 4342

Makishima, K., Maejima, Y., Mitsuda, K., Bradt, H. V., Remillard, R. A., Tuohy, I. R., Hoshi, R., & Nakagawa, M., 1986, ApJ, 308, 635

Malzac, J., Beloborodov, A. M., & Poutanen, J., 2001, MNRAS, 326, 417

Markert, T. H., Canizares, C. R., Clark, G. W., Lewin, W. H. G., Schnopper, H. W., & Sprott, G. F., 1973, ApJ, 184, L67

Markoff, S., Falcke, H., & Fender, R., 2000, A&A, 197, 8401

Markoff, S., Falcke, H., & Fender, R., 2001, A&A, 372, L25

Markwardt, C., 2001, Astrophysics and Space Science Supplement, 276, 209

Markwardt, C., Focke, W., & Swank, J., 2001, in X-ray Emission from Accretion onto Black Holes

Markwardt, C. B., Swank, J. H., & Taam, R. E., 1999, Ap. J., 513, L37

Marshall, F. E., & Smith, D. M., 1997, IAU Circular, 6603

Matteson, J. L., 1978, in AIAA, Aerospace Sciences Meeting

Mauche, C. W., 2002, ApJ, accepted, astro-ph/0207508

McClintock, J. E., Garcia, M. R., Caldwell, N., Falco, E. E., Garnavich, P. M., & Zhao, P., 2001, ApJ, 551, L147

McCollough, M. L., Harmon, B. A., Dieters, S., & Wijnands, R., 1999, IAU Circular, 7165

McConnell, M. L., Ryan, J. M., Collmar, W., Schönfelder, V., Steinle, H., Strong, A. W., Bloemen, H., Hermsen, W., Kuiper, L., Bennett, K., Phlips, B. F., & Ling, J. C., et al., 2000, ApJ, 543, 928

Méndez, M., Belloni, T., & van der Klis, M., 1998, ApJ, 499, 187

Méndez, M., & van der Klis, M., 1997, ApJ, 479, 926

Menou, K., Esin, A. A., Narayan, R., Garcia, M. R., Lasota, J., & McClintock, J. E., 1999, ApJ, 520, 276

Merloni, A., Fabian, A. C., & Ross, R. R., 2000, MNRAS, 313, 193

Miller, J. M., Fabian, A. C., Wijnands, R., Reynolds, C. S., & Ehle, M., 2002a, ApJ, 570, 69

Miller, J. M., Fox, D. W., Di Matteo, T., Wijnands, R., Belloni, T., Pooley, D., Kouveliotou, C., & Lewin, W. H. G., 2001, ApJ, 546, 1055

Miller, J. M., Fox, D. W., Pooley, D., & Lewin, W. H. G., 2000, ATEL, 60

Miller, J. M., Wijnands, R., Wojdowski, P., Groot, P., Fabian, A. C., van der Klis, M., & Lewin, W., 2002b, The Astronomer's Telegram, #81

Miller, M. C., & Hamilton, D. P., 2002, MNRAS, 330, 232

Miller, M. C., Lamb, F. K., & Psaltis, D., 1998, ApJ, 508, 791

Mineshige, S., & Wheeler, J. C., 1989, ApJ, 343, 241

Misra, R., Chitnis, V. R., & Melia, F., 1998, ApJ, 495, 407

Mitsuda, K., Inoue, H., Koyama, K., Makishima, K., Matsuoka, M., Ogawara, Y., Suzuki, K., Tanaka, Y., Shibazaki, N., & Hirano, T., et al., 1984, PASJ, 36, 741

Miyamoto, S., Kimura, K., Kitamoto, S., Dotani, T., & Ebisawa, K., 1991, ApJ, 383, 784

Miyamoto, S., & Kitamoto, S., 1989, Nature, 342, 773

Miyamoto, S., Kitamoto, S., Mitsuda, K., & Dotani, T., 1988, Nature, 336, 450

Molteni, D., Sponholz, H., & Chakrabarti, S. K., 1996, ApJ, 457, 805

Morgan, E. H., Remillard, R. A., & Greiner, J., 1997, ApJ, 482, 993

Morrison, R., & McCammon, D., 1983, ApJ, 270, 119

Murdin, P., & Webster, B. L., 1971, Nature, 233, 110

Narayan, R., Garcia, M. R., & McClintock, J. E., 2001, in Invited review, to appear in Proc. IX Marcel Grossmann Meeting, eds. V. Gurzadyan, R. Jantzen and R. Ruffini, Singapore: World Scientific, 7387

Narayan, R., Mahadevan, R., Grindlay, J. E., Popham, R. G., & Gammie, C., 1998, ApJ, 492, 554

Narayan, R., Mahadevan, R., & Quataert, E., 1998, in Theory of Black Hole Accretion Disks, 148

Narayan, R., McClintock, J. E., & Yi, I., 1996, ApJ, 457, 821

Narayan, R., & Yi, I., 1995, ApJ, 452, 710

Nobili, L., 2002, in accepted for publication in ApJ

Nolan, P. L., Gruber, D. E., Matteson, J. L., Peterson, L. E., Rothschild, R. E., Doty, J. P., Levine, A. M., Lewin, W. H. G., & Primini, F. A., et al., 1981, ApJ, 246, 494

Nowak, M., & Lehr, D., 1998, in Theory of Black Hole Accretion Disks, 233

Nowak, M. A., 2000, MNRAS, 318, 361

Nowak, M. A., 2002, in Proceedings of the 4th Microquasar Workshop, 2002, eds. Durouchoux, Fuchs, Rodriguez, to be published by the Center for Space Physics: Kolkata, 7624

Nowak, M. A., Vaughan, B. A., Wilms, J. ., Dove, J. B., & Begelman, M. C., 1999, ApJ, 510, 874

Nowak, M. A., Wilms, J. ., & Dove, J. B., 1999, ApJ, 517, 355

Nowak, M. A., Wilms, J., & Dove, J. B., 2002, MNRAS, 332, 856

Ogley, R. N., Ash, T. D. C., & Fender, R. P., 1997, IAU Circular, 6726

Oosterbroek, T., Parmar, A. N., Kuulkers, E., Belloni, T., van der Klis, M., Frontera, F., & Santangelo, A., 1998, A&A, 340, 431

Orosz, J., Bailyn, C., & Jain, R., 1998, IAU Circular, 7009

Orosz, J. A., & Bailyn, C. D., 1997, ApJ, 482, 1086

Orosz, J. A., Groot, P. J., van der Klis, M., McClintock, J. E., Garcia, M. R., Zhao, P., Jain, R. K., Bailyn, C. D., & Remillard, R. A., et al., 2002, ApJ, 568, 845

Orosz, J. A., van der Klis, M., McClintock, J. E., Jain, R. K., Bailyn, C. D., & Remillard, R. A., 2001, The Astronomer's Telegram, 70

Osaki, Y., 1985, A&A, 144, 369

Papoulis, A. P., 1991, Probability, Random Variance and Stochastic Processes,

(New York: McGraw-Hill)

Pelling, M. R., Rothschild, R. E., MacDonald, D. R., Hertel, R., & Nishiie, E., 1991, in EUV, X-ray, and gamma-ray instrumentation for astronomy II; Proceedings of the Meeting, San Diego, CA, July 24-26, 1991 (A93-34376 13-35), p. 134-146., Vol. 1549, 134

Pooley, G. G., & Hjellming, R. M., 1999, IAU Circular, 7278

Pooley, G. G., & Waldram, E. M., 2000, IAU Circular, 7390

Pottschmidt, K., Koenig, M., Wilms, J., & Staubert, R., 1998, A&A, 334, 201

Pottschmidt, K., Wilms, J., Nowak, M. A., Heindl, W. A., Smith, D. M., & Staubert, R., 2000, A&A, 357, L17

Pottschmidt, K., Wilms, J., Nowak, M. A., Pooley, P. P., Gleissner, T., Heindl, W. A., Smith, D. M., Remillard, R., & Staubert, R., et al., 2002, A&A, submitted, astro-ph/0202258

Poutanen, J., 1998, in Theory of Black Hole Accretion Disks, eds.Abramowicz, M. A. and Bjornsson, G. and Pringle, J. E.

Poutanen, J., 2001, Advances in Space Research, 28, 267

Poutanen, J., & Fabian, A. C., 1999, MNRAS, 306, L31

Predehl, P., 1998, Ap&SS, 258, 89

Predehl, P., & Schmitt, J. H. M. M., 1995, A&A, 293, 889

Pringle, J. E., 1976, MNRAS, 177, 65

Psaltis, D., 2001, ApJ, 555, 786

Psaltis, D., Belloni, T., & van der Klis, M., 1999, ApJ, 520, 262

Psaltis, D., & Norman, C., 2000, ApJ, submitted, astro-ph/001391

Quataert, E., 1998, ApJ, 500, 978

Remillard, R., 2001, IAU Circular, 7707

Remillard, R., Bradt, H., Cui, W., Levine, A., Morgan, E., Shirey, B., & Smith, D., 1996, IAU Circular, 6393

Remillard, R., Levine, A., Swank, J., & Strohmayer, T., 1997, IAU Circular, 6710

Remillard, R., Marshall, F., & Takeshima, T., 1997, IAU Circular, 6772

Remillard, R., Morgan, E., Smith, D., & Smith, E., 2000, IAU Circular, 7389

Remillard, R. A., 2000, in Evolution of Binary and Multiple Stars, Procs. Conf. in Bormio, Italy, eds. P. Podsiadlowski, S. Rappaport, A. King, F. D'Antona, and L. Burderi, astro-ph/0103431

Remillard, R. A., McClintock, J. E., Sobczak, G. J., Bailyn, C. D., Orosz, J. A., Morgan, E. H., & Levine, A. M., 1999a, ApJ, 517, L127

Remillard, R. A., Morgan, E. H., McClintock, J. E., Bailyn, C. D., & Orosz, J. A., 1999b, ApJ, 522, 397

Remillard, R. A., Muno, M. P., McClintock, J. E., & Orosz, J. A., 2002a, in 11 pages, 5 figs.; Procs. of the 4th Microquasar Workshop, 2002, eds. Durouchoux, Fuchs, Rodriguez, (Center for Physics: Kolkata), 8402

Remillard, R. A., Sobczak, G. J., Muno, M. P., & McClintock, J. E., 2002b, ApJ, 564, 962

Revnivtsev, M., Gilfanov, M., & Churazov, E., 1998, A&A, 339, 483

Revnivtsev, M., Gilfanov, M., & Churazov, E., 2001, A&A, 380, 520

Revnivtsev, M., Sunyaev, R., & Borozdin, K., 2000, A&A, 361, L37

Revnivtsev, M. G., Borozdin, K. N., Priedhorsky, W. C., & Vikhlinin, A., 2000, ApJ, 530, 955

Revnivtsev, M. G., Trudolyubov, S. P., & Borozdin, K. N., 2000, MNRAS, 312, 151

Rhoades, C. E., & Ruffini, R., 1974, Phys. Rev. Lett., 32, 324

Rodriguez, J., Corbel, S., Kalemci, E., & Tomsick, J. A., 2002a, in submitted to ApJ

Rodriguez, J., Corbel, S., Kalemci, E., Tomsick, J. A., & Tagger, M., 2002b, in 4 pages, 3 figures; Proceedings of the 4th Microquasar Workshop, 2002, eds.

Durouchoux, Fuchs, Rodriguez, to be published by the Center for Space Physics: Kolkata, 7649

Ross, R. R., Fabian, A. C., & Young, A. J., 1999, MNRAS, 306, 461

Rothschild, R., Boldt, E., Holt, S., Serlemitsos, P., Garmire, G., Agrawal, P., Riegler, G., Bowyer, S., & Lampton, M., et al., 1979, Space Science Instrumentation, 4, 269

Rothschild, R. E., Blanco, P. R., Gruber, D. E., Heindl, W. A., MacDonald, D. R., Marsden, D. C., Pelling, M. R., Wayne, L. R., & Hink, P. L., et al., 1998, ApJ, 496, 538

Rupen, M. P., Hjellming, R. M., & Mioduszewski, A. J., 1998, IAU Circular, 6938

Rutledge, R. E., Lewin, W. H. G., van der Klis, M., van Paradijs, J., Dotani, T., Vaughan, B., Belloni, T., Oosterbroek, T., & Kouveliotou, C., et al., 1999, ApJS, 124, 265

Rybicki, G. B., & Lightman, A. P., 1979, Radiative processes in astrophysics, (New York: Wiley-Interscience)

Sanchez-Fernandez, C., Zurita, C., Casares, J., Bond, I., Bradt, S., & Lund, N., 2002, IAU Circular, 7989

Schwarzschild, K., 1916, Sitzber. Dtsc. Akad. Wiss. Berlin Math. Phys. Tech. Kl., 189

Serlemitsos, P. J., Becker, R. H., Boldt, E. A., Holt, S. S., Pravdo, S. H., Rothschild, R. E., & Swank, J. H., 1976, in X-ray Binaries, 67

Shakura, N. I., 1972, AZh, 49, 921

Shakura, N. I., & Sunyaev, R. A., 1973, A&A, 24, 337

Shapiro, S. L., Lightman, A. P., & Eardley, D. M., 1976, ApJ, 204, 187

Shapiro, S. L., & Teukolsky, S. A., 1983, Black holes, white dwarfs, and neutron stars: The physics of compact objects, (New York: John Wiley & Sons)

Smith, D. A., 1998, IAU Circular, 7008

Smith, D. A., Levine, A., & Wood, A., 1998, IAU Circular, 6932

Smith, D. A., Levine, A. M., Remillard, R., Fox, D., Schaefer, R., & RXTE/ASM Team 2000, IAU Circular, 7399

Smith, D. M., Belloni, T., Heindl, W. A., Kalemci, E., Remillard, R., Nowak, M., Swank, J. H., & Corbel, S., 2002, IAU Circular, 7912

Smith, D. M., Heindl, W. A., Swank, J., Leventhal, M., Mirabel, I. F., & Rodriguez, L. F., 1997, ApJ, 489, L51

Sobczak, G. J., McClintock, J. E., Remillard, R. A., Cui, W., Levine, A. M., Morgan, E. H., Orosz, J. A., & Bailyn, C. D., 2000, ApJ, 544, 993

Sobczak, G. J., McClintock, J. E., Remillard, R. A., Cui, W., Levine, A. M., Morgan, E. H., Orosz, J. A., & Bailyn, C. D., 2000, Ap. J., 531, 537

Sobczak, G. J., McClintock, J. E., Remillard, R. A., Levine, A. M., Morgan, E. H., Bailyn, C. D., & Orosz, J. A., 1999, ApJ, 517, L121

Sood, R., & Campbell-Wilson, D., 1994, IAU Circular, 6006

Soria, R., Bessell, M. S., & Wood, P., 1997, IAU Circular, 6781

Spruit, H. C., 2001, in The neutron star - black hole connection, Proceedings of the NATO Advanced Study Institute, Elounda, Crete, Greece, 7-18 June 1999. Edited by Chryssa Kouveliotou, Joseph Ventura, and Ed Van den Heuvel. Dordrecht: Kluwer Academic Publishers, 2001. NATO science series C: Mathematical and physical sciences, Vol. 567., 111

Stella, L., Vietri, M., & Morsink, S. M., 1999, ApJ, 524, L63

Strohmayer, T. E., 2001a, ApJ, 552, L49

Strohmayer, T. E., 2001b, ApJ, 554, L169

Sunyaev, R., Churazov, E., Revnivtsev, M., Trudolyubov, S., Vargas, M., Paul, J., Roques, J.-P., & Jourdain, E., 1997, iauc, 6599

Sunyaev, R., & Revnivtsev, M., 2000, A&A, 358, 617

Sunyaev, R. A., & Titarchuk, L. G., 1980, A&A, 86, 121

Sunyaev, R. A., & Trümper, J., 1979, Nature, 279, 506

Svensson, R., 1998, in Theory of Black Hole Accretion Disks, eds.Abramowicz, M. A. and Bjornsson, G. and Pringle, J. E.

Swank, J., 2001, Astrophysics and Space Science Supplement, 276, 201

Swank, J., Smith, E., & Markwardt, C., 2002, IAU Circular, 7792

Tagger, M., & Pellat, R., 1999, A&A, 349, 1003

Takeuchi, M., Mineshige, S., & Negoro, H., 1995, PASJ, 47, 617

Tanaka, Y., & Lewin, W. H. G., 1995, in X-ray Binaries, ed. W. H. G. Lewin, J. Van Paradjs, E. P. J. Van den Heuvel, (Cambridge: Cambridge U. Press), 126

Tanaka, Y., & Shibazaki, N., 1996, ARA&A, 34, 607

Terrell, N. J. J., 1972, ApJ, 174, L35

Titarchuk, L., 1994, ApJ, 434, 570

Titarchuk, L., & Osherovich, V., 2000, ApJ, 542, L111

Tomsick, J. A., Corbel, S. ., & Kaaret, P., 2001, ApJ, 563, 229

Tomsick, J. A., Corbel, S., Kalemci, E., & Kaaret, P., 2002a, submitted to APJ

Tomsick, J. A., & Heindl, W. A., 2000, IAU Circular, 7456

Tomsick, J. A., & Kaaret, P., 2000, ApJ, 537, 448

Tomsick, J. A., & Kaaret, P., 2001, ApJ, 548, 401

Tomsick, J. A., Kaaret, P., Kroeger, R. A., & Remillard, R. A., 1999, ApJ, 512, 892

Tomsick, J. A., Kalemci, E., Corbel, S., & Kaaret, P., 2002b, IAU Circular, 7837

Tomsick, J. A., Smith, E., Swank, J., Wijnands, R., & Homan, J., 2001, IAU Circular, 7575

Trudolyubov, S., Churazov, E., Gilfanov, M., Revnivtsev, M., Sunyaev, R., Khavenson, N., Dyachkov, A., Tserenin, I., Vargas, M., Goldoni, P., Laurent, P., Paul, J., Jourdain, E., Roques, J.-P., Mandrou, P., & Vedrenne, G., et al., 1999, A&A, 342, 496

Turner, M. J. L., Thomas, H. D., Patchett, B. E., Reading, D. H., Makishima, K., Ohashi, T., Dotani, T., Hayashida, K., Inoue, H., Kondo, H., Koyama, K., Mitsusa, K., Ogawara, Y., Takano, S., Awaki, H., Tawara, Y., & Nakamura, N., et al., 1989, PASJ, 41, 345

Ueda, Y., Dotani, T., Uno, S., Inoue, H., Nagase, F., Maeda, Y., Sakano, M., Durouchoux, P., & Swank, J. H., et al., 1997, IAU Circular, 6627

Uemura, M., Kato, T., Matsumoto, K., Iwamatsu, H., Ishioka, R., Cook, L. M., Dmitrienko, E., Simon, V., Honkawa, M., Oksanen, A., Moilanen, M., Novak, R., Martin, B., Lipkin, Y., Leibowitz, E. M., Masi, G., Sano, Y., Nogami, D., Buczynski, D., Yamaoka, H., Takamizawa, K., & Haseda, K., et al., 2002, PASJ, 54, 285

van der Klis, M., 1989, in Timing Neutron Stars, Eds. H. Ogelman, J. van den Huevel, 27

van der Klis, M., 1995, in X-ray binaries, Eds. W. H. G. Lewin, J. van Paradjs, E. P. J. van den Huevel, 252

van Straaten, S., van der Klis, M., di Salvo, T., & Belloni, T., 2002, ApJ, 568, 912

Varnière, P., Rodriguez, J., & Tagger, M., 2002, A&A, 387, 497

Vaughan, B. A., & Nowak, M. A., 1997, ApJ, 474, L43

Vignarca, F., Migliari, S., Belloni, T., Psaltis, D., & van der Klis, M., 2002, A&A, in press.

Wagner, R. M., Foltz, C. B., Shahbaz, T., Casares, J., Charles, P. A., Starrfield, S. G., & Hewett, P., 2001, ApJ, 556, 42

Weisskopf, M. C., Sutherland, P. G., Katz, J. I., & Canizares, C. R., 1978, ApJ, 223, L17

Wijnands, R., Homan, J., & van der Klis, M., 1999, ApJ, 526, L33

Wijnands, R., Miller, J. M., & Lewin, W. H. G., 2001, IAU Circular, 7715

Wijnands, R., & van der Klis, M., 1999, ApJ, 514, 939

Wilms, J., 1998, *Ph.D. Thesis,* Universität Tübingen, Tübingen

Wilms, J. ., Nowak, M. A., Dove, J. B., Fender, R. P., & di Matteo, T., 1999, ApJ, 522, 460

Wilson, C. A., & McCollough, M. L., 2000, IAU Circular, 7390

Wood, A., Smith, D. A., Marshall, F. E., & Swank, J., 1999, IAU Circular, 7274

Wood, K. S., Ray, P. S., Bandyopadhyay, R. M., Wolff, M. T., Fritz, G., Hertz, P., Kowalski, M. P., Lovellette, M. N., Yentis, D., Bloom, E. D., Giebels, B., Godfrey, G., Reilly, K., Saz Parkinson, P., Shabad, G., & Scargle, J., et al., 2000, ApJ, 544, L45

Zdziarski, A. A., 2000, in High Energy Processes in Accreting Black Holes: ASP Conf. Ser. 161: High Energy Processes in Accreting Black Hole: eds. Poutanen, J. and Svensson, R.: (1999)

Zdziarski, A. A., Gilfanov, M., Lubiński, P., & Revnivtsev, M., 2002, submitted to MNRAS, astroph/0209363

Zdziarski, A. A., Poutanen, J., Mikolajewska, J., Gierlinski, M., Ebisawa, K., & Johnson, W. N., 1998, MNRAS, 301, 435

Zhang, W., Jahoda, K., Swank, J. H., Morgan, E. H., & Giles, A. B., 1995, ApJ, 449, 930

Zhang, W., Morgan, E. H., Jahoda, K., Swank, J. H., Strohmayer, T. E., Jernigan, G., & Klein, R. I., 1996, apjl, 469, L29

Zycki, P. T., 2002, MNRAS, in press.